Defect level identification in acceptor-doped polycrystalline barium titanate

Electrical characterization, XPS interface analysis, and degradation behaviour
Zur Erlangung des akademischen Grades Doktor-Ingenieur (Dr.-Ing.)
Genehmigte Dissertation von Katharina Natalie Silvana Lohaus aus Gießen
Tag der Einreichung: 20.04.2023, Tag der Prüfung: 24.07.2023

1. Gutachten: Prof. Dr. Andreas Klein
2. Gutachten: Assist. Prof. Dr. Jurij Koruza
Darmstadt, Technische Universität Darmstadt

TECHNISCHE
UNIVERSITÄT
DARMSTADT

Fachbereich Material- und Geowissenschaften

Electronic Structure of Materials

Defect level identification in acceptor-doped polycrystalline barium titanate
Electrical characterization, XPS interface analysis, and degradation behaviour

Genehmigte Dissertation von Katharina Natalie Silvana Lohaus

Tag der Einreichung: 20.04.2023
Tag der Prüfung: 24.07.2023

Darmstadt, Technische Universität Darmstadt

Erklärungen laut Promotionsordnung

§8 Abs. 1 lit. c PromO

Ich versichere hiermit, dass die elektronische Version meiner Dissertation mit der schriftlichen Version übereinstimmt.

§8 Abs. 1 lit. d PromO

Ich versichere hiermit, dass zu einem vorherigen Zeitpunkt noch keine Promotion versucht wurde. In diesem Fall sind nähere Angaben über Zeitpunkt, Hochschule, Dissertationsthema und Ergebnis dieses Versuchs mitzuteilen.

§9 Abs. 1 PromO

Ich versichere hiermit, dass die vorliegende Dissertation selbstständig und nur unter Verwendung der angegebenen Quellen verfasst wurde.

§9 Abs. 2 PromO

Die Arbeit hat bisher noch nicht zu Prüfungszwecken gedient.

Darmstadt, 20.04.2023

_____

K. N. S. Lohaus

Contents

1. Why defect energy levels matter for the resistance degradation of multi-layer ceramic capacitors

Motivation

Multi-layer ceramic capacitors (MLCC) store and release electrical charge and are used to distribute and control the amount of current flowing through electrical circuits, remove noise and/or prevent from malfunction [1]. MLCC-products play a key role in modern electronic devices and cover almost all areas that require electronic components, such as smart phones, laptops, smart grits, automotive and aerospace electronics, rail transportation, and many more industrial fields [1]. Nowadays, Pb-based MLCCs are avoided due to environmental issues regarding its toxicity and conventional MLCCs are based on polycrystalline barium titanate (BaTiO$_3$) due to its beneficial dielectric properties [1]. The trend toward smaller, lighter, and ubiquitous electronic devices requires high volume-efficiency, high reliability, and low electronic power consumption. The down-scaling of the capacitors thickness with constants electric field leads to an increasing field stress of the dielectric [2].

A characteristic feature and major restriction of BaTiO$_3$-based MLCCs is the increasing leakage current as a result of a decreasing insulation resistance during simultaneous temperature and voltage stress. As the reliability and life time of MLCCs is limited by resistance degradation [3], the process has been extensively studied for more than half a century [2–11]. The most commonly accepted theory describing the underlying mechanism of resistance degradation in titanates is the ionic de-mixing model [4–6]: At elevated temperatures and high electric fields oxygen vacancies migrate towards the cathode, which eventually leads to accumulation in the cathode region and a depletion in the anode region. This oxygen vacancy rearrangement results in an increased electron and hole concentration in the respective region and an overall decreased resistance of the capacitor. Based on the de-mixing model, theoretical studies have simulated the drift-diffusion of oxygen vacancies as well as the resulting concentration profile and resistance changes. These simulations well describe the electrocoloration of degraded single crystals and even allow to reproduce the time-dependent increase of leakage current

for polycrystals [3, 6, 12]. However, neither the ionic de-mixing model nor the corresponding simulation could capture other observations, such as the appearance of a strong chemical reduction of the dielectric near the cathode [13, 14] or the observation of oxygen bubbles underneath a platinum anode [10]. These observations indicate that the ionic de-mixing model well describes the physical process inside the dielectric bulk, but that it is incomplete with regard to the dielectric-electrode interfaces.

Oxygen exchange at the electrode interfaces is of particular importance for the performance of the capacitor, as it will modify the total oxygen vacancy concentration in the dielectric, which determines the leakage current and degradation behavior [10, 15]. The extraction and incorporation of oxygen at the dielectric-electrode interfaces can be effectively modified by ionic space charge regions (SCR) [16]. The difference between the Fermi level in the dielectric bulk and at the interface determines the sign and the magnitude of the band bending. The direction of band bending determines, whether oxygen vacancies are accumulated or depleted in the space charge region. Accordingly, the difference in bulk and interface Fermi level determines if and how fast oxygen is incorporated at the cathode and extracted at the anode. The interface Fermi level can be controlled by the selection of electrode materials. The influence of different electrode material combinations, electrode thicknesses, and electrical polarization states on the oxygen exchange and degradation characteristics of Fe-doped single crystalline $SrTiO_3$ and/or Mn-doped polycrystalline $BaTiO_3$ has been already studied in previous works [14, 17–19].
The bulk Fermi level can be controlled by doping, using dopants with known defect energy levels. This approach is based on the mechanism of Fermi level pinning at defect energy levels. These levels, often also called charge transition points, define the energetic position in the band gap, where valence changes occur. Transition-metal dopants generate defect energy levels deep inside the band gap [20]. Due to these deep traps, the Fermi level cannot move freely and will be pinned at the defect energy levels. If the position of the defect energy levels is known, the bulk Fermi energy can be exactly predicted for given equilibrium conditions by defect chemistry calculations [21, 22].
Moreover, doping of elements with known defect energy level positions can be used to systematical adjust the bulk Fermi level at a desired value. Combined Fermi level engineering of interface (by the selection the electrode material) and bulk Fermi level (by dopant selection based on a desired defect energy level) should allow systematic tuning of the space charge potential, which determines the oxygen incorporation and extraction at the electrodes. Hence, bulk Fermi level adjustment via Fermi level pinning on defect energy levels represents one out of two parameters, which needs to be tuned in order to control the oxygen exchange through the electrode interface. This approach has the potential to provide a new method to decrease resistance degradation and thereby increase the life time of MLCCs.

However, knowledge on the position of the defect energy levels is the key parameter and thus, reliable values for all potential dopants are essential.

In electrical semiconducting materials the position of shallow energy levels can be determined by Hall measurements, while deep energy levels can be identified using deep level transition spectroscopy and admittance spectroscopy [22–24]. However, these techniques cannot be applied to $BaTiO_3$ due to its high resistance [22]. In polycrystalline $BaTiO_3$ the defect energy levels of Mn and Fe have been determined via gravimetric measurements by Hagemann and Hennings [25] and have been collected in the publication by Wechsler and Klein [21]. Schwartz and Wechsler [26] established the position of the defect energy levels from electro-paramagnetic-resonance spectroscopy on Mn- and Fe-doped $BaTiO_3$. The values of both studies are consistent, but other literature reveals a larger range of theses values [27]. Hence, complementary methods for defect level identification in polycrystalline $BaTiO_3$ are highly desirable.

Objective and Structure of this work

The goal of this thesis is to elaborated two promising methods, which enabled defect level identification in thin film semiconductors and/or single crystalline $BaTiO_3$, but which have not been validated to be applicable for polycrystalline $BaTiO_3$, yet. In the following, central aspects of the elaborated interface and re-oxidation approach are briefly reviewed:

1. The interface approach
This approach is based on the Fermi level evaluation by means of photoelectron spectroscopy (PES) measurements during contact formation to materials with different work functions. For a successful defect level identification the SCR width needs to be of a comparable size as the inelastic mean free path (IMFP) of the photoelectrons, which can be achieved by high doping concentrations. Once the SCR is narrower than the IMFP, the PES binding energies refer to the bulk Fermi level, which is pinned on the defect levels. For $SrTiO_3$, ZnO, and Cu_2O, defect-related barrier modifications and Fermi level pinning at the interface have been observed by dedicated PES interface experiments [14, 28–30]. For polycrystalline $BaTiO_3$ no studies on defect energy level identification by means of photoelectron spectroscopy are available, yet.

2. The Re-Oxidation Approach
This approach is based on the evaluation of the activation energy of electrical conductivity as a function of oxygen vacancy concentration during slow re-oxidation. This approach has been first demonstrated by Suzuki *et al.*, who successfully identified the Fe defect level in single crystalline $SrTiO_3$ and $BaTiO_3$ by this method [22]. In polycrystalline materials, the activation

energy of the electrical conductivity is affected by grain boundaries. Thus, a direct extraction of the defect energy levels from the activation energy is not possible for polycrystals. However, simulations of the current flow across the grain boundaries might allow to separate the grain boundary contribution from the measured activation energies. Thereby, it would still be possible to extract defect energy levels via the re-oxidation approach.

The **objective of this work** is to elaborate to which extend both approaches can be used to determine the charge transition levels of muli-valent acceptors in the band gap of polycrystalline $BaTiO_3$. For this purpose, Mn- and Fe-doped polycrystalline $BaTiO_3$ with different doping concentrations have been synthesized via the conventional solid-state-reaction method. Fe has been chosen as dopant, as it is the most abundant impurity in $BaTiO_3$-based MLCCs, with concentrations between 5 to 100 ppm [22, 25, 31, 32]. Mn has been chosen as dopant, as it is commonly used to reduce the leakage current of $BaTiO_3$-based MLCCs and is often used in co-doped $BaTiO_3$ for positive temperature coefficient of resistivity (PTCR) applications [33, 34]. With regard to the chosen dopants, the major goal of this work is to answer the two following questions:

1. *Are PES interface experiments a suitable method to identify the defect energy levels of Mn-doped polycrystalline $BaTiO_3$?*

2. *To which extend can the re-oxidation approach be applied to identify the defect energy levels of Mn- and Fe-doped polycrystalline $BaTiO_3$?*

Besides the main focus on defect level identification, both doping series have been extensively studied by several characterization methods in order to investigate the influence of acceptor doping on:

- *Crystal structure & microstructure*
- *Dielectric & ferroelectric properties*
- *Degradation behavior*

The influence of acceptor doping on the above mentioned properties is widely studied in literature. However, none of the publications provides information about all properties at once. The results of this work represents a comprehensive study on one set of samples and are compared to the state-of-the-art literature in the respective field.

The **structure of this work** is schematically shown in the flow chart in Figure 1.1. The quality of the synthesized samples is validated and compared to literature in Chapter 5. In Chapter 6 the interface approach is elaborated, while Chapter 7 details the re-oxidation approach. The influence of Mn- and Fe-doping on the degradation performance of polycrystalline $BaTiO_3$ is studied in Chapter 8. The main out-come of this work is summarized in Chapter 9.
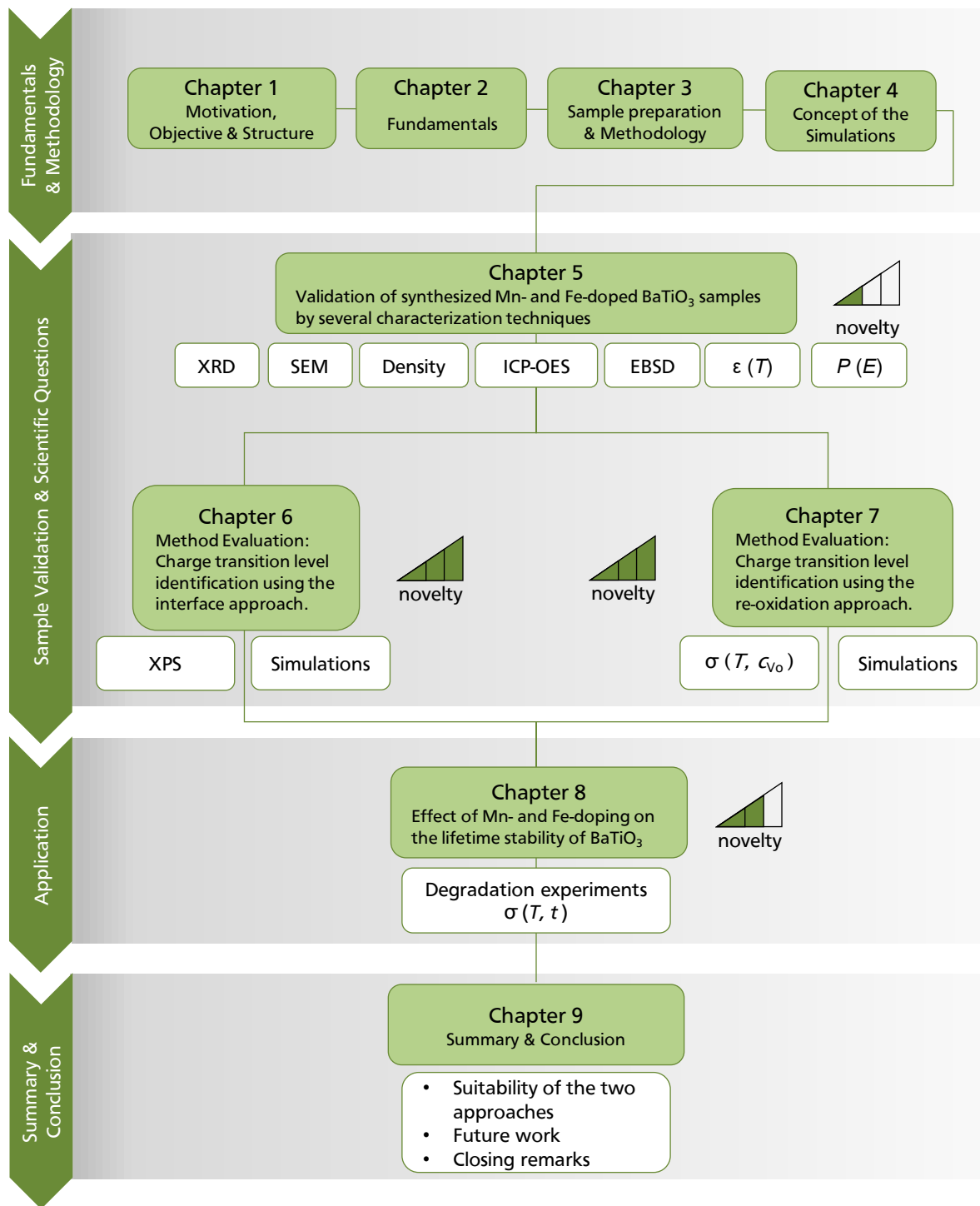
Figure 1.1.: Flow chart showing the structure of this work. The scientific work is separated in four Chapters 5 to 8. First, the quality of the synthesized samples is validated and compared to literature in Chapter 5. Chapters 6 and Chapters 7 detail the evaluation of the interface and the re-oxidation approach for charge transition level identification, respectively. These two Chapters represent the heart of the present work. In Chapter 8 the influence of acceptor doping on the degradation behavior is studied. The novelty of the experiments and simulations with respect to the current available literature is indicated for each Chapter.

2. Fundamentals

2.1. From Dielectrics to Ferroelectrics

The basic dielectic and ferroelectric properties are intensively studied in literature. The following Chapter on the fundamental properties is based on the standard textbooks [35–39].

Ferroelectrics are a sub-group of the broad group of dielectrics. The latter are defined as electric insulators, which can be polarized by an electric field. In addition, ferroelectric materials exhibit a spontaneous polarization, which can be reversed by an external electric field. Whether a material is ferroelectric or not can be extracted from the present symmetry elements of its crystal class as illustrated in Fig. 2.1. Among the 32 different crystal classes, 21 are non-centrosymmetric, i.e. have no inversion center. If mechanical stress is applied, the lattice will be distorted and positive and negative charges will be displaced. For centrosymmetric
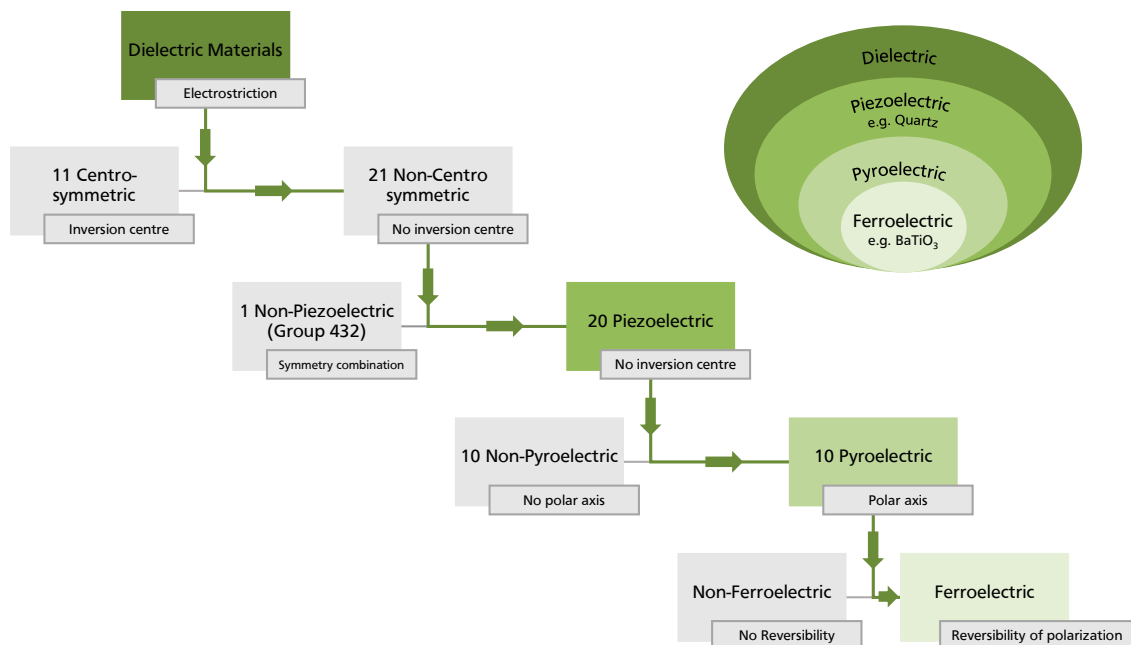
Figure 2.1.: Interrelation among dielectrics, piezoelectrics, pyroelectrics, and ferroelectrics. The division of the 32 classes according to the symmetry requirements for each subgroup are sketched as tree diagram.

systems the overall charge displacement will cancel out, while for non-centrosymmetric systems an overall displacement of positive and negative charge, and thus a polarization, will be generated. The introduction of electric charge polarization by applying strain/stress is defined as piezoelectricity. Due to higher symmetry combinations only 20 of the non-centrosymmetric crystal classes are piezoelectric.

10 of the non-centrosymmetric crystal classes are polar and exhibit a spontaneous polarization, which means that those crystal classes have a temperature-dependent natural charge separation even in absence of an external electric field. The occurrence of a temperature-dependent spontaneous polarization is called pyroelectricity. Ferroelectrics have the same crystallographic precondition as pyroelectrics. The additional characteristic of ferroelectrics is the reversibility of the spontaneous polarization by applying an external electric field.

2.1.1. Macroscopic and microscopic polarization

If an electric field is applied to a material with a high density of free charges, such as a metal, the electronic current can flow easily through the samples. In the case of electric insulators the number of free charge carriers is very low and an applied electric field does not result in long term transport but in short-movement, i.e. a polarization. For an isotropic, linear dielectric the polarization P is proportional to the electric field E given by

$$P = \epsilon_0 \chi E, \qquad (2.1)$$

where ϵ_0 is the vacuum permittivity, and χ the electric susceptibility, which is related to the relative permittivity ϵ_r by $\chi = \epsilon_r - 1$. Even though the relative permittivity is often termed as the dielectric constant, it is not a constant per definition, but depends on extrinsic factors such as the electric field, temperature, frequency etc.

The dielectric displacement D equals the sum of the vacuum contribution $\epsilon_0 E$ and the polarization contribution P, which can be simplified by

$$D = \epsilon_0 E + P = \epsilon_0 E + \epsilon_0 \chi E = \epsilon_0 (1 + \chi) E = \epsilon_0 \epsilon_r E. \qquad (2.2)$$

The capacitance C is defined as the ratio of the total electric charge Q_T to the electric potential U. For a parallel plate capacitor the displacement is linked to the total charge density σ_T by $D = \sigma_T = Q_T/A$, where A defines the area of the capacitor plates. Hence, the capacitance can be expressed by

$$C = \frac{Q_T}{U} = \epsilon_0 \epsilon_r \frac{A}{d}. \qquad (2.3)$$

In linear dielectrics the relation between the polarization and the applied electric field in Equation 2.3 is approximately constant and ϵ_r is field-independent. In non-linear dielectric, ϵ_r becomes strongly field-dependent and can be described by

$$\epsilon_r = \frac{1}{\epsilon_0} \frac{\delta P}{\delta E}. \tag{2.4}$$

The different types of field-dependent polarization are depicted in Figure 2.2. In dielectrics the field-dependent polarization is linear. The paraelectric state is described by a non-linear field-dependence. In the ferroelectric state the field-dependence is characterized by a hysteresis curve. In the initial state the domains are alignment randomly and no net polarization is observed. When increasing the field the unfavorable orientated domains will start to switch. For a certain electric field most of the domains are aligned and the polarization increases only slightly. When the field is removed most of the domains remain orientated and only some domains will start to switch back, resulting in a remanent polarization P_R for an electric field of zero. An electric field lower than the coercive field E_C is required to reverse the polarization. Hence, the polarization of ferroelectric materials not only depends on the direction and magnitude of the applied electric field, but also on the history of polarization.
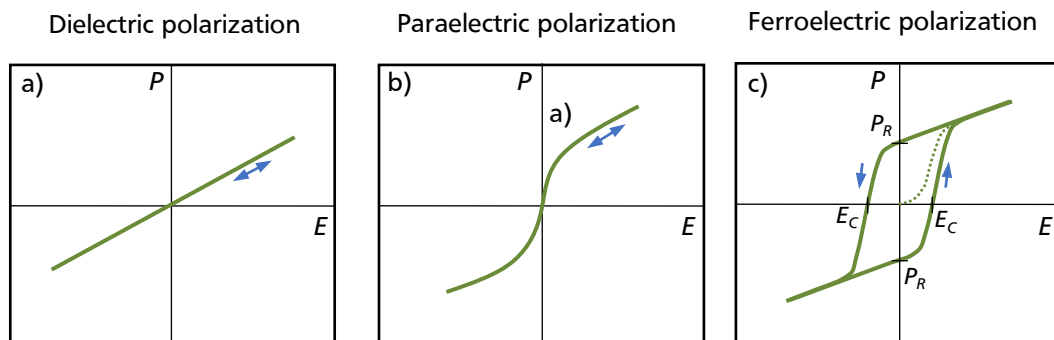
Figure 2.2.: Different forms of polarization: a) dielectric, b) paraelectric, and c) ferroelectric. The illustrations were redrawn from Ref. [40].

On a microscopic point of view different mechanisms contribute to the polarization, which is schematically illustrated for the unpolarized and polarized state in Figure 2.3:
Space charge polarization can be observed as a result of spatial inhomogeneities in the charge carrier density. The space charge potential is caused by the limited transport of mobile ions and/or electrons due to potential barriers. Hence, space charges can occur at electrode/dielectric interfaces or at grain boundaries in ceramics (Maxwell-Wagner-polarization).
Dipolar polarization or orientation polarization describes the alignment of permanent dipoles as response to an applied electric field. The average degree of orientation is affected by the

electric field and by thermal movement of the atoms. While the former promotes the alignment of dipoles, the latter promotes an isotropic distribution of dipoles and, thus, perturbs alignment.

Ionic charge polarization can be observed in ionic crystals, were an applied electric field results in an non-uniform displacement of the cation and anion sublattices.

Atomic charge polarization or electronic polarization describes the displacement of the negative shell against the positive core of an atom. This kind of polarization mainly depends on the shell volume and is temperature-independent. It exists in all dielectric materials.

In ferroelectric materials **domain wall polarization** represents an additional factor to the overall dielectric response. When an electric field is applied the domain walls with favored orientation will grow, which leads to a motion and switching of domains.
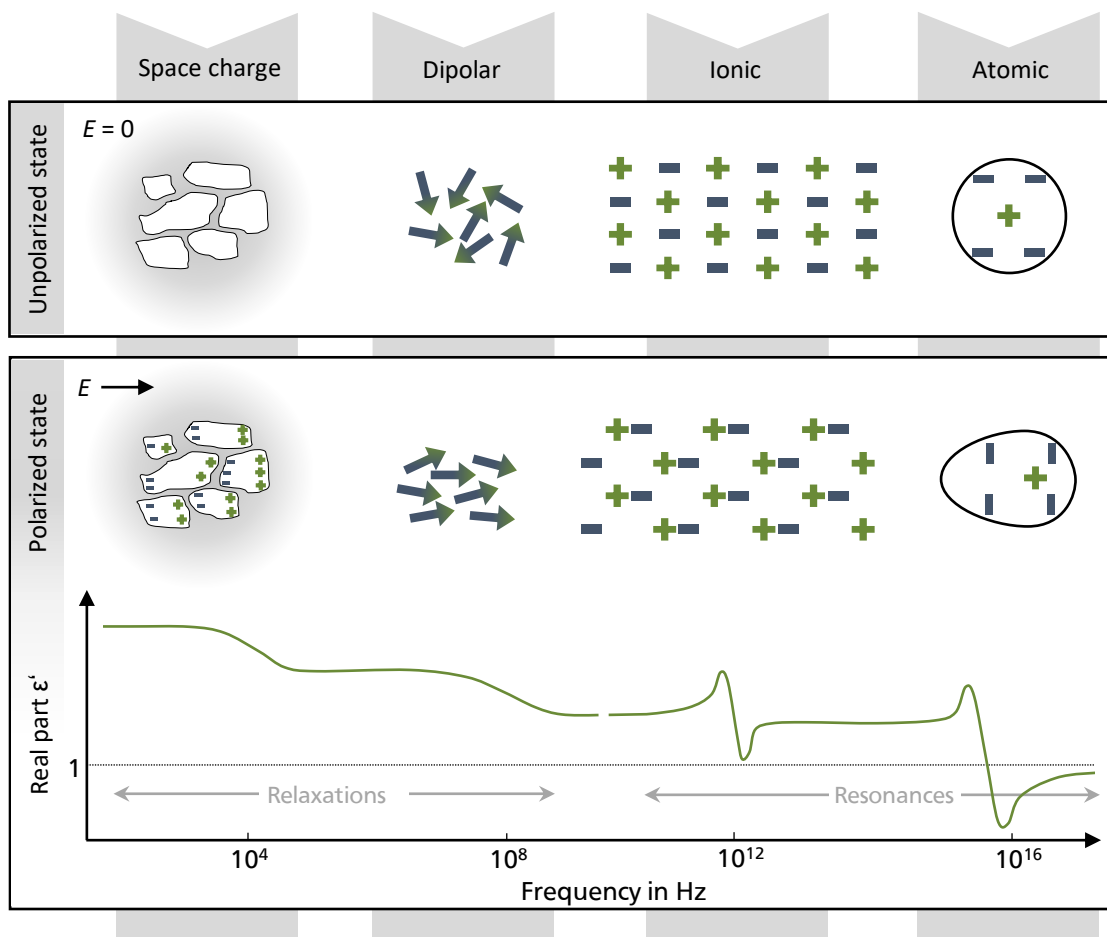
Figure 2.3.: Microscopic polarization mechanisms in the unpolarized and polarized state. The latter includes the frequency-dependence of the real part of permittivity. The illustrations were redrawn from Ref. [39].

All of the above described polarization mechanisms contribute to the total polarization. The time scale for their response to an electric field, however, is considerably different. Hence, the dispersion of the dielectric constant can be expressed mathematically by

$$\epsilon_r = \epsilon'_r + i\epsilon''_r, \tag{2.5}$$

where the real part ϵ'_r refers to the ability to store charges, while the imaginary part ϵ''_r describes the dielectric loss. The dissipation factor $\tan(\delta)$ is defined as the ratio of the imaginary and real part of the relative permittivity

$$\tan(\delta) = \frac{\epsilon''_r}{\epsilon'_r}. \tag{2.6}$$

For the different polarization mechanism the frequency dependence of the real part is schematically shown in Figure 2.3. For space-charge, (domain wall) and the dipolar polarization relaxation behavior is observed, while ionic and atomic polarization show resonance effects. The depicted frequency dependence of the different mechanism allows the experimental separation of the different contributions.

2.2. Barium titanate

2.2.1. Structural polymorphism

Structural polymorphism in materials science describes the existence of different crystal structures of the same chemical material. With increasing temperature undoped $BaTiO_3$ undergoes different structural polymorphic transformations sketched in Fig. 2.4 on the top.
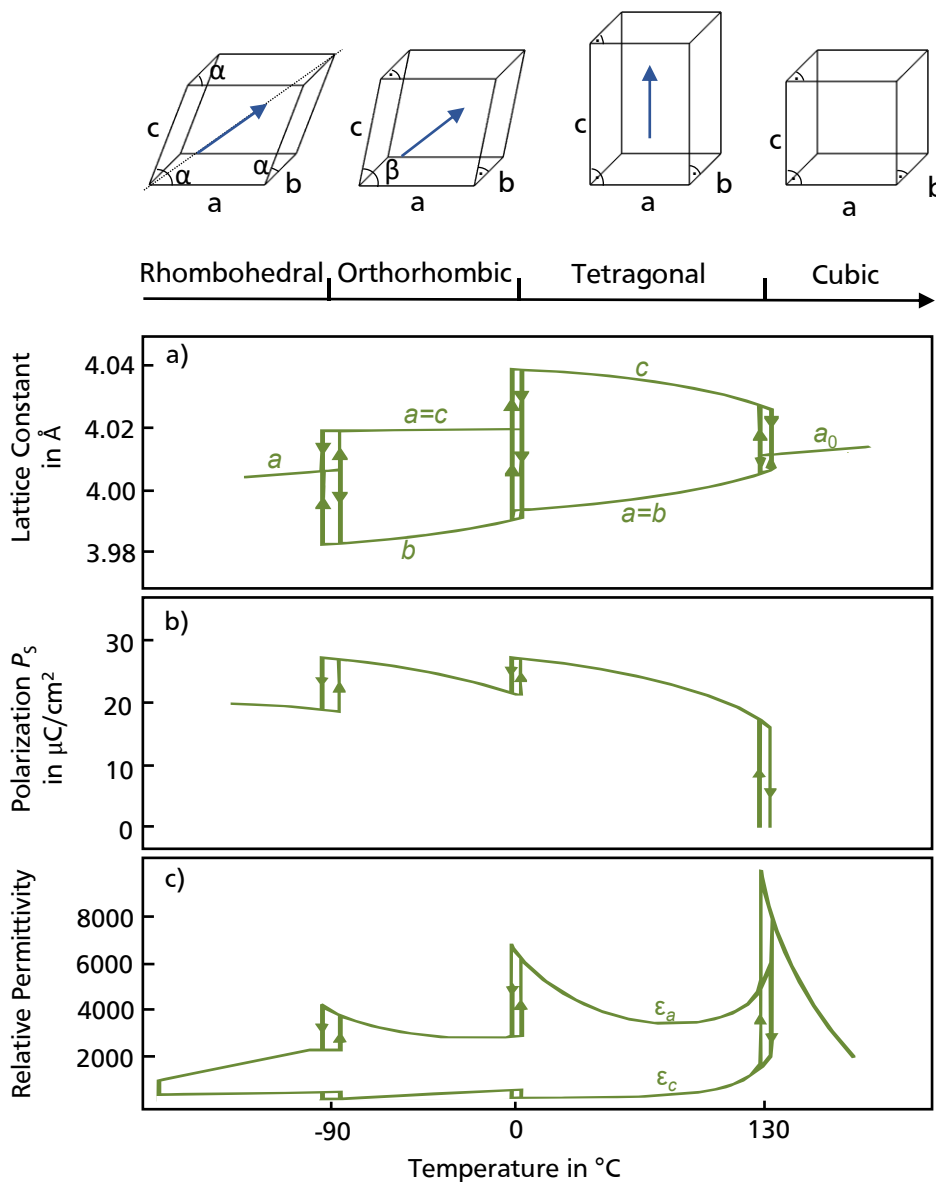
Figure 2.4.: Temperature-dependence of the polymorphic crystal structures (top), a) lattice constants, b) polarization, and c) relative permittivity. Angles and a/c lattice constant ratios have been exaggerated in the crystal structures for clarity. Figure a)-c) were redrawn from [38] with permission. Copyright (2005) John Wiley & Sons - Books.

For the three ferroelectric forms - rhombohedral (R3m) with $a=b=c$ and $\alpha< 90°$, orthorhombic (Amm2) with $a=c\neq b$ and $\beta< 90°$, and tetragonal (P4mm) with $a=b\neq c$ - the polar axis is indicated by the blue arrow and is along the [111], [011], and [001] direction, respectively [41, 42]. Due to centrosymmetry, the cubic polymorph (Pm-3m) with $a=b=c$ is paraelectric. The corresponding temperature-dependent changes in the lattice constant, polarization, and relative permittivity are shown in Figure 2.4 a)-c), respectively. A small thermal hysteresis is observed between the transition temperatures, which is accompanied by distinct anomalies in the mechanical and piezoelectric properties [43].

At room temperature under ambient pressure undoped stoichiometric $BaTiO_3$ typically exhibits the ferroelectric tetragonal crystal structure. For the application of ferroelectric materials the ferroelectric to paraelectric phase transition at approximately 130 °C is the most important phase transition. It is a displacive phase transition and is classified as a first order phase transition within the classification of Ehrenfest [43]. The centrosymmetric cubic crystal structure elongates along the c-axis, which is accompanied by a displacement of the atomic positions along the [001] direction leading to a spontaneous polarization [41, 42].

The displacement between the cubic and the tetragonal unit cell as well as the corresponding potential within the Landau-Ginzburg-Devonshire theory are depicted in Fig. 2.5. Barium titanate crystallizes in the ABO_3 perovskite structure with the barium cation Ba^{2+} on the corners, the titanium cation Ti^{4+} in the body center, and the oxygen anions O^{2-} on the face centers. In the cubic phase the center of the positive and negative charges coincide, while it is shifted in the tetragonal phase. For the description of the paraelectric-to-ferroelectric transition the dielectric displacement D is the order parameter and the free energy G is its analytic function. For the paraelectric case the free energy has a single well with a minimum at $D=0$ and accordingly no displacement and no polarization is present in the cubic structure. In the vicinity of the phase transition temperature the system will start to form the double

Figure 2.5.: Atom positions: Ba at (0, 0, z), Ti at (1/2, 1/2, z), O1 at (1/2, 1/2, z), and O2 at (1/2, 0, z). Displacement and a/c lattice constant ratios have been exaggerated for clarity. The structure was created with VESTA [44].

wall, which is present in the tetragonal phase, leading to different metastable states until the transition is completed. Due to the characteristics of a first order phase transition, a thermal hysteresis appears and, thus, the phase transition temperature for heating and cooling cycles differ. Accordingly, all properties correlated to the order parameter such as lattice constant, polarization, and relative permittivity show a thermal hysteresis as shown in Figure 2.4 a)-c).

All phase transitions of $BaTiO_3$ within the ferroelectric polymorphs as well as the paraelectric to ferroelectric phase transition are first order transitions. They all share the same order parameter within the Landau theory and can, therefore, be understood as the equilibrium phase for the corresponding temperature. Furthermore, they are all subgroups derived by the displacement of the B-atom from the same parent space group Pm-3m [45].

The transitions between the different polymorphs are accompanied by distinct maxima in the relative permittivity as shown in Figure 2.4 c). The transition between the ferroelectric and paraelectric polymorphs involves the appearance/disappearance of the spontaneous polarization as shown in Figure 2.4 b). The permittivity reaches a maximum at the Curie point T_C and decreases at higher temperatures in accordance with the Curie-Weiss law

$$\epsilon'_r = \epsilon_0 + \frac{C}{T - T_0}, \tag{2.7}$$

where T_0 refers to the Curie-Weiss temperature and C to the Curie constant. Here, it should be noted that the Curie point T_C and the Curie-Weiss temperature are near to but not identical [39].

The exact values of the phase transition temperatures depend on a variety of factors such as A/B site ratio, oxygen vacancy concentration, grain size, strain/stress, single vs. polycrystals, impurities/doping etc. In general, acceptor-doping decreases the Curie point of $BaTiO_3$ [46]. Different acceptor dopants show different strong impact on the transitions temperatures. According to Hagemann and Ihrig the valence and the electron configuration of the $3d$ acceptor as well as the presence of oxygen vacancies are critical factors influencing the Curie point [46]. Desu and Sabbaro proposed, that Jahn-Teller active acceptors stabilize the tetragonal phase, while Jahn-Teller inactive ions prefer the cubic phase [47]. In literature, many reports treat the influence of acceptor-doping on the Curie point of $BaTiO_3$. The oxidation state of the introduced acceptor dopants in these studies is most of the time unknown or is based on an estimation of the authors. While the change in Curie point is experimentally well studied, the explanations proposed in different publications are not consistent, however. Therefore, different publications will be reviewed in the scope of the discussion of the present results on the influence of Mn- and Fe-doping in Section 5.4.

2.2.2. Hexagonal $BaTiO_3$ - a brief review

In contrast to the previous depicted phase transitions, the cubic to hexagonal phase transition is a reconstructive phase transition [48–50]. For undoped, stoichiometric $BaTiO_3$ sintered under ambient air conditions the cubic to hexagonal phase transition is taking place at 1460 °C [51]. Any changes on the stoichiometry will influence the transition temperature. While a Ti excess will increase the transition temperature, it is unaffected by a Ba excess [51]. In 1960 Glaister and Kay investigated the influence of firing atmosphere as well as Mn-, Fe-, and Ni-doping on

the stabilization of hexagonal $BaTiO_3$. Firing in hydrogen with subsequent quenching reduced the transition temperature of undoped $BaTiO_3$ below 1330 °C. Also, sintering under ambient air conditions with additional acceptor-dopants promoted the stabilization of the hexagonal phase down to room temperature. The concentration and firing temperature for which the hexagonal phase was observed, differed considerable between the different type of dopants [51]. From the perspective of application the appearance of the hexagonal phase is unfavorable, as its space group is centrosymmetric and non-ferroelectric. Hence, the threshold values of different type of dopants for the stabilization of the hexagonal phase down to room temperature has been intensively studied in a variety of publications [51–56]. In the following the work of Prades *et al.* will be reviewed, in which the appearance of the hexagonal phase in Mn- and Fe-doped $BaTiO_3$ as a function of acceptor-doping concentration has been investigated [54]. In their work Mn- and Fe-doped samples have been derived by the sol-gel method. The samples have been equilibrated at several temperatures for 12 h in air and have been subsequently quenched on a Cu plate to room temperature. Afterwards the composition of the quenched samples has been determined by room temperature XRD measurements.
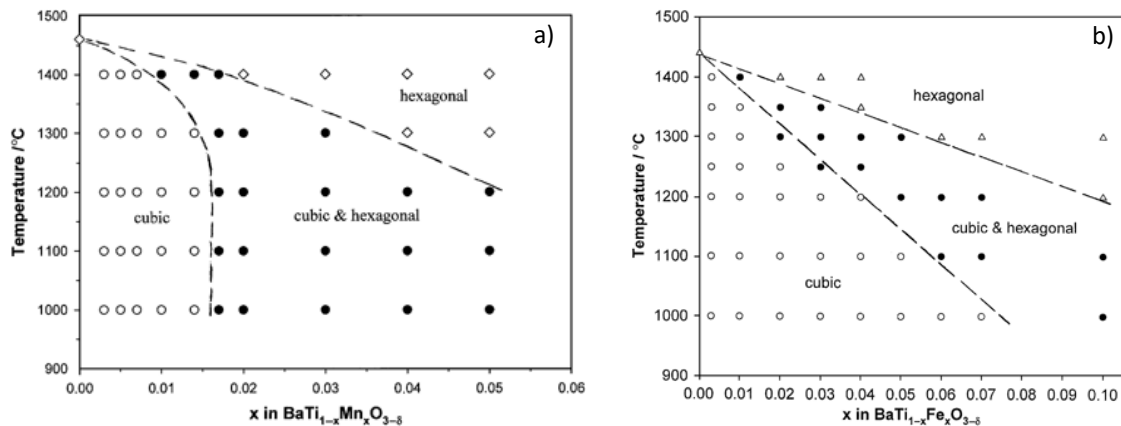
Figure 2.6.: Phase diagram for the solid solution system of a) $BaTi_{1-x}Mn_xO_{3-\delta}$ and b) $BaTi_{1-x}Fe_xO_{3-\delta}$. Please note the different range fo the *x*-axis. The phase diagrams have been constructed on samples that have been equilibrated for 12 h in air and then being quenched to room temperature. Reprinted with permission from [54]. Copyright (2008) Journal of the American Ceramic Society.

The derived phase diagrams of $BaTi_{1-x}Mn_xO_{3-\delta}$ and $BaTi_{1-x}Fe_xO_{3-\delta}$ are displayed in Figure 2.6 a) and b), respectively. Both diagrams show a pure cubic (at *RT* temperature tetragonal), a two phase and, a pure hexagonal region. In general it can be stated that an increasing acceptor doping concentration decreases the temperature for which the phase pure cubic polymorph is derived. The magnitude of temperature decrease, however, significantly differs between Mn and Fe. Mn-doping more effectively lowers the cubic to hexagonal transition temperature and by this opens up a wide region for the two phase mixture. Moreover, for the same temperature and

nominal doping concentration Mn-doping results in a considerable higher amount of hexagonal phase than Fe-doping.

Even though the threshold values for the presence of hexagonal $BaTiO_3$ upon acceptor doping are intensively studied, the underlying mechanism is still under discussion. Potential origins such as oxygen vacancy concentration, $Ti^{3+}/Mn^{3+}/Fe^{3+}$ concentrations, Jahn-Teller distortion, Goldschmidt tolerance factor, *A/B* site ratio, and metal-metal bond-lengths will be more extensively considered in Section 5.2 during the discussion of the data presented in this work.

2.3. Acceptor-doped Barium titanate

In the present work polycrystalline Mn- and Fe-doped $BaTiO_3$ will be investigated. Both dopants are so-called multivalent acceptors and are assumed to be incorporated onto the Ti-site. In the following Sections the influence of acceptor doping on the structure stability, defect chemistry, and conduction mechanism of acceptor-doped $BaTiO_3$ is introduced. These Sections are mainly based on the standard text book of Ref. [20]. Afterwards the resistance degradation of titanate based capacitors is reviewed. Here a focus is set on the different parameters influencing the degradation rate. This Section is mainly based on the work of Waser and co-workers [4–6,57].

2.3.1. Goldschmidt tolerance factor

The Golschmidt tolerance factor t is a measure for the stability of the cubic perovskite structure upon cation doping [41,58]. Here, r_A, r_B, and r_O describe the radii of the *A*-site cation, the *B*-site cation, and the oxygen anion, respectively. An ideal cubic perovskite structure is described by $t=1$.

$$t = \frac{r_A + r_O}{\sqrt{2} \cdot (r_B + r_O)} \tag{2.8}$$

By calculating the value of the tolerance factor t, the structure of the considered component can be predicted. For $t < 0.71$ the component is generally not stable in the perovskite structure, for $t = 0.71 - 0.9$ a distorted structure such as the orthorhombic/rhombohedral phase is preferred, for $t = 0.9 - 1$ cubic is stable, and for $t > 1$ hexagonal or tetragonal distortions are preferred [58,59]. The given ranges for the tolerance factor t are guidelines based on the observed structures of such materials and should, thus, not be taken as hard boundaries. Furthermore, the Goldschmidt tolerance factor cannot be applied to perovskite with a considerable number of ion vacancies [41].

2.3.2. Defect Chemistry

The knowledge and control of the defect structure and mass- and charge-transport is of high importance for the application of BaTiO$_3$ in modern electromechanics and electronics [60]. Accordingly, the defect chemistry of BaTiO$_3$ has been intensively studied and is excessively described in literature [21, 22, 25–27, 60–66]. In acceptor-doped BaTiO$_3$ the dominant defects are electrons e', holes $h^\bullet$, oxygen vacancies $V_O^{\bullet\bullet}$, and the charged acceptors A'_{Ti} and A''_{Ti} [61]. Frenkel and Anti-Frenkel disorder (creation of interstitials) can be neglected due to their high formation enthalpies [67]. Schottky disorder needs to be considered in the case of undoped BaTiO$_3$, but is of minor importance in acceptor-doped BaTiO$_3$ [61, 64, 68]. Hence, the only relevant defect reactions for acceptor-doped BaTiO$_3$ are the electron-hole pair reaction, the oxygen exchange reaction, and the acceptor ionization reactions.

The electron-hole pair reaction Eq. 2.9 describes the excitation of electrons from the valence band into the conduction band. The equilibrium between the oxygen in the vapor phase and the oxygen ions in the lattice is expressed by the oxygen exchange reaction Eq. 2.10.

$$\text{nil} \rightleftharpoons e' + h^\bullet \tag{2.9}$$

$$O_O^x \rightleftharpoons V_O^{\bullet\bullet} + 2e' + \frac{1}{2}O_2(g)\uparrow \tag{2.10}$$

Under reducing conditions Equation 2.10 is valid from left to right. Oxygen is leaving the sample and oxygen vacancies with compensating electrons are created. The electrons can be localized on the Ti-site, which leads to a reduction from Ti^{4+} to Ti^{3+} according to

$$2Ti_{Ti}^x + O_O^x \rightleftharpoons V_O^{\bullet\bullet} + 2Ti_{Ti}^{'} + \frac{1}{2}O_2(g)\uparrow . \tag{2.11}$$
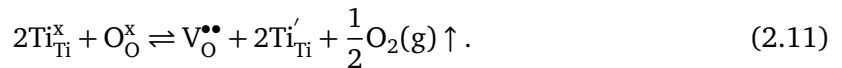
In this work, the valence state of the Mn/Fe acceptor ions substituted on the Ti site can be 4+, 3+, or 2+. While tetravalent acceptor ions are charge neutral compared to the initial Ti site, trivalent or divalent acceptors are singly (Eq. 2.12) or doubly ionized (Eq. 2.13), respectively.

$$A'_{Ti} \rightleftharpoons A_{Ti}^x + e' \tag{2.12}$$

$$A''_{Ti} \rightleftharpoons A'_{Ti} + e' \tag{2.13}$$

The charge compensation for ionized acceptors is achieved by the creation of oxygen vacancies. The equilibrium concentration of the defects depends on the thermodynamic variables. For a given temperature the defect concentrations as a function of oxygen partial pressure/oxygen activity can be extracted from so called Brouwer diagrams as being given in Ref. [69]. The charge neutrality condition for the different equilibrium regions are given in Table 2.1.

Table 2.1.: Charge neutrality conditions of multi-valent acceptor doped BaTiO$_3$ according to [68, 69].

m	Charge neutrality condition
-1/6	$n \approx 2\left[V_O^{\bullet\bullet}\right]$
-1/4	$\left[A_{Ti''}\right] \approx \left[V_O^{\bullet\bullet}\right]$
+1/6	$\left[A_{Ti'}\right] \approx 2\left[V_O^{\bullet\bullet}\right]$

Acceptor dopants are compensated ionically by the creation of oxygen vacancies. The acceptors can be strongly associated with the compensating oxygen vacancies, which results in the formation of so-called defect complexes [64] according to Eq. 2.14 to 2.15. These complexes influence the mobility of oxygen vacancies at lower temperatures [70] and are one major factor for aging of BaTiO$_3$ based capacitors [71].

$$A'_{Ti} + V_O^{\bullet\bullet} \rightleftharpoons (A'_{Ti}V_O^{\bullet\bullet})^{\bullet} \tag{2.14}$$

$$A''_{Ti} + V_O^{\bullet\bullet} \rightleftharpoons (A''_{Ti}V_O^{\bullet\bullet})^{x} \tag{2.15}$$

2.3.3. Conduction Mechanism

The electrical resistance R between two contacts is given by Ohm's law $U = R \cdot I$, where I denotes the current and U the voltage between the two points. For a uniform conductor of a constant thickness d and a cross section A the electrical resistance is given by

$$\sigma = \frac{I \cdot l}{U \cdot A}. \tag{2.16}$$

In a microscopic point of view, electric conductivity is defined as the movement of charges due to an applied electric field. The conductivity of a material depends on the concentration and on the mobility μ of the different types of charge carriers. The electric conductivity of BaTiO$_3$ is described by the sum of electron, hole, and oxygen vacancy contributions

$$\sigma = q \cdot n \cdot \mu_n + q \cdot p \cdot \mu_p + 2q \cdot c(V_O^{\bullet\bullet}) \cdot \mu_{V_O^{\bullet\bullet}}, \tag{2.17}$$

where μ_n, μ_p, and $\mu_{V_O^{\bullet\bullet}}$ denote the mobilities and n, p, $c(V_O^{\bullet\bullet})$ the concentrations of electrons, holes, and oxygen vacancies, respectively. Both quantities depend on thermodynamic conditions such as temperature and oxygen partial pressure.

Charge Carrier Concentration

As known from basic condensed matter physics, electronic bands are derived from a linear combination of atomic (or molecular) orbitals, where the discrete states of the atoms form a continuous band. The fundamental difference between metals and semiconductors is the existence of a electronic band gap, in which no electronic states exist. The uppermost occupied band is called valence band and the lowest unoccupied band is called conduction band. The Fermi level E_F is located inside the band gap and determines the probability of a state to be occupied by an electron. This probability is temperature dependent and is described by the Fermi distribution function

$$f(E) = \frac{1}{1 + e^{\frac{E - E_F}{k_B T}}}.$$
(2.18)

At $T = 0\,\text{K}$ the Fermi distribution function equals a step function with a completely filled valence band and a completely empty conduction band. With increasing temperature the Fermi distribution broadens and the number of charge carrier in the bands increases. In general, only partially occupied bands are contributing to electronic conductance. The electrons in the conduction band and the holes in the valence band can be regarded as delocalized in the whole solid. The electron and hole concentration n and p are given by

$$n = \int_{E_{CB}}^{\infty} N_C(E) \cdot f(E) \mathrm{d}E$$
(2.19)

$$p = \int_{\infty}^{E_{VB}} N_V(E) \cdot (1 - f(E)) \mathrm{d}E,$$
(2.20)

where E_{CB} and E_{VB} are the energy of the conduction band minimum (CBM) and the valence band maximum (VBM) and $N_C(E)$ and $N_V(E)$ are the density of states in the conduction and the valence band. Equations 2.19 and 2.20 can be solved analytically if the parabolic band approximation and the non-degenerate semiconductor approximation are valid. The parabolic band approximation assumes that the energy-momentum *(E-k)* relationship near the band edges can be approximated by the quadratic equation $E(k) = \hbar^2 k^2 / 2m^*$ with m^* being the associated effective mass. A non-degenerate semiconductor describes a semiconductor with a Fermi level at least $3k_B T$ away from the band edges. In this case, the Fermi distribution function can be simplified to $f(E) = e^{-(E - E_F)/(k_B T)}$ for $E - E_F > 3k_B T$ and $f(E) = 1 - e^{-(E_F - E)/(k_B T)}$ for $E_F - E > 3k_B T$. If both approximations are valid, the number of (free) electrons and holes can be expressed by

$$n = N_{CB} \cdot e^{-\frac{E_{CB} - E_F}{k_B T}}$$
(2.21)

$$p = N_{VB} \cdot e^{-\frac{E_F - E_{VB}}{k_B T}}.$$
(2.22)

with N_{CB} and N_{VB} being the effective densities of state:

$$N_{CB,VB} = 2 \left(\frac{2\pi m_{e,h}^* k_B T}{h^2} \right)^{3/2}.$$ (2.23)

The charge neutrality in an undoped homogenous semiconductor is given by $n = p$. Hence, the conductivity solely depends on the band gap, effective density of states, and temperature. The concentration of free electrons and holes can be increased by doping. In this work, Mn and Fe dopants are introduced as acceptors on the Ti-site. The ionization state of the acceptors depends on temperature and on the Fermi level with respect to the defect's energy level. Mn and Fe are multi-valent dopants with two charge transition levels $A^{2+/3+}$ and $A^{3+/4+}$ inside the band gap. The concentration of the doubly ionized, singly ionized, and neutral acceptors A is given by

$$N_{A''_{Ti}} = \frac{N_{A_{Ti}}}{1 + g_A \cdot e^{\frac{E_{A1} - E_F}{kT}}}$$ (2.24)

$$N_{A'_{Ti}} = \frac{N_{A_{Ti}}}{1 + g_A \cdot e^{\frac{E_{A2} - E_F}{kT}}} - N_{A''_{Ti}}$$ (2.25)

$$N_{A^x_{Ti}} = N_{A_{Ti}} - N_{A'_{Ti}} - N_{A''_{Ti}},$$ (2.26)

where $N_{A_{Ti}}$ denotes the acceptor concentration, g_A the ground-state degeneracy, and E_{A1} and E_{A2} the energetic position of the $A^{2+/3+}$ and $A^{3+/4+}$ charge transition level with respect to the valence band maximum [20]. In the case of acceptor-doped BaTiO$_3$ oxygen vacancies are created as ionic compensation. These oxygen vacancies act as donors and can be doubly, singly, or not charged according to Equation 2.27 to 2.29, where N_{V_O} denotes the oxygen vacancy concentration, g_D the ground-state degeneracy, and E_{D1} and E_{D2} the energetic position of the $V_O^{\bullet/\bullet\bullet}$ and $V_O^{x/\bullet}$ charge transition level with respect to the valence band maximum [20].

$$N_{V_O^{\bullet\bullet}} = \frac{N_{V_O}}{1 + g_D \cdot e^{\frac{E_F - E_{D1}}{kT}}}$$ (2.27)

$$N_{V_O^{\bullet}} = \frac{N_{V_O}}{1 + g_D \cdot e^{\frac{E_F - E_{D2}}{kT}}} - N_{V_O^{\bullet\bullet}}$$ (2.28)

$$N_{V_O^x} = N_{V_O} - N_{V_O^{\bullet}} - N_{V_O^{\bullet\bullet}}$$ (2.29)

The Fermi level is determined by the charge neutrality condition, which includes all charge carriers, i.e. charged defects as well as free electrons and holes

$$n(E_F) + N_{A'_{Ti}}(E_F) + 2N_{A''_{Ti}}(E_F) + N_{Ti'_{Ti}}(E_F) = p(E_F) + N_{V_O^{\bullet}}(E_F) + 2N_{V_O^{\bullet\bullet}}(E_F).$$ (2.30)

From Equation 2.24 to 2.26 it is obvious, that at $T = 0\,\text{K}$ all acceptors are charged A^{2+} for high Fermi levels, i.e. $E_F > E_{A1}$, A^{3+} for intermediate Fermi levels, i.e. $E_{A1} > E_F > E_{A2}$, and A^{4+} (neutral) for low Fermi levels, i.e. $E_F < E_{A2}$. At $T > 0\,\text{K}$ the Fermi distribution function broadens and for high Fermi levels electrons from the $A1$ acceptor level will be thermally excited into the conduction band, which increases the number of free electrons and results in n-type conductance. For low Fermi levels electrons from the valence band will be thermally excited to the $A2$ acceptor level, leaving a hole in the valence band, which contributes to p-type conductance. The defect levels $A^{2+/3+}$ and $A^{3+/4+}$ act as pinning level for the Fermi energy, which will define the magnitude of n- and p-type conductance. The Fermi level position, defect concentration, and resulting conductivity depend on the oxygen partial pressure, as being depicted in Figure 2.7 a)-c), respectively. These dependencies can be divided into three characteristic REGIONS I-III. At low oxygen partial pressures in REGION I the Fermi level is pinned at the oxygen vacancy ionization levels close to the conduction band minimum and all acceptors are in the 2+ oxidation state. The total number of oxygen vacancies exceeds the amount of acceptors $[V_O] > [A_{Ti}]$ and the conductivity in this region is determined by oxygen vacancy induced electrons.

For intermediate oxygen partial pressures in REGION II the Fermi level is pinned at the $A^{2+/3+}$ charge transition level. All oxygen vacancies are doubly ionized and the oxygen vacancy concentration is in the range of $[A_{Ti}] > [V_O] > 1/2\,[A_{Ti}]$. The amount of divalent charged acceptors decreases with increasing oxygen partial pressure. The conductivity in this region is still n-type and determined by the thermal excitation of electrons trapped on the $A^{2+/3+}$ level to the conduction band. For high oxygen partial pressures in REGION III the Fermi level is pinned at the $A^{3+/4+}$ charge
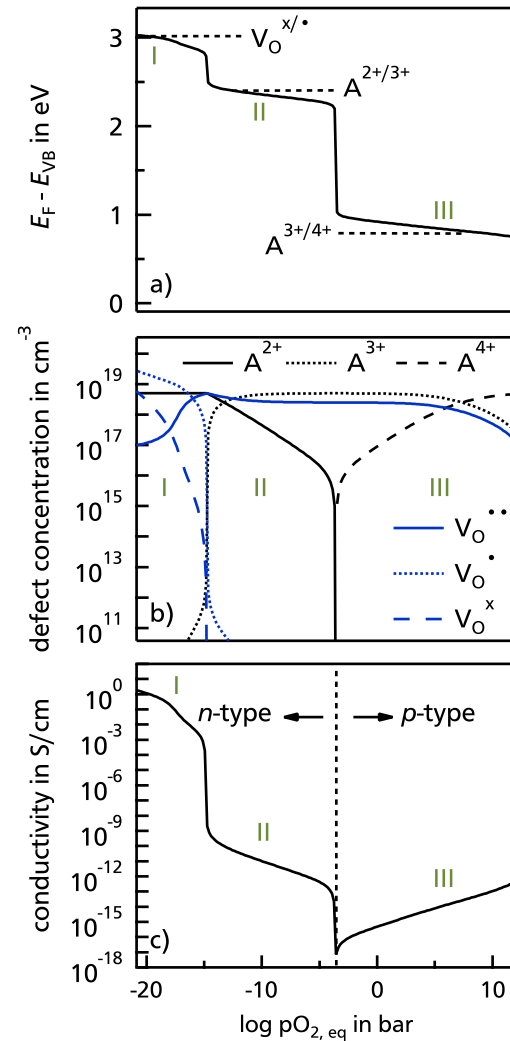
Figure 2.7.: Fermi level position a), defect concentrations b), and electronic conductivity as a function of oxygen partial pressure at room temperature. The defect equilibrium has been established at $1100\,°\text{C}$ and an acceptor concentration of $5.0 \times 10^{18}\,\text{cm}^{-3}$ with $E_{A1} = 2.4\,\text{eV}$ and $E_{A2} = 0.8\,\text{eV}$ has been assumed. The IGOR defect calculation macro version 5.3beta of A. Klein has been used.
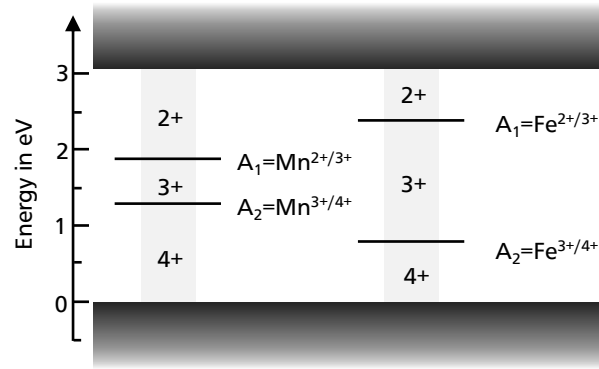
Figure 2.8.: Transition level for Mn- and Fe-dopants in BaTiO$_3$. The values for the charge transition levels are taken from [21] and are listed in Table 2.2.

transition level and the oxygen vacancy concentration is in the range of $[V_O] < 1/2 [A_{Ti}]$. The conductivity in this region is p-type and determined by the thermal excitation of electrons from the valence band to the $A^{3+/4+}$ level.

The position of the Mn and Fe charge transition levels are depicted in Figure 2.8. The energetic position of the Mn- and Fe-levels are given in Table 2.2. The Mn$^{2+/3+}$ and Mn$^{3+/4+}$ level are located at 1.3 eV and 1.2 eV with respect to the VBM and CBM, while the Fe$^{2+/3+}$ and Fe$^{3+/4+}$ level are located 0.8 eV and 0.7 eV [21]. As can be deduced from Equations 2.21 to 2.30, a Fermi level closer to the VBM and CBM will lead to a higher charge carrier concentration and thus a higher conductivity in the n- and the p-type region. Accordingly, the closer distance of the Fe levels to the band edges will result in a considerably higher conductivity of Fe-doped BaTiO$_3$ compared to Mn-doped BaTiO$_3$.

Table 2.2.: Band gap and defect energy values for Mn- and Fe-doped BaTiO$_3$ from Wechsler and Klein [21].

	E_G	$V_O^{x/\bullet}$	$V_O^{\bullet/\bullet\bullet}$	Fe$^{2+/3+}$	Fe$^{3+/4+}$	Mn$^{2+/3+}$	Mn$^{3+/4+}$
$E - E_{VBM}$	3.1	3.05	2.9	2.4	0.8	1.9	1.3

Mobility

The temperature dependence of the charge carrier mobilities strongly depends on all possible scattering events, mostly phonon and defects [72]. The temperature dependent mobility of electrons μ_e is given by Chan *et al*. [73], who performed a fit on the experimental BaTiO$_3$ single crystal data of Seuter [74] by the expression of Ihrig [75]. The mobility of holes μ_h in

dependence of the temperature is estimated as half of the electron mobility [73].

$$\mu_e = 8080 \cdot T^{-1.5} \cdot e^{-\frac{0.021}{k_B T}} \tag{2.31}$$

$$\mu_h = \frac{1}{2} \cdot \mu_e \tag{2.32}$$

The temperature dependent mobility of ions is given by the Einstein–Smoluchowski relation $\mu_{ion} = zqD/k_B T$ [76, 77], with $D = D_0 \cdot \exp(-E_A/k_B T)$ being the temperature dependent diffusion coefficient of the respective species [72]. The oxygen vacancy mobility in single crystalline BaTiO$_3$ was experimentally derived by oxygen diffusion experiments conducted by Kessel *et al.* [78].

$$\mu_{V_O^{\bullet\bullet}} = \frac{zqD}{k_B T} = \frac{2e}{k_B T} \cdot 6.4 \times 10^{-3} \cdot e^{-\frac{0.7}{k_B T}} \tag{2.33}$$

Grain Boundaries in BaTiO$_3$

Grain boundaries are defined as interface between two grains with different crystallographic orientation and can be regarded as two-dimensional lattice defects [79]. The region directly at the interface is called grain boundary core and describes the region where the periodic crystal structure is interrupted, i.e. the average bond length is altered and the average coordination number is reduced compared to the bulk phase [57]. The altered structure in the grain boundary core affects other material's properties such as the Gibbs free energy of defect formation. Unequal formation enthalpies between bulk and grain boundary core result in segregation of mobile charged defects to or away from the core region. This eventually results in the formation of a charged grain boundary core, which is charge compensated by an oppositely charged space charge region [79].

In barium titanate the formation enthalpy of oxygen vacancies is significantly reduced at the grain boundary core, which results in an oxygen vacancy segregation and a positive core charge [79]. The resulting band bending and concentration profile for acceptor-doped BaTiO$_3$ is shown in Figure 2.9 a) and b), respectively. As the width of the grain boundary core is restricted to one or two lattice constants [57], it is not visible in Figure 2.9. The positive core charge compared to the bulk leads to a downward band bending, as depicted in Fig. 2.9 a). Positively charged mobile defects, i.e. oxygen vacancies and holes, are depleted in the space charge region, while negatively charged mobile defects, i.e. electrons, are accumulated. Acceptor dopants are assumed to be immobile at the considered temperatures used in this work. Consequently, the concentration profile of acceptors can be assumed as constant at lower temperatures and hence only the valency of the acceptors alters due to the change in Fermi level in the space charge region.
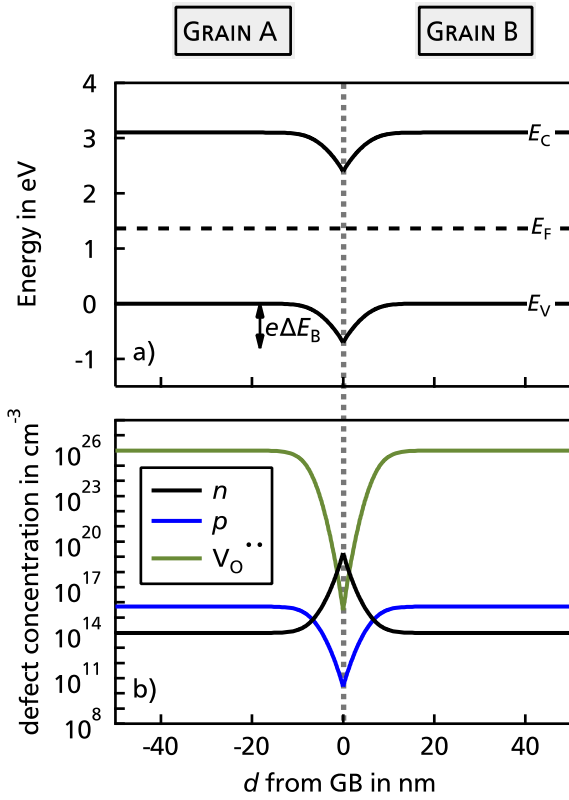
Figure 2.9.: Schematic a) Band bending and b) concentration profile of electron, holes, and oxygen vacancies at the grain boundary of acceptor-doped BaTiO$_3$. $e\Delta E_B$ is defined as the band bending.

The presence of grain boundaries has consequences for the conductivity of polycrystals [80, 81] as the resulting potential barrier at the grain boundary influences the charge carrier mobility across [82]. The charge carrier transport across the grain boundary barrier E_B can be adapted from the thermal emission of charge carriers across a barrier. In case of thermal emission of electrons (holes) across the Schottky barrier at an interface, the barrier is defined as the distance between the conduction band (valence band) and the Fermi level. In the case of grain boundary barriers, the electrons (holes) are already considered to be in the conduction band (valence band) and hence, the barrier E_B is defined as the band bending [81] (see Figure 2.9 a)). The mobility in polycrystals can be expressed by the Petritz relation [83]

$$\mu = \mu_0 \cdot e^{-\frac{e\Delta E_B}{k_B T}}, \qquad (2.34)$$

where μ_0 denotes the mobility in the grain, while the grain boundary contribution is represented by adding an additional exponential term with includes the activation energy across the grain boundary barrier $e\Delta E_B$.

For acceptor-doped BaTiO$_3$ the segregation of oxygen vacancies to the grain boundary core results in a downward band bending as depicted in Figure 2.9. Consequently, positively charged defects need to overcome the barrier, while negatively charged defects experience no barrier.

2.3.4. Resistance Degradation

Dielectric and ferroelectric $BaTiO_3$-based ceramic capacitors suffer from resistance degradation during simultaneous temperature and voltage stress. Resistance degradation is characterized by a slowly increasing leakage current until it eventually leads to an electric breakdown of the capacitor [12]. Hence, reliability and life-time of the capacitors are strongly affected by resistance degradation. Due to its critical importance for the performance, resistance degradation is intensively studied [10, 15]. Based on the work of Waser and coworkers [4–6, 57] the underlying mechanism of resistance degradation in $SrTiO_3$ is discussed in the following. Due to their similar crystal and defect structure $SrTiO_3$ and $BaTiO_3$ are often compared [84].

In $BaTiO_3$ resistance degradation is based on the redistribution of oxygen vacancies with respect to time, field, and temperature [85]. The combined temperature and voltage stress results in the migration of oxygen vacancies towards the cathode, which eventually leads to accumulation in the cathode region and a depletion in the anode region. Due to charge neutrality conditions, this oxygen vacancy accumulation (depletion) results in an increased electron (hole) concentration in the respective region and an overall decreased resistance of the capacitor.

A representative degradation curve of a ceramic capacitor is shown in Figure 2.10. According to Waser *et al.* the degradation time t_{deg} is defined as the time at which the conductivity increased by one decade above its minimum value [4]. The degradation time depends one a variety of parameters such as temperature, voltage, grain size, oxygen vacancy concentration, type and concentration of dopants etc. In the following the influence of the different parameters on the degradation time and degradation characteristics is addressed.
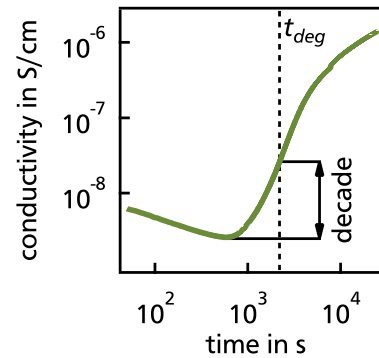
Figure 2.10.: Degradation curve of a 0.2 wt.% Mn-doped $BaTiO_3$ ceramic at 205 °C and an electric field of 0.3 kV/mm.

Influence of temperature and voltage:

The degradation time of an undoped single crystal is mainly affected by two parameters: temperature and voltage. The temperature-dependence of resistance degradation for a constant electric field shows an Arrhenius-type characteristics and can be expressed by

$$t_{deg} \propto e^{-E_A/k_\mathrm{B}T}, \tag{2.35}$$

where E_A denotes the activation energy for resistance degradation [4]. The dependence of

resistance degradation on the electric field E, voltage U, and sample thickness d can be described empirically by power laws [4]. For a constant thickness the relation between degradation time, voltage, and electric field is given by

$$t_{deg} \propto U^{n_1} \big|_{d=\text{constant}} \propto E^{n_1} \big|_{d=\text{constant}}. \tag{2.36}$$

Influence of grain size:

The degradation mechanism of oxygen vacancy concentration polarization between cathode and anode is identical for single crystals, fine- and course-grained ceramics. The degradation time, however, strongly depends on the microstructure, i.e. the grain size of the capacitor material. The degradation curve of a Ni-doped $SrTiO_3$ single crystal, fine-grained ($d \approx 2.5\,\mu m$), and coarse-grained ($d \approx 50\,\mu m$) ceramics have been examined by Waser and Hagenbeck [57] and are depicted in Figure 2.11. The first finding in Figure 2.11 is the different shape of the degradation curves. The altered shape of single crystals and ceramics can be explained when considering the different contributions to the equivalent circuits, which have been included in Figure 2.11 according to Ref. [57]. At the very beginning the current density of all three samples is identical and corresponds to the bulk conduction [57]. The initial current density of the single crystal slightly decreases due to electrode polarization. Afterwards it stays on a constant value, which is determined by the series resistance of bulk and electrode. In the case of a ceramic the initial current density significantly decreases due to the Maxwell-Wagner polarization of the grain boundaries. Electrode polarization is also present in the case of ceramics but its influence is negligible compared to the influence of grain boundary polarization. The leakage current density stays on a constant value, which is determined by the series resistance of the bulk, electrode, and grain boundaries. The onset of resistance degradation is observed at considerable different degradation times and is drastically increasing with decreasing grain size. The slower degradation of ceramics is related to the barrier character of the grain boundaries.
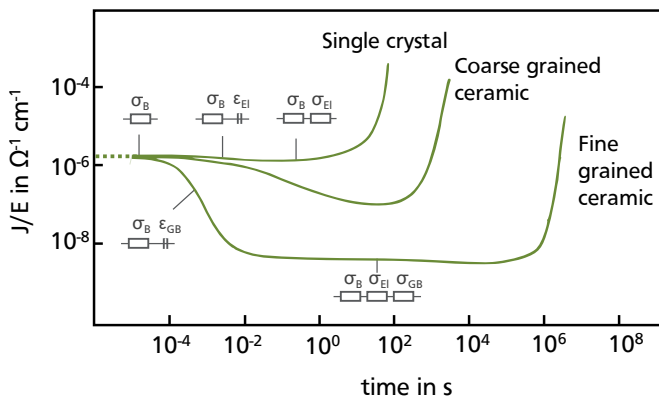
Figure 2.11: Degradation curve of a 0.1 at.% Ni-doped $SrTiO_3$ single crystal, coarse-grained, and fine-grained ceramic according to the data of Ref. [57]. The different contributions in the characteristic regions of the single crystal and fine-grained ceramic are included as equivalent circuits. The Figure was redrawn and adapted using the data of Ref. [57].

As discussed in the previous Section, grain boundaries in BaTiO$_3$ have a positive core charge, which leads to the formation of a space charge region and the characteristic double Schottky barriers (see Figure 2.9). The transport of positively charged ions, i.e. oxygen vacancies, is hindered by the barrier formation at the grain boundaries, which results in a pile up at the grain boundaries. The influence of grain boundaries on the time evolution of the oxygen vacancy profile was simulated by Waser *et al.* and is given for a single crystal and a polycrystal with eight equal-sized grains in Figure 2.12. While the profile is smooth in the case of the single crystal, oxygen vacancies are accumulated at the anode facing side of all seven grain boundaries in the polycrystal. This pile-up decreases with increasing time until a comparable oxygen vacancy concentration profile as for the single crystal is reached.

The blocking behavior of the SCR leads to potential steps at the grain boundaries, which effectively delays the overall oxygen vacancy migration and thus increases the degradation time. The potential drop at the grain boundaries U_{GB} is assumed to be linearly distributed between the electrodes [4] and can be expressed by

$$\Delta U_{GB} = \frac{d_{Gr.}}{d} U = \frac{d_{Gr.}}{d} \cdot Ed = d_{Gr.}E, \tag{2.37}$$

where d denotes the sample thickness and $d_{Gr.}$ the average grain size. For ceramics of similar composition but with different grain size the degradation time can be compared if the electric field is adapted in such a way that ΔU_{GB} is the same for all samples [4].
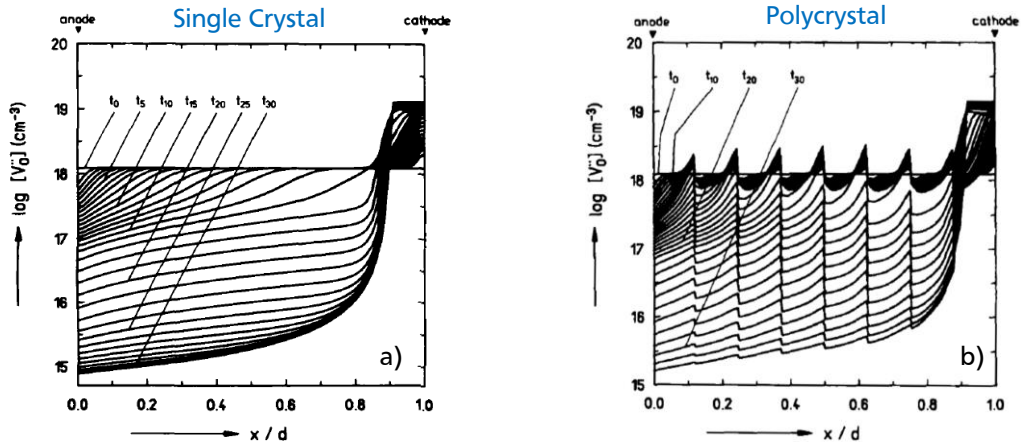
Figure 2.12.: Simulated time-dependent oxygen vacancy profile of a 0.1 at.% acceptor-doped SrTiO$_3$ a) single crystal and b) a polycrystal with eight equally sized grains. Reprinted with permission from [6]. Copyright (1990) Journal of the American Ceramic Society.

Influence of the electrodes:

For the simulation of the ionic de-mixing model Waser and co-workers included the possibly of partially blocking electrodes by adding a transfer factor [5, 6]. However, due to their results on the electrocoloration of a Fe-doped $SrTiO_3$ single crystal [5], blocking electrodes have been assumed, which is not necessarily valid for all kinds of dielectric-electrodes combinations. Wojtyniak *et al.*, for example, observed oxygen bubbles between the surface of a Fe-doped $SrTiO_3$ single crystal and a Pt anode [10]. Rodewald *et al.* performed SIMS measurements during the degradation of Fe-doped $SrTiO_3$ single crystals and observed oxygen incorporation through the Ag/Cr cathodes, which influences the local conductivity profile [15]. Thus, the oxygen exchange at the electrodes has a direct influence on the oxygen vacancy concentration profile and by this on the resistance degradation behavior of the capacitor. The influence of Pt, RuO_2, Sn-doped In_2O_3 (ITO), and $LaSrMnO_3$ (LSMO) electrodes on the degradation of Fe-doped $SrTiO_3$ single crystals has been studied in the scope of the Master thesis of B. Huang [18]. The results of his thesis reveal considerable different degradation curves for different electrode combinations, which indicate different blocking behavior. Based on his data B. Huang assumed that Pt is non-blocking as anode and totally blocking as cathode, LSMO is assumed to be partially blocking as anode and RuO_2 totally blocking as cathode. For ITO films as anode an oxygen exchange is assumed between the dielectric and the electrode, which was confirmed in the Master Thesis of B. Öcal, who studied the properties of ITO anodes during the resistance degradation of Mn-doped $BaTiO_3$ ceramics [19].

Hence, the ionic de-mixing model is only valid to a certain degree, which emphasizes the importance of dielectric-electrode interface for the overall resistance degradation behavior.

Influence of dopants:

In the following the effect of different type of dopants on the resistance degradation in titanates will be discussed. While the absolute leakage current of the capacitor increases due to donor doping, its compensation mechanisms results in a low total number of oxygen vacancies, which eventually suppresses degradation [6]. This was experimentally confirmed for single- and polycrystalline La-doped $SrTiO_3$ [4, 5].

For acceptor dopants the influence of doping on the performance of the capacitor is more complex. On one hand the acceptor dopants increase the total number of oxygen vacancies, which promotes resistance degradation. On the other hand, the number of charged oxygen vacancies is fixed through ionic compensation $\left[A'\right] \approx 2\left[V_O^{\bullet\bullet}\right]$, which suppresses the electron generation and increases the insulation resistance of the capacitor [86]. For mono-valent acceptor doped $BaTiO_3$ the increase in compensating oxygen vacancies results in fast degradation time with increasing acceptor concentration. This was experimentally proven by Yoon *et al.* who studied resistance degradation of $BaTiO_3$ ceramics with different Mg-concentration but a comparable grain size (one set of coarse-grained and fine-grained samples). Their results confirm a

considerably faster degradation with increasing Mg-concentration [9, 86]. For multi-valent acceptors an improved degradation behavior is observed in titanate based capacitors. The improvement is explained by the ability of the multi-valent acceptor to change its oxidation state in the n- and p-type regions at the electrodes [9]. By this electrons and holes are trapped by the acceptors, which efficiently increases the degradation time. The change in the acceptors oxidation state during degradation of Fe-doped $SrTiO_3$ single crystals can be visualized in so-called electrocoloration experiments[1] [4]. In the beginning of the electrocoloration experiment the crystal is colorless. With ongoing degradation a dark reddish color front grows from the anode region, while the cathode region exhibits a smaller bright color front. The changed colors are related to the presence of mainly Fe^{4+} in the anodic region and Fe^{3+} in the cathodic region. The reddish color front grows with increasing degradation time due to increasing de-mixing and subsequent oxidation of Fe^{3+} to Fe^{4+} (see time-evolution Figure 2.12 a)).

The influence of the charge transition level of the multi-valent acceptor on the degradation curve has been simulated by Baiatu *et al.* and is depicted in Figure 2.13. The position of the charge transition level E_{A2} determines the magnitude of the starting current density as well as the final current density after degradation. Both values decrease with increasing E_{A2}. Additionally, the difference between initial and final current density is decreasing with increasing E_{A2}. Based on this simulation, the degradation time does not seem to be significantly influenced by the position of the charge transition level. However, it should be mentioned, that the independence of the degradation time on the charge transition level position has not been experimentally proven within the work of Baiatu *et al.*.
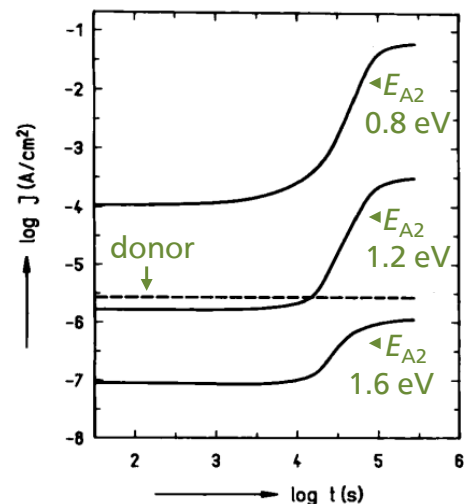
Figure 2.13.: Simulated time-dependent oxygen vacancy profile of a 0.1 at.% acceptor-doped $SrTiO_3$ a) single crystal and b) a polycrystal with eight equally sized grains. Reprinted with permission from [6]. Copyright (1990) Journal of the American Ceramic Society.

From the comparison of Figure 2.11 and Figure 2.13, it is obvious that degradation curves of multi-valent acceptor doped titanates typically differ from the "standard" degradation curves. In the case of multi-valent acceptor doped titanates the increase of leakage current is limited, i.e. it stabilizes at a higher value after degradation [4].

---

[1]Electrocoloration is also observed in undoped $BaTiO_3$. Here, a blueish color front grows at the cathodic region due to the reduction of Ti^{4+} to Ti^{3+}, while the anode appears brownish [87].

3. Sample Preparation and Methodology

3.1. Sample Preparation

3.1.1. Synthesis and Sintering

Nominally undoped $BaTiO_3$, 0.05 wt.% to 0.6 wt.% Mn-doped, and 0.1 wt.% to 0.5 wt.% Fe-doped $BaTiO_3$ have been fabricated by means of the mixed oxides route using oxides/carbonates of the respective elements. The schematic work flow is sketched in Figure 3.1. The starting materials $BaCO_3$ (99.8 % purity), TiO_2 (99.6 % purity), $MnCO_3$ (99.985 % purity), and Fe_2O_3 (99.9 % purity) purchased from *Thermo Fisher Scientific* were weighted on a precision balance according to the calculated stoichiometric formula without considering the charge balance.

Ball milling/homogenization of the raw powders was performed for 12 h with 250 rpm in a planetary Pulverisette 5 mill from *Fritsch GmbH* with ethanol as milling medium and 250 g zirconia milling balls. Afterwards, the slurry was dried in an oven at 90 °C to 100 °C and the dried powders were manually pressed and calcined in a covered aluminum oxide crucible. A platinum foil was placed between the powders and the crucible in order to avoid contact reactions. Calcination[1] was conducted in a box furnace from *Nabertherm GmbH* for 3.6 h to 5 h at temperatures of 1100 °C to 1150 °C with a heating and cooling rate of 5 K/min. During calcination the following reactions were taking place to form $BaTiO_3$ [89–92]:

$$BaCO_3 + TiO_2 \rightarrow BaTiO_3 + CO_2, \tag{3.1}$$

$$BaCO_3 + BaTiO_3 \rightarrow Ba_2TiO_4 + CO_2, \tag{3.2}$$

$$Ba_2TiO_4 + TiO_2 \rightarrow 2\,BaTiO_3. \tag{3.3}$$
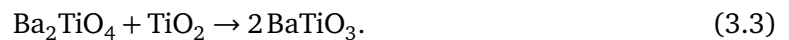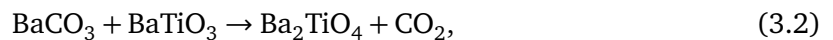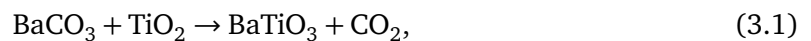
During calcination, Ba^{2+} and O^{2-} ions of the decomposed $BaCO_3$ are diffusing into the shell of the TiO_2 grains, creating a metatitante $BaTiO_3$, which opposes the diffusion of further Ba

---

[1]Precise calcination parameters for Mn-doped and Fe-doped batches are given in Figure 3.1. The high calcination temperatures were chosen due to the report of Simon-Seveyrat *et al.*, who received phase-pure $BaTiO_3$ for calcination temperatures higher than 1050 °C [88].
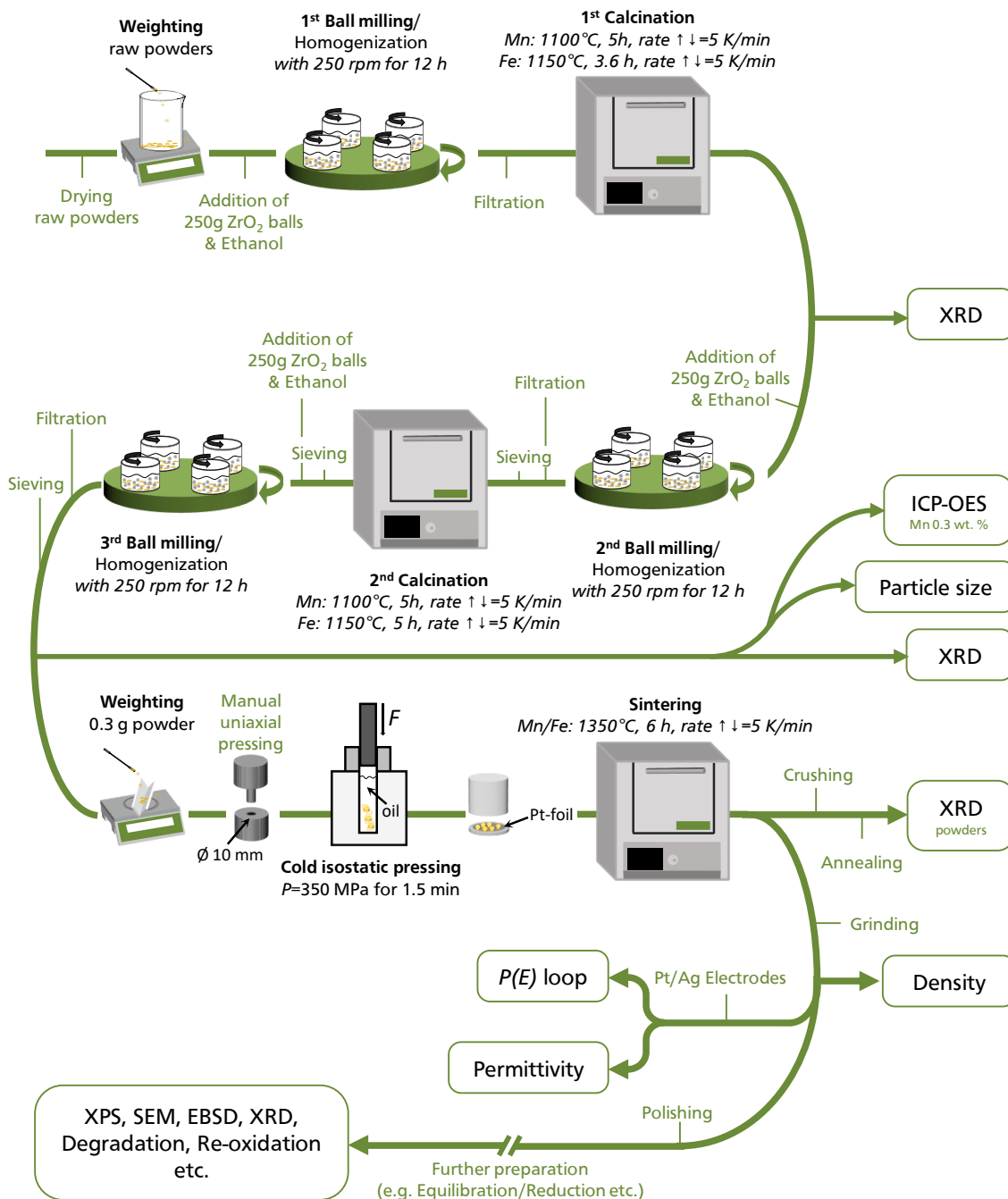
Figure 3.1.: Schematic work flow of synthesis and sintering of polycrystalline acceptor-doped $BaTiO_3$. As raw powders $BaCO_3$, TiO_2, $MnCO_3$, and Fe_2O_3 have been used. Characterization of calcined powders and sintered ceramic pellets was conducted during different steps of synthesis and sintering and is added into the work flow. After polishing of the sintered pellets, equilibration/reduction and further necessary preparation steps for specific analysis methods have been conducted. The latter are described in more detail in the corresponding sample preparation Sections.
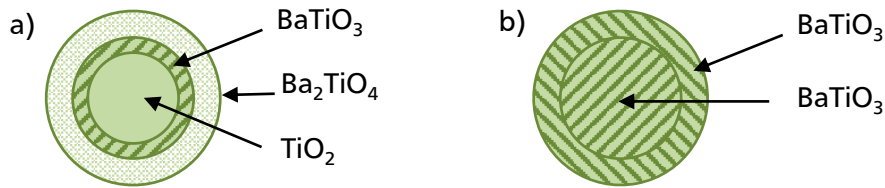
Figure 3.2.: Schematic representation of the calcination process of $BaCO_3$ and TiO_2 to $BaTiO_3$. Pictures are redrawn from [91] according to the mechanism proposed by [90]. a) Reaction according to Eq. 3.1 and Eq. 3.2 of TiO_2 with decomposed $BaCO_3$ to $BaTiO_3$ and further reaction of the $BaTiO_3$ shell with decomposed $BaCO_3$ to Ba_2TiO_4. b) final reaction according to Eq. 3.3 of Ba_2TiO_4 and TiO_2 to $BaTiO_3$.

towards the TiO_2 core (Eq. 3.1). The metatitante $BaTiO_3$ further reacts with $BaCO_3$ to the Ba-rich Ba_2TiO_4 (Eq. 3.2). Finally, Ba_2TiO_4 reacts with TiO_2 to $BaTiO_3$ (Eq. 3.3). The reactions are sketched in Figure 3.2.

Already slight deviations in stoichiometry of the Ba/Ti ratio may lead to the formation of side products such as $Ba_6Ti_{17}O_{40}$ and $Ba_4Ti_{13}O_{30}$ during the last reaction step of calcination (Eq. 3.3) [92]. Thus, X-ray diffraction was conducted to confirm the main perovskite phase.

The calcined powders were pestled manually by hand, followed by a second milling, drying and sieving with a 315 µm mesh. To ensure a complete synthesis of the raw powders to $BaTiO_3$, a second calcination was conducted. The calcined powders were again pestled manually by hand, followed by sieving, third milling, drying and final sieving. After calcination, X-ray diffraction measurements were conducted to confirm the main perovskite phase[2].

Dense ceramics can be derived from the calcined powders via sintering. The latter is a consolidation process to transform compacted powders into solid ceramics by the use of thermal energy. The overall driving force during sintering is the decrease in surface energy. This can happen via two mechanisms, first the reduction of the total surface by the increase in particle/grain size and second by the elimination of solid/vapor interfaces (pores) and the creation of grain boundaries, followed by grain growth. Here, only the second mechanism leads to the decrease in pore size and a densification, while the first even increases the pore size due to increasing grain sizes. In order to obtain high dense ceramics, the coarsening needs to be suppressed until the densification is completed [93].

Several basic atomistic mechanisms are involved in the material transport during sintering, which are depicted in Figure 3.3. Coarsening occurs for all mechanisms, where the material originates from the surface (1-3), resulting in changed grain shapes, but not in densification. Apart from viscous or plastic deformation, only material transport mechanisms from the grain boundary can lead to densification (4-5).

---

[2]Already a small hexagonal phase contribution was observed during XRD on the calcined powders.

No. #	Mechanism
1	Evaporation/condensation
2	Surface diffusion
3 + 5	Volume Diffusion (S + GB)
4	Grain boundary diffusion
	Viscous or creep flow
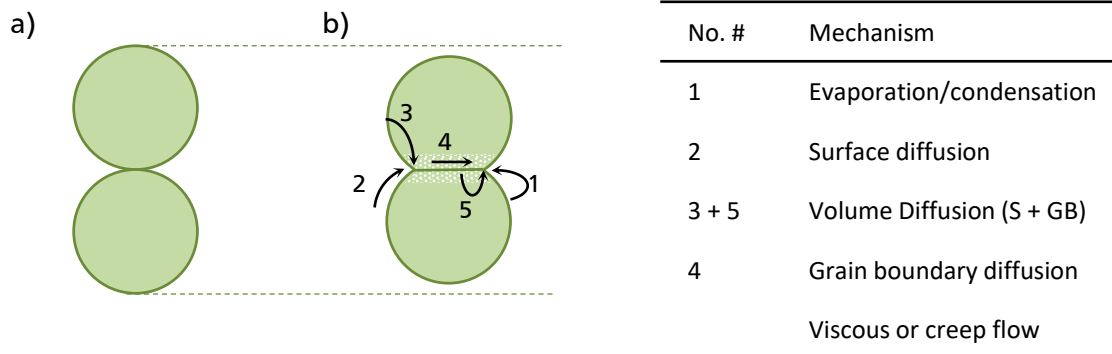
Figure 3.3.: Schematic representation of material transport during sintering. a) two particles before any material transport and b) shrunk particles with different transport mechanism. The transport mechanism 1-5 are named in the right hand table. Mechanism 1-3 result in grain growth/coarsening and mechanisms 4-5 in densification and shrinkage. Pictures are redrawn form [93].

Three different sintering stages have been identified in Ref. [93], namely the initial, the intermediate, and the final stage. During the first stage the neck growth starts and the relative density increases to 60 % to 65 %, during the second stage continuous pore channels are present with three-grain edges and the density increases to 65 % to 90 %, and during the final stage pores are eliminated and the pore and grain boundary mobility increases, which leads to an increase in grain size due to grain growth [93].

Sintering can be divided into two categories, i.e. with and without the occurrence of liquid phase, which refers to liquid-phase-sintering and solid-state-sintering, respectively [93]. During the latter all proportions of the calcined powder are present as solids at the sintering temperature. In contrast, liquid-phase-sintering is taking place, if the sintering temperature is higher than the melting temperature of at least one proportion of the calcined powder. The binary phase diagram of the $BaO-TiO_2$ system under ambient air conditions has an eutectic temperature of $\sim$1320 °C (see Figure A.1) [48]. Thus, in case of $BaTiO_3$, sintering at temperatures above 1320 °C can lead to a liquid phase assisted sintering for Ti-excess[3].
More extended literature on the extensively studied solid-state-sintering process is given in [93].

The present $BaTiO_3$ ceramics were sintered via a conventional solid-state-reaction method. For this purpose, pellets of 0.3 g were manually uni-axially pressed to pellets with a diameter of 10 mm. The pellets were put into a rubber sheath, which was subsequently evacuated. Inside the latter, the pellets were cold-pressed with an isostatic pressure of 350 MPa for 1.5 min and a constant pressure release of 1.5 min by use of a KIP 100E, purchased from *Weber*. The pellets were sintered for 6 h at 1350 °C in air in a covered aluminum oxide crucible in a box furnace

---

[3]Impurities or (un)intentionally dopants will influence the binary phase diagram and the threshold value for the occurrence of liquid phase will be decreased.

from *Nabertherm GmbH*. Again, a platinum foil was placed between the pellets and the crucible in order to avoid contact reactions. The underlying Pt-foil and the pellets were partially covered by powder of the respective composition in order to create a sintering atmosphere, which prevents the evaporation of volatile elements.

The samples had a height of about 1.1 mm to 1.3 mm after sintering (depending on the initial weight). Grinding of the pellets was consecutively conducted using silicon carbide abrasive paper with a grit size of 800, 1200, 2400, and 4000 purchased from *STRUERS*. Polishing of the samples was conducted by use of a semiautomatic polishing machine PHOENIX 4000 purchased from *BUEHLER*. MD-polishing cloth purchased from *STRUERS*, diamond paste with 6 μm, 3 μm, 1 μm, and 1/4 μm diamond particle size and lubricant was used. The final surface finishing particle size and sample thickness varied according to the requirements of the corresponding characterization method. Details on the preparation is described in the corresponding Sections. After grinding/polishing the samples have been cleaned in an ultrasonic bath in acetone for 5 - 10 min, followed by rinsing the sample surface with acetone, isopropyl alcohol, ethanol, and de-ionized water.

The produced samples had the nominal composition of:

$$\text{BaTiO}_{3-\delta} + xA \tag{3.4}$$

with $0 < x < 0.6$ wt.%, $A = $ Mn, Fe and δ depending on the oxygen partial pressure during annealing, which will be discussed in the next Section.

The synthesis of the Mn-doped BaTiO_3 powders as well as parts of the Fe-doped BaTiO_3 powders have been performed by Hui Ding during her Master thesis as well as during her work as a student research assistant. Synthesis and sample processing have been carried out using the equipment provided by the *Nonmetallic-Inorganic Materials group* of the Materials Science Department at TU Darmstadt.

3.1.2. Heat treatments

XRD and brief Rietveld refinement were conducted using powder of crushed sintered samples. The powders have been annealed for 2 h at 200 °C in air in order to release the stress before the XRD measurements. These annealing steps have been conduced in an Al_2O_3 container located in a small box furnace from *Nabertherm GmbH*.

The ground/polished ceramics have been equilibrated in order to establish uniform defect concentration in all specimen. The corresponding set-up is sketched in Figure 3.4. The sample was placed close to the closed end of an one side open quartz tube, which was located in the middle of the hot zone of a tube furnace. During equilibration the samples have been heated for at least 12 h at 900 °C in air followed by quenching to room temperature by a fan with a rate of > 60 K/s. The corresponding treatment parameters are summarized in Table 3.1.

In order to achieve conductive samples some specimens have been heated in highly reducing atmosphere, which resulted in an increased oxygen vacancy concentration and an altered oxidation state of the acceptors. The reduction treatment required a controllable gas flow and an air tight construction to establish the desired low oxygen partial pressure. Therefore, the quartz tube was sealed with a homemade stopper with a gas-inlet and gas-outlet connected to the gas flow meter. A 5 % H_2/95 % Ar gas flow was controlled by a flow meter from *KOBOLD Instruments* and was set to approximately 0.3 Nl/min. During reduction the samples have been heated for at least 12 h at 1100 °C followed by quenching to room temperature by a fan with an estimated rate of > 60 K/s.
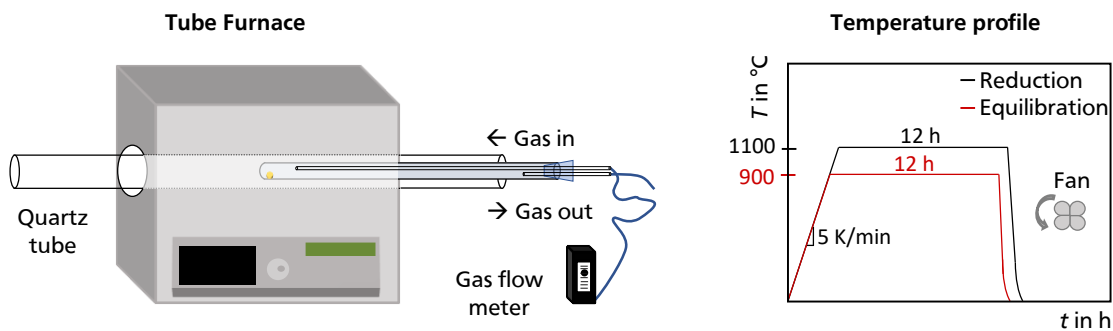
Figure 3.4.: The schematic set-up for the equilibration and reduction treatments is shown on the left. Equilibration was conducted by placing the respective specimen in an one-side open quartz tube, which was located in the middle of a tube furnace. For reduction the quartz tube was sealed with a homemade stopper with an gas-inlet and gas-outlet connected to the gas flow meter. The 5 % H_2/95 % Ar gas flow was controlled by a flow meter from *KOBOLD Instruments* and was set to approximately 0.3 Nl/min. Quenching to *RT* was conducted by a fan with an estimated rate of > 60 K/s. The corresponding temperature profile is depicted on the right.

During both treatments the samples have been in direct contact with the inner quartz tube. The surface appearance of the tube was unchanged after equilibration. After several reduction treatments, however, the quartz tube turned blurry in the area where the specimens have been located, indicating a possible reaction.

Table 3.1.: Heat treatment parameters for the XRD annealing, equilibration, and reduction. The XRD annealing has been conducted in an Al_2O_3 container located in a small box furnace from *Nabertherm GmbH*, while equilibration and reduction have been conducted in a quartz tube located in a tube furnace from *Nabertherm GmbH*. The set-up is depicted in Figure 3.4.

Treatment	Temperature	Atmosphere	Heating rate	Dwell time	Cooling rate
XRD Annealing	200 °C	Air	5 K/min	2 h	5 K/min
Equilibration	900 °C	Air	5 K/min	12 h	quenching
Reduction	1100 °C	5 % H_2/95 % Ar	5 K/min	12 h	quenching

3.1.3. Surface Cleaning, Oxygen Plasma, and Thin Film Deposition

Surface cleaning and *in situ* oxidation of the ceramic samples as well as electrode thin film deposition was conducted in the **DA**rmstadt **I**ntegrated **SY**stem for **MAT**erials research (DAISY-MAT). A schematic representation of the DAISY-MAT is shown in Figure 3.5. The ultra-high-vacuum cluster tool combines a central distribution chamber connected to several preparation chambers and a photoelectron spectrometer. The tunnel connection of the latter allows sample transfers without breaking the ultra-high-vacuum conditions. The spectrometer as well as the distribution chamber have a base pressure of approximately 1×10^{-9} mbar.

Within the different chambers thin film deposition is feasible by means of magnetron sputtering and atomic layer deposition (ALD). All magnetron sputtering chambers are equipped with a heating system with a range of up to 700 °C. The temperature was adjusted by controlling the applied voltage through a radiative heater, i.e. a halogen lamp, which was located directly below the sample stage. A pressure range of 10^{-2} mbar to 10^{-8} mbar is adjustable by adapting the pumping cross section. The gas flow of the connected process gases (Ar, O_2, Ar/O_2 mixture, N_2) is controlled by mass flow controllers from *MKS Instruments*. Surface treatments are feasible by water exposure in the ALD/CVD chamber and by usage of a plasma source, which can operate with O_2 and H_2 plasma.
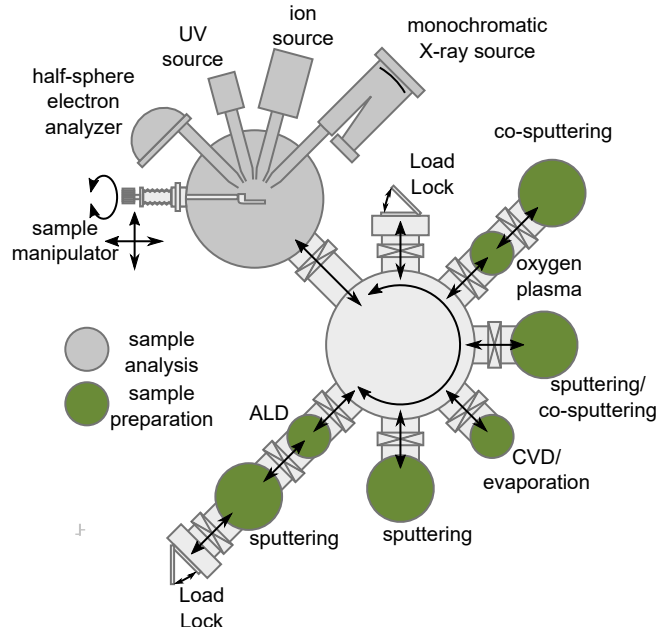
Figure 3.5.: Schematic drawing of the **DA**rmstadt **I**ntegrated **SY**stem for **MAT**erials research. The tunnel connection between the distribution, deposition, and treatment chambers to the photoelectron spectrometer enables a sample transfer without breaking vacuum. Drawing adapted from Ref. [94].

Surface Cleaning Procedure

The ceramic pellets have been processed outside the ultra-high-vacuum cluster tool. Therefore, the sample surface is contaminated by hydrocarbon hydroxides and/or water/moisture. Such contaminations need to be removed as they will affect the contact formation to the electrodes.

As the samples have been equilibrated and/or reduced beforehand, it was necessary to adjust the cleaning procedure to avoid any changes in the established oxidation state. The used cleaning parameters are summarized in Table 3.2.

Equilibrated samples have been cleaned by the standard procedure of heating for at least 1 h at 400 °C in 0.5 Pa oxygen atmosphere. The ceramic samples have been rather sensitive to heating/cooling rate due to the phase transition at approximately 130 °C. Thus, the heating/cooling rate was adjusted to 5 K/min to avoid cracks. The oxygen gas flow was set to 5 sccm.

The standard surface cleaning procedure would most likely result in an undesirable re-oxidation of the surface of reduced samples. Thus, the cleaning for reduced samples was conduced by heating for at least 1 h at 500 °C in vacuum.
Oxygen is more effective in removing carbon hydroxides species from the surface. For this reason the cleaning of reduced samples in vacuum was conducted at higher temperatures than the cleaning of equilibrated samples in oxygen.

Table 3.2.: Surface cleaning parameters for equilibrated and reduced specimens. Samples labeled with "oxidized" in this work have been equilibrated and cleaned with respective cleaning procedure before oxidation.

Status	Temperature	Time	Pressure	O_2 flow	Heating/cooling rate
Equilibrated	400 °C	1-2 h	5×10^{-3} mbar	5 sccm	5 K/min
Reduced	500 °C	1-2 h	1×10^{-8} mbar	—	5 K/min

Oxygen Plasma Source Treatments

In order to analyze the lower limits of the Fermi level the samples have been oxidized in an oxygen plasma. For the creation of the oxygen plasma a multi-purpose GenII plasma source from *tectra* was used. The plasma source can work in the atom, the ion, and a hybrid mode by changing the beam optics. All treatments in this work have been conducted using the atom mode. Therefore, a specially designed aperture plate was installed [95], which solely allows the sample surface bombardment of atoms (and inhibits ions to escape the plasma).

The magnetron is operating at 2.45 GHz with a microwave power of 180 W and the plasma is enhanced by the electron cyclotron resonance (ECR) action of a quadrupole magnetic field. The resulting atom flux is $>2\times10^{16}$ atoms/cm^2/s at a distance of 100 mm. More details on the design and the specifications of the plasma source can be found in Ref. [96] and the user's manual [97].

The samples have been equilibrated and cleaned according to the conditions in Table 3.2. After surface cleaning, the samples have been exposed to an oxygen plasma for 15 min. The plasma current was set to 40 mA and the oxygen gas flow to 2.5 sscm resulting in an average pressure of 2×10^{-4} mbar. The sample temperature during oxygen plasma treatment was varied for the different interfaces and is given in Table 3.3. The heating and cooling rate was 5 K/min for the temperature treatment at 200 °C.

As a side note it should be stated, that for longer plasma treatments molybdenum contamination have been observed on some samples, which most likely originate from the extraction grids of the ion source, which is composed of molybdenum.

Table 3.3.: Oxygen plasma source treatment parameters used for the oxidation of the sample surface before interface formation. All samples have been equilibrated and cleaned in oxygen according to the conditions in Table 3.2 beforehand. The oxygen plasma source was used in the atom mode.

Interface	Temperature	Time	Pressure	Current	O$_2$ flow
RuO$_2$	200 °C	15 min	2×10^{-4} mbar	40 mA	2.5 sccm
ITO	25 °C	15 min	2×10^{-4} mbar	40 mA	2.5 sccm

Thin Film Deposition

The electrode thin films were deposited using the physical vapor deposition technique of magnetron sputtering. Here, an electric field is applied between the cathode (target) and the anode (chamber), which leads to the creation of an ion plasma from the used process gas [98]. The positively charged ions are accelerated towards the target and expel atoms/species from the latter, which can then condense on the substrate. Usually, Ar is used as process gas as it is inert and prevents for undesired reactions. If necessary, also reactive gases such as O_2 and N_2 can be used (additionally). In the case of magnetron sputtering from a metallic Ru target, for example, the addition of oxygen changes the stoichiometry from metallic Ru to RuO_x to RuO_2 with increasing oxygen content in the process gas [99].

Magnetron sputtering can be utilized with direct current (*DC*) or radio-frequency (*RF*). In the case of *DC* magnetron sputtering a constant voltage is applied between the cathode and the anode. Thus, only targets with a high conductivity, such as the metallic Ru and Pt target in this work, can be used with direct current. Otherwise, the surface will built up a positive charge and will prevent further bombardment [100].

Table 3.4.: Deposition parameters for RuO_2, PtO_x, and 10 % Sn-doped In_2O_3 thin film electrodes. Conditioning of the targets was conducted prior the first daily deposition. The pre-sputtering was carried out with the same power and process gas into the closed shutter. Due to a higher sensitivity of the target surface composition of oxides on the oxygen partial pressure, the conditioning for the Sn-doped In_2O_3 target was set to 20 min to 30 min. The more insensitive Ru and Pt metal targets have been pre-sputtered for 5 min to 10 min.

Parameters	RuO₂	PtOₓ	Sn-doped In₂O₃	
			RT	*HT*
Temperature in °C	25	25	25	400 °C
DC/RF	*DC*	*DC*	*RF*	*RF*
Power in W	10	5	25	25
Ar flow in sscm	9.25	5.00	6.60	6.60
O₂ flow in sscm	0.75	5.00	0	0
Pressure in Pa	1.0	0.5	0.5	0.5
Target-sample distance in cm	9.4	7.5	10.0	10.0
Rate in nm/min	3.0	4.0	5.0	5.0

Targets composed of a less conductive material, such as Sn-doped In_2O_3, can be sputtered using radio-frequency. *RF*-sputtering uses an alternating potential (*AC*-signal) at a frequency range of 0.5 MHz to 30 MHz, were a frequency of 13.56 MHz is set as industrial standard and is most often used [98]. Due to the *AC*-signal the target acts alternating as cathode and anode. At frequencies above 0.5 MHz the response time of the lighter electrons to the AC signal is much faster than the one of the more heavy ions. As a consequence of the different response times, the target becomes negatively charged, resulting in a so-called self bias.

For the thin film deposition of RuO_2 and PtO_x electrodes a MDX500 DC power supply from *Advanced Energy* was used, while a PFG 300 *RF*-generator and a match box from *Hüttinger* was used for the deposition of the Sn-doped In_2O_3 electrodes. The diameter of the used targets was 2". The deposition parameters for the different electrodes are given in Table 3.4.

A typical interface experiment starts with the characterization of a clean surface using PES. Afterwards, the contact material is stepwisely deposited until the substrate emissions are completely attenuated. Between each deposition steps, survey and high resolution core level spectra are recorded. The deposition time for each step depends on the desired step width and the deposition rate of the contact material. The interface experiments in this work were focused on the final barrier height. Thus, in almost all cases only two deposition steps have been conducted with a thickness, for which the barrier is expected to be already fully developed. The bulk contact material has only been measured once within this work.

The deposited electrode thickness of <5 nm is most likely not sufficient enough for a reliable electrical contact to the mask of the sample holder and thus to the ground. In order to avoid charging during photoelectron spectroscopy, approximately 1/4 of the sample has been coated with platinum, which serves as contact between the substrate, the electrode, and the mask. This platinum contact was deposited in a Q300T D bench top sputter coater from *Quorum* and had a thickness of roughly 50 nm.
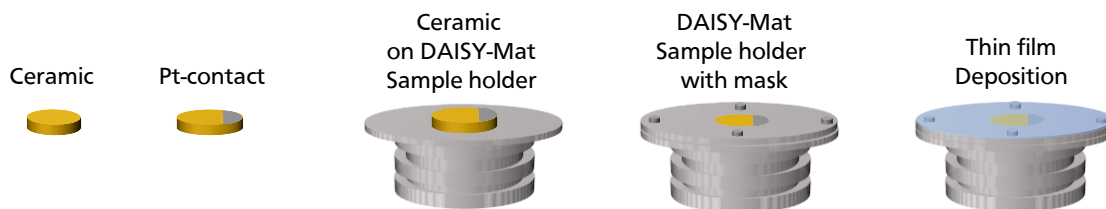
Figure 3.6.: Schematic flow chart of the sample preparation for interface experiments. The sample edge has first been deposited with platinum. After mounting to the DAISY-Mat sample holder, the platinum is in contact with the mask. After thin film deposition, it facilitates the electrical contact between sample, thin film, and mask/sample holder and thus ensures an electrical grounding during PES.

3.2. Methodology

3.2.1. Purity, Particle Size, and Density

Inductively coupled plasma - optical emission spectrometry

Inductively coupled plasma - optical emission spectrometry (ICP-OES) has been performed in order to analyze the elemental composition and purity of the calcined 0.3 wt.% Mn-doped $BaTiO_3$ powder in the frame of a device test measurement. The inductively coupled plasma is used as energy source of this technique. The analyzing aerosol of the digested sample is introduced into the plasma torch. The high temperature plasma breaks the sample molecules into atoms and ions and excites electrons from a lower to a higher energy level [101].
Upon relaxation of the electrons to their initial lower energy level, photons of a specific wavelength are emitted. The photon's wavelength depends on the difference of the energy levels and is thus characteristic for the respective element. A spectrometer analyzes the emission lines from the sample. By analyzing the intensities of the emission lines the concentration of the corresponding element can be deduced.

The introduction of solid samples into the plasma is not possible. Thus, the samples need to be dissolved or digested into a solution. One main techniques, which was also used in this work, is the acid digestion.
The calcined 0.3 wt.% Mn-doped $BaTiO_3$ powder has been digested by the use of a ETHOS.lab by *MLS Mikrowellen GmbH*. Within the ETHOS.lab the mixture has been heated to 225 °C for 45 min. The following acids have been used for digestion:
5 ml H_2O + 5 ml HCl (32 %) + 5 ml HNO_3 (65 %) + 1 ml HF (48 %) .

After digestion, a white crystalline precipitate remained in the liquid. The corresponding ICP-OES measurements indicated an incomplete digestion of Ba and/or Ti. A second digestion step with 10 ml H_3BO_3 (ca. 5 % (cold saturated)) could dissolve the precipitate. After the second step a clear colorless mixture is achieved.

ICP-OES has been performed by an iCAP PRO XP from *ThermoFisher Scientific*. The fully digested 0.3 wt.% Mn-doped $BaTiO_3$ samples as well as the reference blind value of the acid mixture have been analyzed.

Particle Size Analyzer

The particle size distribution of the calcined powders has been evaluated using a Saturn DigiSizer II 5200 particle size analyzer from *Micromeritics*. This technique is based on the light scattering of a laser with a wavelength of 658 nm. The coherent beam of the parallel monochromatic light straightly propagates the homogenous analyzing liquid and scatters at the surface of the dissolved particles. The scattered light is focused by a lens on a detection plane, on which a particle size and shape (and refractive index) dependent scattering pattern is created. Based on the Mie theory [102], the particle size distribution is calculated from the angular distribution and intensity of the scattering pattern [103, 104]. According to the user's manual [105], a possible analyzing particle range of 0.1 to 1000 μm is feasible with an accuracy of 10 % and 3 % for a particle size of 0.1 to 1 μm and 1 to 1000 μm, respectively.

The calcined powder was added into a small beaker filled with isopropyl alcohol, which was used as analyzing liquid. In order to avoid agglomeration, the mixture has been additionally dispersed by an ultrasonic disperser for 2 min with an amplitude of 60 %. Afterwards, the mixture was added into the reservoir of the particle size analyzer until an obscuration of 5 % to 15 % was reached.

Archimedes Density

The density of the samples was determined using the Archimedes method [106] by means of a density determination set-up from *Sartorius*. Archimedes assumed that every solid, which is immersed in a liquid is exposed to the buoyancy force of the liquid. Accordingly, the weight of the immersed solid is lowered by the weight of the liquid being displaced by the volume of the solid.

$$\rho = \frac{W_a \cdot \rho_{fl}}{W_a - W_{fl}} \tag{3.5}$$

With ρ being the density of the sample, ρ_{fl} being the density of the liquid, W_a the weight of the sample in air, and W_{fl} the weight of the sample in the liquid. In the present work distilled water was used as a liquid and its temperature dependent density was determined by the use of a thermometer.

For a better accuracy, the air buoyancy during the weight measurement need to be considered. Thus, the density of air ρ_a is added into Equation 3.5. Furthermore, the depth of immersion of the sample holder increases, which leads to an additional buoyancy when the sample is weighted in the liquid. Therefore, a set-up specific correction factor *Corr* of 0.99983 is added.

This results in the following formula:

$$\rho = \frac{W_a \cdot (\rho_{fl} - \rho_a)}{(W_a - W_{fl}) \cdot Corr} + \rho_a.$$

(3.6)

In order to avoid errors resulting from air bubbles, the samples have been evacuated for 20 min in distilled water.

For the determination of the relative density, the measured sample density has been compared to a theoretical density of $6.02 \frac{g}{cm^3}$ for $BaTiO_3$ [41].

3.2.2. Di- and Ferroelectric measurements

Temperature- and Frequency dependent Permittivity

The temperature-dependent dielectric behavior of as-sintered/annealed unpoled specimens was measured with an HP4284A impedance analyzer from *Hewlett Packard*. The samples have been ground to a thickness of 500-700 μm and 50 nm thick platinum electrodes of a diameter of 7 mm were deposited in Q300T D bench top sputter coater from *Quorum*. The samples were placed in a home-made sample holder, which was embedded into a box furnace purchased from *Nabertherm GmbH*. The temperature profile was controlled by a Eurotherm temperature controller and the data-acquisition was realized via a home made LabVIEW program.

The temperature-dependent permittivity was measured at frequencies of 10^2 Hz, 10^3 Hz, 10^4 Hz, 10^5 Hz, and 10^6 Hz and temperatures up to 250 °C. A measuring amplitude of 1 V and a heating and cooling rate of 2 K/min and 5 K/min was used. The used temperature profile with all relevant parameters is depicted in Figure 3.7. Two temperate cycles have been conducted to exclude any changes due to temperature annealing. As no changes have been observed between the two cycles, the characteristic values have been determined during the first heating cycle.
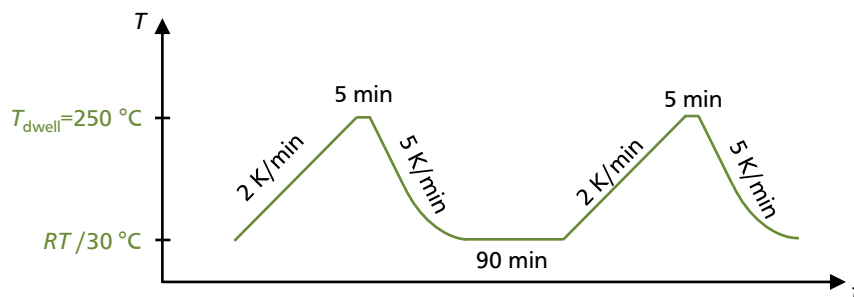
Figure 3.7.: Temperature profile for the permittivity measurements. A heating and cooling rate of 2 K/min and 5 K/min was used, respectively. The dwell temperature of 250 °C was held for 5 min and the rest time at 30 °C between both cycles was set to 90 min.

The capacitance and the loss factor $\tan(\delta)$ are measured as a function of temperature and frequency. The relative permittivity was calculated from the measured capacitance according to Equation 3.7.

$$C = \epsilon \epsilon_0 \frac{A}{d} \tag{3.7}$$

Where C denotes the capacitance, ϵ the relative permittivity, ϵ_0 the vacuum permittivity, and A and d the electrode area and the dielectric thickness, respectively.

Electric field dependent polarization and strain

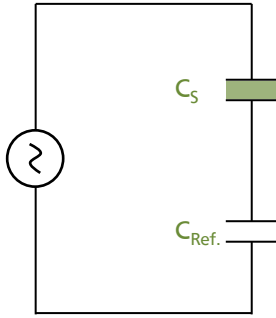Many commonly used measurement set-ups for the determination of ferroelectric hysteresis loops are based on the Sawyer-Tower circuit [107]. The Sawyer-Tower circuit is illustrated in Figure 3.8. Within the latter the sample is connected in series with a reference capacitor of a known capacitance $C_{\text{Ref.}}$. The capacitance of the reference capacitor is chosen in such a way, that the voltage drop across the reference is much less than that across the sample (typically $C_{\text{Ref.}} \geq 1000 \times C_{\text{S}}$). During the measurement the voltage drop $U_{\text{Ref.}}$ across the reference capacitor is recorded, which is proportional to the stored charge $Q_{\text{Ref.}} = C_{\text{Ref.}} \cdot U_{\text{Ref.}}$. Generally, capacitors connected in series will store the same charge $Q = Q_{\text{Ref.}} = Q_{\text{S}}$. Thus, the measured charge on the reference capacitor via the voltage drop is identical to the one of the sample.

Figure 3.8.: Schematic of the Sawyer-Tower circuit.

The stored charge is proportional to the polarization P by $Q = P \cdot A$, where A denotes the electrode area. Accordingly, the desired polarization P_{S} of the sample is determined by $P_{\text{S}} = Q/A_{\text{S}} = (U_{\text{Ref.}} \cdot C_{\text{Ref.}})/A_{\text{S}}$.

Before the measurements, the as-sintered samples have been ground and 50 nm thick platinum electrodes of a diameter of 7 mm were deposited on both sides.

During the measurements the samples have been submerged in silicon oil. The measurements have been carried out with a bipolar triangle wave form with an amplitude of 3 kV/mm. The measurements have been conducted at frequencies of 0.1 Hz, 1 Hz, 10 Hz, and 50 Hz and the time between the data points was set to 0.1 ms. Three cycles have been conducted. A reference capacitor of 10 µF has been used during all measurements.

The strain S was measured simultaneously to the electric field dependent polarization. The displacement was monitored by an optical sensor that detected the intensity of reflected light. More detailed information on the used modified Sawyer-Tower circuit and the strain measurements can be found in Ref. [108, 109].

The di- and ferroelectric measurements have been carried out using the equipment provided by the *Nonmetallic-Inorganic Materials group* of the Materials Science Department at TU Darmstadt.

3.2.3. Electrical measurements

Re-oxidation

The aim of the re-oxidation experiments is the identification of defect energy levels. The measurements are based on the idea that the activation energy of electrical transport depends on the oxygen vacancy concentration. Thus, a pinning of the Fermi level on the defect levels during oxygen incorporation should result in a pinning/a plateau of the activation energy as well. This approach was first presented by Suzuki *et al.*, who used this method to successfully determine the defect energy levels of the Fe impurities in $BaTiO_3$ and $SrTiO_3$ single crystals [22]. In contrast to Suzuki *et al.*, who used single crystals, the re-oxidation experiments in this work have been conducted on ceramic samples. Thus, an additional influence of grain boundaries on the measured activation energy is expected in this work.

Prior to re-oxidation, the samples have been ground/polished followed by equilibration and reduction. During reduction, the oxygen vacancy concentration is increased, which results in an increased conductivity and a Fermi level expected to be close or even inside the conduction band. During the successive re-oxidation oxygen is in cooperated and the Fermi level is lowered.

The electrical measurement during re-oxidation was conducted in the furnace illustrated in Figure 3.9. In order to realize a stepwise re-oxidation, the samples were heated up and cooled down repetitively with a rate of 2.5 K/min and 5 K/min, respectively. Between heating and cooling, the samples were hold at a certain temperature for a certain dwell time. As re-oxidation atmosphere an O_2/N_2 mixture has been used. The *DC* conductivity of the samples was continuously measured with a sampling rate of 20 s/meas with a Keithley 6487 picoammeter/voltage source from *Keithley Instruments*. The latter was connected to the electrodes with mechanically attached gold wires. The applied voltage was between 0.01 V to 4 V depending on the resistivity of the sample. Low voltages have been chosen in order to avoid polarization of the sample during measurement[4]. The data-acquisition was realized via a home made LabVIEW program. All parameter ranges are given in Table 3.5.
Additionally, fast re-oxidation measurements have been conducted, which represent a single-loop measurement with $T_{dwell} = 450\,°C$ and $t_{dwell} = 1\,h$.

---

[4]In the scope of the measurements it has been shown that 4 V are already affecting the measurements. For more details see Ref. [110].
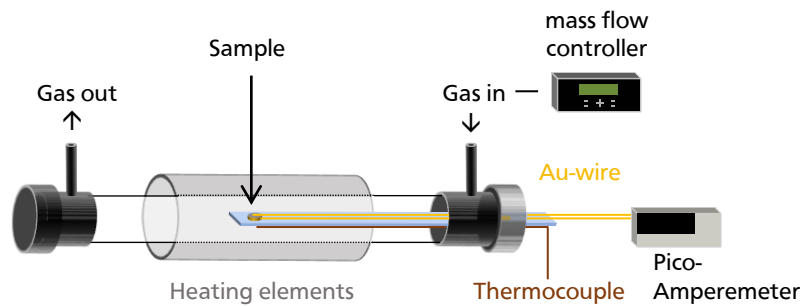
Figure 3.9.: Schematic set-up of the re-oxidation experiments. The sample was mounted on a homemade holder, with Au wires serving as front and back contact and a thermocouple underneath the sample recording the temperature. The furnace temperature has been controlled by programming an Eurotherm 2416 connected to a reference thermocouple. The gas flow during repetitive heating was controlled by a flow meter. The *DC* conductivity of the samples was continuously measured by a Keithley 6487 picoammeter/voltage source. The parameters for the different re-oxidation measurements are given in Table 3.5 and in the text.

The re-oxidation experiments of Mn- and Fe-doped $BaTiO_3$ have been performed by several students in the framework of their advanced research laboratories and/or Bachelor and Master theses. Hui Ding performed the measurements of 0.1 wt.% Mn-doped $BaTiO_3$ as part of her Master thesis, Nicola Gutmann the ones of 0.5 wt.% Mn-doped $BaTiO_3$ as part of her Bachelor thesis, and Lisanne Gossel the ones of 0.1 wt.% and 0.5 wt.% Fe-doped $BaTiO_3$ as part of her advanced research laboratory and Master thesis.

In 2-point measurements, the conductivity σ of the sample can be calculated from the dielectric thickness d, the electrode area A, the applied voltage U, and the recorded current I. The correlation of the parameters is given by

$$\sigma = \frac{I \cdot d}{U \cdot A}. \tag{3.8}$$

The activation energy of electrical transport is calculated from the corresponding Arrhenius law, where E_A denotes the activation energy, k the Boltzmann constant and T the temperature

$$\sigma \sim \exp^{-\frac{E_A}{k \cdot T}}. \tag{3.9}$$

As can be seen from Table 3.5, the re-oxidation parameters such as dwell temperature and time have been individually adjusted for each sample. Thus, the grade of re-oxidation is strongly affected by the loop parameter history and varies between the different samples. In order to compare the results of the different re-oxidation experiments, an effective re-oxidation time (*ERT*) has been introduced in the work of H. Ding [111].

Table 3.5.: Preparation parameters of the ceramic samples before and during re-oxidation. Essential parameters are the thickness d, the electrode area A, and the equilibration and reduction temperature. Pt with a thickness of approximately 50 nm has been used for all samples as electrode material. A heating rate 2.5 K/min and a cooling rate 5 K/min was used. The oxygen content in the gas, the dwell temperature T_{dwell}, and time t_{dwell} and the applied voltage U during re-oxidation were adjusted between the loops. The Al-doped $SrTiO_3$ has been synthesized in Clive Randalls group at PennState University. *= d and A are not available for this sample.

| | | SrTiO$_3$ | BaTiO$_3$ | | | |
		Al-doped	0.1 wt.% Mn	0.5 wt.% Mn	0.1 wt.% Fe	0.5 wt.% Fe
Preparation	d$_{dielectric}$ in μm	968	*	790	884	565
	A$_{electrode}$ in cm^2	0.212	*	0.416	0.385	0.385
	Eq T in °C	900	900	900	900	900
	Red T in °C	1000	1100	1100	1100	1100
ReOx	Gas (% O$_2$)	5	1-10	5	20	20
	T_{dwell} in °C	150-575	300-600	100-420	450-600	450-700
	t_{dwell} in h	0.5-10	1-20	0.05-0.33	1-57	1-12
	U in V	0.01-0.3	0.03-0.3	0.03-0.1	0.03-4	0.003-4

The *ERT* is based on the assumption that the grade of re-oxidation during one loop can be described by the diffusion length of the incorporated oxygen during dwell time. The *ERT* is based on

$$L = \sqrt{\tau \cdot D}, \tag{3.10}$$

where L denotes the diffusion length, τ the life time, and D the diffusion coefficient. Equation 3.10 was adapted to receive the *ERT*. Therefore, τ was replaced by the dwell time t_i of the loop number i. The temperature dependence of the loops is represented by the diffusion coefficient, which is proportional to $D \sim \exp^{-\frac{E_A}{k \cdot T_i}}$, where E_A denotes the migration enthalpy of oxygen vacancies and T_i the dwell temperature. An activation energy of 0.7 eV is assumed for the oxygen migration in BaTiO$_3$ [27]. The previously made assumptions result in the final definition for the *ERT* of the nth re-oxidation cycle

$$ERT_n \equiv \sum_{i=1}^{n} \sqrt{t_i \cdot \exp\left(-\frac{E_A}{k \cdot T_i}\right)}. \tag{3.11}$$

ERT is dimensionless per definition [111]. However, it is important to use a consistent unit for the dwell time. The latter was set to hours in the present work and in the work of all students.

Electrical Degradation

Resistance degradation experiments have been conducted in a homemade set-up, which enabled a simultaneous measurement of the resistance degradation of the dielectric bulk and the electrode conductivity. Beside sample specific properties, two main external parameters are essential for the resistance degradation, namely the temperature and the applied electric field.

A schematic of the degradation set-up is illustrated in Figure 3.10. Within the set-up a hotplate is used as heater. Even though the heat is solely coming from the bottom and is not distributed uniformly as it is the case in the re-oxidation oven, a negligible temperature gradient between the bottom and the top of the sample is assumed.
The hot plate is connected to a multimeter model 2002 from *Keithley* and, thus, serves as the electrical back contact to measure the perpendicular current through the dielectric.
Four gold coated tungsten tips are connected to small platinum contacts on top of the to be examined electrode. Probe 1 simultaneously serves as the front contact for the perpendicular current through the dielectric. A current source model 6220 from *Keithley* was used to apply the current between the 4-point conductivity contacts, whereas a multimeter model 2700 from *Keithley* was used to measure the voltage difference between the contacts.

This set-up has been built as a part of the Master thesis of Baris Öcal. For more information and details on the electronic circuits and the LabVIEW program see Ref. [19].

The dielectric conductivity can be calculated according to Equation 3.8 from the dielectric thickness, the electrode area, the applied perpendicular voltage, and the measured perpendicular current.
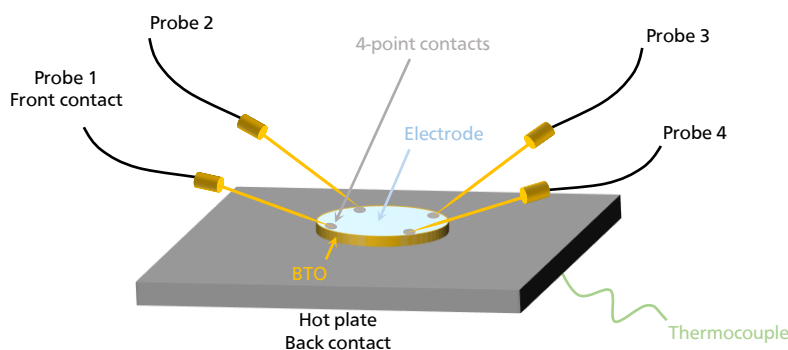
Figure 3.10.: Schematic of the degradation set-up. Within this set-up the dielectric and electrode conductivity can be measured simultaneously during degradation. The hot plate serves as heater and back contact for the conductivity measurement of the dielectric.

The electrode conductivity is derived in the van der Pauw geometry [112]. During the latter four point contacts are used to measure the conductivity of the electrode. A scheme of the geometry for this measurements is illustrated in Figure 3.11. The four contacts are required to be small and on the edge of the sample. The geometry of the sample can have any arbitrary shape as long as it provides a homogeneous film thickness d, which needs to be known for the determination of the resistivity.

A current is applied between two neighboring contacts, while the voltage is measured between the other two. The measurement setup is changing the contact combinations and the current direction during one measurement cycle. Ideally, no discrepancy in the resistivity upon changed current direction and contact combination is observed. Pt contacts were chosen for all experiments.

Figure 3.11.: Schematic representation of the 4-point conductivity measurement for a square shape sample.

The resistivity can be calculated from Equation 3.12. Here, $R_{AB,CD}$ corresponds to U_{AB}/I_{CD} and $R_{BD,AC}$ to U_{BD}/I_{AC}. The van der Pauw correction factor $f\left(\frac{R_{AB,CD}}{R_{BD,AC}}\right)$ is related to the homogeneity and the shape of the sample. For a homogenous and symmetric sample $f=1$ [112].

$$\rho = \frac{1}{\sigma} = \frac{\pi d}{ln2} \cdot \frac{R_{AB,CD} + R_{BD,AC}}{2} \cdot f\left(\frac{R_{AB,CD}}{R_{BD,AC}}\right) \tag{3.12}$$

For a typical degradation experiment the samples have been ground/polished and top and bottom platinum electrodes of 7 mm diameter and a thickness of roughly 30 nm to 50 nm have been deposited in Q300T D bench top sputter coater from *Quorum*. The perpendicular voltage was set in such a way that the electric field was 0.3 kV/mm. For a better comparison, the electric field was set constant to 0.3 kV/mm through most of the experiments, while only the temperature has been varied.

Degradation temperatures between 160 °C to 295 °C have been used to achieve comparable degradation times.

Studies on the electrode conductivity during degradation of Mn-doped BaTiO$_3$ have been conducted for ITO as an anode. The ITO electrode thickness has been varied between 5 nm to 50 nm.

Parts of the degradation experiments have been performed by students in the framework of their advanced research laboratories and Master theses. Baris Öcal built the set-up and performed all measurements on the influence of ITO as an anode and parts of the degradation measurements on Mn-doped BaTiO$_3$, while Lisanne Gossel performed the measurements on Fe-doped BaTiO$_3$ as part of her advanced research laboratory.

3.2.4. Crystal- and Microstructure

X-Ray Diffraction

X-ray diffraction (XRD) is one of the most important non-destructive method to analyze the crystal structure of fluids, powders, and crystals [113].

If the wavelength of an incident wave and the periodicity of a crystal are of similar magnitude, diffraction effects occur. Lattice constants typically have a magnitude of several Å. Besides the used X-rays in this work, also electrons and neutrons with the respective energies can be used for diffraction experiments [114].

X-rays are electromagnetic waves with a wavelength between 10 pm to 10 nm. The interaction of X-rays with matter can be dissipated into the ejection of orbital electrons and scattering. The former interaction is called photoelectric effect, on which the photoelectron spectroscopy described in Section 3.2.5 is based.

The latter interaction can be divided into elastic (Thomson) and inelastic (Compton) scattering. Due to the conversion of energy and momentum, an inelastic scattering event of X-rays on electrons results in a loss in energy and, thus, in an increase in wavelength. These inelastically scattered X-rays do not result in diffraction and are of minor importance for the present XRD method [113].

In contrast, elastic scattering without change in wavelength is the main type of scattering involved in X-ray diffraction. During the latter the energy of the photon is conserved and solely the direction of propagation is altered by the scattering event. Therefore, Thomson and Compton scattering are also called coherent and incoherent scattering, respectively [113].

In general, the elastically scattered waves from a crystal lattice can undergo constructive and destructive interference. Constructive interference between two scattered waves occurs when the delay between the waves being scattered form different lattice planes is a multiple number of the wavelength. The directions of constructive interference are determined by Bragg's law

$$n\lambda = 2d_{hkl} \cdot \sin(\theta), \tag{3.13}$$

where λ denotes the wavelength of the X-rays, θ the angle between the lattice planes and the incident beam, d the distance of the lattice planes for which the reflection occurs, and n an integer number. The geometric derivation of Bragg's law is illustrated in Figure 3.12.
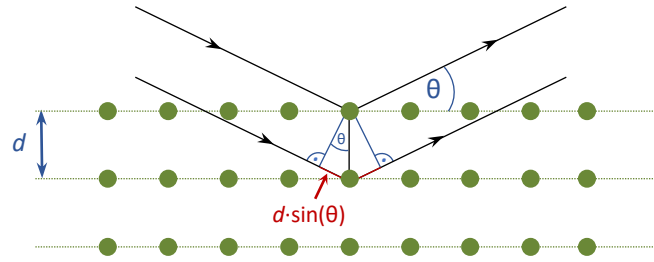
Figure 3.12.: Geometric derivation of Bragg's law from X-rays being scattered on two different lattice planes with a lattice spacing of d. θ corresponds to the angle between the incident X-rays and the lattice planes. The delay between both scattered waves is highlighted in red and corresponds to $2d \cdot \sin(\theta)$.

In a conventional diffraction pattern the intensity is plotted as a function of the diffraction angle 2θ. First, the d-spacing can be deduced from the Bragg equation. The d-spacing depends on the (hkl) lattice plane that fulfills the Bragg equation. The correlation between the d-spacing, the (hkl), and the lattice parameters a, b, and c is given by

$$d_{hkl} = \frac{1}{\sqrt{\left(\frac{h}{a}\right)^2 + \left(\frac{k}{b}\right)^2 + \left(\frac{l}{c}\right)^2}}. \tag{3.14}$$

Nowadays the phase identification is realized by comparing the measured diffractogram to a database containing standard reference powder-diffraction-pattern (PDF). During this work, the DIFFRAC.EVA software from *Bruker AXS* was used to compare the measured diffraction pattern with the database. It should be stated, that the represented reference PDF cards shown in this work have solely been used for phase identification. In order to receive further reliable information from the pattern (e.g. lattice constants, phase fractions, density, stain) a deeper analysis via the Rietveld method is necessary.

Within this work XRD measurements have been performed in the reflection/Bragg-Brentano and the transmission/Debye-Scherrer geometry, which are illustrated in Figure 3.13 on the left and right hand side, respectively.
The conventional θ-2θ scans have be carried out in the Bragg-Brentano geometry. Here, the incident angle ω is defined as the angle between the X-ray tube and the sample. The diffraction angle 2θ is defined as the angle between the incident X-ray beam and the detector. For a θ-2θ scans it holds $\omega = \frac{2\theta}{2} = \theta$. Here, both, the X-ray source and the detector are moving during the measurement. The signal of the topmost surface can be enhanced by performing scans with an fixed grazing incidence angle. This measuring geometry is known as grazing incidence X-ray diffraction (GIXRD), where the incident angle ω is fixed and only the detector is moving.

Transmission XRD has been carried out in the Debye-Scherrer geometry. Here, the incident X-ray beam has a fixed angle and solely the detector moves. According to the application report of the manufacturer [115], the transmission geometry has a variety of advantages when analyzing powders. The transmission geometry provides reliable intensities even at small θ angles as there is no unaffected beam. Furthermore the height displacement is rather sensitive for reflection data leading to a zero shift in 2θ, which is less sensitive in transmission as the aligned capillary is always in the center of the goniometer. Furthermore, transmission leads to less broadened lines for weak absorber and a better statistical distribution of the particles.
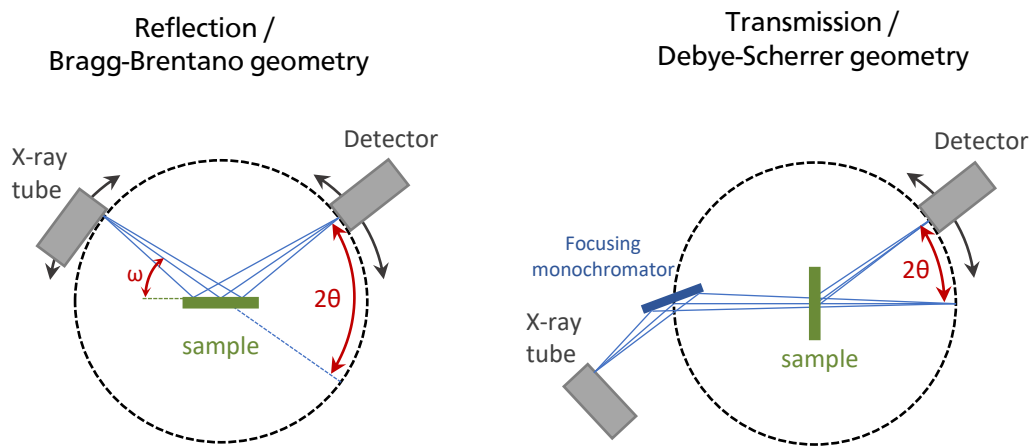
Figure 3.13.: Schematically set-up for the XRD measurements in reflection and transmission geometry. ω corresponds to the incident angle between the X-ray tube and the sample and 2θ is defined as the angle between the incident X-ray beam and the detector. Figures inspirited by Ref. [116].

Besides the geometry, also the used X-ray source is of importance [117]. The X-ray source shall be chosen in such a way, that as much intensity as possible reaches the sample. Therefore, the diffraction in air and the absorption inside the material should be minimized. For the latter it is recommended to compare the absorption edges of the analyzing material with the wavelength of the X-ray. Samples, which for example contain Fe, Cr, or Mn, will fluoresce under an incident beam from a Cu K$_\alpha$ source and create polychromatic radiation, which elevates the background and is undesirable.

On the other hand, a change in source results in a change in X-ray wavelength and thus in energy, which results in different penetration depth of the X-rays. Even though the exact correlation is a bit more complicated, in general it holds that the higher the X-ray energy the higher the penetration depth. Further reading on most suitable geometries and X-ray sources for a specific problem is available in Ref. [117].

The pattern of the calcined powders and equilibrated/reduced pellets were recorded by a D8 Advance diffractometer from *Bruker AXS* with Cu K_α radiation with a wavelength Cu $K_{\alpha 1}$ of $\lambda = 1.540\,56\,\text{Å}$ and an energy dispersive Sol-X detector. This conventional θ-2θ scans have been performed in reflection in the Bragg-Brentano geometry as depicted in Figure 3.13 on the left. The scans have been conducted for $10° \leq 2\theta \leq 90°$ with a step width of $0.02\,°$. GIXRD measurements on a reduced 0.5 wt.% Mn-doped $BaTiO_3$ pellet have been carried out on the same diffractometer for $\omega = 5°$ and $10° \leq 2\theta \leq 70°$.

The pattern of the sintered and crushed powders were recorded by a STADI P diffractometer from *STOE* with Mo $K_{\alpha 1}$ radiation with a wavelength of $\lambda = 0.7093\,\text{Å}$ and a position sensitive detector. The scans have been conducted for $5° \leq 2\theta \leq 50°$ with a step width of $0.01\,°$. The used transmission configuration is derived from the Debye-Scherrer geometry and is depicted in Figure 3.13 on the right. Within the latter, a curved focusing Ge(111) monochromator has been used. The NIST standard Si640d was added as reference material to all powders, which later have been analyzed by Rietveld refinement.

All XRD and GIXRD measurements in this work have been thankfully performed by Jean-Christophe Jaud from the *Structure Research group* of the Materials Science Department at TU Darmstadt. The Rietveld refinement on the diffraction data of the sintered powders has been thankfully carried out by Leif Carstensen from the same working group using the FullProf software.

Scanning electron microscopy

Scanning electron microscopy (SEM) is an imaging method, which is based on the interaction of a primary electron beam with the surface [118, 119]. An image of the latter is created by detecting the scattered electrons by a scanning motion.

The primary electrons originating from a thermionic, Schottky, or field-emission cathode are accelerated through a voltage (between 0.1 keV to 50 keV) difference towards an anode. The electron beam is first focused by condenser lenses before it is passing through the scanning coils, which are responsible for the x and y beam deflection during the raster scanning motion. Finally, the beam is focused by a objective lens onto the sample surface.

The primary electron beam generates a variety of signals at the surface of a solid specimen. The different signals and their corresponding information depths and volumes are illustrated in Figure 3.14. Elastic and inelastic scattering are the basic interactions resulting in image formation. Inelastic scattering of the primary electron beam results in the creation of secondary electrons (SE) from outer shell electrons of the specimen. Surface imaging using the SE mode is the most common operation mode in SEM. The low energy SE electrons originate from the topmost 5 nm and reveal the surface topography. The contrast is given by the brightness, which depends on the number of secondary electrons reaching the detector.

Elastic scattering of the primary electron beam results in backscattered electrons (BSE). Since the primary electron only lost a small fraction of its energy during the elastic scattering event, the energy of the backscattered electrons is much higher than the one of the secondary electrons.
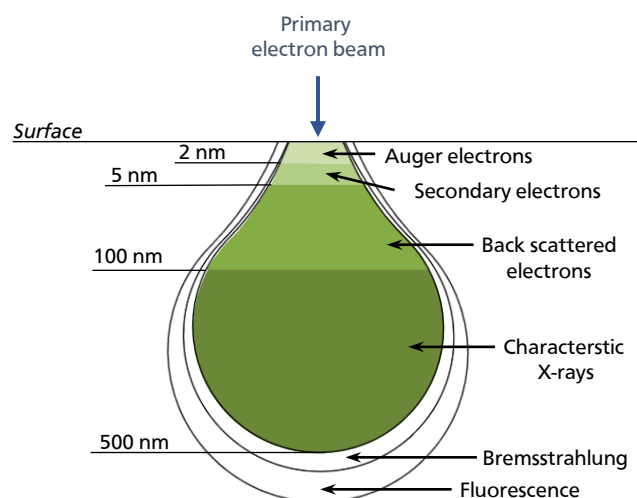
Figure 3.14.: Schematic of the information depth and volume of the primary electron beam - matter interactions.

Thus, BSE originate from deeper depths of the specimen. Their intensity also depends on the tilt of the sample and, thus, the BSE mode can also be used for imaging the surface. Furthermore, the intensity of backscattering depends on the atomic number Z of the elements in the specimen and, thus, BSE in addition provides compositional information. A higher atomic number, which means heavier element, acts as a stronger scattering center and results in a higher BSE intensity and brightness in the final image.

Additionally, the back scattered electrons can also be used to determine the crystallographic structure of the specimen. This method is called electron backscatter diffraction (EBSD). The backscattered electrons, which are diffracted at the Bragg conditions (see Equation 3.13), form so-called Kikuchi bands. An exemplary electron backscatter diffraction pattern is shown in Figure 3.15. The bright lines corresponds to Kikuchi bands, which can be indexed individually by Miller indices of the corresponding diffracting lattice plane. Therefore, the diffraction pattern can be used to determine the crystal phase and enables an orientation mapping of the surface grains.
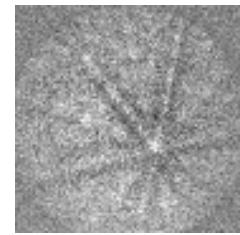
Figure   3.15.:   Electron backscatter diffraction pattern of a 0.5 wt.% Mn-doped $BaTiO_3$.

Furthermore the interaction of the primary electron beam with the specimen results in the creation of material characteristic X-rays. The latter are analyzed in energy dispersive X-ray spectroscopy (EDX). The analysis of the characteristic X-ray can be used for qualitative and quantitative analysis. Furthermore, mapping can help to estimate compositional distribution (e.g. to identify a possible segregation between grain interior and grain boundary). More detailed information on the different modi and information derived by SEM can be found in Ref. [118] and Ref. [119].

Sintered, equilibrated, and reduced specimens have been evaluated using SEM. All samples have been ground and polished with a final diamond paste size finish of 1/4 µm to provide a smooth surface. Afterwards the samples for grain size analysis using the SE and BSE mode have been thermally etched[5] at 1150 °C for 30 min in air with a heating and cooling rate of 5 K/min. In order to prevent charging, some samples were coated with carbon (3-5 pulses in the K950X sputter coater from *EmiTech*). The samples for EBSD have been ground and polished in the same manner. Thermal etching was omitted in order to prevent any changes in the structure. The samples have been coated with 5 pulses carbon.

---

[5]Different thermal etching procedures have been conducted within this work. A thermal etching time of 60 min at 1150 °C with constant slow heating and cooling rates of 5 K/min seemed to be too long, while etching at 1150 °C for 10 min with quenching appeared to be insufficient for some doping concentrations.

Most of the SEM images and EDX analysis in this work have been conducted on a JSM-7600F SEM from *JEOL* with an EDX X-Max detector from *Oxford*. The acceleration voltage was set to 10 kV. The EBSD measurements on 0.5 wt.% Mn-doped $BaTiO_3$ have been carried out on a Mira 3 SEM from *Tescan* with a DigiView system EBSD detector from *AMETEK Inc.*. For the latter an acceleration voltage of 15 kV was used.

The SEM measurements have been thankfully performed by Hui Ding and Ulrike Kunz from the *Advanced Electron Microscopy group* of the Materials Science Department at TU Darmstadt. The EBSD measurements have been thankfully carried out by Tom Keil from the *Physical Metallurgy group* of the Materials Science Department at TU Darmstadt.
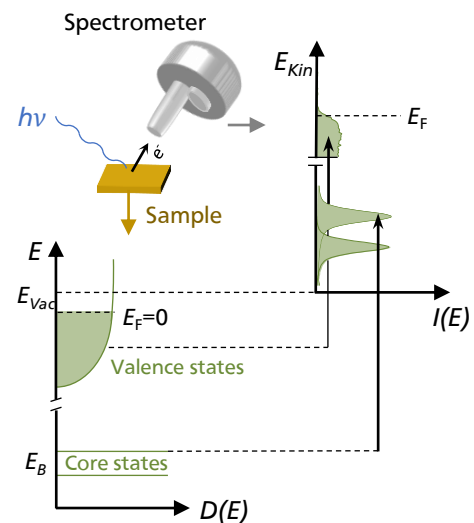
3.2.5. Photoelectron Spectroscopy

Photoelectron spectroscopy (PES, XPS) is a surface sensitive method for the investigation of the electronic structure [120]. PES is based on the photoelectric effect, where so called photoelectrons of the sample are emitted due to the excitation by an incident photon beam. PES is an umbrella term for a variety of sub-techniques, which are classified by the photon energy used for the photoelectron excitation. Typical excitation sources are X-ray tubes, UV lamps, and synchrotron radiation. The former two techniques refer to X-ray photoelectron spectroscopy (XPS) and ultraviolet photoelectron spectroscopy (UPS) and are often utilized in common laboratory systems.

The Physical Electronics PHI 5700 multi-technique surface analysis system used in this work is integrated into the ultra-high-vacuum cluster tool DAISY-Mat, which has been illustrated in Figure 3.5. The system is equipped with a Mg/Al dual anode and a monochromatic Al anode for XPS, a Helium discharge lamp for UPS, and a multi-gas ion source for Ar ion sputtering. Monochromatic Al K_{α} radiation with a photon energy of $h\nu = 1486.6\,\text{eV}$ has been used for the present XPS analysis. XPS can access the valence band region as well as the deeply bound core level states [122]. The valence band spectra give information about the valence band density of states of the material, whereas the core level states are more characteristic for the respective chemical element and its binding environment. A schematic correlation between the density of states in a solid and the received photoemission spectrum is illustrated in Figure 3.16.

Figure 3.16.: Schematic diagram depicting the correlation between the density of states in a solid and the received photoemission spectrum. Only photoelectrons excited above the vacuum level E_{Vac} can leave the sample and contribute to the spectrum. Schematic adapted from [121].

The sample is illuminated with X-rays and due to the photoelectric effect, photoelectrons excited above the vacuum level E_{Vac} are ejected. The intensity and kinetic energy E_{kin} of the photoelectron is analyzed by a hemispherical analyzer. The binding energy E_{B} of the photoelectron can be deduced from the measured kinetic energy by:

$$E_{\text{kin}} = h\nu - E_{\text{B}} - \phi_{\text{Spec}}, \tag{3.15}$$

where $h\nu$ denotes the photon energy and ϕ_{Spec} the work function of the spectrometer. The

latter is an instrumental parameter, which needs to be adjusted by a standard sample with known binding energy. Typically metals such as Au, Ag, or Cu are used for the adjustment. In this work, the binding energies were calibrated by setting the binding energy of the Fermi edge of a freshly cleaned Ag sample to 0 eV.

Only the primary non-scattered electrons carry the desired chemical and electronic information, whereas the inelastically scattered electrons contribute as background signal and as satellite emissions in the spectra.

Thus, PES is a surface sensitive technique with its information depth being related to the inelastic mean free path of the generated photoelectrons in the material.

The dependence of the inelastic mean free path of electrons in solids on the kinetic energy is illustrated in Figure 3.17. The minimum of the mean free path at about 50 eV is mainly related to the excitation of plasmons.
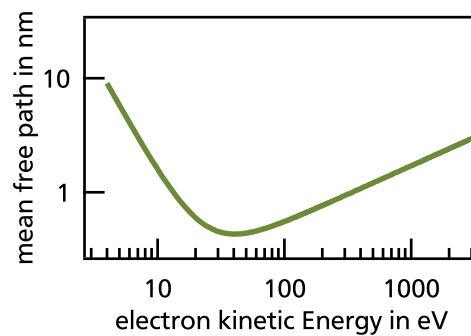
Figure 3.17.: Dependence of the inelastic mean free path of electrons in solids on the kinetic energy. The curve has been calculated using the equations given in Ref. [123].

Background subtraction

The inelastically scattered electrons contribute to a continuous background in the spectra. The composition analysis is based on the extraction of the peak intensity/integrated area and, therefore, the background needs to be subtracted in a first step. Several methods are presented in literature for the fitting of the inelastic background. In principle, background subtraction can be done by using a straight line, polynomials of any order, or by physical approaches like the Shirley [124] or Tougaard method [125].

In this work, a polynomial function was used for the background subtraction of the Ba $3d_{5/2}$ and Ba $4d$ core level emissions, while the Shirley method was used for O $1s$ emission, and the Tougaard method for the Ti $2p_{3/2}$ emission. An exemplary background subtraction for the four core levels using the respective methods is depicted in Figure 3.18 by the dashed line.
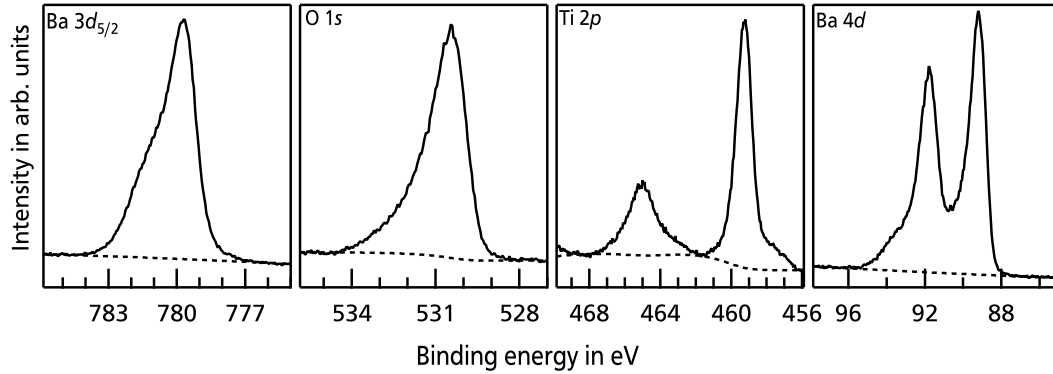
Figure 3.18.: XP-spectra of the Ba $3d_{5/2}$, O $1s$, Ti $2p$, and Ba $4d$ core-level emissions of a bare reduced BaTiO$_3$ surface. The subtracted background is indicated by the dashed line in the spectra. A polynomial function was used for the background subtraction of the Ba $3d_{5/2}$ and Ba $4d$ core level emissions, while the Shirley method was used for O $1s$ emission and the Tougaard method for the Ti $2p_{3/2}$ emission.

Composition analysis

XPS is often used for quantitative analysis of the sample surface. As the peak intensity is affected by a large number of influences, the absolute element concentration has an accuracy of 90 % or less. The relative composition, however, has a high reproducibility [122]. The atomic fraction c_A for a homogenous multi element sample can be calculated according to

$$c_{A} = \frac{\frac{I_{A}}{\text{ASF}_{A}}}{\Sigma_i \frac{I_i}{\text{ASF}_i}}, \tag{3.16}$$

where I_A denotes the integrated intensity and ASF$_A$ the atomic sensitivity factor of the respective element specific emission line. The atomic sensitivity factors for the acquired core levels are listed in Table 3.6.

Table 3.6.: Atomic sensitivity factors for the acquired core levels of BaTiO$_3$. The values are taken from Ref. [126] for the composition analysis using the integrated peak area.

Emission line	Ba $3d_{3/2}$	Ba $4d$	Ti $2p$	O $1s$
ASF	6.361	2.627	1.798	0.71

Interface formation

The barrier formation at the interface between a metal and a semiconductor can be estimated from the Schottky model, which was first described by W. Schottky in 1939 [127]. The model is based on the alignment of the vacuum level of both contact materials and can be best explained from the graphical illustration in Figure 3.19. The distance between the conduction band E_{CB} and the vacuum level E_{Vac} is defined as electron affinity χ, while the distance between the Fermi level E_F and the vacuum level is defined as work function ϕ. For a metal, electron affinity and work function, are identical.
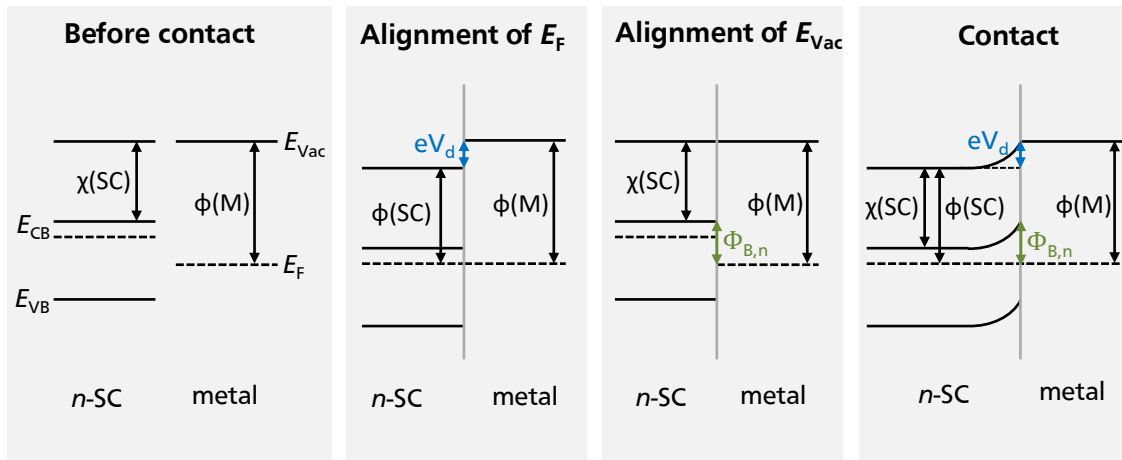
Figure 3.19.: Band alignment between a metal and a n-type semiconductor according to the Schottky-model.

In the presented scenario in Figure 3.19 the n-type semiconductor has a lower work function than the metal. In contact, the Fermi level of both materials line up and an electron transfer occurs from the semiconductor to the metal. The electron transfer leads to a negative built up at the metal surface and an equal opposite positive charge in the n-type semiconductor. In the latter the ionization of dopants close to the interface results in the formation of a space charge region (SCR), while in the metal the charge at the interface is confined to a very small area due to its high charge density. The difference in work function of both materials defines the magnitude of the band bending eV_d, while the difference in the electron affinities of both materials defines the Schottky barrier height for electrons

$$\Phi_{B,n} = \phi(M) - \chi(SC) = \chi(M) - \chi(SC). \tag{3.17}$$

Hence, the barrier height is completely independent on the Fermi level position inside the semiconductor and is solely determined by the alignment of the vacuum levels.
However, the Schottky-model describes an ideal case, without taking interface states or other

factors into account and experimentally derived Schottky barrier heights often differ from the estimations [20].

In practice, XPS is able to follow the interface formation between a substrate and a contact material. Here, especially the resulting Schottky barrier height can be evaluated by following the binding energy shifts of the substrate during stepwise deposition of the contact material. As the valence band of the substrate will be superimposed with the one of the contact material, the direct determination of the substrate's Fermi energy is no longer possible.
However, the shift of the Fermi level during the interface formation can be monitored by subtracting the material characteristic core level to valence band maximum distances [128].
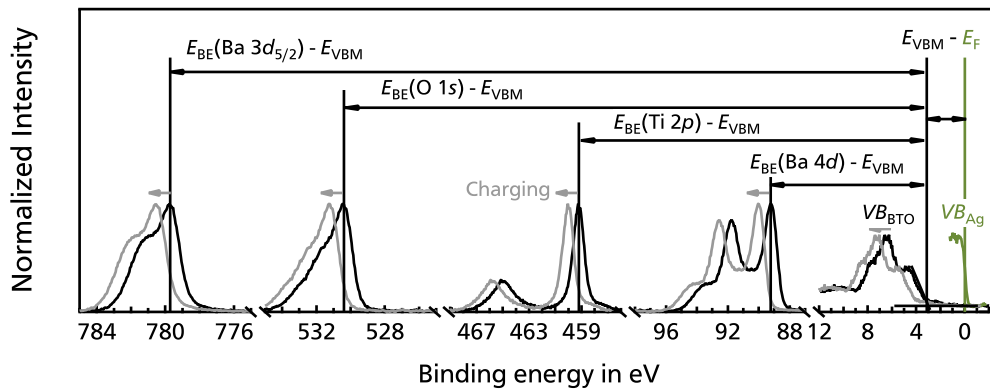
Figure 3.20.: XP-spectra of the Ba $3d_{5/2}$, O $1s$, Ti $2p$, and Ba $4d$ core-level and valence band emissions of a bare reduced BaTiO$_3$ surface (black) with a freshly sputter-cleaned Ag Fermi-edge (green) as a reference. The binding energy difference between the respective core level and the valence band maximum of the bare reduced BaTiO$_3$ surface are labeled. Homogeneous charging, which occurred for the highly resistive equilibrated and oxidized BaTiO$_3$ samples, is indicated by the gray shifted spectra. The representation of the characteristic values was adapted from [129].

The average core level to valence band maximum distances have been determined based on the evaluation of all bare reduced[6] (ground and non-ground) surfaces. A schematic illustration on the determination is given in Figure 3.20. The Ba I bulk component of the $3d_{5/2}$ and $4d_{5/2}$ emissions as well as the Ti $2p_{3/2}$ have been used.
The following average core level to VBM distances have been derived: $E_{\text{Ba}\,3d}^{\text{VBM}} = 776.38 \pm 0.1\,\text{eV}$, $E_{\text{Ti}\,2p}^{\text{VBM}} = 455.96 \pm 0.1\,\text{eV}$ and $E_{\text{Ba}\,4d}^{\text{VBM}} = 85.95 \pm 0.1\,\text{eV}$. These values have been used for the subtraction of all samples in this work, independent on the oxidation state or Mn-content.
The procedure of an interface experiment is depicted in Figure 3.21. Usually, the bare surface of the sample is measured in a first step to determine the starting Fermi level position. This

---

[6]Equilibrated and oxidized samples were heavily charging (even while using a neutralizer). Thus, they could not be included in the determination of the core level to valence band maximum distances.

refers to the situation on the left, where only the core level of the BaTiO$_3$ substrate is detected. Upon stepwise electrode deposition the substrate emission is attenuated, while the signals of the electrode are growing. The last step of an interface experiment is usually a thick electrode film, where the substrate emissions are fully attenuated and only the emissions of the electrode are detectable.
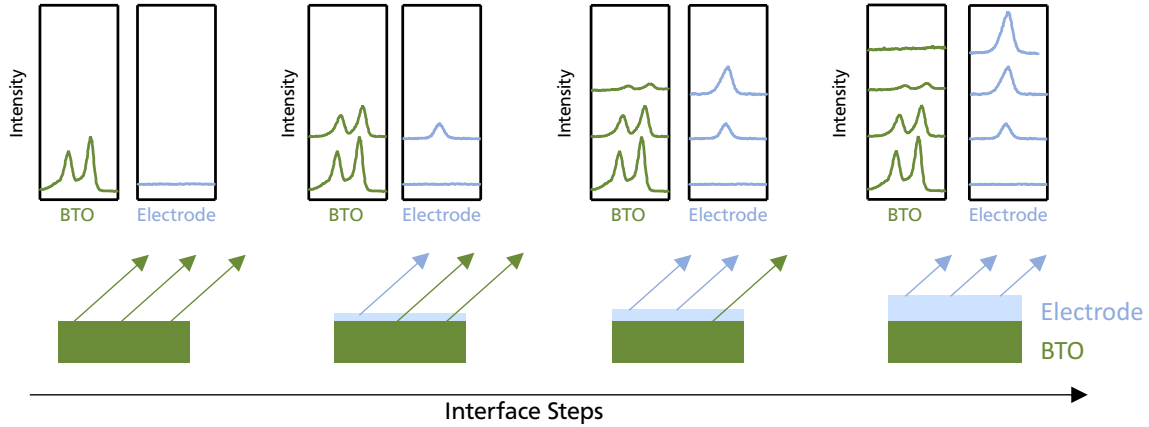
Figure 3.21.: Schematic illustration of an interface experiment. The interface steps are shown from left to right with increasing electrode film thickness. The development of the corresponding XP-spectra are shown from bottom to top. The representation of the interface procedure was inspired by [130].

From the binding energy shifts between the steps and the known core level to VBM distances, the Fermi level shift upon contact formation can be calculated. Usually, the deposition steps are chosen in such a way, that a full development of the barrier can be proven (which manifests in no further shifts of the core levels).

The resulting Schottky barrier $\Phi_{B,n}$ height for electrons at the interface can be determined by

$$\Phi_{B,n} = E_G - (E_F - E_{VBM}), \tag{3.18}$$

where E_G denotes the material's band gap and $E_F - E_{VBM}$ the Fermi level at the interface.

Acquisition parameters

As already stated, as excitation source monochromatic Al Kα radiation with a photon energy of 1486.6 eV was used. The angle between the sample surface and the detector was set to 45°. In order to measure the maximum intensity, the sample has been aligned before the first acquisition. Therefore, the sample was moved in x, y, and z direction until the O 1s core level emission line was maximized in intensity.

XP survey spectra have been carried out in a binding energy range from -1 eV−1400 eV, whereas high resolution spectra (HRES) of the core level and valence band have been recorded with individual binding energy ranges. The corresponding parameters for the pass energy of the analyzer and the step width are listed in Table 3.7. Usually, an aperture with a spot size of 800 µm x 2000 µm has been used.

During the time frame of this work a new XPS sample holder was built in the ESM group, which enables XPS measurements at temperatures up to 300 °C, while optionally applying a voltage. The sample was held for >30 min at the desired dwell temperature to ensure a constant sample temperature before the measurement.

Table 3.7.: Parameters for the pass energy and the step width.

mode	pass energy in eV	step width in eV
XPS-Survey	187.85	0.8
XPS-HRES	5.85	0.05

4. Space Charge Potential Simulations

For a better understanding of the experimental results, the space-charge potential for the interface formation between Mn-doped BaTiO$_3$ and RuO$_2$ electrodes has been simulated. Additionally, the simulation tool implemented by L. Gossel [110] has been used, which enables the simulation of grain boundary potentials and the resulting conductivity of polycrystals as a function of oxygen vacancy concentrations during re-oxidation experiments. As grain boundaries can be regarded as a one-dimensional, symmetric double Schottky barrier, it is sufficient to restrict the simulations to one side of the boundary, i.e. to half of a grain. In both cases the space-charge potential can be derived by solving the Poisson equation

$$\frac{\partial^2 \phi(x)}{\partial x^2} = -\frac{\rho(x)}{\epsilon \epsilon_0}, \tag{4.1}$$

where ϵ denotes the material's permittivity, ϵ_0 the vacuum permittivity, and ρ the charge density, which includes all electronic and ionic charges. In this work, the space-charge potential ϕ is defined as

$$\phi(x) = \frac{-(E_{CB}(x) - E_F(x))}{q} \tag{4.2}$$

The Poisson equation is a second order differential equation and, hence, two boundary conditions are required in order to derive a numerical solution. This ordinary differential equation (ODE) can be solved by using one of the built-in boundary value problem (BVP) solvers *bvp4c* and *bvp5c* of the software MATLAB [131]. In principle, any of the two solvers can be used as they are both designed to solve a system of ODEs with respect to the specified boundary conditions. Both solvers are based on finite difference methods that use the three-stage and the four-stage Lobatto Illa formula for the *bvp4c* and *bvp5c* solver, respectively [132]. In this work the *bvp5c* solver has been used for both simulations as it provided a higher accuracy.

The implementation of the interface and grain boundary simulation is similar in several points. In both cases the charge density of Mn/Fe-doped BaTiO$_3$ is calculated according to the Equations in Section 2.3 and one boundary condition is the flat band potential in the bulk. The second boundary condition is determined experimentally in the case of the interface formation, while it is based on an initial guess and an iterative procedure for the grain boundary simulations. Due to this differences, both simulations are introduced separately in the following.

4.1. Simulation of the barrier formation at the electrode interface

One objective of this work is the defect level identification by means of XPS interface experiments. As the information depth of this technique is restricted to several nm, the width of the *SCR* is of critical importance for the interpretation of the experimentally determined Fermi level position. Thus, the aim of this simulation is the calculation of the potential profiles for the experimentally studied substrate - electrode combinations.

During contact formation, the Fermi level of both materials line up (see Section 3.2.5). For the interface being sketched in Figure 4.1 an electron transfer occurs from the semiconductor to the metal, which eventually results in the formation of a space charge region inside the semiconductor and a subsequent band bending. For the simulations the position of the interface is defined as $x = 0$.
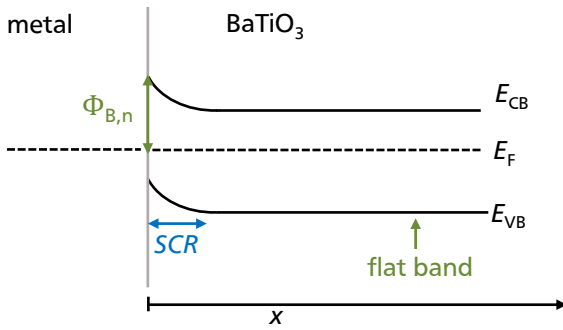
Figure 4.1: Schematic band alignment between a metal and a semiconductor ($BaTiO_3$). The height of the Schottky barrier for electrons $\Phi_{B,n}$ in given by Equation 3.17 and can be determined experimentally by XPS interface experiments. For the simulations the position of the interface is defined as $x = 0$. Flat band potential is derived for $x > SCR$.

The resulting potential profile can be calculated by solving the Poisson equation. As already mentioned, the first boundary condition is the flat band condition in the bulk, which is expressed by Equation 4.3. The second boundary condition is derived experimentally and corresponds to the Schottky barrier height for electrons $\Phi_{B,n}$, which can be derived from XPS studies[1] (see Section 3.2.5). Thus, the second boundary conditions corresponds to the potential $\phi(x = 0)$ directly at the interface and is expressed by Equation 4.4.

$$\phi'(x = \infty) = 0 \tag{4.3}$$

$$\phi(x = 0) = \Phi_{B,n}/q \tag{4.4}$$

The defect chemistry of acceptor-doped $BaTiO_3$ is described in Section 2.3.2 and the relevant defect reactions are given in Equations 2.9 to 2.13. According to the defect calculations of Ref. [65, 66] on $BaTiO_3$, only doubly charged oxygen vacancies are considered. The corresponding

---

[1]It should be stressed, that the information derived from XPS measurements depends on the width of the SCR. For a SCR larger than the inelastic mean free path of the photoelectrons, the measured Fermi level refers to the interface value and, thus, the Schottky barrier height. In this case, the experimentally derived value can be used as second boundary condition. For a SCR smaller than the inelastic mean free path of the photoelectrons, the measured Fermi level rather refers to the bulk and hence the defect energy level.

charge density for acceptor-doped BaTiO$_3$ is consequently given by:

$$\rho(\phi) = e \cdot \left(p(\phi) - n(\phi) - 2N_{A_{Ti}''}(\phi) - N_{A_{Ti}'}(\phi) + 2N_{V_O^{\bullet\bullet}}(\phi) \right) \tag{4.5}$$

The concentrations of holes, electrons, singly- and doubly-charged acceptor dopants, and doubly-charged oxygen vacancies depend on the Fermi level according to Equation 2.22 to 2.27, respectively. Using the definition of the space-charge potential ϕ in Eq. 4.2, the mentioned Equations for the charge carrier concentrations need to be rewritten and are given by

$$n(\phi) = N_{CB} \cdot e^{\frac{e\phi}{k_B T}} \tag{4.6}$$

$$p(\phi) = N_{VB} \cdot e^{-\frac{e\phi + E_G}{k_B T}} \tag{4.7}$$

$$N_{A_{Ti}''}(\phi) = \frac{N_{A_{Ti}}}{1 + g_A \cdot e^{-\frac{e\phi + E_G - E_{A1}}{kT}}} \tag{4.8}$$

$$N_{A_{Ti}'}(\phi) = \frac{N_{A_{Ti}}}{1 + g_A \cdot e^{-\frac{e\phi + E_G - E_{A2}}{kT}}} - N_{A_{Ti}''} \tag{4.9}$$

$$N_{V_O^{\bullet\bullet}}(\phi) = \frac{N_{V_O}}{1 + g_D \cdot e^{\frac{e\phi + E_G - E_{D1}}{kT}}}. \tag{4.10}$$

For the present model all ionic defects, i.e. acceptor dopants as well as oxygen vacancies, are assumed to be immobile. This assumption seems to be reasonable, as RuO$_2$ has been deposited at room temperature and the XPS measurements for the determination of the Schottky barrier height have been conducted at room temperature as well.

In principle, the simulation can be applied to any acceptor-doped BaTiO$_3$ - electrode combination. Thus, the MATLAB input script is divided into physical constants and variable (material/experimental) constants. The physical constant script includes k_B, h, e, m_e, and ϵ_0, while the variable constants script includes the permittivity and the band gap of the material, the acceptor and oxygen vacancy concentration as well as the position of their defect levels. Additional variable constants are the effective mass and the degeneracy factors. The only experimental parameter is the temperature T, which should be equal to the temperature during the XPS measurement. Another important parameter is the domain of the mesh, as the first and the last points in the mesh are the positions for which the boundary condition are enforced. For a successful simulation the mesh needs to be chosen in such a way, that the sample is thick enough to reach flat band potential in the bulk.

In this work, simulations have been conducted for the interface formation of 0.5 wt.% Mn-doped BaTiO$_3$ to RuO$_2$ electrodes. The corresponding parameters for the simulations are given in Table 4.1. Three different oxygen vacancy concentrations have been used in order to simulate reduced, equilibrated, and oxidized 0.5 wt.% Mn-doped BaTiO$_3$. Due to the different widths of

the *SCR* the mesh width was set to 500 nm for reduced and 100 nm for equilibrated and oxidized 0.5 wt.% Mn-doped BaTiO$_3$. Another set of simulations has been conducted for $\epsilon_{\mathrm{BTO}}=1900$, 500, and 10 to determine the influence of ϵ_{BTO} on the *SCR* width.

Table 4.1.: Parameter set for the interface simulations. The MATLAB version R2019b has been used. The output data includes potential profiles as well as defect concentration profiles. One set of simulations has been conducted for $\epsilon_{\mathrm{BTO}}=1900$, 500, and 10 as well.

| Parameter	Value	Reference	Comment
T [K]	300	-	T during XPS measurement
m_e* [m_e]	5	[22]	-
m_h* [m_e]	1	[22]	-
g_{A}	4	[20]	-
g_{D}	2	[20]	-
E_{G} [eV]	3.1	[21]	-
E_{Mn1} [eV]	1.9	[21]	Mn^{2+}/Mn^{3+} transition
E_{Mn2} [eV]	1.3	[21]	Mn^{3+}/Mn^{4+} transition
E_{VO1} [eV]	3.0	[65]	$V_{\mathrm{O}}^{\mathrm{x}}$/$V_{\mathrm{O}}^{\bullet\bullet}$ transition
N_{Mn} [m^{-3}]	3.3×10^{26}	-	0.5 wt.% Mn-doped BaTiO$_3$
$N_{\mathrm{V_O}}$ [m^{-3}]	3.31×10^{26}	-	reduced state
$N_{\mathrm{V_O}}$ [m^{-3}]	1.8×10^{26}	-	equilibrated state
$N_{\mathrm{V_O}}$ [m^{-3}]	1.0×10^{26}	-	oxidized state
ϵ_{BTO}	1900	Exp.	-

## 4.2. Simulation of the electrical conductivity across the grain boundaries

The simulations on the electrical conductivity across the grain boundaries have the main objective to understand the different contributions to the experimental recorded conductivity during the re-oxidation experiments. By this, it should be possible to interpret the measured activation energies and possibly identify the charge transition levels of the acceptors.

Within this work the MATLAB simulation tool implemented by L. Gossel [110] has been used. The simulation is based on the work of De Souza, who proposed a model for the simulation of grain boundaries in acceptor-doped $SrTiO_3$ [79]. In the following the physical model and the important assumptions of the model are briefly reviewed. Details on the physical background of the grain boundary formation as well as the basics of the simulation procedure can be found in the publication of De Souza [79], while details on the code implementation and conductivity calculations can by found in the Master thesis of L. Gossel [110].

The model of De Souza is based on the assumption, that grain boundaries in acceptor-doped SrTiO (and acceptor-doped $BaTiO_3$) have a positive core charge due to a reduced formation enthalpy for oxygen vacancies in the grain boundary core (see Section 2.3.3). Additionally, it is assumed, that the resulting oxygen vacancy redistribution is the main driving force for space charge formation and that equilibrium is reached in all simulations. An exemplary potential curve, oxygen vacancy concentration profile, and formation energy profile between two grain is depicted in Figure 4.2. Important parameters are the core width d_{core}, the change in formation energy Δg, the SCR width and the difference in potential between bulk and core $\Delta\phi$. The model of De Souza is based on an iterative procedure to determine the space charge potential. The different steps of the procedure and the most important equations and assumptions are depicted in the flow diagram in Figure 4.3. First, an initial guess for the potential difference
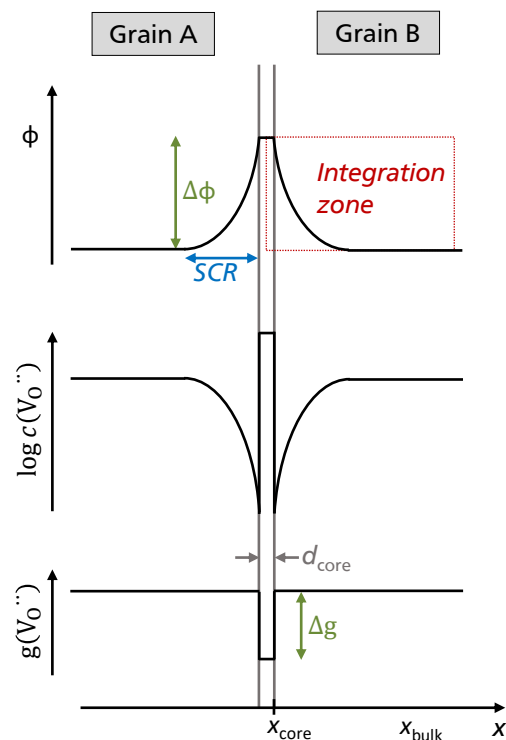
Figure 4.2.: Schematic potential, oxygen vacancy concentration, and formation energy profile for oxygen vacancies across a bi-crystal. Figures are inspired by Ref. [110] and [79].
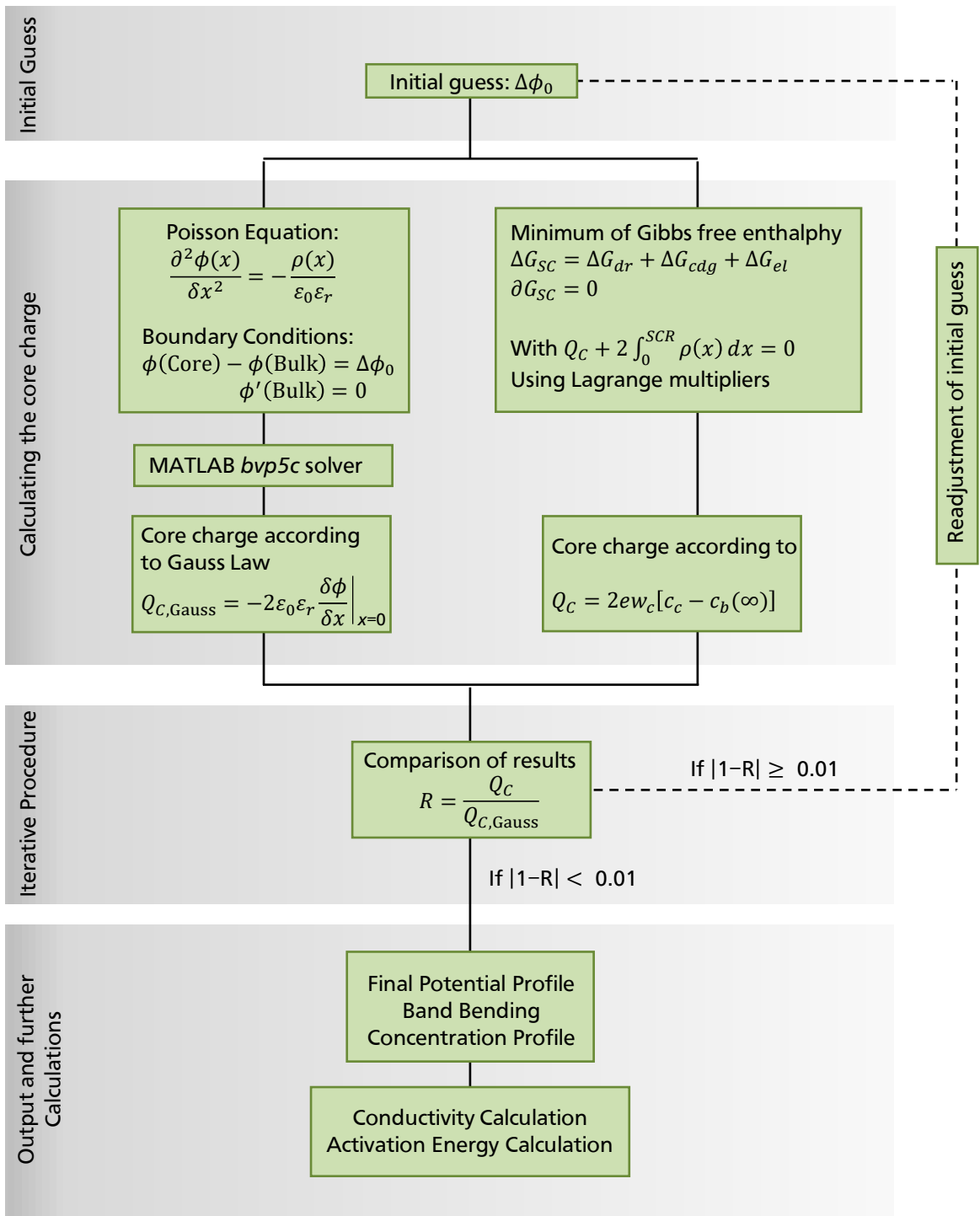
Figure 4.3.: Flow diagram of the grain boundary simulations based on the model of De Souza [79]. The heart of this model is the iterative procedure for determining the space-charge potential. The core charge Q_C is determined by the Gauss Law and compared to the value derived with value of the minimum Gibbs free enthalpy Ansatz. Then, the initial guess for the difference in potential is varied until both values for Q_C equal.

$\Delta\phi_0$ between the bulk and the core is entered. Then, the Poisson Equation 4.1 is solved with respect to the two boundary conditions

$$\phi'(x = \infty) = 0 \tag{4.11}$$

$$\phi(x_{\text{core}}) - \phi(x_{\text{bulk}}) = \Delta\phi_0. \tag{4.12}$$

The charge density of electrons, holes, and doubly and singly charged acceptors in the Poisson Equation can be calculated according to Equations[2] 4.6 to 4.9. Having solved the Poisson Equation, the core charge can be calculated via Gauss' law

$$Q_{\text{C, Gauss}} = -2\epsilon_0\epsilon_r \left.\frac{\delta\phi}{\delta x}\right|_{x=x_{\text{core}}}. \tag{4.13}$$

where $Q_{\text{C, Gauss}}$ represents the first result for the core charge and refers to the left branch in Figure 4.2. Within the iterative procedure $Q_{\text{C, Gauss}}$ is compared to the results of an alternative route, which is expressed by the right branch. Here, De Souza extended the global thermodynamic approach in such a way, that an equilibrium space-charge layer has been formed when the Gibbs free energy reaches its minimum. The change in the Gibbs free energy $\Delta_{\text{sc}}G$ upon oxygen vacancy redistribution is given by

$$\Delta_{\text{sc}}G = \Delta_{\text{dr}}G + \Delta_{\text{cdg}}G + \Delta_{\text{el}}G, \tag{4.14}$$

where $\Delta_{\text{dr}}G$ denotes the driving energy for space-charge formation, $\Delta_{\text{cfg}}G$ the loss of configuration entropy, and $\Delta_{\text{el}}G$ the electrostatic energy for defect rearrangement. The minimum in Gibbs free energy can be derived by the method of Lagrange multipliers, assuming that the core charge Q_{C} is exactly compensated by the charge in the two space-charge regions

$$Q_c + 2\int_0^{l_{SCR}} \rho(x)dx = 0. \tag{4.15}$$

For every species with a different formation energy Δg between grain boundary core and bulk this lead to

$$\Delta g + k_{\text{B}}T \cdot ln\left(\frac{c_c}{N_c - c_c}\right) - k_{\text{B}}T \cdot ln\left(\frac{c_b}{N_b - c_b}\right) - ze\Delta\phi = 0, \tag{4.16}$$

where N_c/N_b are the state densities in the core/bulk, and c_c/c_b are the concentrations in the core/bulk for the respective defect. Within the implemented tool of L. Gossel, Δg is assumed to be frozen in for all defects expect oxygen vacancies. The core concentration of oxygen vacancies

---

[2]Due to the high Fermi level in the beginning of the re-oxidation experiments, oxygen vacancies can also be singly charged. Hence, L. Gossel also considered singly charged oxygen vacancies in the charge density. The Equations for the oxygen vacancy concentrations implemented by L. Gossel differ slightly from the representation in Equation 4.10 and are based on the Equations of Wechsler and Klein [21]. The only difference between both representations is the degeneracy factor.

can be detected from Equation 4.16, when assuming $c_b << N_b$ and is given by

$$c_{c,V_O} = \frac{N_{c,V_O} \cdot c_{b,V_O} \cdot e^{\frac{-(\Delta g_{VO} + z_{VO}(\phi) \cdot e \Delta \phi)}{k_B T}}}{N_{b,V_O} + c_{b,V_O} \cdot e^{\frac{-(\Delta g_{VO} + z_{VO}(\phi) \cdot e \Delta \phi)}{k_B T}}}. \tag{4.17}$$

Here, z denotes the average valency of the oxygen vacancies, which depends on the potential

$$z_{V_O}(\phi) = \frac{2 \cdot c(V_O^{\bullet\bullet})(\phi) + c(V_O^{\bullet})(\phi)}{c(V_O)_{\text{tot.}}}. \tag{4.18}$$

According to Equations 4.15 to 4.18 the core charge can be calculated

$$Q_C = e \cdot w_c \cdot \left(z_{V_O}(\phi) \cdot c_{c,V_O} - n(\phi(x_{\text{core}})) + p(\phi(x_{\text{core}})) - N_{A'_{Ti}}(\phi(x_{\text{core}})) - 2N_{A''_{Ti}}(\phi(x_{\text{core}})) \right). \tag{4.19}$$

The concentrations of electrons, holes and singly/doubly charged acceptors depend on the absolute potential in the core $\phi(x_{\text{core}}) = \phi(x_{\text{bulk}}) + \Delta \phi$ and can be calculated according to Equations 4.6 to 4.9.

The values for the core charge are calculated according to Equation 4.13 and 4.19 and their deviation is compared by

$$R = \frac{Q_C}{Q_{C,\text{Gauss}}} \tag{4.20}$$

The value for the initial guess $\Delta \phi_0$ is then shifted until $|1 - R| < 0.01$. The adaption of $\Delta \phi_0$ is based on the formula developed by L. Gossel and can be found in Ref. [110].

Within this work the simulation tool *Model 2* of L. Gossel has been used [110]. This model assumes mobile electronic charge carriers and immobile acceptors. Additionally, oxygen vacancies are assumed to be mobile, which allows a redistribution between the core and the SCR. Thus, the oxygen vacancy concentration depends on the potential itself and is given by

$$c_{V_O}(\phi) = c_{c,V_O,bulk} \cdot e^{-\frac{z_{V_O}(\phi) \cdot e(\phi - \phi_{\text{bulk}})}{k_B T}}. \tag{4.21}$$

The simulation tool of L. Gossel [110] allows the calculation of potential profiles either with the Fermi level or the bulk oxygen vacancy concentration as free variable. Within this work, the bulk oxygen concentration is set as free variable. The simulations have been conducted with the set of parameters given in Table 4.2.

Table 4.2.: Parameter set for the grain boundary simulations. The simulation tool of L. Gossel [110] implemented in the MATLAB version R2019b has been used. Material parameters have been varied in order to simulate 0.1 wt.% and 0.5 wt.% Mn- and Fe-doped BaTiO$_3$. The experimentally recorded permittivity curves of the respective composition are interpolated according to the Curie-Weiss law. Unknown and variable parameters are taken from the work of L. Gossel [110]. For further technical parameters of the simulation tool see Ref. [110].

|	Parameter	Value	Reference	Comment
Material parameter	E_G [eV]	3.1	[21]	$E_{VB} = 0\,$eV
	E_{A1} [eV]	2.4	[21]	Fe^{2+}/Mn^{3+} transition
		1.9	[21]	Mn^{2+}/Mn^{3+} transition
	E_{A2} [eV]	0.8	[21]	Fe^{3+}/Mn^{4+} transition
		1.3	[21]	Mn^{3+}/Mn^{4+} transition
	N_A [m^{-3}]	3.25×10^{26}	-	0.5 wt.% Fe-doped BaTiO$_3$
		6.5×10^{25}	-	0.1 wt.% Fe-doped BaTiO$_3$
		3.3×10^{26}	-	0.5 wt.% Mn-doped BaTiO$_3$
		6.6×10^{25}	-	0.1 wt.% Mn-doped BaTiO$_3$
	E_{VO1} [eV]	3.05	[21]	V$_O^x$/V$_O^\bullet$ transition
	E_{VO2} [eV]	2.9	[21]	V$_O^\bullet$/V$_O^{\bullet\bullet}$ transition
	$\epsilon_{BTO:A}$	-	Exp.	interpolated according to Curie-Weiss law
	C Curie constant	$1.7 \times 10^5\,$K	[133]	
	$N_{O,\,bulk}$ [m^{-3}]	5×10^{28}	-	bulk density of oxygen sites
Unknown and variable parameter	$N_{O,\,core}$ [m^{-3}]	$N_{O,\,bulk}/10$	[79]	core density of oxygen sites
	$\frac{w_g}{2}$ [µm]	12.5	Exp.	0.1 wt.% A-doped BaTiO$_3$
		0.5	Exp.	0.5 wt.% A-doped BaTiO$_3$
	w_c [µm]	8 Å	[79]	ca. 2 × lattice constant
	$\Delta\phi_0$ [eV]	0.5	-	initial guess
	T [K]	673.15 & 653.15	-	for E_A determination
	N_{V_O} [m^{-3}]	0.1 to 2 $\times N_A$	-	variable step-size
	Δg_{V_O} [eV]	- 1 to -2	-	step-width of -0.25 eV

Conductivity and activation energy

Due to the *DC*-measurement configuration of the re-oxidation experiments, only electron and hole and no ionic contributions are expected in the total conductivity [22]. Hence, the simulation also considers only electron and hole conductivity.

The simulation tool of L. Gossel [110] gives a *2D-* and a *3D*-conductivity output. In both cases, the simulation tool first calculates the integrated grain conductivity of a *2D*-grain. Due to the characteristics of the positive grain boundary core, the *SCR* acts as a parallel path for electrons, while it represents a potential barrier for holes, as being depicted in Figure 4.4. Hence, the conductivity calculation for both charge carriers has been treated differently by L. Gossel. For electrons the calculation is done via Equation 4.22, which represents an integration in the middle of the grains, because the grain resistivity dominates the SCR resistivity and $\sigma = 1/\rho$. For holes the conductivity is calculated exactly via Equation 4.23, as the resistivity in the grain and the SCR strongly depends on the band bending and the SCR width.

$$\sigma_{e,2D} = \frac{1}{w_g} \int_0^{w_g} \sigma_e(x) \, \mathrm{d}x \approx \frac{1}{w_g} \int_0^{w_g} n(\phi(x, \frac{w_g}{2})) \cdot \mu_e \cdot e \, \mathrm{d}x \tag{4.22}$$

$$\sigma_{h,2D} = \frac{1}{w_g} \int_0^{w_g} \sigma_h(x) \, \mathrm{d}x = \int_0^{w_g} \frac{1}{\int_0^{w_g} \frac{\mathrm{d}y}{p(\phi(x,y)) \cdot \mu_e \cdot e}} \mathrm{d}x \tag{4.23}$$

The total *2D*-conductivity is then given by the sum of electron and hole conductivity. The *3D*-conductivity is calculated from the *2D*-conductivity via geometric considerations. Please refer to the Master thesis of L. Gossel [110] for details on the conductivity calculations.
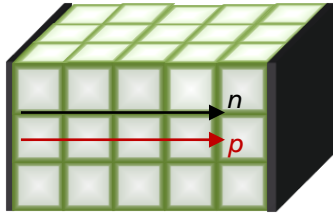
Figure 4.4: Brick wall model of a acceptor-doped BaTiO$_3$ capacitor. The conduction path of electrons and holes are highlighted.

In order to compare the experimentally derived activation energy at 400 °C with the simulation, the activation energy has to be calculated from the simulated conductivities. Therefore, the simulation has always been conducted with the same material parameter set at 400 °C and 380 °C. Then, the activation energy has been calculated from the two conduction data sets according to

$$E_A = \frac{\left(\ln\left(\sigma_{673.15\,\mathrm{K}}\right) - \ln\left(\sigma_{653.15\,\mathrm{K}}\right)\right) \cdot k}{\left(\frac{1}{673.15\,\mathrm{K}} - \frac{1}{653.15\,\mathrm{K}}\right) \cdot e}, \tag{4.24}$$

where $\sigma_{673.15\,\mathrm{K}}$ and $\sigma_{653.15\,\mathrm{K}}$ denote the conductivity curves at 400 °C and 380 °C, respectively.

5. Influence of acceptor-doping on the structural and electrical properties of BaTiO$_3$

The focus of this Chapter is the validation of the synthesized samples in order to provide reliable information about basic properties, which are essential for the main objective of this thesis. Hence, this Chapter represents a comprehensive study on the influence of Mn- and Fe-doping on the crystal structure, microstructure, and di- and ferroelectric properties of polycrystalline BaTiO$_3$ and simultaneously includes defect chemistry calculations regarding the acceptors oxidation state. As acceptor-doped BaTiO$_3$ is a standard material for MLCCs the influence of Mn- and Fe-doping on these properties is extensively studied [27, 46, 47, 51–56, 134–137]. However, none of the articles provides these information on one set of samples. With respect to the available literature in the field of acceptor-doped polycrystalline BaTiO$_3$, the following influence of Mn- and Fe-doping on as-sintered polycrystalline BaTiO$_3$ has been expected:

- **Crystal structure:** Acceptor-doping is widely known to stabilize the high temperature hexagonal phase down to room temperature [51–56]. The threshold value for the appearance of hexagonal BaTiO$_3$ considerable varies between different acceptor-dopants. For BaTi$_{1-x}$Mn$_x$O$_{3-\delta}$ and BaTi$_{1-x}$Fe$_x$O$_{3-\delta}$ Prades and co-workers have published the working phase diagrams [54] (see review in Section 2.2.2). The threshold value for the hexagonal phase stabilization is considerable lower upon Mn-doping than Fe-doping.

- **Microstructure:** In general a decreasing grain size is expected upon acceptor-doping due to solute drag effects in the boundary motion [138]. Additionally, elongated plate-like grains are expected for hexagonal BaTiO$_3$ [52, 56, 139].

- **Dielectric properties:** According to the present literature, a strong decrease in Curie point is expected upon Fe-doping, while a conservative decrease is expected upon Mn-doping [27, 46, 47, 134–137]. The room temperature permittivity is expected to decrease with increasing hexagonal phase fraction.

- **Ferroelectric properties:** The creation of V$_O^{\bullet\bullet}$ upon acceptor doping can lead to the formation of ($A_{Ti}{}'$-V$_O^{\bullet\bullet}$)$^\bullet$ or ($A_{Ti}{}''$-V$_O^{\bullet\bullet}$) defect complexes hindering the domain wall motion, resulting in ferroelectric hardening [43, 140]. Hence, pinched $P(E)$ loops are expected

for acceptor-doped BaTiO$_3$ with high V$_\text{O}^{\bullet\bullet}$ and A'_Ti concentrations [141, 142]. Additionally, the centrosymmetric non-ferroelectric hexagonal phase reduces the total fraction of ferroelectric grains, which is expected to decrease the overall ferroelectricity of the samples [140, 143].

In order to establish a reproducible oxygen vacancy concentration, as-sintered samples have (partially) been equilibrated and reduced before interface and/or re-oxidation experiments. Hence, the crystal- and microstructure of Mn- and Fe-doped samples have been investigated after both treatments. No literature on the influence of annealing atmosphere on Fe-doped BaTiO$_3$ is available. For Mn-doping the following is expected:

- **Annealing atmosphere:** For Mn-doped BaTiO$_3$ a restoration of the tetragonal phase is expected upon annealing in reducing atmosphere [52, 144, 145]. Additionally, the amount of elongated plate-like grains is expected to decrease upon annealing in reducing atmosphere [52].

The results of the present Chapter are compared to the literature in the respective field. Due to the high number of available articles on Mn- and Fe-doped BaTiO$_3$ the obtained results are not expected to provide new experimental findings. Nevertheless, some topics such as the stabilization mechanism of hexagonal BaTiO$_3$ are still under ongoing discussion. For this purpose, different proposed models have been reviewed and are being discussed with regard to their plausibility considering the results obtained in this Chapter.

5.1. Preconditions: Densities, Purities, and Oxidation States

The structural and electrical properties strongly depend on the quality of the evaluated ceramics. Thus, the preconditions of the samples in terms of density and purity are crucial for the interpretation of the results. As the chosen acceptors are variable valence dopants, the oxidation state of the incorporated ions plays another major role for the evaluation.

The relative densities were measured using the Archimedes method [106] and were found to be between 94.5 % to 98.5 % of the theoretical density (see Figure 5.1). While the relative density of Fe-doped samples remains approximately constant at values of 97.5 %, a decrease in density down to 94.5 % is observed for Mn-doped samples. The different influence of Mn- and Fe-doping on the density depends strongly on the crystal structure and morphology and will therefore be discussed in the following Section 5.2.

Figure 5.1: Relative densities of acceptor-doped BaTiO$_3$ ceramics after sintering. The relative density was determined using the Archimedes method. A theoretical density of 6.02 g/cm^3 for BaTiO$_3$, a density of 0.0012 g/cm^3 for air and a correction factor of 0.99983 was used. The nominal concentration x was calculated according to BaTi$_{1-x}$A$_x$O$_3$ with A=Mn, Fe.
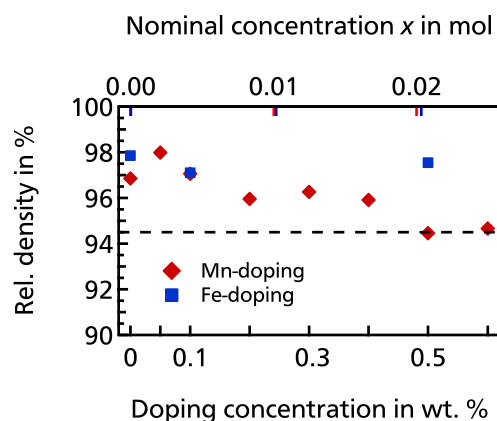
In order to quantify the level of impurities, an ICP-OES measurement has been conducted on the calcined powder of 0.3 wt.% Mn-doped BaTiO$_3$. The detailed results of the measurement are given in Table A.1. The calculated amount of the respective elements are sorted according to their commonness in Table 5.1. The most prevalent impurities are Si, Sr, K, Ca, V, Na, Zn, and Mg. Si was most likely introduced during solid sample digestion, as the blind value of the acid has a similar Si level. The other impurities are also observed in the analysis of the precursor powders provided by the manufacturer, as can be seen in Table A.2 and A.3. For the calcined powder of 0.3 wt.% Mn-doped BaTiO$_3$ no further main impurities are detected.

The evaluated Mn-doping level with respect to the B-site is 1.21 %, which is in good agreement with the theoretical level of 1.26 % (see Table 5.2). The evaluation of the Ba/Ti ratio revealed a ratio of 1.017, which is markedly higher than the expected ratio of 1, resulting from the weight calculations. As the net-weight of the precursors were close to the calculated values, it is assumed that the change in stoichiometry either occurred during processing or originates from

Table 5.1.: Calculated amount of respective element n derived from the solid concentration [mg/kg] as given in Table A.1. n has been calculated via $n = \frac{m}{M} = \frac{[\text{mg/kg}]}{[\text{g/mol}]} = 10^{-6}\left[\frac{\text{mol}}{\text{g}}\right]$. The impurities have been arranged according to their appearance. Possible origins are given in the last column.

Element	n in mol (pro g)	Possible Origin
Ba	0.004221	
Ti	0.004147	
Mn	5.06×10^{-5}	
Si	5.51×10^{-5}	Acid
Sr	1.83×10^{-5}	precursor
K	1.74×10^{-5}	precursor/acid
Ca	3.70×10^{-6}	precursor
V	2.62×10^{-6}	precursor
Na	1.59×10^{-6}	precursor
Zn	9.83×10^{-7}	
Mg	9.12×10^{-7}	precursor
Fe	3.00×10^{-7}	precursor
Li	1.67×10^{-7}	
Cr	1.60×10^{-7}	precursor
Mo	7.40×10^{-8}	

Table 5.2.: Calculated ratios according to the values derived by ICP-OES (Table A.1) and due to the weighted sample. Theoretical* implies the expected ratio according to the conducted weight calculations.

Ratio	ICP-OES	Theoretical*
Ba/Ti	1.017	1.000
Ba/(Ti+Mn)	1.006	0.987
Mn/(Mn+Ti)	0.0121	0.0126

an improper digestion of Ti during the preparation for ICP-OES. As the derived experimental Ba/(Ti+Mn) ratio differs significantly from the calculated one, it is unclear whether Mn is incorporated on the A- or B-site. Due to the given ionic radii of Ba and Ti compared to the introduced transition metal, an incorporation on the B-site is assumed [52, 146]. However, recent first principle calculation from Bowes *et al.* revealed that Mn substitutes predominantly on the Ba-site for Ti-rich cation nonstoichiometry and vice versa [147]. Without further systematic analysis of all doping concentrations, it remains unclear whether the acceptor-dopants are incorporated on the A- or B-site. However, for the defect calculations the site occupation is essential as the defect chemistry is based on the resulting compensation mechanism. For the presents samples, electrical measurements indicate that the acceptors are rather incorporated on the B-site than on the A-site. Hence, B-site doping is assumed in the following.

The introduced acceptor-dopants are so-called multivalent dopants, which means that they can be incorporated as A_{Ti}, A'_{Ti} or A''_{Ti} with $A = $ Mn, Fe. Accordingly, the amount of created oxygen vacancies will differ and by this their influence on a wide range of sample properties. Thus, the dopant's oxidation state is another essential parameter. Therefore, the dopant's oxidation state

have been calculated by means of defect chemistry calculations for 0.5 wt.% Mn- and Fe-doped $BaTiO_3$. The defect concentrations have been calculated as a function of oxygen partial pressure and are depicted in Figure A.3. The resulting distribution of the oxidation states are listed in Table 5.3. After sintering a predominate valence of Fe^{3+} is expected in the Fe-doped samples, while the Mn-doped samples are expected to show a mixture of 60 % Mn^{3+} and 40 % Mn^{4+}. The different predominant valence of Mn and Fe is related to the different position of the charge transition level inside the band gap of $BaTiO_3$, which will be discussed in Chapter 7.

Table 5.3.: Calculated oxidation state concentrations of 0.5 wt.% acceptor-doped $BaTiO_3$ at room temperature extracted from the calculations presented in Figure A.3. The defect equilibrium has been established at the respective sintering/annealing temperature and has been quenched to room temperature. The defect equilibrium has been established at 1350 °C for the calculation of as-sintered samples, while 900 °C have been utilized for equilibration and 1100 °C for reduction. An oxygen partial pressure of 0.2 bar has been assumed for sintering and equilibration, while an oxygen partial pressure of 10^{-22} bar was assumed for reduction. The concluded predominant valence state and Jahn-Teller effect (JTE) activity of the latter are added. The predominant state of Fe after reduction is marked by *, because the interpretation of the simulation is controvertible, as the the simulation reveals that Fe is directly at the transition between Fe^{2+} and Fe^{3+} for the used reduction parameters.

Treatment	Mn^{2+}	Mn^{3+}	Mn^{4+}	Predominant State	JTE
Sintering	0.00	56.21	43.79	$Mn^{3+/4+}$	**x**/-
Equilibration	0.00	6.96	93.04	Mn^{4+}	-
Reduction	100.00	0.00	0.00	Mn^{2+}	-

Treatment	Fe^{2+}	Fe^{3+}	Fe^{4+}	Predominate State	
Sintering	0.00	95.80	4.20	Fe^{3+}	-
Equilibration	0.00	76.15	23.85	$Fe^{3+/4+}$	-/**x**
Reduction	81.16	18.84	0.00	*Fe^{2+}	x

5.2. Crystal structure

The crystal structure of acceptor-doped $BaTiO_3$ was examined by X-ray diffraction on the powder of sintered samples. The powder was mixed with a Si standard in order to conduct Rietveld refinement[1] for lattice parameter and phase determination. Thus, all diffraction patterns show Si reflections. The refinement is not shown in the pattern and has solely been used for phase quantification.

In Figure 5.2 a) the X-ray diffraction patterns of nominally undoped, 0.1 wt.%, and 0.5 wt.% Fe-doped $BaTiO_3$ are displayed. The powder diffraction patterns of tetragonal and hexagonal $BaTiO_3$ as well as Si are shown in the lower panels. In addition to the Si reflections, nominally undoped and 0.1 wt.% Fe-doped $BaTiO_3$ reveal exclusively reflections from the tetragonal structure. For 0.5 wt.% Fe-doped $BaTiO_3$ additional reflections are visible, which correspond to
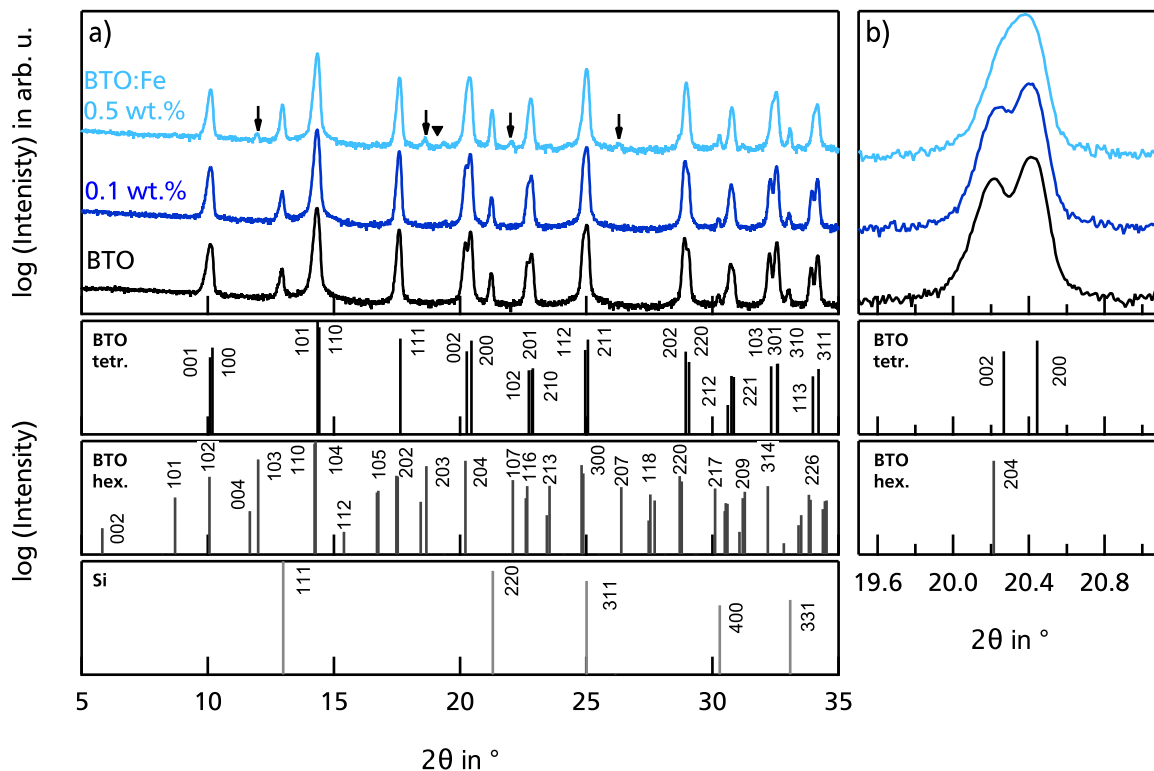
Figure 5.2.: a) X-ray diffraction pattern of nominally undoped, 0.1 wt.% and 0.5 wt.% Fe-doped $BaTiO_3$. b) Zoom-In into the (200) and (002) reflections. In the lower panel the powder diffraction pattern (PDF) of Si [01-089-2749] (light gray), ICSD collection code: 043403; $BaTiO_3$ [01-082-1175] - hex. - P63/mmc (gray), ICSD collection code: 075240 and $BaTiO_3$ [01-075-0583] - tetr. - P4mm (black), ICSD collection code: 029280 are displayed. Only the high intensity reflections of the hex. PDF are labeled. The powder diffraction pattern are only used for phase assignment. The pattern were recorded using Mo K_α radiation with $\lambda = 0.7093$ Å.

---

[1]Rietveld refinement was conducted by Leif Carstensen from the structural research group.

reflections assigned to the hexagonal structure. Hexagonal reflections, which are not superimposed with the tetragonal ones, are indicted by the arrows in Figure 5.2 a). The quantification of the tetragonal and hexagonal phase fractions will be discussed after the presentation of the XRD pattern of Mn-doped $BaTiO_3$.

A low intensity reflection at approximately 19.36° marked by the black triangle in the pattern of 0.5 wt.% Fe-doped $BaTiO_3$ could neither be assigned to the tetragonal nor to the hexagonal phase. The position of the reflection was compared to different phases originating from incomplete synthesis such as Ba_2TiO_4, $BaTi_2O_5$ and other reasonable phases within the BaO-TiO_2 phase diagram such as $Ba_6Ti_{17}O_{40}$ (Appendix A.1). Due to the superimpose of potential phase with reflections of t-$BaTiO_3$ and h-$BaTiO_3$ neither reasonable Ba-Ti-O nor potential Ba-Fe-O, Fe-Ti-O or Fe-O could clearly be assigned to the unknown reflection at 19.36° (see Appendix Fig. A.11). The single (200) reflection being present for the cubic phase splits into (200) and (002) reflections for the tetragonal structure due to the change in lattice constants from $a=b=c$ to $a=b\neq c$, respectively. According to the Bragg Equations 3.13 and 3.14 the position of the (200) and (002) reflections is directly correlated to the a and c lattice parameters. The (200) and (002) reflections are shown in Figure 5.2 b). With increasing Fe-doping concentration the spacing between the reflections decreases, which implies that the difference between a and c decreases upon Fe-doping.

The X-ray diffraction patterns of nominally undoped and 0.05 wt.% to 0.6 wt.% Mn-doped $BaTiO_3$ are displayed in Figure 5.3 a). Again, the powder diffraction pattern of tetragonal and hexagonal $BaTiO_3$ as well as Si are shown in the lower panels. Nominally undoped and 0.05 wt.% to 0.3 wt.% Mn-doped $BaTiO_3$ reveal the tetragonal structure. Higher doping contents show a mixture of tetragonal and hexagonal structure. The hexagonal content gradually increases with increasing Mn-doping concentration. The unknown low intensity reflection marked by the black triangle, which was already observed in the pattern of 0.5 wt.% Fe-doped $BaTiO_3$, is observed in all patterns with a Mn-doping concentration higher than 0.2 wt.%. The position of the unknown reflection has been compared to reasonable Mn-Ti-O, Ba-Mn-O and Mn-O phases (see Appendix Fig. A.12). Again, none of the potential phases could clearly be assigned to the unknown reflection.

The (002) and (200) reflections are shown in Figure 5.3 b). In contrast to Fe-doped $BaTiO_3$, the spacing between both reflections remains more or less constant upon Mn-doping. The position of the reflections varies slightly between the patterns, which originates from an overall shift of the whole pattern indicated by a parallel shift of the corresponding Si reflections. An overall shift can arise from a specimen displacement or an instrument misalignment. Furthermore, the intensity ratio between the (200)/(002) reflections seems to inverse upon Mn-doping. This observation is misleading, as it most likely originates from the rising intensity of the hexagonal (204) reflection, which is close to the position of the tetragonal (002) reflection.

The lattice constants as well as the percentage of tetragonal and hexagonal phases have been evaluated by Rietveld refinement. The tetragonality c/a as a function of acceptor-doping concentration is displayed in Figure 5.4 a). The observed tetragonality of approximately $c/a = 1.01$ for nominally undoped $BaTiO_3$ is consistent with literature values [148–150]. As already seen in the diffraction pattern, the c/a ratio remains constant upon Mn-doping, while it is decreasing upon Fe-doping. The linear decrease in tetragonality up to a nominal Fe-doping concentration of $x = 0.03$ is well known in literature [133, 148].

The percentage of tetragonal phase as a function of acceptor-doping concentration is displayed in Figure 5.4 b). Nominally undoped and 0.1 wt.% Fe-doped $BaTiO_3$ are phase-pure tetragonal, while 0.5 wt.% Fe-doped $BaTiO_3$ has approximately 3 % hexagonal phase. For the Mn-series,
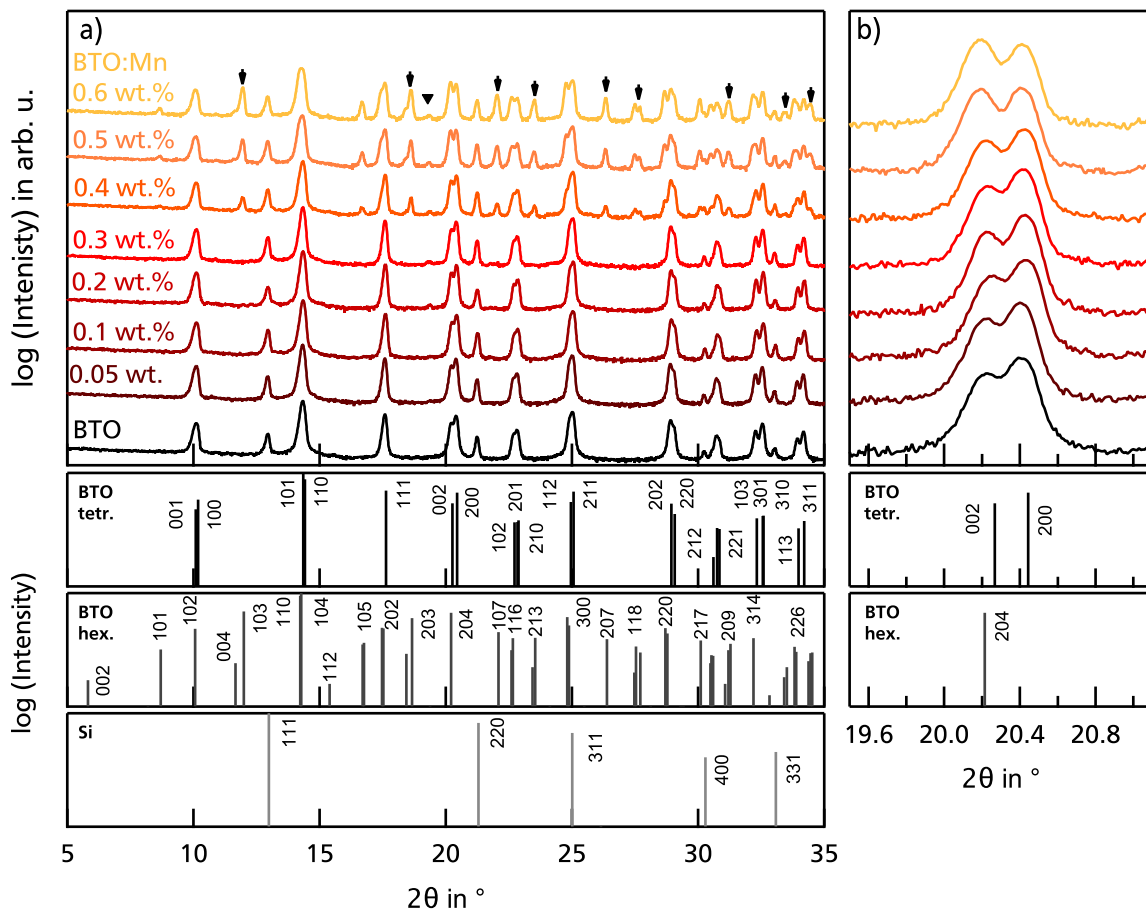
Figure 5.3.: a) X-ray diffraction pattern of nominally undoped, 0.05 wt.% to 0.6 wt.% Mn-doped $BaTiO_3$. b) Zoom-In into the (200) and (002) reflections. In the lower panel the powder diffraction pattern (PDF) of Si [01-089-2749] (light gray), ICSD collection code: 043403; $BaTiO_3$ [01-082-1175] - hex. - P63/mmc (gray), ICSD collection code: 075240 and $BaTiO_3$ [01-075-0583] - tetr. - P4mm (black), ICSD collection code: 029280 are displayed. Only the high intensity reflections of the hex. PDF are labeled. The powder diffraction pattern are only used for phase assignment. The pattern were recorded using Mo K_α radiation with $\lambda = 0.7093$ Å.
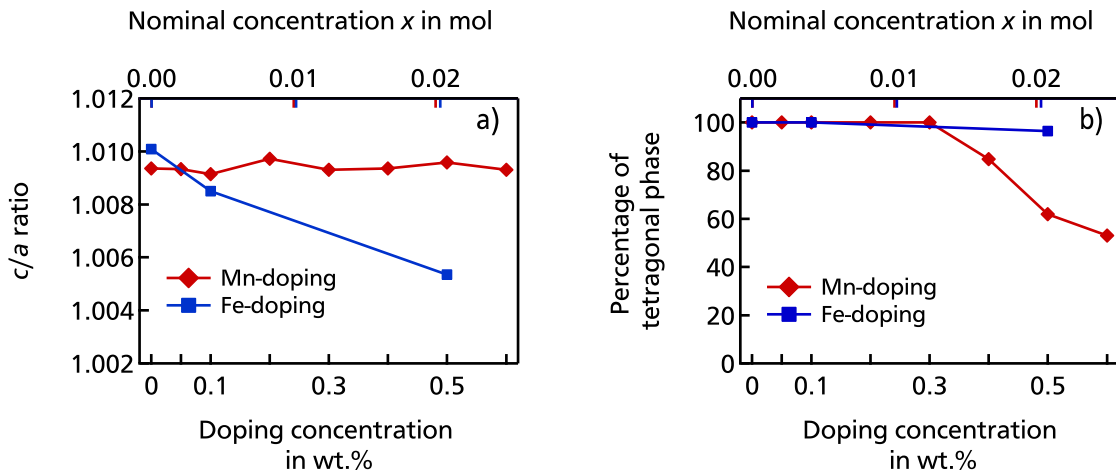
Figure 5.4.: a) c/a ratio and b) percentage of tetragonal phase as a function of acceptor doping concentration. Mn-doped BaTiO$_3$ is displayed in red and Fe-doped BaTiO$_3$ is displayed in blue. The values were derived by Rietveld refinement of the diffraction patterns displayed in Figure 5.2 and 5.3. The nominal concentration x was calculated according to BaTi$_{1-x}A_x$O$_3$ with A=Mn, Fe.

samples up to 0.3 wt.% are tetragonal. The 0.4 wt.%, 0.5 wt.%, and 0.6 wt.% Mn-doped BaTiO$_3$ show approximately 15 %, 38 %, and 47 % hexagonal phase, respectively. Obviously, the same doping concentration of Mn leads to a drastically higher amount of hexagonal phase than observed for Fe. Furthermore, the density of the hexagonal BaTiO$_3$ is 5.87 g/cm^3 and thus lower than the one of tetragonal BaTiO$_3$ with 6.02 g/cm^3 [41]. Accordingly, the decreased density of highly Mn-doped samples presented in Figure 5.1 is most likely related to the appearance of the hexagonal structure.

The combined observation of tetragonality and phase fraction changes raises the question, whether both acceptors are dissolved to the same amount in the tetragonal phase. For Fe it seems to be the case that the acceptors are fully dissolved in the lattice[2]. The crystal structure remains nearly completely tetragonal and the Fe-doping shows a considerable effect on the c/a ratio upon incorporation. For Mn-doping the scenario might be different. The structure remains tetragonal up to 0.3 wt.% Mn-doping concentration and the c/a ratio remains unaffected. For Mn-doping concentrations >0.3 wt.% the hexagonal phase rises. In contrast to Fe-doping, no effect on the c/a ratio is observed for higher Mn-doping concentrations. Thus, it is questionable if Mn is dissolved homogeneously in both phases or if it is only dissolved to a certain solubility limit in the tetragonal phase (0.3 wt.% in this case) and all additional Mn is dissolved in a secondary phase (i.e. the hexagonal polymorph).

---

[2]Without considering a possible segregation to grain boundaries or triple points, which is often observed in acceptor-doped BaTiO$_3$ [52, 151].

The different strong impact of Mn- and Fe-doping on the stabilization of the hexagonal phase is consistent with literature reports [51, 52, 55, 56]. However, in all literature reports on Mn- and Fe-doping it remained unclear, if the acceptors are dissolved homogeneously in both phases. For Cr-doped BaTiO$_3$, electron paramagnetic resonance (EPR) studies on the different lattice sites indicate that the percentage of Cr^{3+} centers in the hexagonal surrounding is higher than the respective hexagonal phase fraction in the samples, indicating that the Cr-concentration is enhanced in the hexagonal polymorph [151].

Without conducting further experiments on the local composition (grain interior of tetragonal and hexagonal grains, grain boundaries, and triple points) it remains unclear, whether the introduced acceptor-concentrations are distributed homogeneously and to the same percentage as calculated or if the percentage is altered due to grain boundary segregation or the rising secondary hexagonal phase. The different strong impact of the different acceptor-dopants on the stability of the hexagonal polymorph down to *RT* is, in any case, an interesting phenomenon, which deserved further discussions on the mechanism.

Hexagonal BaTiO$_3$ (*h*-BTO) is the high temperature polymorph and is for pure, stoichiometric BaTiO$_3$ under ambient air conditions only observed for samples being quenched from sintering temperatures above 1460 °C (see Section 2.2.1) [51]. As the samples were sintered under ambient atmosphere below the cubic-hexagonal phase transition temperature, the appearance of hexagonal structure was not expected from a first glance. In literature, two main possibilities to stabilize the *h*-BaTiO$_3$ at room temperature are reported[3]: First, for undoped BaTiO$_3$ the hexagonal phase can be stabilized under reducing conditions at temperatures notable below the transition temperature of 1460 °C [51, 152–155]. Second, acceptor-doping especially with 3*d*-transition metals, such as Cr, Mn, Fe, Co, Ni and Cu, is the second approach to stabilize the hexagonal structure [51–53, 55]. However, the introduced acceptors show different threshold values for the appearance of the hexagonal phase. In order to understand the reason for the different strong impact, the fundamental stabilization mechanism needs to be elucidated. In the following, five different mechanism/factors [156] are reviewed, which are debated as potential origin in literature. The plausibility of the different reviewed mechanisms is discussed with respect to the present results of this thesis:

---

[3]Please refer to Section 2.2.2 in the Fundamentals for further information.
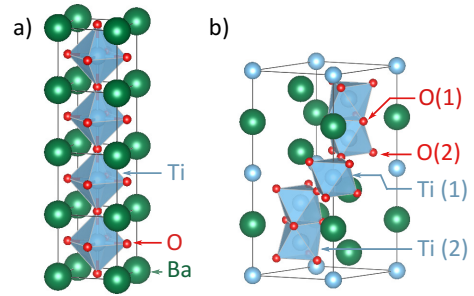
I. Sufficiently high oxygen vacancy concentration/A_{Ti} concentration

Under reducing conditions the amount of oxygen vacancies increases, which simultaneously reduces Ti_{Ti} to Ti_{Ti}' (see Equation 2.11). Wakamatsu *et al.* stated that the hexagonal phase is proportional to the amount of Ti_{Ti}' and that a minimal amount of 0.3 mol % of Ti_{Ti}' is necessary to stabilize the high temperature hexagonal structure down to room temperature [153]. This assumption is corroborated by the model that oxygen vacancies enhance the stability of h-BaTiO$_3$. Rietveld refinement of neutron diffraction studies on h-BaTiO$_3$ revealed that face-sharing oxygen vacancies O(1) are more favorable than corner-sharing O(2) sites [53, 154]. Density functional theory (DFT) studies on oxygen vacancies in the hexagonal phase of BaTiO$_3$ confirmed that the O(1) lattice site is energetically more favorable for oxygen vacancies [50]. The corresponding crystal structures of cubic and hexagonal BaTiO$_3$ are depicted in Figure 5.5.

As known from the defect chemistry of BaTiO$_3$, acceptor doping is accompanied by the creation of oxygen vacancies to maintain charge neutrality. Thus, A_{Ti}'

Figure 5.5.: Crystal structure of a) cubic and b) hexagonal BaTiO$_3$. The two different O- and Ti-sites in the hexagonal structure are labeled by O(1) and O(2) and Ti(1) and Ti(2), respectively. The structure was created with VESTA [44].

acceptor-doping should have the same influence on the stabilization of the hexagonal phase as the creation of Ti_{Ti}' under reducing conditions. This hypothesis is supported by the work of Keith *et al.* who investigated the stabilization of h-BaTiO$_3$ by different A_{Ti} dopants, with A=Mg, Al, Cr, Mn, Fe, Co, Zn, Ga, Ni and In [53]. All dopants stabilized the hexagonal structure at firing temperatures below 1460 °C. As those elements belong to the s-, p-, and d-block of the periodic system, the only common feature seems to be the creation of oxygen vacancies by acceptor-doping. Nevertheless, it should be stressed, that several studies revealed that the amount of hexagonal phase strongly depends on the type of dopant, its doping-concentration and firing temperature [51, 56].

Mn and Fe are so called multi-valent dopants and can, in theory, be incorporated as A_{Ti}, A_{Ti}' or A_{Ti}''. Accordingly, the amount of created oxygen vacancies varies with respect to the corresponding charge neutrality law.

For the present sintering conditions, it is most likely that the Fermi level is pinned at the Fe^{4+}/Fe^{3+} and Mn^{4+}/Mn^{3+} level, leading to a mixture of A_{Ti} and A_{Ti}'. As the ratio will depend on the position of the defect transition level in the band gap, different ratios are expected for both dopants. This was confirmed by the conducted defect chemistry calculations, estimating a 60 % Mn^{3+} / 40 % Mn^{4+} mixture for Mn-doped samples and a predominate Fe^{3+} oxidation state for Fe-doped samples at room temperature (see Appendix A.2.3 and Table 5.3).

Thus, even more oxygen vacancies are expected to be created by Fe-doping than by Mn-doping, which is contradictory to the observed higher efficiency of Mn-doping. Accordingly, the discussed mechanism of oxygen vacancies stabilizing the hexagonal phase cannot be the only mechanism for the present doping case and another driving force needs to be present in the case of $3d$-transition metal doping.

II. Metal-Metal bond length in the B_2O_9 dimers and resulting repulsion/distortion

According to Pauling's third rule, corner sharing octahedra are more stable than face-sharing octahedra. In the latter the nominal bond length between the Ti(2)-Ti(2) sites is decreased compared to the bond length of Ti-ions in corner-sharing octahedra, resulting in a higher electrostatic repulsion [50].

In acceptor-doped $BaTiO_3$ the hexagonal phase is stabilized, which exhibits face-sharing octahedra. According to Jayanthi *et al.*, the subsequent increase in electrostatic repulsion in $3d$-element doped $BaTiO_3$ may be reduced by either metal-metal bonds due to overlapping d-orbitals, covalent interactions between the Ti(2) and the oxygen ions, or shorter O(1)-O(1) triangle distances, shielding the charge of the metal cations [56]. The first argument seems to be ruled out, as for Mn-doping, it has been shown, that the Mn-Mn d-overlapping is minimal in face sharing octahedra [157]. Burbank *et al.* evaluated the Ti(2)-Ti(2) and O(1)-O(1) distances in cubic and hexagonal $BaTiO_3$ and observed a remarkable shortening of the O(1)-O(1) and increase of the Ti(2)-Ti(2) distances for the face-sharing ocahedra in hexagonal $BaTiO_3$ [158]. The changed bond lengths lead to an overall distortion of 14 % (calculated from the increase in Ti(2)-Ti(2) distance) for the face-sharing octahedra in hexagonal $BaTiO_3$, whereas no distortion was observed for the corner-sharing octahedra in cubic $BaTiO_3$ [158]. Thus, the distortion of the face-sharing octahedral along the hexagonal c-axis is proposed as compensation mechanism. Furthermore, a computational study revealed that besides the site preference of the oxygen vacancies on the O(1) site, the A'_{Ti} are preferably located in the face-sharing octahedra, i.e. on the Ti(2) site in Figure 5.5, which would lead to a reduced repulsion between A'_{Ti} and A_{Ti}/A'_{Ti} ions compared to only A_{Ti} ions [52, 159]. Moreover, the creation of the oxygen vacancy on the O(1) might be energetically more favorable because the Ti(2)-Ti(2) bond length is increased in the octahedra where the O(1) vacancy is created [50].

In summary, a distortion of the B_2O_9 dimers is most likely to be the reason for the stabilization of the hexagonal phase. However, the fundamental mechanism leading to the distortion, e.g. O(1) vacancies or the influence of the B-site atom, remains inconclusive.

III. Electron configuration of the B-site cation (dopant) – Jahn-Teller distortion

According to Langhammer, Böttcher, and co-workers, the Jahn-Teller distortion and by this the electron configuration of the B-site ion is the common driving force for the cubic-hexagonal transition [52, 55, 151, 160]. As previously discussed, the B-site ion has an octahedral BO_6

coordination[4]. The electron configuration of the Mn and Fe dopants exhibit the high-spin ground state, due to a weak crystal field splitting of the oxygen atoms within the crystal field theory. According to the Jahn-Teller theory, a distortion of the octahedron by an elongation along the z-axis is expected, when the degenerate orbitals are unevenly occupied with electrons [162]. This holds for the electron configurations d^1, d^2, d^4, d^6, d^7, and d^9. Here, the d^4 and d^9 configurations show an even stronger Jahn-Teller effect due to their partially filled e_g orbital (the higher sub-level) [52].

The corresponding electron configuration for the different oxidation states of the B-site cations are tabulated in Table 5.4. Accordingly, Ti^{3+}, Mn^{3+}, Fe^{4+}, and Fe^{2+} are Jahn-Teller active ions. As discussed in the previous paragraph, reduced undoped $BaTiO_3$ exhibits a certain fraction of Ti'_{Ti} and thus a Jahn-Teller active ion on the B-site. Furthermore, it would also explain the different strong stabilization of the hexagonal polymorph for the different $3d$-transition metals.

Table 5.4.: Electron configuration, Coordination number, effective ionic radius, Goldschmidt tolerance factor, and presence of Jahn-Teller effect (JTE) for the possible ions of Ba, Ti, Mn, Fe and O being present in $BaTiO_3$. All values taken from [163]. *=Values taken for the high spin configuration. The Goldschmidt tolerance factor was calculated according to Equation 2.8.

Ion	Electron Configuration	Coordination Number	Effective ionic radius in Å	Tolerance factor	JTE
Ba^{2+}	[Xe] $6s2^0$	12	1.61	-	
O^{2-}	[He] $2s^22p^4$	6	1.40	-	
Ti^{4+}	[Ar]$4s^03d^0$	6	0.605	1.06	-
Ti^{3+}	[Ar]$4s^03d^1$	6	0.670	1.03	x
Mn^{4+}	[Ar]$4s^03d^3$	6	0.530*	1.10	-
Mn^{3+}	[Ar]$4s^03d^4$	6	0.645*	1.04	**x**
Mn^{2+}	[Ar]$4s^03d^5$	6	0.830*	0.95	-
Fe^{4+}	[Ar]$4s^03d^4$	6	0.585*	1.07	**x**
Fe^{3+}	[Ar]$4s^03d^5$	6	0.645*	1.04	-
Fe^{2+}	[Ar]$4s^03d^6$	6	0.780*	0.98	x

According to literature, for the same sintering conditions (1400 °C, 1 h, air) 1.7 mol % Mn-doping is necessary to obtain phase pure h-BaTiO$_3$, while even at 10 mol % Fe-doping only 50 % h-BaTiO$_3$ is reached [52, 55]. Similar results have been published by Glaister and Kay, indicating, that Mn-doping is much more efficient in stabilizing the h-BaTiO$_3$ than Fe or Ni [51]. For the present sintering conditions the dopants are expected to be incorporated as a Mn^{3+}/Mn^{4+}

---

[4]The octahedral BO_6 coordination is only valid for small oxygen vacancy concentrations. For higher V_O concentrations the coordination lowers to a square-pyramid BO_5 coordination [161]. The following classification of Jahn-Teller activity has been conducted assuming an octahedral BO_6 coordination.

mixture and solely Fe^{3+}. Hence, the presence of the Jahn-Teller active Mn^{3+} could explain the stronger stabilization of the hexagonal phase for Mn-doped samples compared to Fe-doped ones. However, also Jahn-Teller inactive ions such as Ga, Zn and Mg promote a the stabilization of the hexagonal phase [56, 139]. Even though the sintering temperature and necessary doping-concentration are markedly higher than for Jahn-Teller active ions, a stabilization was successfully below the phase transition temperature of 1460 °C. Thus, the Jahn-Teller distortion can not be the only mechanism stabilizing the hexagonal phase, but the *d*-electron configuration of the *B*-site ions seems to have a clear influence on the effectiveness.

IV. Goldschmidt tolerance factor

Another aspect which is discussed to be responsible for the different effectiveness of different dopants is the Goldschmidt tolerance factor [144]. The corresponding ionic radii of the different oxidation states of the *B*-site cations and the resulting tolerance factors are summarized in Table 5.4. Ren *et al.* argue that $BaTiO_3$ with $t = 1.06$ adopts the cubic structure (below $T = 1460$ °C) while $BaAO_3$ with $A = Mn^{4+}$ and $t = 1.10$ exclusively adopts the hexagonal structure [144]. This argument would also hold with regard to the different strong stabilization of Fe dopants: A $BaAO_3$ unit cell with $A = Fe^{4+}$ and Fe^{3+} corresponds to $t = 1.07$ and $t = 1.04$, respectively. These values are close to or even below the value of undoped $BaTiO_3$ which adopts the cubic structure. However, the difference in Goldschmidt tolerance factor does not explain the described occurrence of *h*-$BaTiO_3$ of undoped $BaTiO_3$ under reducing conditions, as $BaTi^{3+}O_{3-\delta}$ has a tolerance factor of $t = 1.03$, which is lower than the one of stoichiometric $BaTiO_3$. Furthermore, when calculating the tolerance factor for the most prevalent oxidation state of acceptor-dopants, which lead to an observation of the hexagonal phase, no consistent picture can be drawn[5].

Here, it should be mentioned, that the application of the Goldschmidt tolerance factor is questionable for perovskite structures with a considerable number of vacancies [41].

In summary, the tolerance factor is a measure for the stability of the perovskite structure in general, but does not give a clear indication for the stabilization of the hexagonal phase upon different acceptor-doping.

V. The Ba/Ti ratio

It is commonly known that the cation ratio has major influence on the properties of polycrystalline $BaTiO_3$ [48, 92, 164]. Thus, it is not surprising that the Ba/Ti ratio also plays a role in the stabilization of the hexagonal phase. For acceptor-doped $BaTiO_3$ the *A/B*-site ratio also seems to have a significant influence on the amount of hexagonal phase. For Mn-doped samples Jayanthi *et al.* observed that for $A/B > 1$, i.e. Ba-excess, the hexagonal phase is more stabi-

---

[5]E.g.: Mg^{2+} (r=0.72, t=1.004), Cr^{3+} (r=0.615, t=1.056), Co^{2+} (r=0.745, t=0.992), Cu^{2+} (r=0.73, t=0.999), Ni^{2+} (r=0.69, t=1.018), Ga^{3+} (r=0.62, t=1.054) ionic radii taken from [163]

lized [56]. In contrast, for Cu-doping $A/B < 1$ leads to a higher stabilization of the hexagonal phase [56]. These results are contrary and at the moment no uniform picture can be drawn on the influence of the A/B-site ratio. Nevertheless, in all cases it had a considerable influence on the amount of hexagonal phase. Thus, the A/B ratio should always be considered in the discussions.

Following the above discussion on the presented literature, two main mechanism seem to play a role in the stabilization of the hexagonal phase, which was also concluded by Langhammer *et al.* [160]. First, a sufficiently high oxygen vacancy concentration needs to be present to promote the transformation from cubic to hexagonal phase. For undoped $BaTiO_3$ this is either reached by sintering/heating in reducing atmosphere or at temperatures above $1460\,°C$ were the amount of oxygen vacancies is high enough. For acceptor-doped $BaTiO_3$ the transition temperature is considerable lowered due to the formation of oxygen vacancies compensating for the negatively charged acceptors $A_{Ti}^{'}$ and $A_{Ti}^{''}$. However, the threshold values for the different acceptor-dopants for the occurrence of the hexagonal phase are markedly different, as has been confirmed for the present case of Mn- and Fe-doping.

Thus, a second mechanism seems to be involved. Here, the electron configuration of the B-site cation and by this the presence of a Jahn-Teller distortion seems to have a considerable influence on the lowering of the transition temperature and the efficiency of the dopant. For Jahn-Teller active ions the originally symmetric BO_6 octahedra of the cubic phase will be distorted, which results in the transformation into the hexagonal structure (which has distorted octahedra as been discussed in **II**). In addition to the mentioned mechanisms, also the A/B-site ratio and the ionic radii of the B-site ion are expected to have an influence on the stabilization of the hexagonal phase. However, its influence is inconclusive, yet.

Thus, when comparing literature reports, it is highly recommended to have a detailed look on the sintering temperature and atmosphere, the type of acceptor-dopant, its oxidation state and concentration as well as the A/B-site ratio in order to conclude on the effectiveness of the respective dopant.

5.3. Microstructure

Scanning electron microscopy images conducted in the BSE mode of undoped, 0.1 wt.%, and 0.5 wt.% Mn- and Fe-doped BaTiO$_3$ are shown in Figure 5.6. When comparing the pictures of undoped BaTiO$_3$ between both batches (Figure 5.6 a) and d)) it is clearly visible that the grain size of the second batch is remarkably bigger than the one of the first batch. Several factors may have affected the different grain growth: i. the 50 °C higher calcination temperature of the Fe-doped batch[6], resulting in a slightly different particle size distribution after calcination, ii. the expected *B*-site excess according to the net-weight calculations, iii. Liquid-phase assisted sintering, and/or iv. Zr or Si impurities promoting exaggerated grain growth.
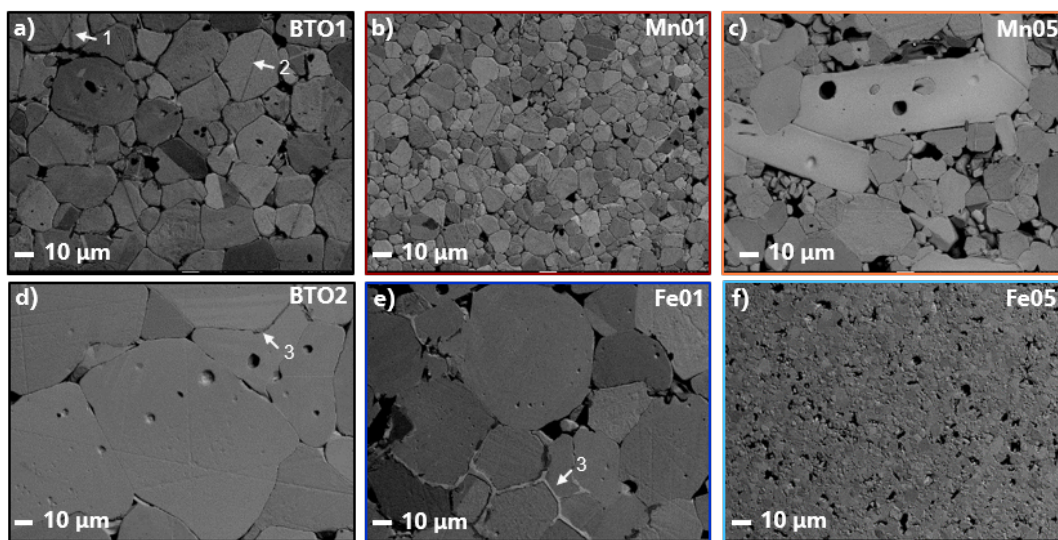
Figure 5.6.: a)-f) Scanning electron microscopy images of undoped, 0.1 wt.%, 0.5 wt.% Mn- and Fe-doped BaTiO$_3$ samples, respectively. The samples have been polished to $^1/_4$ µm diamond finish with lubricant followed by a thermal etching for 30 min at 1250 °C. All pictures have the same magnification for simplicity. The measurements have been conducted in the BSE mode with a *JEOL-JSM-7600F* SEM and an EDX from *Oxford-X-Max*. Higher magnification SEM pictures of 0.5 wt.% Fe-doped BaTiO$_3$ are shown in Appendix A.4.

The particle size distribution of the calcined powders is given in Figure A.2. Indeed a slightly higher particle size is observed for the undoped BaTiO$_3$ of the second batch with some additional particles of a size around 9 µm. Even this is only a small fraction and the particle size distribution is not dramatically different, this may have an influence on the resulting grain size. As no ICP-OES measurements have been preformed on the undoped BaTiO$_3$ batches, also no exact Ba/Ti ratio is reported. Nevertheless, according to the net-weight calculations a *B*-site excess is assumed. It is known that already a minor nonstiochiometry between the *A/B*-site can lead to different grain growth in BaTiO$_3$. Under similar sintering conditions Ba-excess decreases

---

[6]The calcination and sintering parameters can be found in Section 3.1.

the grain size, while Ti-excess increases the grain size [92]. Furthermore, a liquid phase is observed at some grain boundaries of the second batch samples, indicated by arrow 3 in Figure 5.6 d) and e). The BaO-TiO$_2$ phase diagram indicates, that already a small Ti-excess will lead to the formation of BaTiO$_3$ as solid solution and liquid phase (see Figure A.1) [48, 165]. As liquid phase is observed at some grain boundaries of the second batch samples (indicated by arrow 3 in Figure 5.6 d) and e)), a slight Ti-excess is assumed for the second batch samples. In addition, impurities such as Si or Zr can form secondary phases, which may promote bi-modal or exaggerated grain growth as well. Here, Zr-impurities may originate from the ball-milling process [166]. Furthermore, EDX on polished Fe-doped specimens partially revealed small contamination of Al and P, which haven't been detected for Mn-doped samples. Al-impurities may originate from the Al$_2$O$_3$ crucible used during synthesis and sintering. A more detailed discussion on the grain growth mechanism of titanates in context of non-stoichiometry and secondary phase segregation is given by Rheinheimer and Hoffmann [138].

The introduction of 0.1 wt.% acceptor-dopant concentration results in a slightly decreased grain size compared to the undoped BaTiO$_3$ of the respective batch, as shown in Figure 5.6 b) and e). Additionally, the grain size distribution becomes bi-modal for both dopants. The 0.1 wt.% Fe-doped BaTiO$_3$ exhibits considerable bigger grains than the 0.1 wt.% Mn-doped BaTiO$_3$. Furthermore, a liquid phase is observed on some grain boundaries of the 0.1 wt.% Fe-doped BaTiO$_3$. With increasing Fe-doping concentration to 0.5 wt.%, the grain size further decreases exhibiting a bimodal distribution, as shown in Figure A.4 (magnification of Fig. 5.6 f)). Similar observations are presented in literature for Fe-doped BaTiO$_3$ [55]. With increasing acceptor-doping concentration the space charge at the grain boundaries rises, which may lead to a solute drag effect on the boundary motion and a non-Arrhenius grain growth during sintering [138].

The 0.5 wt.% Mn-doped BaTiO$_3$ also shows a bimodal grain size distribution. In contrast to Fe-doping, the bimodal distribution upon Mn-doping reveals huge elongated plate-like grains (Fig. 5.6 c)), which have also been reported in literature [52, 167]. As the occurrence of the elongated grains is only observed for the doping concentrations showing partially hexagonal structure a correlation is likely. The correlation between plate-like grains and the occurrence of hexagonal structure is also reported for Cr-, Mn-, and Ga-doped h-BaTiO$_3$ in literature [52, 56, 139]. Nevertheless, the correlation remains a hypothesis without conducting electron backscatter diffraction (EBSD).

5.3.1. EBSD on 0.5 wt.% Mn-doped BaTiO$_3$

EBSD has been performed on 0.5 wt.% Mn-doped BaTiO$_3$. The image quality map and phase map images are depicted in Figure 5.7 a) and b), respectively. The hexagonal phase is colored in red while the tetragonal phase is colored in green. The black fraction in the phase map corresponds to diffraction patterns, which could neither be assigned to one of the latter phases.
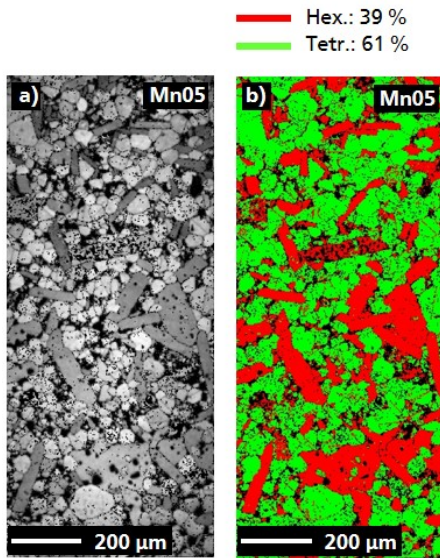
Figure 5.7.: a) EBSD quality map and b) phase map of 0.5 wt.% Mn-doped BaTiO$_3$. Unknown structure is black, hexagonal structure is red and tetragonal structure is green.

This might be reasoned in some surface inhomogeneities such as pores resulting in no or low signal. The quantitative analysis of the relative phase fractions revealed 61 % tetragonal phase and 39 % hexagonal phase. This is in good agreement with the phase fraction extracted from Rietveld of 62 % and 38 % (see Section 5.2). Furthermore, all elongated grains have been assigned to the hexagonal structure. Besides the elongated grains, also some smaller grains exhibit the hexagonal structure. Either the hexagonal polymorph exhibit different grain shapes or those smaller grains also have an elongated structure, but are simply cut along a different plane due to a statistically distribution of orientation inside the ceramic pellet. As the inverse pole figure map doesn't show any preferential orientation of the phases, a random grain orientation is assumed. In order to understand how the hexagonal phase enables the exaggerated grain growth of such elongated grains, the stacking sequence of the cubic and hexagonal lattice as well as the exaggerated grain growth of undoped BaTiO$_3$ needs to be considered.

For undoped BaTiO$_3$ two scenarios are known, which promote the formation of elongated plate-like grains:

i. Under ambient sintering conditions, undoped BaTiO$_3$ with Ti-excess forms a Ti-rich Ba$_6$Ti$_{17}$O$_{40}$ phase, which is believed to promote the exaggerated grain growth below the eutectic temperature of 1332 °C [168–170]. This secondary phase usually acts as a nucleation site for the formation of {111} twins with an epitaxial growth parallel to the {111} planes resulting in lamellar grains [168, 171].

ii. Under reducing conditions, undoped BaTiO$_3$ can be stabilized in the hexagonal polymorph. Several literature reports on the microstructure of undoped h-BaTiO$_3$ revealed the occurrence of elongated plate-like grains [172–174]. Kolar, Rečnik, and co-workers observed an anisotropic

exaggerated grain growth for undoped h-BaTiO$_3$ with plate-like microstructure. For the latter, the authors performed Monte-Carlo simulations revealing that the difference in surface energy anisotropy in the prismatic and basal planes of the hexagonal polymorph is responsible for the anisotropic grain growth [173, 174].

For the present samples single and double twins are observed in the SEM pictures of undoped BaTiO$_3$ in Figure 5.6 a) marked by the arrows 1 and 2. However, no twins are observed in the elongated grains of 0.5 wt.% Mn-doped BaTiO$_3$ (Fig. 5.6 c)). Thus, solely the anisotropic grain growth based on the different surface energies of the hexagonal planes is assumed to be responsible for the shape of the hexagonal grains.

In summary, the undoped BaTiO$_3$ of the second batch has remarkably larger grains, which might be related to a different Ba/Ti ratio and a resulting liquid-phase assisted sintering with additional effects due to possible Si/Zr impurities or the higher calcination temperature. 0.1 wt.% Mn- and Fe-doped BaTiO$_3$ show a bimodal grain size distribution with an overall bigger grain size for Fe-doping. 0.5 wt.% Mn-and Fe-doped BaTiO$_3$ show a bimodal distribution, with a drastically decreased grain size for the Fe-doped sample and elongated plate-like grains for the 0.5 wt.% Mn-doped BaTiO$_3$.

The occurrence of elongated plate-like grains is related to the hexagonal phase observed in the XRD pattern of 0.5 wt.% Mn-doped BaTiO$_3$. The growth mechanism might be comparable to the one observed for undoped h-BaTiO$_3$ were the anisotropy in surface energy seems to be responsible for the anisotropic grain growth and the resulting elongated shape of such grains [174].

5.4. Dielectric properties

The real part of the dielectric constant of the first heating-cycle[7] of Mn- and Fe-doped poly-crystalline $BaTiO_3$ are shown in Figure 5.8 a) and b), respectively. The corresponding Curie points and room temperature dielectric constants are given in Figure 5.8 c) and d). The room temperature permittivity is decreasing from 1900 for undoped $BaTiO_3$ to 1662 for 0.1 wt.% Fe-doped and to 1563 for 0.5 wt.% Fe-doped $BaTiO_3$. For Mn-doped $BaTiO_3$ the RT-ϵ' is also slightly decreasing to 1700 for doping concentrations up to 0.3 wt.%. For Mn-doping concentration from 0.4 wt.% to 0.6 wt.%, the room temperature permittivity is linearly decreasing down to 515.

The dielectric constant depends on the chemical composition, the microstructure (considering the grain size effect [175]), internal stress, aging, temperature, and several other aspects [176]. Thus, any changes due to acceptor-doping on the B-site and the creation of compensating
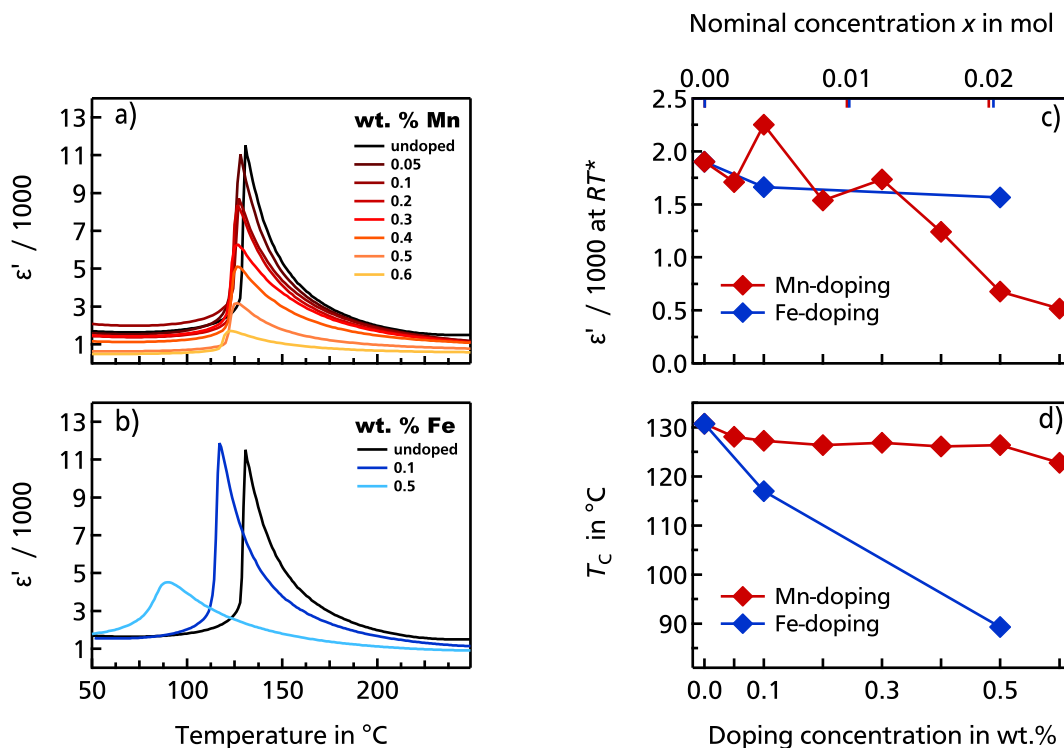
Figure 5.8.: a) and b) real part of the permittivity as a function of temperature for a frequency of 1000 Hz for Mn- and Fe-doped $BaTiO_3$, respectively. c) Determined RT^* permittivity as a function of doing concentration and d) determined Curie point during the first heating cycle at 1000 Hz. Curves of undoped $BaTiO_3$ belong to the pellets of the second batch. All samples were measured with Pt electrodes and a heating rate of 2 K/min. RT^* = temperature range between 23 °C to 50 °C. The nominal concentration x was calculated according to $BaTi_{1-x}A_xO_3$ with A=Mn, Fe.

---

[7]Two temperature cycles have been conducted for all measurements. The corresponding temperature profile is given in Section 3.2.2. No changes have been observed between the tow cycle and, thus, the first heating-cycle is shown.

oxygen vacancies will affect the dielectric constant. The creation of $(A_{\mathrm{Ti}}{'}\text{-}V_{\mathrm{O}}^{\bullet\bullet})^{\bullet}$ or $(A_{\mathrm{Ti}}{''}\text{-}V_{\mathrm{O}}^{\bullet\bullet})$ defect complexes, for example, has a pinning effect on the domain wall motion, which results in a reduced dielectric constant [177, 178]. The latter effect might be responsible for the decrease in RT-permittivity of Fe-doped samples and for samples up to 0.3 wt.% Mn-doping concentration.

Furthermore, fine grained ceramics show higher RT-permittivity than coarse grained ceramics [175, 179]. The higher RT-permittivity may be due to mechanical compression/internal stress. Thus, the decrease in grain size upon Fe-doping may act as a counterpart and lowers the doping-induced decrease of RT-permittivity. The higher decrease in RT-ϵ' upon Mn-doping with a concentration > 0.3 wt.% is most likely related to the occurrence of the hexagonal phase. Undoped h-BaTiO$_3$ has a RT dielectric constant of approximately 60 at 1 kHz [180], which would explain the linear decrease for Mn-doped samples with a doping concentration higher than 0.3 wt.% for which the content of the hexagonal phase increases. Additionally, the tetragonal to orthorhombic phase transitions is located at approximately 0 °C [41], which may affected the room temperature permittivity as well. Especially, if the introduction of acceptor-dopants also affects the position of latter phase transition.

Even though the maximum dielectric constant at the phase transition temperature decreases with Mn-doping concentration, the characteristic sharp and narrow shape is maintained upon Mn-doping (Figure 5.8 a)). In contrast, for high Fe-concentrations a broad maximum is observed in the vicinity of the phase transition (Figure 5.8 b)). Usually, a broad transition is not observed for normal ferroelectrics but for relaxor ferroelectrics. Here, the broadening can originate from a disorder on the B-site ions. However, according to the theory of disorder (and ferroelectric relaxors) the broadening of the transition goes along with a strong frequency dependence of the dielectric constant [181], which is not observed for 0.5 wt.% Fe-doped BaTiO$_3$ (see Figure A.6). Thus, a grain-size effect seems to be more likely to explain the broadening of the phase transition. Kinoshita and Yamaji examined the grain size dependent dielectric properties of BaTiO$_3$ ceramics and observed a (slight) broadening of the ferroelectric to paraelectric phase transition with decreasing grain size [175]. The small grain size of 1-5 μm for 0.5 wt.% Fe-doped samples can result in mechanical (intergranular) stress, which may result in a broader distribution of phase transitions for different grains/regions.

The Curie point of the present undoped BaTiO$_3$ is 130.7 °C (see Figure 5.8 d)), which is in good agreement with literature reports of polycrystalline undoped BaTiO$_3$ [41]. The Curie point only slightly decreases by approximately 5 °C upon Mn-doping, while a drastic decrease of 40 °C is observed upon Fe-doping. The observed different influence on the phase transition temperature of both dopants is consistent with literature reports for similar sintering conditions [27, 46, 47, 134–137].

In general, a lowering of the Curie point is observed for even slight perturbation in the cationic

or anionic lattice. Thus, the introduction of acceptors in the cationic lattice and the creation of oxygen vacancies in the anionic lattice of $BaTiO_3$ are both prone to have an influence on the Curie point [136, 176, 178, 182]. For reduced $BaTiO_3$, Härdtl and Wernicke observed a lowering of the Curie point of 41 °C to 50 °C per 10^{20} oxygen vacancies/cm^3 [182]. Similar dopant and oxidation state related linear dependencies have been found for the amount of Al^{+3}, Mg^{2+}, Mn^{3+} and Mn^{2+} dopant concentration [137, 183, 184]. Here, it is assumed that the creation of charged oxygen vacancies upon acceptor-doping reduces locally the tetragonality (c/a-ratio) and is responsible for the decrease in the transition temperature [178].

The decrease in the c/a-ratio could be one possible reason for the different influence of Mn- and Fe-doping on T_C. While the tetragonality of the Fe-doped sample is decreased from 1.01 to 1.005, it remains constant upon Mn-doping[8]. Simultaneously, the Curie point drastically decreases upon Fe-doping, while it only slightly decreases upon Mn-doping (see Fig. 5.8 d)).

Table 5.5.: Summary of the phase fractions of tetragonal and hexagonal phase received by Rietveld refinement of the XRD pattern and the determined Curie point of as-sintered samples with corresponding calculated oxidation states (Ox. State) and electron configurations (El. Conf.). The Jahn-Teller active electron configuration is highlighted in bold.

	$BaTiO_3$	0.5 wt.% Mn-doped	0.5 wt.% Fe-doped
% (Tet.)	100	60	97
% (Hex.)	0	40	3
T_C in °C	130	125	90
Ox. State	Ti^{4+}	$Mn^{3+/4+}$	Fe^{3+}
El. Conf.	d^0	$\mathbf{d^4}$/ d^3	d^5

As already mentioned above, the influence of the acceptor-dopants on T_C depends on the type and oxidation state of the acceptor. Ihrig and Hagemann systematically studied the phase stability of 3d-doped $BaTiO_3$ under reducing and oxidizing conditions [46, 136]. The oxidation state of the dopants has been determined by magnetic susceptibility measurements and the temperature for the rhombohedral-orthorhombic, the orthorhombic-tetragonal, and the tetragonal-cubic transitions have been examined by measuring the temperature-dependent dielectric constant. From the observed correlations between the phase stability and the oxidation state of the dopants with the corresponding electron configuration the authors concluded, that the phase transition of 3d-doped $BaTiO_3$ depends on the symmetry properties of the electron in the unfilled 3d-shell and the presence of oxygen vacancies [46]. This was supported by Desu

---

[8]Following the discussion in Section 5.2, it remains again unclear, whether Fe- and Mn-dopants are dissolved to the same amount in the tetragonal lattice. As the permittivity and thus T_C mainly represents the tetragonal phase, a different percentage of Fe- and Mn-acceptors in the latter may also result in different strong impact on the phase transition.

and Subbarao, who stated that based on the distortion of Jahn-Teller active ions, the Mn^{3+} ion is stabilizing the tetragonal phase, while the Jahn-Teller inactive ions Mn^{4+} and Mn^{2+} favor the cubic phase [47]. The stabilization mechanism of the tetragonal phase follows the same argumentation being presented in Section 5.2 on the stabilization of the hexagonal polymorph by Jahn-Teller active ions during sintering. To sum up the results, the major aspects of the phase analysis by Rietveld refinement, the evaluated Curie point and the calculated oxidation states with the corresponding electron configuration are summarized in Table 5.5.

For Mn-doped $BaTiO_3$ a mixture of Mn^{3+}/Mn^{4+} is expected, accompanied by a significant percentage of hexagonal phase and only a small lowering of the Curie point. For Fe-doped samples a Fe^{3+} oxidation state is expected, with an almost phase pure tetragonal structure and a drastic decrease in tetragonal-cubic transition temperature. The correlation of this observations leads to a different phase-stability range of the cubic phase for Mn- and Fe-doped $BaTiO_3$. Mn-doping seems to favor the distorted hexagonal and tetragonal structures, while Fe-doping seems to enhance the stability range of the cubic structure.

The incorporation of the acceptor-ions on the A_{Ti}-site is accompanied by the creation of $V_O^{\bullet\bullet}$ as charge compensation. Hence, under the present sintering conditions, Fe-doping is expected to create more $V_O^{\bullet\bullet}$ than Mn-doping. Thus, the creation of oxygen vacancies mainly decreases T_C, which leads to an enhanced stability range of the cubic phase. On the other hand, the Jahn-Teller active Mn^{3+}-ion may be responsible for the contraction of the cubic phase. The cubic phase is highly symmetric and thus the distortion of the BO_6 octahedra due to the Jahn-Teller effect seems to be energetically more favorable in the tetragonal and hexagonal structures.
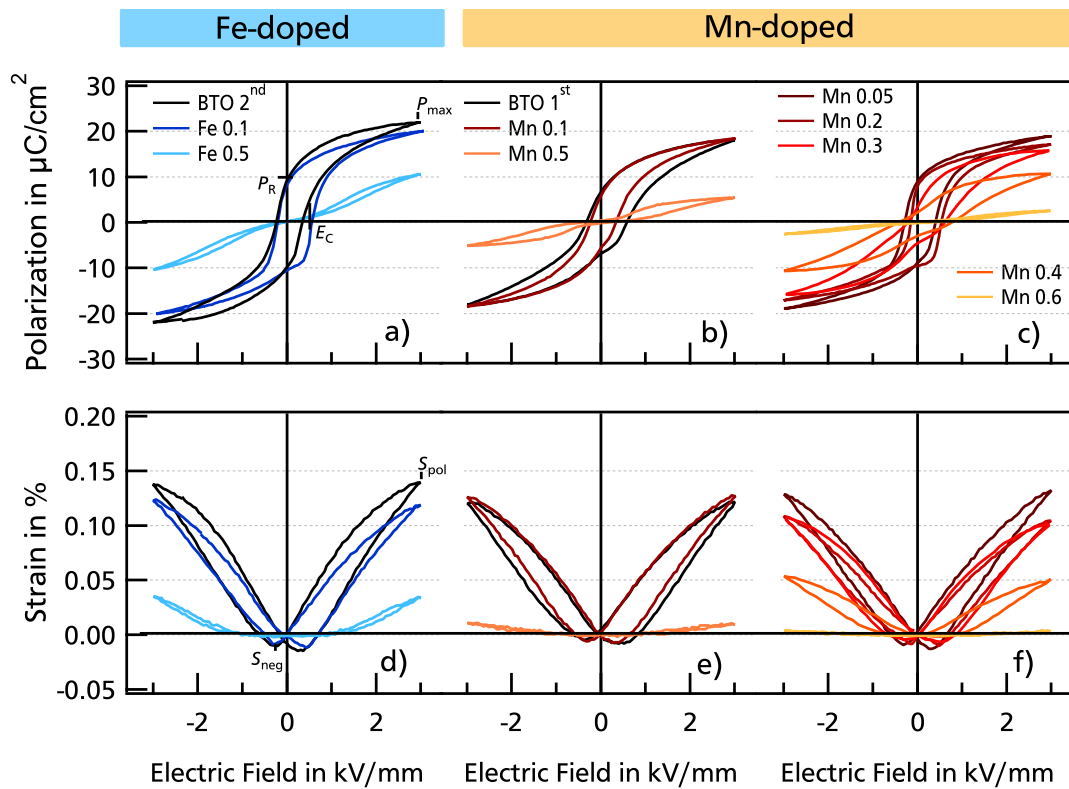
5.5. Ferroelectric properties

The polarization and strain loops of BaTiO$_3$ with different Fe- and Mn-doping concentrations are displayed in Figure 5.9. The characteristic properties are summarized in Figure 5.10.

In general, the introduction of acceptor-dopants leads to a decrease of the ferroelectric properties. This is most characteristically observed for the higher doping concentrations ($\geq$ 0.5 wt.%), as the maximum polarization P_{max} as well as the remanent polarization P_R are drastically decreased, which is accompanied by a pinched and constricted appearance of the $P(E)$ loops.

For Fe- and Mn-doping two main aspects are expected to have a major influence on the polarization response. First, the creation of V$_O^{\bullet\bullet}$ upon acceptor doping, which can lead to the formation of $(A_{Ti}'$-V$_O^{\bullet\bullet})^{\bullet}$ or $(A_{Ti}''$-V$_O^{\bullet\bullet})$ defect complexes hindering the domain wall motion, resulting in ferroelectric hardening [43, 140].

Figure 5.9.: Polarization and strain loops as a function of the electric field of polycrystalline BaTiO$_3$ with different Fe- and Mn-content measured at 50 Hz and 3 kV/mm. For a better comparison, the $P(E)$ and $S(E)$ loops for the same acceptor-doping concentrations of undoped, 0.1 wt.%, and 0.5 wt.% Fe- and Mn-doped BaTiO$_3$ are depicted in a)/d) and b)/e), respectively. The additional Mn-concentrations are shown in c) and f). Characteristic properties are marked on the $P(E)$ and $S(E)$ loops of second batch undoped BaTiO$_3$ in a) and d). The second loop is depicted. The frequency dependent $P(E)$ and $S(E)$ loops are presented in Figure A.7 and A.8, respectively. The nominal concentration x was calculated according to BaTi$_{1-x}A_x$O$_3$ with A=Mn, Fe

Second, the formation of the hexagonal phase leads to a phase mixture of the ferroelectric tetragonal phase and the centrosymmetric non-ferroelectric hexagonal phase, which will decrease the overall ferroelectricity of the samples [140, 143]. Furthermore, changes in the grain size as well as aging/relaxation may affect the appearance of the presented $P(E)$ and $S(E)$ loops [185–187].

The oxidation state of Mn is expected to be a $Mn^{3+}/Mn^{/4+}$ mixture, while Fe is expected to be mainly Fe^{3+}. Furthermore, Mn-doping leads to a considerable amount of hexagonal phase, while Fe-doped samples showed only a very small amount. Thus, the influence of acceptor-doping with its main aspect of the creation of oxygen vacancies can be discussed on Fe-doped $BaTiO_3$.

Upon Fe-doping the maximum polarization P_{max} as well as the remanent polarization P_R are decreasing with increasing Fe-concentration. The poling strain S_{pol} (strain at $3\,kV/mm$) follows, as expected, the same trend as P_{max}. While undoped and $0.1\,wt.\%$ Fe-doped $BaTiO_3$ show the well-known single $P(E)$ loop, $0.5\,wt.\%$ Fe-doped $BaTiO_3$ shows a so called double $P(E)$ loop, which can also be described as constricted or pinched loop. Furthermore, for small doping concentrations a shift of the loop along the field axis is observed. Both observations may originate from an internal bias field [141, 188]. The latter can occur when the direction of poling coincide with the preferential orientation of defects dipoles [43]. The internal bias field E_i has been determined from the differentiated hysteresis loops according to Carl and Härdtl [189], as depicted in Figure A.9. The resulting internal bias field is shown in Figure 5.10 and is increasing with increasing Fe-doping concentration.

The appearance of double $P(E)$ loops is often observed for acceptor-doped $BaTiO_3$ with a high $V_O^{\bullet\bullet}$
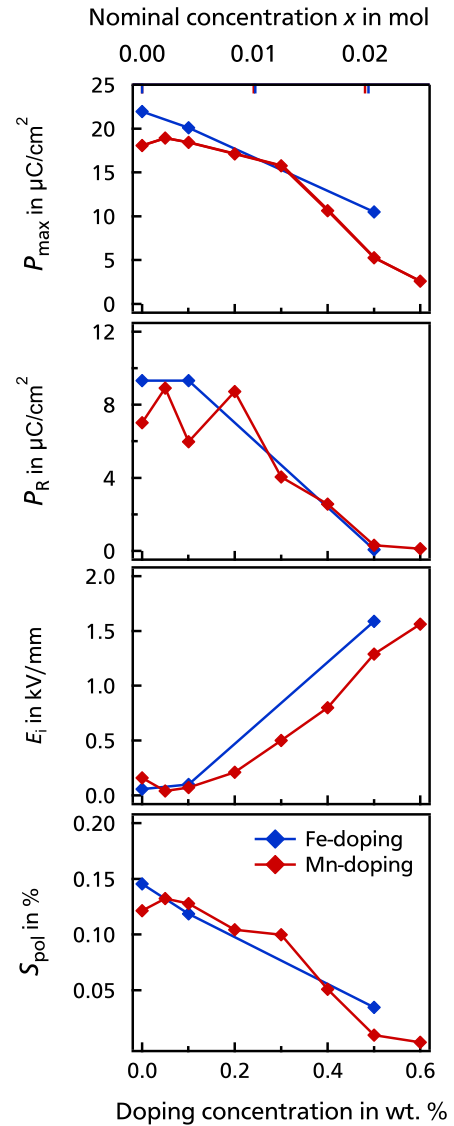
Figure 5.10.: Maximum polarization P_{max}, remanent polarization P_R, internal bias field E_i, and poling strain S_{pol} of polycrystalline $BaTiO_3$ with different Fe- and Mn-content. The values have been examined on the second loop measured at RT at $50\,Hz$. The internal bias field has been examined from current curves, i.e. from differentiated hysteresis loops depicted in Figure A.9. The nominal concentration x was calculated according to $BaTi_{1-x}A_xO_3$ with A=Mn, Fe

and A'_{Ti} concentrations [141, 142]. The formation of $(A'_{\text{Ti}}\text{-}V_O^{\bullet\bullet})^\bullet$ defect dipoles can lead to modified electrostatic and elastic fields in the vicinity of the complex. Furthermore, the alignment of these defect dipoles along the spontaneous polarization direction of the ferroelectric lattice has high impact on the domain switching and by this on the appearance of the $P(E)$ loop.

Ren *et al.* termed this the symmetry-conforming short-range ordered (SC-SRO) configuration of point defects for aged ferroelectrics [190]. For the present acceptor-doped case the point defects would be the $(A_{\text{Ti}}'\text{-}V_O^{\bullet\bullet})^\bullet$ defect dipole, which conforms the symmetry of the tetragonal BaTiO$_3$ along the spontaneous polarization direction ($(A_{\text{Ti}}'\text{-}V_O^{\bullet\bullet})^\bullet \parallel P_S$). The present samples have not been stored (aged) for more than one day. Thus, it is likely that the short range migration (diffusion) of oxygen vacancies didn't reach equilibrium. Hence, the effect of $(A_{\text{Ti}}'\text{-}V_O^{\bullet\bullet})^\bullet$ alignment is only weak, resulting in the observed internal bias and the narrow double $P(E)$ loop observed for 0.5 wt.% Fe-doped BaTiO$_3$.

Furthermore, the 0.5 wt.% Fe-concentration exhibits a broad dielectric response in the vicinity of the phase transition, which could be related to a B-site disorder or the more likely grain-size effect (see discussion in Section 5.4). The latter is also known to significantly affect the shape of the $P(E)$ loops. Thus, an interplay of both effects is proposed as origin for the appearance of the $P(E)$ and $S(E)$ loops.

As the degree of domain wall pinning on defect complexes is controlled by the oxygen vacancy concentration, the pinning effect is expected to be more intense for Fe-doping as it is incorporated as Fe^{3+} and thus creates more oxygen vacancies than the Mn^{3+}/Mn^{4+} mixture. This could explain the higher degree of constriction of the $P(E)$ loops and the slightly higher internal bias of 0.5 wt.% Fe-doped BaTiO$_3$ compared to 0.5 wt.% Mn-doped BaTiO$_3$. Besides the influence of defect complexes, the rising amount of hexagonal phase in Mn-doped BaTiO$_3$ will influence the ferroelectricity. Upon Mn-doping, $P_{\max}$ and S_{pol} are only slightly decreasing in the range of 0.05 wt.% - 0.3 wt.% followed by a stronger (approximately linear) decrease in the doping range of 0.4 wt.% - 0.6 wt.%. The onset of the strong decrease in $P_{\max}$ and S_{pol} coincides with the onset of the formation of the centrosymmetric non-ferroelectric hexagonal phase. Samples with an intermediate Mn-content (0.3 wt.% and 0.4 wt.%) as well as the undoped BaTiO$_3$ of the first batch show a strong frequency dependence (see Appendix Figure A.7) with a high leakage[9] at low frequencies, which needs to be considered in the interpretation of the characteristic properties in Figure 5.10.

---

[9]The respective samples are leaky at low frequencies. Thus, the $P(E)$ and $S(E)$ in Figure 5.9 were presented for 50 Hz instead of the commonly used 1 Hz.

5.6. Influence of heat treatment on acceptor-doped BaTiO$_3$

One main objective of this work is to answer the fundamental question whether the defect energy levels of acceptor-dopants in polycrystalline BaTiO$_3$ can be identified by means of *DC*-conductivity measurements during re-oxidation and/or XPS analysis of electrode interfaces. In both methods the Fermi level will be altered either by the successive incorporation of oxygen during re-oxidation or electronically due to the formation of a Schottky barrier.

BaTiO$_3$ needs to be reduced in order to access the whole band gap during the re-oxidation approach. For the interface approach both, reduced and oxidized, BaTiO$_3$ are ideal in order to observe an E_F pinning during contact formation to low and high work function electrodes, respectively. The reduction was accomplish by annealing at 1100 °C for 12 h in 5 % H$_2$/95 % Ar atmosphere with quenching to *RT*. In order to achieve an uniform defect concentration before reduction and oxidation, an equilibration at 900 °C for 12 h in air with quenching to *RT* was conducted. The altered oxidation states and corresponding amount of V$_\mathrm{O}^{\bullet\bullet}$ after the heat treatments are expected to have considerable influence on the structural properties (see discussion in Section 5.2 - 5.3). Furthermore, the specimen surface is essential for the barrier formation, and thus any influence of heat treatments on the surface composition and possible impurities is crucial.

5.6.1. Crystal structure

The XRD pattern of equilibrated Mn- and Fe-doped BaTiO$_3$ are displayed in Figure 5.11. In order to avoid any changes due to crushing, the samples have been measured as ceramic pellets. The reflection marked with * at 30.22 ° corresponds to an artificial tungsten reflection, which results from the X-ray tube. The XRD pattern have been measured with Cu K_α radiation filtered by a Sol-X detector. Hence, the pattern contain Cu $K_{\alpha 1}$ and Cu $K_{\alpha 2}$ reflection doublets, which are easily visible in the Zoom-In of the $(002)_t$ and $(200)_t$ reflections. According to the Bragg Equation, the distance between the reflection doublet increases with increasing 2θ angle. Undoped and 0.1 wt.% Fe-doped BaTiO$_3$ show a phase pure tetragonal structure, while 0.5 wt.% Fe-doped BaTiO$_3$ exhibits additional small reflections from the hexagonal polymorph. For Mn-doping, samples with < 0.4 wt.% doping concentration are tetragonal. For 0.4 wt.% only additional $(203)_h$ and $(118)_h$ reflections are visible, while for higher doping concentrations several h-reflections are observed.

Besides the tetragonal and hexagonal reflections two small unknown reflections are visible at approximately 28.6 ° and 42.98 °. These low intensity reflections cannot be clearly assigned to commonly observed secondary phases, as already discussed for the sintered powders. A more detailed comparison is given in Figure A.10 in the Appendix.

In order to quantify the tetragonality, a Zoom-In of the $(002)_t$ and $(200)_t$ reflections is shown in Figure 5.11 on the right hand side. As already observed for the sintered powders, Fe-doping leads to an decrease in tetragonality, while the latter remains approximately constant with Mn-doping. In addition, for higher Mn-doping concentrations a broadening of the $(002)_t$ is observed, which is most likely originating from the rising intensity of the $(204)_h$ reflection.
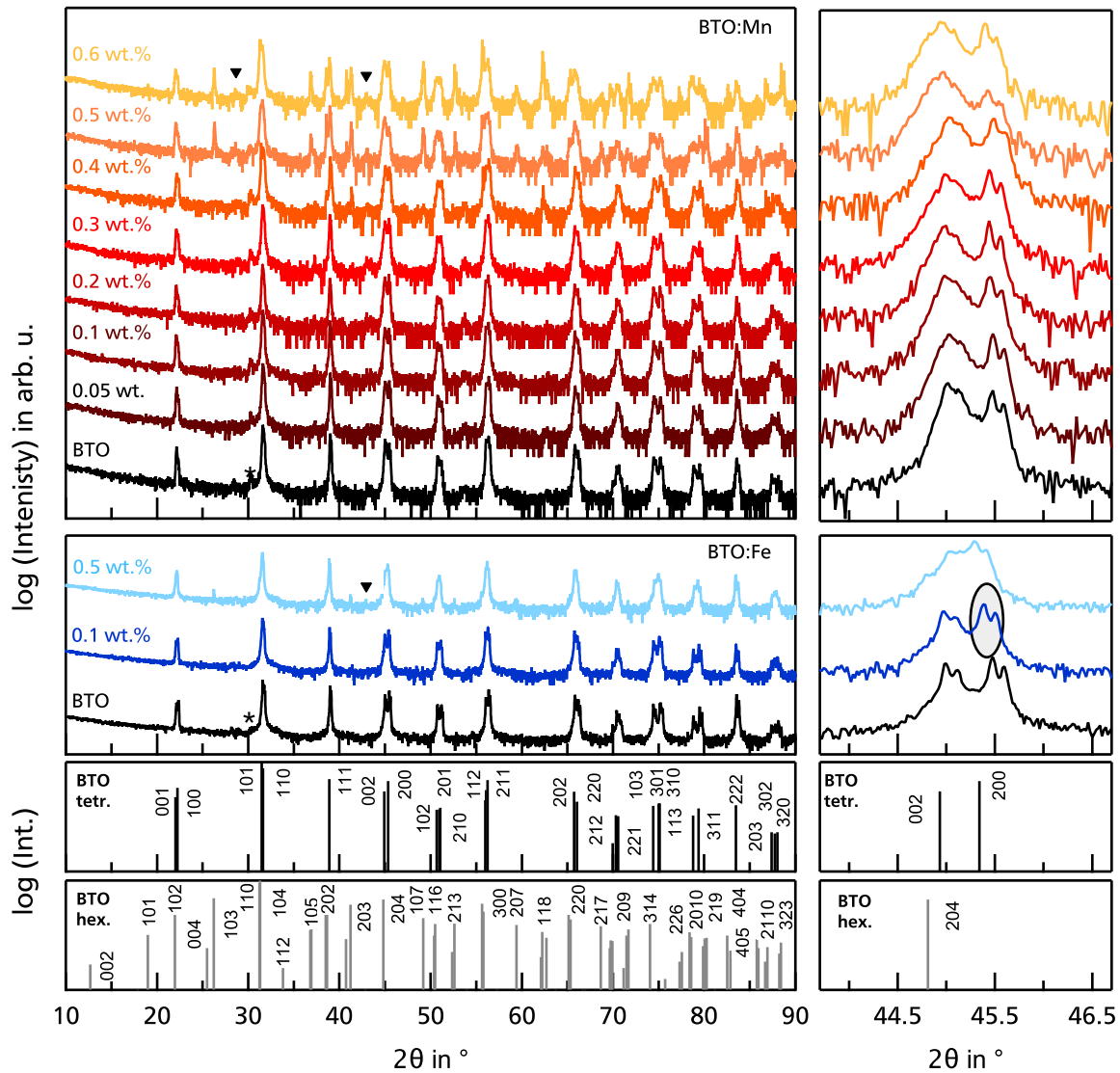
Figure 5.11.: Left: X-ray diffraction pattern of equilibrated Mn- and Fe-doped BaTiO$_3$. Samples have been equilibrated at 900 °C for 12 h in air and have been quenched to *RT*. Right: Zoom-In into the $(200)_t$ and $(002)_t$ reflections. In the lower panel the powder diffraction pattern of BaTiO$_3$ [01-082-1175] - hex. - P63/mmc (gray), ICSD collection code: 075240 and BaTiO$_3$ [01-075-0583] - tetr. - P4mm (black), ICSD collection code: 029280 are displayed. The powder diffraction pattern are only used for phase assignment. The pattern were recorded by Cu K_α radiation with $\lambda_{CuK_{\alpha 1}} = 1.5406$ Å filtered by a Sol-X detector. The reflection marked with * at 30.22° corresponds to an artificial tungsten reflection, which results from the X-ray tube.

However, the experimentally derived intensity ratio of the $(002)_t$ and $(200)_t$ reflections is markedly changed for the Mn-doped samples. The intensity ratio of the latter reflections is often used for XRD studies on the domain orientation [191]. At *RT* the direction of spontaneous polarization is along the [001] direction. Thus, the $(002)_t$ reflection corresponds to the *c*-axis perpendicular to the surface and the $(200)_t$ reflection to the *a*-axis perpendicular to the surface and thus *c*-domain orientation (out-of-plane polarization) and *a*-domain orientation (in-plane polarization), respectively. The ratio between the $(200)_t/(002)_t$ is determined to be approximately 1.7 [192] for ceramics in the unpoled and unstressed state[10], although the theoretical value is nearly 2 [191, 193]. As the $(200)_t/(002)_t$ ratio is lower or even below one for some samples, a preferential *c*-domain orientation is present after equilibration. The samples have not been poled before the XRD-measurement, but have been ground and partially polished followed by equilibration with quenching from 900 °C to *RT*. Thus, the samples should be considered as stressed. The detailed discussion on the influence of heat treatments on the domain orientation will be given after the presentation of the reduced samples.
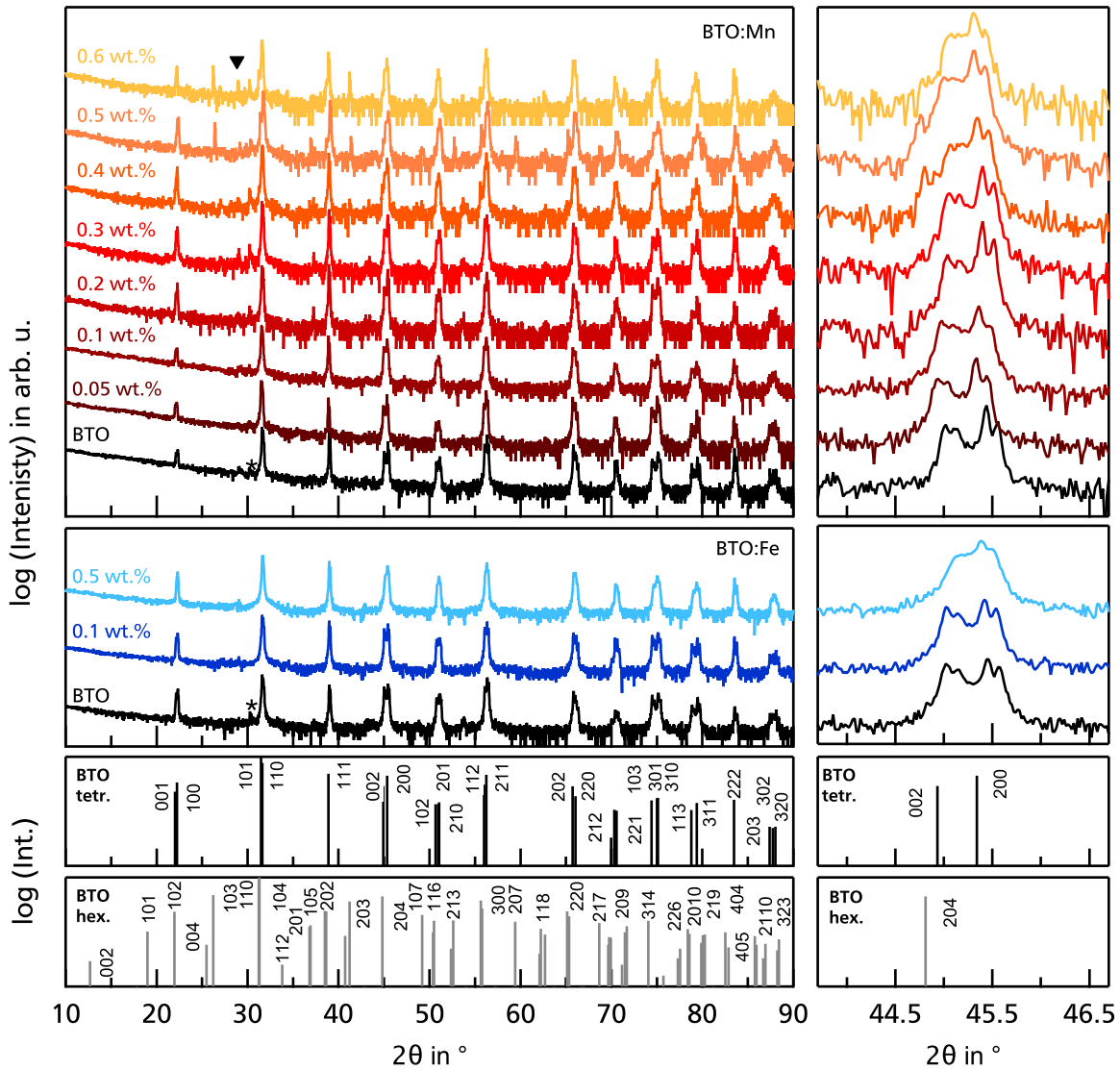
The XRD pattern for reduced Mn- and Fe-doped $BaTiO_3$ are shown in Figure 5.12. All Fe-doped samples exhibit the tetragonal structure. Besides the tetragonal reflections again two small unknown reflections are visible at approximately 28.6 ° and 42.98 °. Mn-doped samples <0.5 wt.% exhibit the tetragonal structure. For higher doping concentrations again reflections from the hexagonal polymorph are observed. As the evaluated samples are pellets, a texture is most likely. Thus, the intensity of specific *t*- and *h*-reflections differs from the powder diffraction pattern and between the samples.

The Zoom-In of the $(002)_t$ and $(200)_t$ reflections shows a change in the reflection intensity when being compared to the equilibrated samples. The observed ratio for the reduced samples is in most cases close to or higher than the experimentally expected value of 1.7. As the samples have been ground and/or polished before reduction and then being quenched from 1100 °C to *RT*, they can also be considered as stressed. In order to explain this observations, the evaluated $(200)_t/(002)_t$ ratio of samples without considerable hexagonal contribution have been plotted against the annealing temperature, as depicted in Figure 5.13. Furthermore the ratios of the sintered powder are given as reference. In addition, the systematical evaluation of the domain orientation of abraded samples in dependence of the annealing temperature (in air) studied by Cutter *et al.* [193] and Khanal *et al.* [191] are added. The samples in the latter publications have been abraded by different SiC papers and diamond particles. As indicated in Figure 5.13 the abrasion results in a $(200)_t/(002)_t$ ratio <2, which means a preferential orientation of *c*-domains to *a*-domains. For both reports, the preferential orientation remained unaffected up

---

[10]The derivation of the experimentally value from the theoretical one might be related to very thin surface layer with enhanced defect concentration, which result in a space charge and a preferred *c*-domain orientation in the topmost surface [192].

to an annealing temperature of approximately 900 °C. Thermal annealing at 1000 °C results in a partial removal of the *c*-domain preference, while higher temperatures results in a complete removal or even a slight *a*-domain preference in the case of Cutter *et al.* [193]. Furthermore, the depth of the distorted surface layer was determined to be approximately 10 μm [193]. Those findings on the surface domain orientation seem to be material independent, as they are

Figure 5.12.: Left: X-ray diffraction pattern of reduced Mn- and Fe-doped BaTiO$_3$. Samples have been reduced at 1100 °C for 12 h in 5 % H$_2$ and have been quenched to *RT*. Right: Zoom-In into the (200)$_t$ and (002)$_t$ reflections. In the lower panel the powder diffraction pattern of BaTiO$_3$ [01-082-1175] - hex. - P63/mmc (gray), ICSD collection code: 075240 and BaTiO$_3$ [01-075-0583] - tetr. - P4mm (black), ICSD collection code: 029280 are displayed. The powder diffraction pattern are only used for phase assignment. The pattern were recorded by Cu K_α radiation with $\lambda_{CuK_{\alpha1}} = 1.5406$ Å filtered by a Sol-X detector. The reflection marked with * at 30.22 ° corresponds to an artificial tungsten reflection, which results from the X-ray tube.

also observed for other materials such as lead zirconate titanate (PZT) [194]. For the latter, also an influence of the finishing particle size was observed. When comparing the present values to the ones derived by the publications, a similar trend is observed. Sintered powders show a $(200)_t/(002)_t$ ratio close to 2, which is in line with literature, as those powers are unstressed and should be randomly orientated. Equilibrated samples have a ratio considerable lower than 2, while reduced samples show a markedly increase in the $(200)_t/(002)_t$ ratio. The scattering of the values is most likely explained by in different surface preparation of the pellets. The Fe-doped pellets have been polished with 1 µm diamond particle finish, while the Mn-doped samples have been (partially) ground by SiC paper. Nevertheless, the mean values of the evaluated XRD pattern follow the trend depicted by the literature values. Thus, an influence of grinding/polishing on the surface domain orientation is assumed, which can be removed by high temperature annealing. Here, the different dwell temperatures for equilibration and reduction are responsible for the observed differences in the $(200)_t/(002)_t$ ratio.

In order to prove the assumption of grinding/polishing influence on the phase and surface domain orientation, the reduced 0.5 wt.% Mn-doped sample in Figure 5.12 has been ground after the first XRD measurement and has then been remeasured. The comparison of both XRD pattern is depicted in Figure A.13 in the Appendix. Both samples show t- and h-reflections with changes in the texture, due to different distribution in the grain orientation of the probed surface as a result of re-grinding. The corresponding $(200)_t/(002)_t$ ratio (marked green in Fig. 5.13) is drastically decreased after re-grinding compared to the reduced sample. Even though the absolute value of the ratio is imprecise due to the rising $(204)_h$ reflection, the trend seems trustworthy. Thus, the grinding/polishing of the samples before heat treatment is most
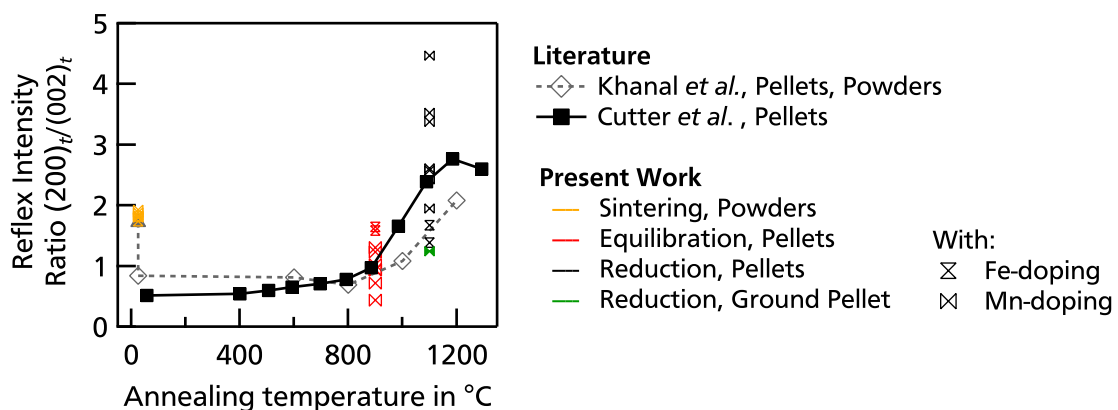
Figure 5.13.: Intensity ratio of the $(200)_t$ and $(002)_t$ reflections of Mn- and Fe-doped samples after sintering, equilibration, and reduction. Only ratios for samples without hexagonal phase are shown as the $(204)_h$ and the $(002)_t$ reflections overlap. The ratios of the present work are compared to the one achieved by Cutter et al. [193] and Khanal et al. [191], who investigated the influence of abrasion on the surface domain orientation of undoped polycrystalline $BaTiO_3$.

likely the reason for the observed changes in the $(200)_t/(002)_t$ ratio upon equilibration and reduction. Here, the annealing temperature is assumed to be the important parameter and not the annealing atmosphere.

Besides the changes in the $(200)_t/(002)_t$ ratio also changes in the intensity ratio of the t- and h-reflections have been observed. As the samples have been measured as pellets, a slight texture is most likely due to the restricted amount of grains being probed. Even though the EBSD evaluation (see Section 5.3) didn't show a preferential orientation, the distribution is not assumed to be as random as for the reference powder diffraction pattern. Therefore, the texture also depends on the specific surface plane being present after grinding/polishing and thus, the pattern of the pellets differ slightly in the reflection intensity ratios.

Due to the texture of the ceramic pellets, a Rietveld refinement on the latter was unfeasible. In order to roughly quantify the amount of tetragonal and hexagonal phase, the average reflection intensity ratio[11] of the hexagonal $(103)_h$ and $(203)_h$ to the tetragonal $(111)_t$ reflection has been evaluated [52, 195]. As this evaluation only includes a straight baseline subtraction and does not include any texture of the samples, an accuracy not better than 10 % is assumed. The percentage of the tetragonal phase as a function of acceptor-doping concentration after sintering, equilibration, and reduction is shown in Figure 5.14. It is clearly observable that the heat treatments lead to a restoration of the tetragonal polymorph, with the reduction being more effective than the equilibration. This observation is inline with literature reports on the influence of sintering and annealing atmosphere on the crystal structure of Mn-doped $BaTiO_3$ [52, 144, 145]. Two aspects need to be considered: one is the different atmosphere (H_2 vs. air) and the other one is the different temperature (1100 °C vs. 900 °C). As the hexagonal phase transition is a reconstructive phase transition, a certain energy is needed. For undoped $BaTiO_3$ the restoration transition between hexagonal to cubic polymorph starts in air at annealing temperatures of about 1050 °C [158]. Thus, the higher temperature of the reduction is most likely one factor being involved. The second aspect is the atmosphere of the heat treatments. Here, the observation that reduction is more effective for the tetragonal restoration of Mn- and Fe-doped $BaTiO_3$ seems to be in contradiction to the observation that undoped $BaTiO_3$ exhibits the hexagonal polymorph after reduction.

Langhammer *et al.* performed similar annealing experiments on Mn-doped $BaTiO_3$ and proposed that the oxidation state of the acceptor, and by this its electron configuration and Jahn-Teller activity, is one major aspect explaining the difference in restoration upon annealing in different atmospheres [52]. From the defect chemistry calculations conducted in this work, a

---

[11] The reflection intensity ratio has been evaluated by normalizing the experimentally derived reflection intensity to the intensity of the powder diffraction pattern of the respective pure phase. The average intensity ratio of the $(103)_h$ and $(203)_h$ to the $(111)_t$ reflection is used.
E.g. $I_{tetr.} = (I_{(111)t}/I^0_{(111)t})/\left((I_{(203)h}/I^0_{(203)h}) + (I_{(111)t}/I^0_{(111)t})\right)$; $I_{(111)t}$ = experimental intensity, $I^0_{(111)t}$ = reference intensity from the PDF of t-$BaTiO_3$.

Figure 5.14: Percentage of tetragonal phase (*RT*) as a function of acceptor concentration for as-sintered powders, equilibrated, and reduced pellets. The nominal concentration x was calculated according to BaTi$_{1-x}A_x$O$_3$ with A=Mn, Fe. The corresponding XRD pattern are shown in Fig. 5.2, Fig. 5.3, Fig. 5.11 and Fig. 5.12.

The phase content has been evaluated by analyzing the intensity ratios of the hexagonal $(103)_h$ and $(203)_h$ to the tetragonal $(111)_t$ reflections assuming no texture of the examined pellets. The accuracy of the percentage data compared to the Rietveld refinement of the as-sintered powders shown in Fig. 5.4 b) is not better than 10 %.
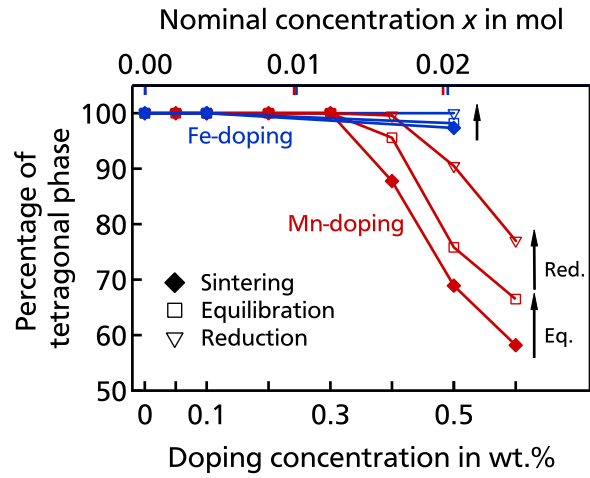
60 % Mn^{3+} / 40 % Mn^{4+} mixture is expected after sintering, where the Jahn-Teller active Mn^{3+} ion promoting the stabilization of the hexagonal polymorph. Oxidation states of 100 % Mn^{2+} and 7 % Mn^{3+} / 93 % Mn^{4+} are expected after reduction and equilibration (see Figure A.3 and Table 5.3), respectively. Thus, for reduced Mn-doped BaTiO$_3$ only the Jahn-Teller inactive Mn^{2+} is present. Furthermore, two different O-sites are present in h-BaTiO$_3$, with the oxygen ion on the O(2)-site in the face sharing ocahedra being more weakly bond than on the O(1)-site in corner sharing ocahedra [52]. Consequently, the oxygen vacancies are preferentially created on the O(2)-site, which are solely present in h-BaTiO$_3$ and not in t-BaTiO$_3$. A high number of oxygen vacancies will destroy the B_2O$_9$ dimers, which might lead to a restoration of the t-BaTiO$_3$ [52]. In addition, the Goldschmidt tolerance factor, which is >1 for Ti^{3+}/Ti^{4+} and Mn^{3+}/Mn^{4+}, decreases to <1 for Mn^{2+} (see Table 5.4). These properties of the Mn^{2+} may favor the restoration of the cubic perovskite phase [52]. In the equilibrated samples a Mn^{3+}/Mn^{4+} mixture is expected, with a significant higher amount of the Jahn-Teller inactive Mn^{4+} ion. Furthermore, the annealing temperature is considerable lower than for the reduction. Thus, the restoration upon equilibration is assumed to be less effective.

For Fe-doping the same argumentation holds. After equilibration a 76 % Fe^{3+} / 24 % Fe^{4+} mixture is expected with Fe^{4+} being a Jahn-Teller active ion. Additionally, a high amount of oxygen vacancies is present in the sample to compensate for the 76 % Fe^{3+}. Thus, the hexagonal phase is not vanishing. After reduction mainly Fe^{2+} is assumed to be present in the samples[12]. As Fe^{2+} is a Jahn-Teller inactive ion, the restoration of the cubic phase is observed.

The different efficiency of 3d-transition metal doping on the stabilization of the hexagonal polymorph of BaTiO$_3$ discussed in Section 5.2 combined with the findings on the annealing

---

[12] See discussion on the oxidation state of reduced Fe-doped BaTiO$_3$ in the Appendix A.2.3.
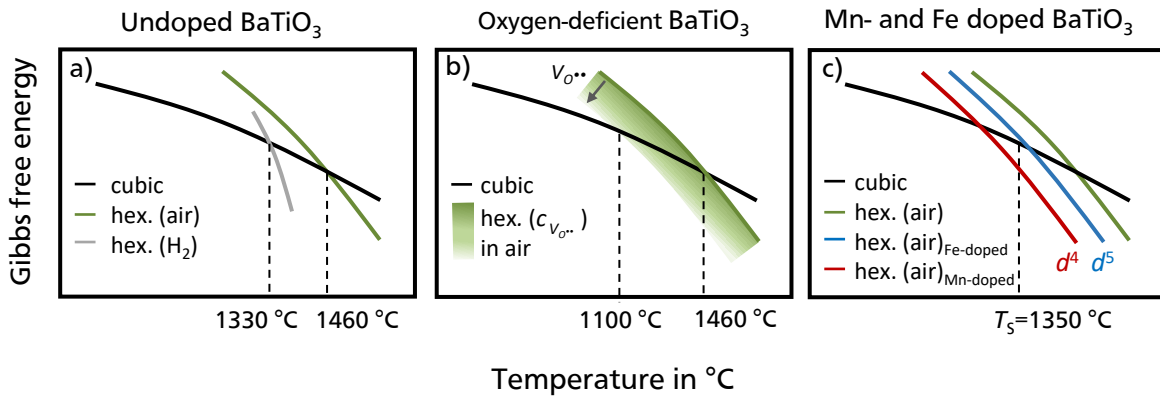
Figure 5.15.: Schematic Gibbs free energy of the cubic and hexagonal polymorph of BaTiO$_3$ as a function of temperature. a) Free energy for undoped BaTiO$_3$ in dependence of the sintering/annealing atmosphere, when assuming that defect equilibrium is reached in the corresponding atmosphere. b) Free energy for oxygen-deficient BaTiO$_3$, with V$_O^{\bullet\bullet}$ being introduced by acceptors/impurities or by reducing atmosphere. The model of oxygen vacancy sensitive free energy of the hexagonal polymorph has been introduced by Glaister and Kay [51]. Figure a) and b) are redrawn and adapted from [51], keeping the characteristic temperatures. The scenario of Glaister and Kay is extended by c) taking into account the sensitivity of the free energy of the hexagonal polymorph on the electron configuration of the acceptors. T_S in c) marks the sintering temperature for present Mn- and Fe-doped samples.

treatments can be summarized in Figure 5.15. For this purpose, the model of Glaister and Kay of oxygen vacancy sensitive free energy of the hexagonal polymorph has been extended [51]. For undoped BaTiO$_3$ the cubic-hexagonal transition can be significantly lowered from 1460 °C for sintering/annealing in air to 1330 °C for sintering/annealing in reducing conditions (hydrogen), as depicted in Figure 5.15 a). Thus, the authors claim that the creation of oxygen vacancies is responsible for the reduction of the free energy of the hexagonal polymorph. Within this model acceptor dopants are assumed to have the same effect as reducing atmosphere, namely the creation of compensating oxygen vacancies and by this lowering of the transition temperature as depicted in Figure 5.15 b).

However, the oxygen vacancy sensitivity of the free energy of the hexagonal phase does not explain the different efficiencies of Mn- and Fe doping. Thus, an extension of the model is included in Figure 5.15 c). Here, the influence of the electron configuration of the 3d-transition metal on the free energy of the hexagonal phase is added. It is assumed that the reduction of the free energy is more pronounced for Jahn-Teller active ions (i.e. d^4 configuration) than for Jahn-Teller inactive ions (i.e. d^5 configuration). Thus, for the determination of the intersection of the cubic and hexagonal Gibbs free energies, which refers to the phase transition temperature, two factors need to be considered. First, the influence of oxygen vacancy concentration and second the influence of the electron configuration of the 3d-transition metal on the free energy of the hexagonal polymorph.

5.6.2. Microstructure

The influence of the heat treatments on the morphology has been evaluated by SEM and EBSD measurements on 0.5 wt.% Mn-doped $BaTiO_3$. As the information on the microstructure is the same for both methods, only the EBSD images are shown in Figure 5.16. The EBSD quality and phase maps are depicted for 0.5 wt.% Mn-doped $BaTiO_3$ after sintering, equilibration, and reduction. The corresponding phase fractions are given in the diagram below the corresponding phase map.

The elongated grains being present after sintering, which refer to the hexagonal phase, are also present in the equilibrated and reduced samples. The phase fraction of the tetragonal to hexagonal phases is slightly decreasing upon equilibration from initially 39 % hexagonal phase to 34 %, respectively. In contrast, for reduced 0.5 wt.% Mn-doped $BaTiO_3$ the amount of hexagonal phase is significantly decreased to 21 %. The evaluated phase fraction by means of EBSD are in agreement with the phase evaluation derived by the reflection intensity ratio calculations of the $(103)_h$ and $(203)_h$ to the $(111)_t$ reflections in the corresponding XRD pattern (see Figure 5.14). For the latter the amount of hexagonal phase seems to be slightly underestimated, which most likely originates from the relatively high inaccuracy due to rough quantification by using
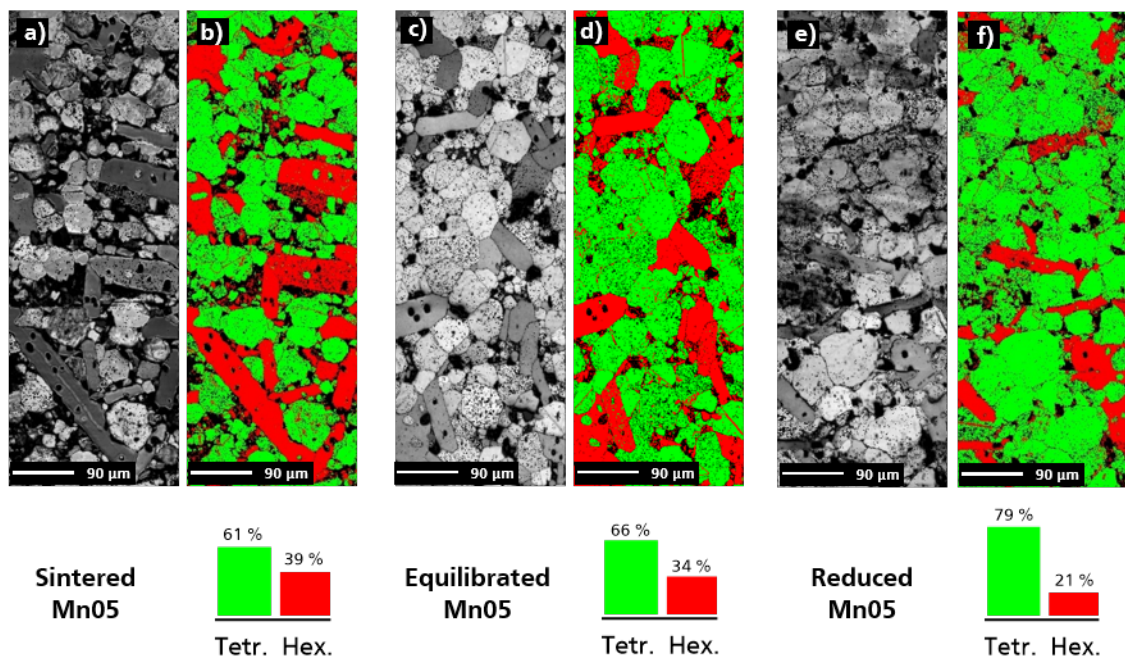

Figure 5.16.: a), c), e) EBSD quality map and b), d), f) phase map of 0.5 wt.% Mn-doped $BaTiO_3$ after sintering, equilibration, and reduction, respectively. Unknown structure is black, hexagonal structure is red and tetragonal structure is green.

only three reflections (due to the texture of the pellets, a Rietveld refinement was unfeasible). However, the recovery of the tetragonal structure is observed by means of XRD and EBSD and, thus, seems to be clearly taking place upon reduction. Besides the recovery of the tetragonal phase, the hexagonal grains are smaller after reduction than the ones observed in the sintered and equilibrated counterparts. Hence, the restoration of h-BaTiO$_3$ to c-BaTiO$_3$ is accompanied by a change in the grain size, which raises two questions.

i. Why and how are the grain size and shape changed during heat treatment?

Here, similar observation have been reported by Langhammer *et al.* during their investigation of the crystal structure and microstructure of Mn-doped BaTiO$_3$ under different annealing treatments [52]. In their work, the changes in microstructure exactly reflects the changes in the crystal structure, which is similar to the EBSD observations for the present 0.5 wt.% Mn-doped BaTiO$_3$ samples. For such high annealing temperatures the recrystallization process starts and for undoped BaTiO$_3$ it is known that annealing temperatures of about 1050 °C are necessary for the restoration of the hexagonal to cubic polymorph [158]. However, the mechanism of the grain growth is inconclusive. At such temperatures a liquid phase assisted mechanism is not expected [52]. Thus, the decreasing grain size of the hexagonal grains and the grain growth of the tetragonal grains should be a totally diffusion-controlled material transport process [52].
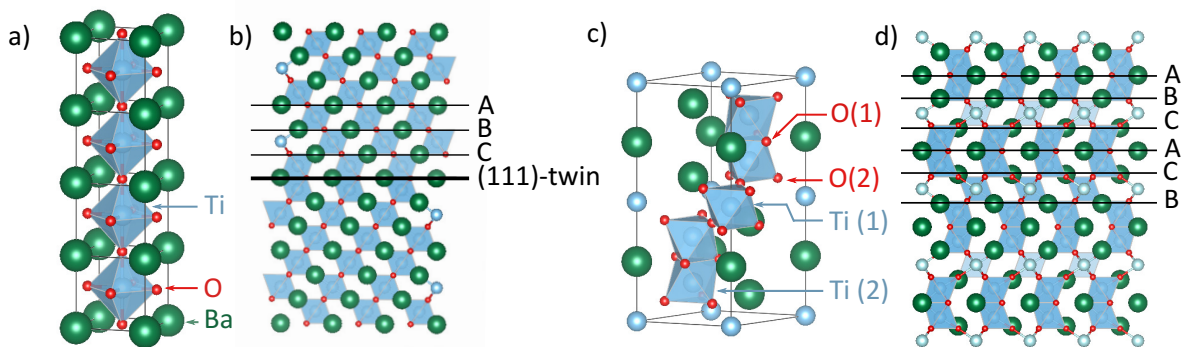
Figure 5.17.: a) Crystal structure of cubic BaTiO$_3$ and b) atomic stacking sequence along the cubic [111] direction. c) Hexagonal crystal structure of BaTiO$_3$ and b) atomic stacking sequence along the hexagonal [001] direction. A (111) twin with a mirror plane is included in b). The structure was created with VESTA [44] and the representation adapted from [196].

ii. What is the mechanism of the reconstructive phase transition from the hexagonal to the cubic phase and vice versa?

The cubic {111} and hexagonal {001} planes have the same chemical composition within the layers [172] as is depicted in Figure 5.17 b) and d). The only difference is the stacking sequence of these planes, which is ABCABC and ABCACB for the cubic and hexagonal phase, respectively.

As already stated, the cubic to hexagonal phase transition is a reconstructive transition, which means that bonds will be broken and reformed. In general two mechanisms are discussed for the transition from c-BaTiO$_3$ to h-BaTiO$_3$. One is the formation of (111) twin boundaries and the other one is the gliding of two lattice planes [196]. The cubic stacking along the [111] direction with a (111) twin boundary mirror plane is shown in Figure 5.17 b). It can be seen that a (111) twin mirror plane in cubic BaTiO$_3$ results in an ABCACB stacking. In addition, a gliding of the B and C layers, would also result in the ABCACB hexagonal stacking depicted in Figure 5.17 d) [52,196]. The latter mechanism is most often favored in literature [52,172,197]. Eibl *et al.* observed Shockley partial dislocations in the hexagonal phase of BaTiO$_3$, which could be responsible for the gliding mechanism and the transition from h-BaTiO$_3$ to c-BaTiO$_3$ [172]. As no twins are observed in SEM images of Mn-doped BaTiO$_3$ ceramics before and after heat treatment, the gliding seems to be the more likely mechanism being involved during the transition of Mn-doped h-BaTiO$_3$ to c-BaTiO$_3$ upon reduction.

5.7. Summary

Within this Chapter the as-sintered Mn- and Fe-doped polycrystalline $BaTiO_3$ samples have been validated by several characterization techniques. The systematic increase of doping-concentration from 0 to 0.6 wt.% was essential to identify trends in crystal structure, microstructure, and di- and ferroelectric properties. Additionally, the influence of annealing atmosphere on the crystal and microstructure has been investigated. Acceptor-doped polycrystalline $BaTiO_3$, and especially Mn- and Fe doping, has been extensively studied in literature due to their relevance for applications. Thus, a high number of articles are available on the influence of Mn- and Fe-doping on fundamental properties such as crystal- and microstructure as well as di- and ferroelectric properties. In the following the main results of this Chapter are summarized and shortly linked to respective literature, if available:

Defect oxidation state: The acceptor-dopants are expected to be incorporated on the *B*-site. For the present sintering conditions (1350 °C, 6 h in air) defect chemistry calculations for 0.5 wt.% doped samples revealed that Fe is pre-dominantly present as Fe^{3+}, while Mn is present as a 60 % Mn^{3+} / 40 % Mn^{4+} mixture. Thus, for the same acceptor-doping concentration Fe is expected to create more $V_O^{\bullet\bullet}$ than Mn. The different average oxidation state of Mn- and Fe-dopants for the similar sintering conditions is consistent with literature reports [46, 55, 198]. Oxidation states of 100 % Mn^{2+} and 7 % Mn^{3+} / 93 % Mn^{4+} are expected after reduction and equilibration, respectively. After equilibration a 76 % Fe^{3+} / 24 % Fe^{4+} mixture, while after reduction mainly Fe^{3+} is expected.

Crystal structure: The introduction of transition-metal acceptor-dopants leads to a partial *RT*-stabilization of the high temperature hexagonal polymorph. The threshold value for the present sintering conditions is between 0.3 - 0.4 wt.% for Mn-doping and slightly below 0.5 wt.% for Fe-doping. For 0.5 wt.% doped samples, 38 % hexagonal phase are observed for Mn-doping, while only 3 % hexagonal phase are observed for Fe-doping. The stronger stabilization of the hexagonal phase upon Mn-doping is well known in literature [51–56]. The threshold values observed in this work are in the same order of magnitude as have been reported in literature. The results of this Chapter support the model of Langhammer and co-workers, who proposed a Jahn-Teller induced stabilization of the hexagonal phase [52, 55, 151, 160]. Mn^{3+} has a d^4 electron configuration and is *JT*-active, while Mn^{4+} and Fe^{3+} have a d^3 and d^5 electron configuration, respectively, and are *JT*-inactive. Hence, *JT*-active Mn^{3+} is expected to be responsible for the stabilization of *h*-$BaTiO_3$ [52]. The tetragonality for nominally undoped $BaTiO_3$ of approximately $c/a = 1.01$ is consistent with literature values [148–150]. The tetragonality remains almost unaffected upon Mn-doping and decreases approximately linearly from 1.01 to 1.005 upon Fe-doping, which is in accordance with literature reports [133, 148].

Microstructure: SEM images of both undoped BaTiO$_3$ batches revealed a considerable bigger grain size of the second batch. This could potentially originate from a different *A/B*-site ratio or impurities, which can lead to liquid phase assisted sintering. Fe-doping leads to a drastic decrease in grain size with a bimodal distribution ($< 5\,\mu m$). An increasing acceptor-ion and/or oxygen vacancy concentration is expected to have a considerable influence on the space charge regions at the grain boundaries, which could lead to a solute drag effect, i.e. a decreased grain boundary motion during the sintering process, resulting in a lower grain size [138]. Low Mn-doping leads to a decrease in grain size, while higher Mn-doping leads to a bimodal grain size distribution with elongated grains ($> 200\,\mu m$). EBSD revealed that all elongated grains exhibit the hexagonal structure. The appearance of elongated grains with rising hexagonal phase fraction is well known in literature [52, 56, 139]. Most likely, the difference in surface energy of the different hexagonal planes is responsible for the anisotropic grain growth [173, 174] .

Dielectric properties: The *RT* dielectric constant slightly decreases from 1900 to ~ 1600 upon Fe-doping and ≤ 0.3 wt.% Mn-doping. For higher Mn-doping concentrations the hexagonal phase rises and the *RT* dielectric constant decreases approximately linearly to 515. The Curie point of undoped BaTiO$_3$ of 130.7 °C is in agreement with literature reports [41] and only slightly decreases by approximately 5 °C upon Mn-doping, while a drastic decrease of 40 °C is observed upon Fe-doping. The observed different influence on the phase transition temperature of both dopants is consistent with literature reports for similar sintering conditions [27, 46, 47, 134–137]. The higher decrease of the Curie point upon Fe-doping is most likely attributed to the higher amount of oxygen vacancies and the decrease in tetragonality. The low decrease of the Curie point upon Mn-doping might be related to the presence of the *JT*-active Mn^{3+} ion, which has a stabilizing effect on the distorted tetragonal structure [47].

Ferroelectric properties: P_R at 50 Hz decreases from initially $\approx 8\,\mu C/cm^2$ for undoped to close to $0\,\mu C/cm^2$ for ≥ 0.5 wt.% Mn- and Fe-doped samples. The introduction of $A_{Ti}{}'$ acceptors and the creation of $V_O^{\bullet\bullet}$ most likely results in the formation of $(A_{Ti}{}'\text{-}V_O^{\bullet\bullet})^{\bullet}$ defect complexes, which lead to a domain wall pinning and ferroelectric hardening [43, 140].

Annealing atmosphere: Grinding/polishing seems to induce a surface *c*-domain orientation. In accordance to literature, temperatures above 1000 °C are necessary to remove the *c*-domain orientation [193]. The reduction treatment seems to be more efficient for the restoration of the tetragonal phase, which is consistent with literature reports on Mn-doped BaTiO$_3$ [52, 144, 145]. For 0.5 wt.% Mn-doped BaTiO$_3$ the percentage of tetragonal phase increased from 61 % for sintered to 66 % for equilibrated and to 79 % for reduced samples. The restoration of the cubic/tetragonal phase is accompanied by a change in grain size and a total rearrangement, resulting in size reduction of the hexagonal grains.

The characteristics of Mn- and Fe-doped polycrystalline $BaTiO_3$ summarized above coincide with the corresponding literature reports on this field. Hence, the synthesized Mn- and Fe-doped $BaTiO_3$ samples satisfy the expected literature standards and can be used for the main experiments planed in this work. For the elaboration of the interface and re-oxidation approach as well as the resistance degradation experiments the following properties of the samples are again highlighted, as they may have non-negligible influence on the interpretation of the results of following Chapters:

⇒ The extracted oxidation states from the defect chemistry calculations reveal considerable different average valencies for Mn and Fe. Especially, the incomplete reduction of Fe upon reduction will play a major role in the interpretation of the re-oxidation experiments.

⇒ From the results of the XRD measurements it remains unclear, whether the acceptor dopants are dissolved homogeneously in both phases. An inhomogeneous distribution of acceptor dopants influences the charge neutrality conditions in the respective phases, which should be considered when discussing the re-oxidation experiments.

⇒ Grain boundaries in acceptor-doped $BaTiO_3$ have a blocking character for positively charged carriers [79]. Hence, the grain size distribution of the Mn- and Fe-doped samples is of particular importance for the validation of the re-oxidation approach and the degradation characteristics. Especially the appearance of elongated grains ($> 200\,\mu m$) for highly Mn-doped $BaTiO_3$ should be kept in mind.

⇒ The dielectric constant is of particular importance for the simulation of the space charge potentials (see Poisson Equation). The recorded $\epsilon(T)$ data is interpolated according to the Curie-Weiss law and is used for the grain boundary conductivity simulations. The *RT* dielectric constant is used for the simulation of the space charge potential at the interface. Here, it should emphasized, that the lateral position of the PES spot could be of particular importance. Hexagonal grains are expected to have a considerable lower ϵ than tetragonal grains, which could result in considerable different space charge characteristics.

Due to the great interest of the community in Mn- and Fe-doped $BaTiO_3$, a high number of articles is available - especially in the filed of basic characterization methods. Hence, the results summarized above do not represent new experimental findings. Nevertheless, the present comprehensive study on the Mn- and Fe-doping series could contribute to a better understanding of the stabilization of the hexagonal phase. Five different mechanisms have been reviewed from literature and discussed with regard to their plausibility. The present result support the theory of Langhammer and co-workers, who proposed a Jahn-Teller-induced stabilization of hexagonal $BaTiO_3$.

Additionally, the combined results of XRD and $\epsilon(T)$ reveal an extended stability range of the cubic phase upon Fe-doping, while it is reduced upon Mn-doping. None of the literature reports embraces the appearance of h-$BaTiO_3$ in combination with changes in T_C. The present work

proves that both observations can be explained by the theory of *JT*-active ions, which has separately been proposed by Langhammer and co-workers [52, 55, 151, 160] for the stabilization of *h*-BaTiO$_3$ and by Hagemann and Ihrig [46] followed by Desu *et al.* [47] for the changes in T_C. Additionally, several studies show a strong correlation between hexagonal BaTiO$_3$ in XRD pattern and elongated grains in SEM pictures. To the author's best knowledge, no EBSD measurements have been available so far. Here, the present EBSD measurement on 0.5 wt.% Mn-doped BaTiO$_3$ doubtless confirm this correlation.

6. Defect level identification in polycrystalline acceptor-doped BaTiO$_3$ using the interface approach

Several parameters, such as temperature and voltage, density, grain size, type of dopant as well as the dielectric - electrode interface have an essential influence on the electrical resistance degradation of BaTiO$_3$-based ceramic capacitors. The properties of the dielectric - electrode interface in particular are important for the electron injection and the possibility of oxygen exchange from the dielectric through the electrode. Both, the charge carrier injection and the oxygen exchange are affected by the barrier height, which is defined as the difference of the Fermi energy at the interface and in the bulk, and the resulting space charge region [16]. Well-directed modifications of the Fermi level at the interface and in the dielectric bulk are assumed to result in controllable tuning of the interface properties and thereby of the resistance degradation.

In previous works it has been shown that the interface Fermi level position can be varied by more than 1 eV [30] with low work function Sn-doped In$_2$O$_3$ and high work function RuO$_2$ as contact materials. Ionic defects in BaTiO$_3$ are immobile [27, 78] at *RT* and, thus, the Fermi level in the bulk remains unaffected upon contact formation. However, the latter can be modified by either the introduction of acceptor-dopants with different concentrations and/or by modifying the V$_O^{\bullet\bullet}$ concentration by use of oxidized, equilibrated, and reduced specimens. The evaluation of the Fermi level during Schottky barrier formation is straight-forward by means of X-ray photoelectron spectroscopy. The interpretation of the measured Fermi level, however, is dependent on the inelastic mean free path (see Figure 3.17) of the photoelectrons in comparison to the SCR inside the bulk material. If the resulting SCR width in BaTiO$_3$ is comparable to the inelastic mean free path (and the tunneling distance of electrons), the binding energies measured by XPS do no longer reflect the Fermi level directly at the interface [14, 199]. For extreme defect concentrations, the width of the SCR can become less than 1 nm and the resulting XPS binding energies might reveal a Fermi energy close to that in the bulk of the material [200]. In the latter scenario, the narrow SCR enables the study of the bulk Fermi level and thereby it should be possible to reveal the energy levels of defects in the band gap.

This Chapter addresses the first main objective of this work and has the aim to elaboration if it is possible to access the defect energy levels of acceptor-doped polycrystalline BaTiO$_3$ by XPS measurements during interface formation. For this purpose, the Schottky barrier formation during contact formation to *RT*-deposited RuO$_2$ and Sn-doped In$_2$O$_3$ has been studied for nominally undoped and Mn-doped BaTiO$_3$ ceramics with different V$_O^{\bullet\bullet}$-content. The resulting energy band diagrams are simulated based on the experimentally derived values for the Schottky barrier formation by solving the Poisson equation. The following modifications of the surface and bulk Fermi levels have been expected:

- **Influence of electrode material on the interface Fermi level of BaTiO$_3$:** RuO$_2$ has an effective work function of 5.6 eV [201], while *RT*-deposited Sn-doped In$_2$O$_3$ typically has a work function of 4.2 eV to 5.5 eV, which depends on the E_F(*RT*-ITO) [202, 203]. Assuming 3.9 eV for the electron affinity of BaTiO$_3$ [204], the expected Schottky barrier for electrons, defined by the Schottky-Mott rule given in Equation 3.17, is 1.7 eV for the BaTiO$_3$/RuO$_2$ and 0.6 eV for the BaTiO$_3$/ITO interfaces (assuming ϕ(*RT*-ITO) = 4.5 eV).

- **Influence of the Mn-doping and oxidation state on the bulk Fermi level of BaTiO$_3$:** The interface formation has been studied for different Mn- and V$_O^{\bullet\bullet}$-content. The introduced Mn-doping concentration of up to 3.3×10^{20} cm^{-3} is assumed to be sufficient for a considerable bulk Fermi level pinning on the Mn charge transition levels. For the reduced specimens the bulk Fermi level is expected to be close or even inside the conduction band. For the equilibrated and oxidized specimens the bulk Fermi level is expected to be pinned on the Mn charge transition levels inside the band gap. The latter is, of course, only expected for the Mn-doped samples and not for the nominally undoped BaTiO$_3$.

The space charge region width is the essential parameter, which defines whether the measured Fermi level using XPS refers to the interface or to the bulk Fermi level. On the basis of the introduced defect concentrations and on previous works on Fe-doped SrTiO$_3$/RuO$_2$ interfaces [14] the following output of the present experiments has been expected:

- **Expected SCR width:** The high Mn and V$_O^{\bullet\bullet}$ defect concentrations are assumed to narrow the space charge region < 1 nm. In this case, the measured Fermi level by means of XPS would rather correspond to the bulk Fermi level and an identification of the manganese charge-transition levels by the evaluation of the measured Fermi level was expected.

Before the interface experiments, the bare specimen surface has been examined to identify possible contamination and to study the influence of the reduction/equilibration on the composition. Additionally, selected interfaces have been post-heated at elevated temperatures in different atmospheres to promote diffusion and, thus, changes of the space charge region width. More over, *RT* voltage experiments have been performed to exclude any impact of the X-rays on the oxygen diffusivity.

6.1. Analysis of bare Mn-doped BaTiO$_3$ ceramic surfaces

Before electrode deposition, the samples were cleaned by heating in one of the deposition chambers of the DAISY-Mat system. In order to maintain the oxidation states after the *ex situ* annealing, the cleaning procedure was different for reduced and equilibrated samples. Reduced samples have been heated for at least 1 h at 500 °C in vacuum (1×10^{-8} mbar), while equilibrated samples have been heated for at least 1 h at 400 °C in 5×10^{-3} mbar oxygen.

In order to track and evaluate the efficiency of the different cleaning processes, core level and survey spectra of equilibrated 0.1 wt.% Mn-doped BaTiO$_3$ have been recorded before and after oxygen cleaning and are compared to vacuum cleaned reduced 0.1 wt.% Mn-doped BaTiO$_3$. In addition, Ar-sputtering was conducted on the clean surfaces of equilibrated 0.1 wt.% Mn-doped BaTiO$_3$. The corresponding XP-survey spectra are shown in Figure 6.1 in the lower panel. A magnification on the binding energy regions of the Ca, C, and Si impurities is given on the right. In addition, the XP-survey spectra of cleaned reduced and reduced and ground 0.5 wt.% Mn-doped BaTiO$_3$ are shown in Figure 6.1 in the upper panel.

As the equilibrated as-is sample is measured without further cleaning treatment, the surface is highly carbon contaminated, recognizable by a large C 1s peak. Thus, the signal of the sample emissions (Ba, Ti, O) is significantly suppressed and only the high intensity emissions such as Ba 3d, Ti 2p, O 1s and Ba 4d are clearly visible in the survey spectra. After surface cleaning for 1 h at 400 °C in 5×10^{-3} mbar oxygen the C 1s disappeared, which confirms that the carbon species are effectively removed from the surface. The XP-spectra of cleaned equilibrated 0.1 wt.% Mn-doped BaTiO$_3$ contains the common core level and Auger emissions of the substrate elements Ba, Ti, and O. In addition, impurity Ca 2s and Ca 2p emissions are observed. In order to evaluate, if Ca can be removed by further heating, a second cleaning for 1 h at 400 °C in 5×10^{-3} mbar oxygen was conducted. However, the peak intensity of the Ca emissions remained constant upon second heating. Thus, Ar-sputtering has been conducted for depth profiling. The surface has been removed in two sputtering steps by ~10 nm and ~30 nm. The Ca emissions remained unaffected after both treatments. Furthermore, Pt 4f and Pt 4d emission are observed, which most likely originate from the platinum on the edge of the samples[1]. Thus, it can be concluded that 1 h at 400 °C in 5×10^{-3} mbar oxygen is sufficient to remove the carbon species. However, the samples contain a Ca contamination/impurity[2], which couldn't be removed by neither heating in oxygen nor Ar-sputtering.

---

[1]The Pt on the edge of high resistive BaTiO$_3$ samples is needed to ensure a good contact of the thin electrodes (which are used during interface studies) to the samples holder.

[2]No distinct Ca impurity of this magnitude has been determined in the test ICP-OES measurement on 0.3 wt.% Mn-doped BaTiO$_3$ nor in the EDX analysis of the Mn-doped samples. Thus, it remains unclear whether Ca is only present at the surface or also in the bulk. As possible origin the grinding/polishing process is proposed as the emission intensity of Ca decreased, after using new polishing equipment (which was at first cleaned using tap water).

In contrast, the vacuum cleaning procedure for reduced $BaTiO_3$ samples is less efficient in removing the carbon species. This can most likely be explained by the fact, that the carbon species at the surface can form CO_2 in the presence of oxygen, which is more efficient for removal [205]. However, the usage of oxygen would re-oxidize the surface region of the reduced samples. The intensity of the C 1s emission is decreasing, but not vanishing, after heating for 1 h at 500 °C in vacuum (1×10^{-8} mbar). In addition to the remaining carbon contamination,
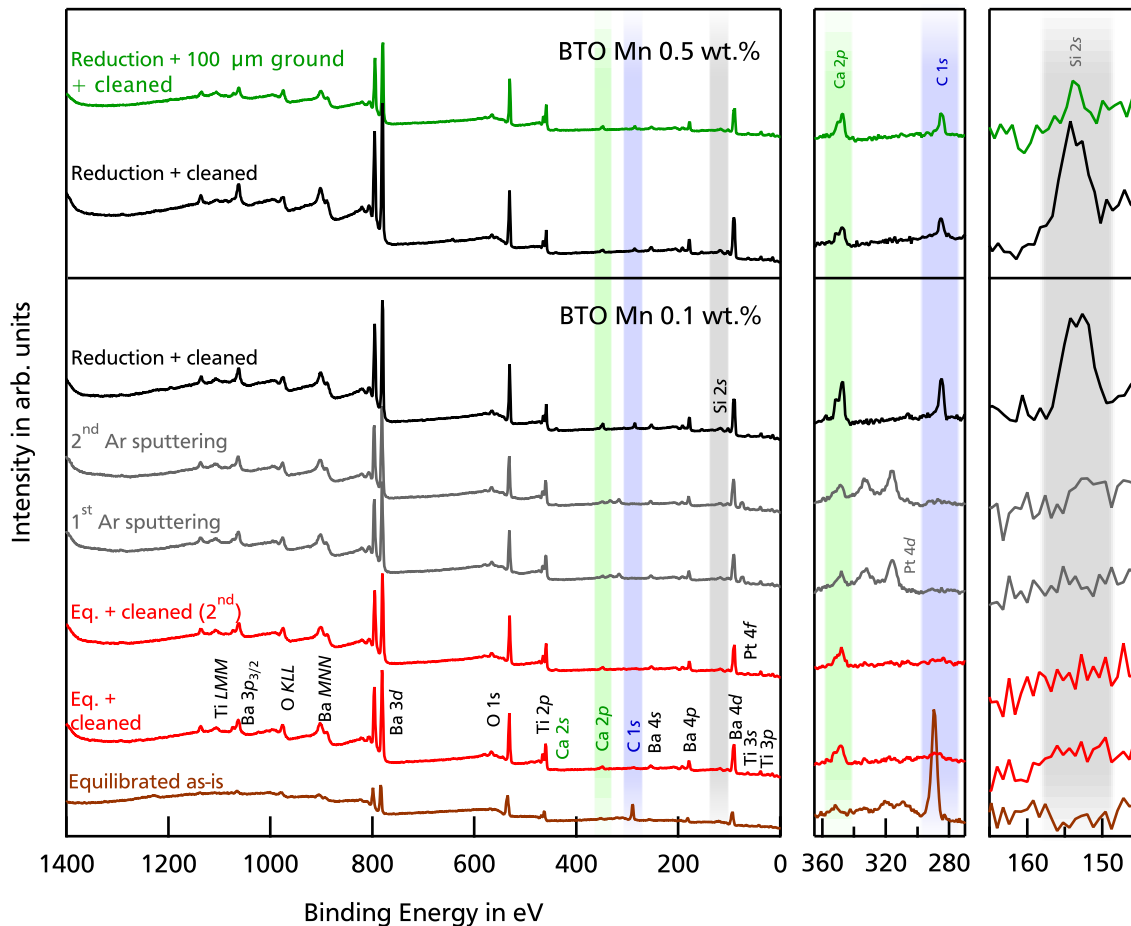
Figure 6.1.: X-ray photoelectron survey spectra of 0.1 wt.% Mn-doped $BaTiO_3$ before and after different heat- and cleaning-treatments (lower panel). X-ray photoelectron survey spectra of cleaned reduced and reduced-ground 0.5 wt.% Mn-doped $BaTiO_3$ (upper panel). The Ca, Si, and C impurities are magnified on the right for better evaluation. All spectra have been recorded with monochromatic Al K_α radiation. Equilibrated samples have been measured using a neutralizer. The labels in the graph refer to the following treatments: Equilibrated as-is: as introduced to the vacuum system without further treatment; Eq.+cleaned and Eq.+cleaned (2nd): clean heating for 1 h and 2 h at 400 °C in 5×10^{-3} mbar oxygen, respectively; 1st and 2nd Ar-sputtering: stepwise surface removal of ~10 nm and ~30 nm using Ar-sputtering; Reduction+cleaned: clean heating for at least 1 h at 500 °C in vacuum (1×10^{-8} mbar); Reduction + 100 μm ground + cleaned: surface removal after reduction by grinding and polishing followed by clean heating in vacuum.

again emissions of Ca are detected on the surface. Furthermore, a Si 2s emission is observed for reduced 0.1 wt.% and 0.5 wt.% Mn-doped BaTiO$_3$. The reduction was conducted in a quartz (SiO$_2$) tube at 1100 °C with the samples being in direct contact to the tube. Thus, it is most likely that the Si impurity originates from the reduction setup. This is confirmed by the removal of 100 μm surface after reduction for which the intensity of the Si emission decreased markedly to close to zero.

The Ba/Ti ratio of the samples has been calculated using the Ba 3d$_{5/2}$ and Ti 2p emission lines and is presented in Figure 6.2. The composition evaluation of the dirty specimen is most likely affected by the high carbon contamination, showing a Ba/Ti ratio lower than one. The equilibrated and Ar-sputtered specimens exhibit a Ba/Ti ratio of approximately one, while the reduced samples exhibit a Ba/Ti ratio significantly higher than one, indicating a Ba-rich surface. Furthermore, the Ba-enrichment seems to be higher for higher Mn-doping concentrations. In contrast, the reduced and ground 0.5 wt.% Mn-doped BaTiO$_3$ specimen exhibits a Ba/Ti ratio below one. Thus, the Ba-rich surface seems to be removed by grinding the samples after reduction treatment. Either the bulk of reduced samples is Ba-deficient (as Ba/Ti<1) or the Ba/Ti ratio below one results from the remaining carbon contamination due to the incomplete cleaning of reduced samples in vacuum, which results in a stronger suppression of the Ba 3d$_{5/2}$ emission.

In summary, it can be stated that the cleaning procedure of equilibrated samples in oxygen successfully removed the carbon species from the surface. In order to avoid surface re-oxidation the reduced samples have been cleaned by heating in vacuum, which revealed to be less effective resulting in an incomplete carbon removal. For all samples a Ca contamination/impurity has

Figure 6.2: Ba/Ti ratio as a function of Mn-doping concentration for the samples shown in Figure 6.1 and additional reduced and reduced and ground specimens. The Ba/Ti ratio has been obtained from the integrated intensities of the Ba 3d$_{5/2}$ and Ti 2p core level emission lines and respective spectrometer sensitivity factors [126] according to Equation 3.6. The specimens have been reduced by annealing for 12 h at 1100 °C in Ar/H$_2$ and were measured before (black) and after (green) removal of the 100 μm surface layer by grinding/polishing.
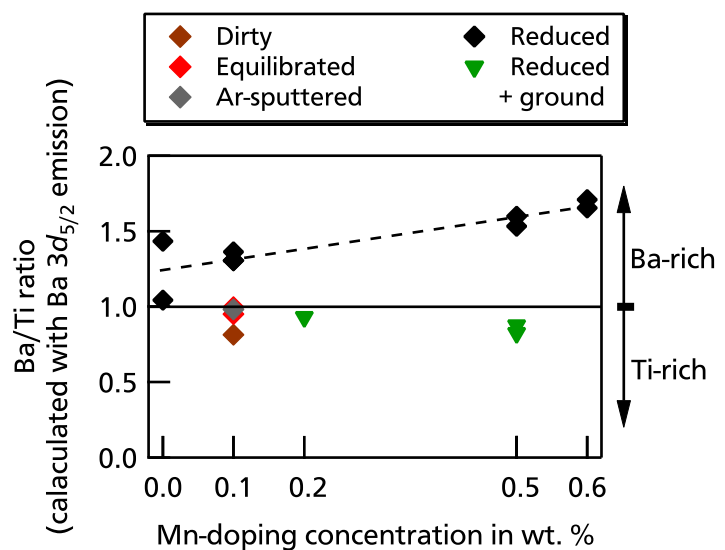
been observed on the specimen surface. If this result reflects only a surface contamination due to processing or if Ca is present as an impurity in the bulk remains unclear. In addition, reduced samples exhibit a Si contamination, which is most likely originating from the heat treatment in reducing atmosphere at elevated temperatures in a quartz tube. The Si contamination can be (partially) removed by grinding the surface after reduction.

Cleaned equilibrated 0.1 wt.% Mn-doped $BaTiO_3$ exhibits a Ba/Ti≈1, while cleaned reduced Mn-doped $BaTiO_3$ reveals a Ba/Ti>1, indicating a Ba-rich surface. The magnitude of the latter seems to be Mn-doping concentration dependent. Grinding of the reduced surface results in a removal of the Ba-rich surface and Ba/Ti<1. It is questionable if this indeed indicates a Ba-deficiency or if it is a result of the remaining surface contamination after vacuum cleaning.

6.1.1. Surface properties of reduced Mn-doped BaTiO$_3$ ceramics[3]

The altered surface stoichiometry of Mn-doped $BaTiO_3$ upon reduction could be an indication for the formation of secondary phases, which can affect the barrier formation to the electrodes. Cations are mobile at temperatures of 1100 °C, which were used for reduction, possibly resulting in the formation of secondary surface phases [16, 207, 208]. Thus, the surface stoichiometry of reduced specimens with different Mn-doping concentrations are of specific interest in order to set the baseline for the following electrode interface formation analysis. In order to identify a possible secondary phase, the core level spectra have been studied in a first step.
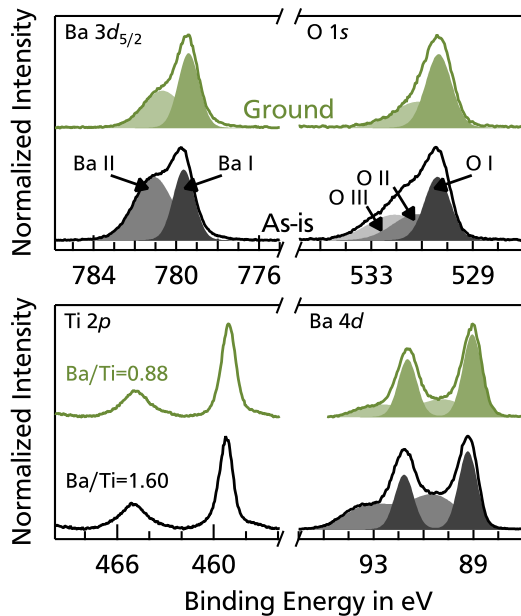
The spectra of the background subtracted and normalized Ba $3d_{5/2}$, O $1s$, Ti $2p$, and Ba $4d$ emissions of reduced 0.5 wt.% Mn-doped $BaTiO_3$ samples before and after removal of the surface layer by grinding are shown in Figure 6.3. Both Ba peaks exhibit a Ba I and Ba II component, which are indicated by the darker and lighter filling of the respective curve fits. This double peak structure of the Ba emissions is well known for $BaTiO_3$ and is commonly assigned to a bulk (Ba I) and a surface emission (Ba II) [209–215]. The intensity ratio of the Ba II/Ba I components of the ground specimen corresponds well with those observed for $BaTiO_3$ single crystals. The O $1s$ emission of the ground specimen exhibits an asymmetry towards higher binding energies, which is also observed for clean single crystalline $BaTiO_3$ [216]. According to literature, the O I component is assigned to bulk oxygen in the perovskite structure, while the origin of the asymmetry (O II) is unclear. Here, a possible origin for the O II component could be adsorbed oxygen.

The Ba $3d_{5/2}$, Ba $4d$, and O $1s$ emission spectra recorded before and after removal of the surface layer by grinding are noticeably different. The O $1s$ emission of the non-ground specimen is substantially more broadened towards higher binding energies, indicated by the third component

---

Figure 6.3.: Normalized X-ray photoelectron core level spectra of a reduced 0.5 wt.% Mn-doped $BaTiO_3$ sample before (black) and after (green) removal of the 100 μm surface layer by grinding/polishing. Background subtraction and normalization were performed for better comparison. Curve fitting was conducted for Ba and O emissions using Gauß-Lorentz functions. The derived Ba/Ti ratio calculated with the Ba $3d_{5/2}$ emission is given for both samples in the Ti $2p$ spectrum.

O III. The surface related high binding energy components Ba II of both Ba emissions are significantly higher before removal of the surface layer. Moreover, the Ba/Ti ratio, obtained from the integrated intensities of the Ba $3d_{5/2}$ and Ti $2p$ core level emissions and the respective spectrometer sensitivity factors [126] calculated according to Equation 3.6 differs by almost a factor of 2, which indicates a substantial enrichment of Ba after reduction.

The composition analysis of the Ba/Ti ratio of reduced $BaTiO_3$ specimens with different Mn-concentrations calculated using the Ba $3d_{5/2}$ and the Ti $2p$ core level emission lines is depicted in Figure 6.2. The evaluation revealed a higher Ba-enrichment for higher Mn-doping concentrations (already taking into account the high scatter of some values). Independent on the Mn-concentration, surface grinding after reduction results in a removal of the Ba-rich surface phase and in a Ba/Ti ratio slightly lower than one. Furthermore the evaluation of the Ba/Ti ratio using the less surface sensitive Ba $4d$ (and Ti $2p$) core level emission lines revealed a similar trend, but with a lower magnitude for the Ba-enhancement.

The chemical nature of the surface phase forming during reduction remains unclear. Potential phases, which might occur are BaO, $BaCO_3$, $Ba(OH)_2$, $BaTi_2O_4$ or Ruddlesden-Popper phases with incorporated additional BaO layers. The latter have been observed for $BaTiO_3$ thin films [217]. In contrast, the solubility of BaO in $BaTiO_3$ has been reported to be below 0.1 % for bulk samples sintered in air [218]. Samples with higher BaO excess exhibit secondary Ba_2TiO_4 phases (see $BaO–TiO_2$ phase diagram in Figure A.1). However, a higher solubility for the highly reducing conditions during the reduction treatment used in this work cannot be excluded. The formation of $Ba(OH)_2$ and $BaCO_3$ is also not likely, as hydroxides are usually not stable at higher temperatures and the observed carbon contamination in the survey is too low to explain the intensities of the additional Ba and O components of the reduced samples. Furthermore, the binding energy of the C $1s$ emission at ∼ 285 eV does not match with a $BaCO_3$ phase, where

the C 1s emission is expected at $\sim$289 eV [126, 219, 220]. The binding energy distance between the Ba II component of the Ba 3$d_{5/2}$ emission and the O III component of the O 1s emission is $\Delta E_{\text{Ba II–O III}} = 249.02$ eV for the reduced 0.5 wt.% Mn-doped BaTiO$_3$ specimen depicted in Figure 6.3. The literature values for the distance of the latter core levels for BaO formed on Ba metal during oxidation differ significantly from 249.2 eV to 251.2 eV [219, 221]. Still, the additional Ba and O components for reduced BaTiO$_3$ could correspond to the formation of BaO at the surface. However, the formation of a BaO phase of acceptor-doped material under reducing conditions is unusual, as cation vacancy formation is generally favored under oxidizing conditions and for donor-doped materials [60–64]. Such a behavior has been documented for SrTiO$_3$ [16, 207, 222] and Na$_{1/2}$Bi$_{1/2}$TiO$_3$-BaTiO$_3$ [223].

Moreover, scanning electron microscopy images reveal small particles at the surface of the reduced specimen (see Figure 6.1.1 on the right). The coverage of the particles is estimated to be less than 10 % of the total surface area, which is not enough to explain the increased intensity of the Ba II components and the appearance of the third high binding energy component O III in the O 1s emission of reduced specimens. Therefore, it is assumed that the Ba-rich surface phase is homogeneously covering the reduced surface. This is consistent with the higher intensity of the surface related Ba II component of the Ba 3$d_{5/2}$ compared to the Ba 4$d_{5/2}$ emission, which is related to the higher surface sensitivity of the former. Based on the Ba II/Ba I intensity ratios, the thickness of the Ba-rich surface phase is estimated to be 1 nm to 2 nm.

 A possible origin of the formation of the Ba-rich surface phase may be related to the formation of a surface space charge region. Oxygen vacancies will have lower formation enthalpies at the surface than in the bulk (see e.g. Ref. [224]), which results in a higher concentration of oxygen
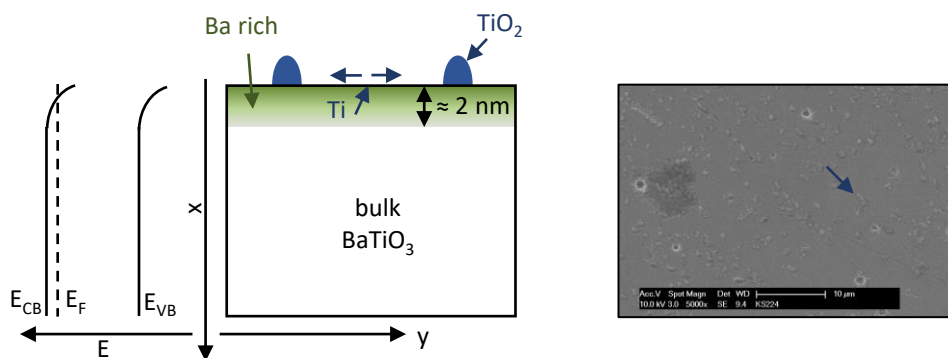
Figure 6.4.: Energy band diagram (left), schematic composition (middle) and SEM image (right) of 0.5 wt.% Mn-doped BaTiO$_3$ reduced by annealing at 1100 °C in Ar/H$_2$. Surface oxygen vacancies generate a positively charge surface. As the Fermi energy is already close to the conduction band in the bulk after reduction, a two-dimensional electron gas can form at the surface, which could results in the formation of Ti vacancies. The Ti atoms diffuse to the surface, form TiO$_2$ precipitates and leave behind a Ba-rich surface phase. Picture adapted and extended from [206].

vacancies at the surface. This leads to a positive surface charge and consequently to a downward band bending towards the surface (see Figure 6.1.1 on the left). The Fermi energy in the bulk of the reduced sample is already close to the conduction band. Due to the resulting downward band bending the Fermi level will cross the conduction band and the surface will become highly degenerate. This would be consistent with the very high Fermi energies observed by XPS at the reduced surfaces and the formation of Ti^{3+} species, which is evident from the small peak at low binding energies in the $Ti\,2p$ spectra in Figure 6.3. The formation of a degenerate surface is furthermore consistent with the observations of two-dimensional electron gases at $SrTiO_3$ and $BaTiO_3$ surfaces [225, 226], which have been assigned to surface oxygen vacancies.

The high Fermi energy at the surface will lower the formation enthalpy of cation vacancies. Density functional theory calculations [65, 66] and defect chemical measurements of donor-doped samples [60–64] reveal, that $BaTiO_3$ will form B-site (Ti) vacancies rather than A-site (Ba) vacancies. The formation of Ti vacancies will proceed by segregation of Ti to the surface, where it forms TiO_2 particles and leaves behind a Ba-rich surface phase. Such a scenario is consistent with all experimental observations and with the formation of Ti-rich precipitates in donor-doped $BaTiO_3$ [227]. The resulting surface chemical structure is illustrated in Figure 6.4 in the middle. EDX analysis on the surface of the sample being depicted in Figure 6.4 on the right did not confirm a Ti-enrichment, but rather indicates a Ba-enrichment of both, the surface and the precipitates. However, the close energetic position of the Ti $K\alpha$ and Ba $L\alpha$ results in a high inaccuracy[4] and a reliable quantification of both elements is not possible. Nevertheless, an enhanced Si content[5] is observed in some of the precipitates.

Another possible origin of the Ba-rich surface may be related to the recovery of the hexagonal to the tetragonal phase during reduction, which was observed by XRD and EBSD measurements. The recovery is a reconstructive phase transition, assuming the gliding of lattice plane units [172, 197]. During the transition several intermediate stacking fault steps are necessary in order to complete the transition from cubic to hexagonal structure (for more detailed information see Ref. [197]). Interestingly, Qi *et al.* stated in a recent publication, that in the case of compressive-strained ABO_3 perovskite thin films, Shockley partial dislocation bounded to a stacking fault can rise in the formation of Ruddlesden-Popper faults with an additional AO-layer [229]. And indeed, Shockley partial dislocation are observed in hexagonal $BaTiO_3$ [172]. Furthermore, for the $Ba_5Nb_4O_{15}$-$BaTiO_3$ system, B-cation deficient hexagonal perovskites of the $A_nB_{n-1}O_{3n}$ series are observed, which form shift and twin type structures [230]. Thus, any changes in the local Ba/Ti ratio upon reduction may also promote changes in the stack-

---

[4]The characteristic X-ray lines of Ti $K\alpha$ and Ba $L\alpha$ are located at 4.508 keV and 4.465 keV, respectively. Such a small energy separation of $\Delta E_{TiK\alpha-BaL\alpha}=43$ eV is on the edge of the resolution limit [228] of a silicon drift detector and a reliable quantification was not possible without a reference sample.

[5]The latter is inline with the finding of a Si contamination on the surface of reduced specimens observed by means of XPS.

ing/structure. As the ground specimen exhibit a Ba/Ti ratio lower than one, the Ba-enrichment of reduced samples is assumed to be completely restricted to the surface. Thus, a possible Ruddlesden-Popper phase would also only form in the vicinity of the surface. Possible reasons for a preferential formation of a Ruddlesden-Popper phase at the surface may be a gradient in the oxygen vacancy concentration between bulk and surface or an enhanced strain in the surface region (due to rapid quenching). In general, a relation between the Ba-rich surface and the reconversion of the hexagonal phase to the tetragonal phase would also explain the higher Ba-enrichment for higher Mn-content, as the hexagonal phase is proportional to the latter. However, any relation to the phase transition and stacking faults remain a hypotheses and cannot be proven by the conducted experiments.

In summary, none of the above theories could be proven within the accessibility of the used characterization techniques. Thus, a final statement on the composition of the small particles reported in the scanning electron microscopy images of the reduced sample is not possible without further measurements. Here, cross sectional high-resolution transmission electron microscopy (HRTEM) could be a powerful technique to elucidate the chemical and structural nature of the precipitates.

6.2. Interface formation of Mn-doped BaTiO$_3$ to RuO$_2$ electrodes[6]

X-ray photoelectron survey spectra of a reduced, nominally undoped BaTiO$_3$ ceramic before and after deposition of 5 nm RuO$_2$ are shown in the upper panel of Figure 6.5. The survey spectra of the bare reduced specimen surface reveals the typical Ba, Ti, and O emission lines. On some specimens Si, Ca, and C contamination are detected on the surface (for more information follow discussion in Section 6.1).

During the stepwise deposition of RuO$_2$ the signal of the substrate emissions (Ba and Ti) attenuates, while the Ru lines are growing. At a thickness of 5 nm RuO$_2$, emissions originating from the substrate and the RuO$_2$ electrode are detected. The lower panel of Figure 6.5 shows
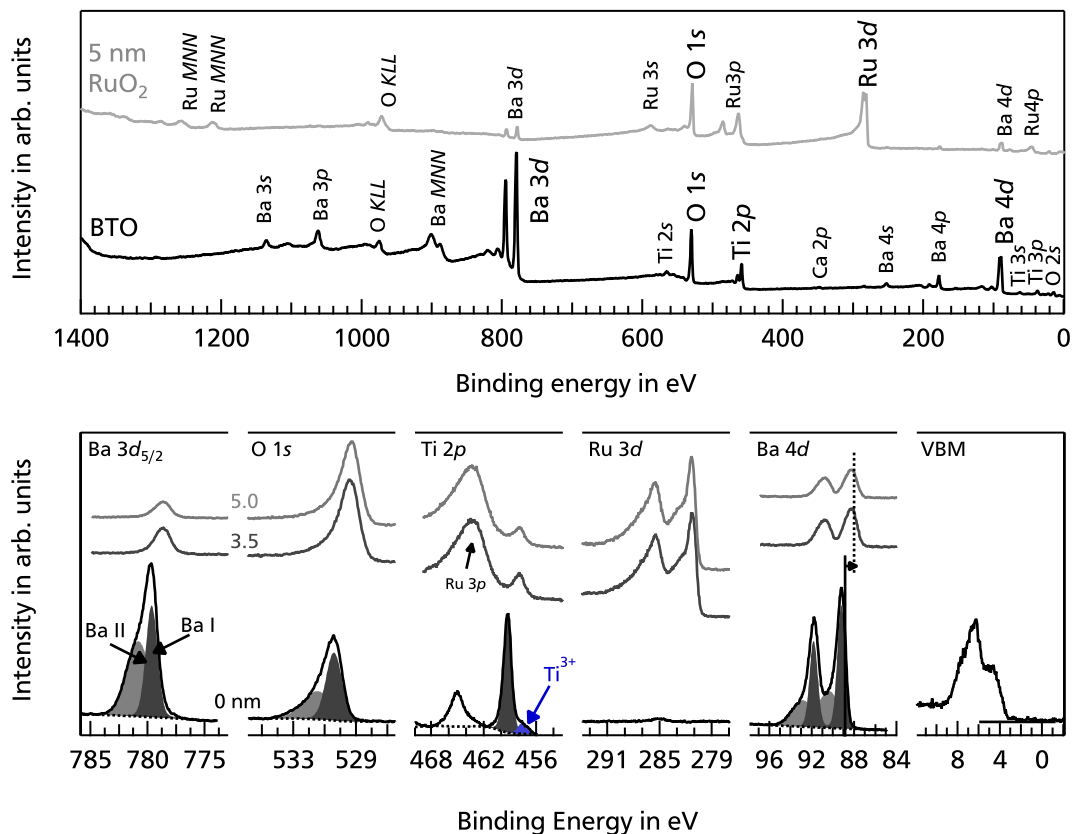
Figure 6.5.: X-ray photoelectron survey spectra (upper panel) and core level/valence band emissions (lower panel) of a reduced, nominally undoped BaTiO$_3$ ceramic recorded with monochromatic Al K$_\alpha$ radiation. The RuO$_2$ electrode thickness is indicated in nanometers. Curve fitting was conducted for all BaTiO$_3$ emissions using Gauss−Lorentz functions. The binding energy shift before and after contact formation is indicated by the two lines in the Ba 4d spectrum.

[6]Parts of this Section have been published in: Schuldt, Katharina NS, et al. "Influence of Defects on the Schottky Barrier Height at BaTiO$_3$/RuO$_2$ Interfaces." physica status solidi (a) (2021) [206].

the core level emissions of Ba $3d_{5/2}$, O $1s$, Ti $2p$, Ru $3d$, and Ba $4d$ as well as the valence band of the bare BaTiO$_3$ surface. The core level emissions during stepwise deposition of RuO$_2$ are illustrated from bottom to top, respectively. Curve fitting using Gauss–Lorentz functions was conducted for all BaTiO$_3$ emissions of the bare surface. The Ba $3d_{5/2}$ and Ba $4d$ core-level spectra are composed of two component assigned to a bulk and a surface emissions as described in Section 6.1.1. The Ti $2p$ spectrum shows a symmetric line shape with a shoulder at lower binding energies, indicated by the blue fit in Figure 6.5, which is attributed to Ti^{3+}. The small intensity in the Ru $3d$ spectral region at 285 eV for the bare BaTiO$_3$ surface originates from some remaining C species, which have not been completely removed by the cleaning procedure for reduced specimens by heating in vacuum.

The intensity of the Ba and Ti core levels gradually decreases with increasing RuO$_2$ thickness, while the intensity of the Ru emission increases. The Ti $2p$ emission, especially the binding energy range of the Ti $2p_{1/2}$, is superimposed with the growing Ru $3p$ emission. Nevertheless, the main Ti $2p_{3/2}$ emission remains well separated and can, thus, still be used for determining the Ti $2p$ binding energy. As BaTiO$_3$ and RuO$_2$ both contain oxygen, the O emission is not attenuated with increasing RuO$_2$ thickness. RuO$_2$ deposition leads to a shift of the Ba and Ti emissions towards lower binding energies, as indicated by the solid and dashed lines in the Ba $4d$ spectrum.

During stepwise RuO$_2$ deposition the valence bands of RuO$_2$ and BaTiO$_3$ are superimposed, making $E_F - E_{VBM}$ inaccessible. As explained in the methodology Section 3.2.5 on the interface formation, the core level to valence band distance is a material constant, which can be used to obtain the Fermi level during the interface experiment by subtracting the respective distance from the corresponding core level binding energies [128]. Thus, the course of the Fermi level during interface formation and by this the resulting barrier can be determined by knowing the respective core level to valence band distances.

6.2.1. The barrier heights

The evolution of the Fermi energy during the contact formation to RuO$_2$ was derived by subtracting the following core level to VBM distances: $E_{\mathrm{Ba}\,3d}^{\mathrm{VBM}} = 776.38$ eV, $E_{\mathrm{Ti}\,2p}^{\mathrm{VBM}} = 455.96$ eV, and $E_{\mathrm{Ba}\,4d}^{\mathrm{VBM}} = 85.95$ eV. These values correspond to the average distance extracted from the measurements of all bare surfaces of the reduced (Mn-doped) BaTiO$_3$ samples (ground and non-ground). The values for Ba $3d$ and Ba $4d$ emissions were calculated using the bulk Ba I components of the $3d_{5/2}$ and $4d_{5/2}$ emissions, while the binding energy of the Ti $2p_{3/2}$ was used for the Ti $2p$ emission. The derived distances are in good agreement with the values of previous studies of BaTiO$_3$ single crystals [213, 215] and BaTiO$_3$ thin films [231].
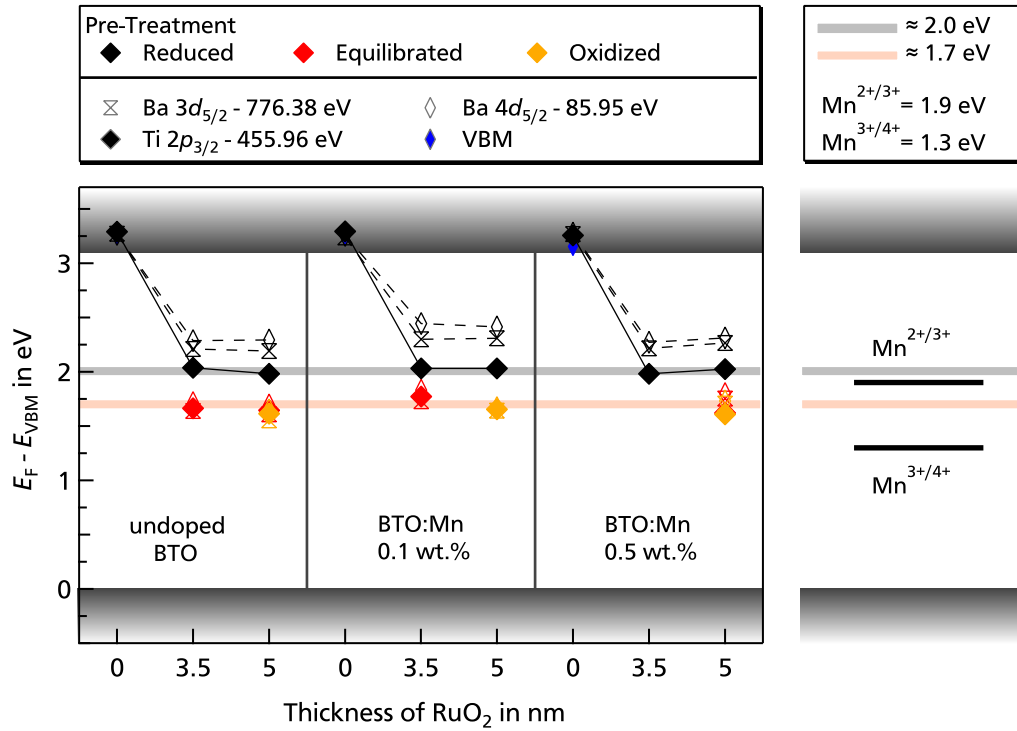
Figure 6.6.: Left: Evolution of the Ba $3d_{5/2}$, Ti $2p_{3/2}$, and Ba $4d_{5/2}$ binding energies with increasing RuO$_2$ thickness for undoped, 0.1 wt.%, and 0.5 wt.% Mn-doped BaTiO$_3$ ceramics in an oxidized (orange), equilibrated (red), and reduced state (black). The valence band maximum binding energies $E_F - E_{VBM}$ are derived by subtracting the respective core level to VBM distances given in the legend above. The film thickness of RuO$_2$ was calculated based on the respective accumulated deposition time with an assumed deposition rate of 3 nm/min. Dashed lines connect values derived from the Ba $3d$ and $4d$ emissions and solid lines those from Ti $2p$ emissions. Independent on the Mn-doping concentration, equilibrated and oxidized samples exhibit $E_F - E_{VBM} \approx 1.7$ eV, while reduced samples exhibit $E_F - E_{VBM} \approx 2.0$ eV at the interface, which is indicated by the reddish and greyish horizontal line, respectively. Right: Comparison of the derived interface $E_F - E_{VBM}$ values to the literature values of manganese charge transition levels [21] inside the band gap of BaTiO$_3$.

The Schottky barrier formation during contact formation to RuO$_2$ has been studied for nominally undoped, 0.1 wt.%, and 0.5 wt.% Mn-doped BaTiO$_3$ ceramics in different oxidation states. The Fermi level positions at the interfaces are derived from the shift of the Ba $3d_{5/2}$, Ti $2p_{3/2}$, and Ba $4d_{5/2}$ core levels and are displayed in Figure 6.6 as a function of RuO$_2$ thickness. Fermi level positions for the bare surfaces (0 nm) are only obtained for the reduced specimens, as equilibrated and oxidized specimens are heavily charging due to a low conductivity of $< 10^{-9}$ S/cm. For reduced specimens the value of $E_F - E_{VBM} = 3.2 \pm 0.05$ eV is close or even inside the conduction band of BaTiO$_3$. These high Fermi level positions also agree with the observation of Ti^{3+} and the high conductivity of the reduced samples. Conductivities of 0.01 to 0.1 S/cm have been recorded for undoped an Mn-doped reduced BaTiO$_3$, which correspond to an electron concentrations of $10^{17} - 10^{18}$ cm^{-3} for an electron mobility of 0.5 cm^2/Vs. For detailed information on the conductivity of the different samples see Chapter 7. The extracted

Fermi level positions of the respective core levels are identical after the deposition of 3.5 nm and 5 nm RuO$_2$, indicating that the barrier is already fully developed at a RuO$_2$ thickness of 3.5 nm. This value is in agreement with previous studies on the contact formation between dielectric oxides and RuO$_2$, in which the contact formation seems to be already completed at a RuO$_2$ thickness of 1 nm to 2 nm [28, 99, 213]. When comparing the achieved Fermi levels in Figure 6.6 three main observations can be made, which will be addressed in the following:

i. For reduced specimens the binding energy shift of the Ba 3d and 4d core levels is smaller than for the Ti 2p core level.

During contact formation the resulting binding energy shifts of the reduced specimens are smaller for the Ba core levels as compared to the shifts of the Ti core levels. Consequently, the subtraction of the core level to VBM distance results in an apparent dependence of the Fermi level position on the respective core level used for its derivation. Different shifts of the core levels can be an indication for an interfacial reaction as a result of the contact formation. However, the equilibrated and oxidized samples show identical Fermi level position for all three core levels. Thus, an interfacial reaction as origin of the different binding energy shifts can be excluded.

Another reason for the different binding energy shifts of the core levels could be a very narrow space-charge region as a result of the Schottky barrier formation. This would result in a dependency of the core level shift on the mean free path of the respective photoelectrons. The mean free path as a function of electron kinetic energy is depicted in Figure 3.17. Hence, the core levels with the lowest kinetic energy (highest binding energy) of the photoelectrons originate from lower depths and thus should then exhibit the largest shift. In the case of BaTiO$_3$, it is expected that the binding energy shifts are largest for Ba 3d ($E_{\text{Kin.}}$=1486.6 eV-780 eV=706.6 eV)[7] and smallest for Ba 4d ($E_{\text{Kin.}}$=1486.6 eV-89 eV=1397.6 eV). The results in Figure 6.6 clearly show similar binding energy shifts of both Ba emissions. Thus, a narrow space charge region can be excluded as possible origin for the different shifts of both Ba emissions compared to the Ti emissions.

It has recently been demonstrated that in the case of ZnO contact formation to RuO$_2$ the Zn 2p core level and Zn LMM Auger emission also exhibit different binding energy shifts [28]. In the latter case, the authors assigned the different shifts to a change in the screening of the photoelectron core hole during evolution of the Schottky barrier. However, the origin of the different screening could not be finally illuminated. The authors suggested that the large observed band bending due to the high work function of RuO$_2$ could induce a high electric field, resulting in the observed change in screening during the evolution of the barrier. The situation of Wendel *et al.* is very similar to the case of the present reduced specimens in contact to RuO$_2$,

---

[7] Monochromatic Al-K$_\alpha$ radiation with an energy of 1486.6 eV was used.

where the Fermi energy at the interface differs by more than $1.2\,\mathrm{eV}$ from that in the bulk of the reduced samples ($E_\mathrm{F} - E_\mathrm{VBM}(0\,\mathrm{nm}, \mathrm{bulk}) = 3.2\,\mathrm{eV}$ and $E_\mathrm{F} - E_\mathrm{VBM}(5\,\mathrm{nm}, \mathrm{interface}) = 2.0\,\mathrm{eV}$). In contrast, considering the treatment parameters of equilibrated and oxidized samples, the bulk Fermi energy should be comparable or even lower than that at the RuO_2 interface (see simulation on the space charge region in Section 6.2.2). No high electric fields should therefore be present at these interfaces. Hence, the different Fermi energies derived from the different shifts of the core levels during the interface formation between reduced $BaTiO_3$ towards RuO_2, are consistent with the presence of a high electric field in the space charge region as proposed for the ZnO/RuO_2 interface [28]. Additionally, the moderate difference in Fermi energy from the different core levels at the interface of RuO_2 towards equilibrated and oxidized specimens could also be explained by the absence of high electric field in the space charge region.

The change of the Ba $3d$ and $4d$ line shapes during the evolution of the contact formation towards RuO_2 deposition also indicates a change of core hole screening during interface formation. In particular, the intensity ratio and binding energy separation of the bulk (Ba I) and the surface (Ba II) component are changing during interface formation. Such effects have also been observed in previous works of other $BaTiO_3$ and $(Ba, Sr)TiO_3$ interfaces [232–235]. Another potential origin could be related to the observed Ba-rich surface phase on top of the Mn-doped $BaTiO_3$ bulk. If the Ba and Ti core level emission would not represent the same phase, a different shift of both phases upon interface formation would be reasonable.

ii. Different Schottky barrier heights have been observed for reduced specimens ($E_F - E_{VBM} = 2.0 \pm 0.05\,eV$) and equilibrated/oxidized ones ($E_F - E_{VBM} = 1.7 \pm 0.05\,eV$).

The surface analysis of reduced specimens in Section 6.1.1 revealed a Ba-rich surface layer, which might affect the barrier formation towards electrodes. Thus, the Ba-rich surface was removed after reduction and the interface formation towards RuO_2 was repeated. The resulting $E_\mathrm{F} - E_\mathrm{VBM}$ as a function of RuO_2 derived from the cation core levels are shown in Figure 6.7. The barrier formation of reduced and ground $0.5\,\mathrm{wt.\%}$ Mn-doped $BaTiO_3$ is completed after the deposition of $3\,\mathrm{nm}$ RuO_2.

For the ground specimen the evolution of the Ba and Ti core level binding energies still reveals a different strong shift upon contact formation, but with a considerable lower difference than for the specimen with the Ba-rich surface. The removal of the Ba-rich surface layer of a reduced $0.5\,\mathrm{wt.\%}$ Mn-doped $BaTiO_3$ specimen results an interface Fermi energies of $E_\mathrm{F} - E_\mathrm{VBM} = 1.7 \pm 0.05\,\mathrm{eV}$ (derived from the Ti $2p_{3/2}$ core level). The latter value is identical with the one derived for equilibrated and oxidized specimens. Furthermore, the value of $E_\mathrm{F} - E_\mathrm{VBM} = 1.7 \pm 0.05\,\mathrm{eV}$ at the interface of equilibrated and oxidized specimens towards RuO_2 is independent on the Mn-dopant concentration (see Figure 6.6). Only the reduced, non-ground samples exhibit a clearly higher Fermi level position in contact with RuO_2. Thus, the difference in Schottky barrier height between reduced, non-ground samples and equilibrated/oxidized
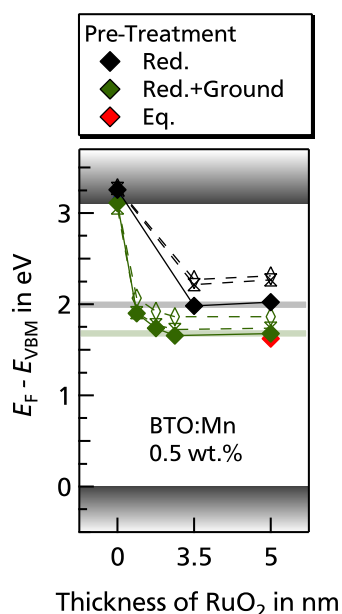
Figure 6.7.: Evolution of the Ba $3d_{5/2}$, Ti $2p_{3/2}$, and Ba $4d_{5/2}$ binding energies with increasing RuO$_2$ thickness for reduced (black) and reduced and ground (green) 0.5 wt.% Mn-doped BaTiO$_3$.

specimens towards RuO$_2$ is attributed to the Ba-rich surface phase. The observed Fermi level position at the Mn-doped BaTiO$_3$/RuO$_2$ interfaces corresponds to a Schottky barrier height for the electrons of $\Phi_{B,n} = E_G - E_F = 3.1 - 1.7 = 1.4$ eV, where 3.1 eV is taken for the band gap of BaTiO$_3$ [21]. Such high Schottky barriers are reasonable considering the high (effective) work function of RuO$_2$ of 5.6 eV (for more information see discussion in Ref. [201]). The observed barrier heights in this work of $\Phi_{B,n} = 1.4$ eV are comparable to the previous reported limits for the height of the Schottky barrier for electrons. The highest reported barrier height for BaTiO$_3$ was obtained by Long *et al.*, who observed a Schottky barrier height for electrons of $\Phi_{B,n} = 1.49$ eV at BaTiO$_3$/NiO interfaces [216]. Slightly higher Fermi levels at the interface have been reported for SrTiO$_3$/RuO$_2$ interfaces (with $E_F - E_{VBM} = 1.85$ eV) [14]. Furthermore, the Schottky barrier heights at ZnO/RuO$_2$ interfaces are also amongst the highest reported for this material [28].

iii. Independence of the barrier height on the Mn-doping concentration and oxidation state. For such high defect concentrations the independence of the barrier height on the Mn-doping and V$_O^{\bullet\bullet}$-concentration is surprising. Here, similar defect concentration in Fe-doped SrTiO$_3$ seemed to be sufficient for a dopant dependent Schottky barrier height at RuO$_2$ interfaces [14]. It is worth mentioning again, that for a rather narrow space charge region the measured XPS binding energies would be close to that in the bulk. In such a case the following scenario was expected for the present samples:

In the case of Mn-doped BaTiO$_3$ specimens the bulk Fermi level is expected to be pinned on the Mn-level. If the XPS binding energies rather correspond to the bulk (due to a narrow SCR), an influence of the Mn-doping on the measured $E_F - E_{VBM}$ is expected. However, the experimental results depicted in Figure 6.6 reveal no considerable influence of the Mn-doping concentration. The V$_O^{\bullet\bullet}$-concentration and by this the bulk Fermi level is altered by the respective pre-treatment. Consequently, the bulk Fermi level is expected to be pinned on the Mn$^{2+/3+}$ and Mn$^{3+/4+}$ charge transition levels dependent on the amount of V$_O^{\bullet\bullet}$. If the XPS binding energies rather correspond to the bulk (due to a narrow SCR), the measured $E_F - E_{VBM}$ is expected to correspond to a pinning on one of the defect levels. Hence, the measured $E_F - E_{VBM}$ was expected to vary between the different pre-treatments. However, the experimental results depicted in Figure

6.6 reveal no considerable influence of the pre-treatment. The absent influence of either the Mn-doping or the $V_O^{\bullet\bullet}$-concentration indicates, that the measured Fermi level corresponds to the interface and not to the bulk. This was not expected prior to the experiments, as the introduced high doping concentration was expected to narrow the space charge region to a width compatible to the inelastic mean free path of the photoelectrons. Thus, the presented results contrast the expectations. Here, the resulting space charge region width is the essential parameter, which can be simulated based on the experimental data by solving the Poisson equation. The calculated space charge region width for the contact formation to RuO_2 is addressed in the following.

6.2.2. Simulation of the space-charge region

In order to quantify the width of the resulting space charge region, the electronic contact formation of 0.5 wt.% Mn-doped $BaTiO_3$ towards RuO_2 has been simulated by solving the Poisson equation 4.1. Flat band potential have been set as boundary condition in the bulk and the experimentally derived Schottky barrier height for electrons of $\Phi_{B,n} = 1.4\,\text{eV}$ has been used as boundary condition at the interface. The following charge transition levels for Mn-dopants and oxygen vacancies have been used: $E_{A1} - E_{VBM} = 1.9\,\text{eV}$, $E_{A2} - E_{VBM} = 1.3\,\text{eV}$ [21] and $E_D - E_{VBM} = 3.0\,\text{eV}$ [65, 66]. For further information on the simulations see Chapter 4.1.

The simulations of the interface formation towards RuO_2 have been conducted for a 0.5 wt.% Mn-doped sample corresponding to an acceptor concentration of $N_{Mn} = 3.30 \times 10^{20}\text{cm}^{-3}$. The simulated energy band diagrams shown in Figure 6.8 correspond to three different values of oxygen vacancy concentration. To simulate reducing conditions, an oxygen vacancy concentration of $3.31 \times 10^{20}\text{cm}^{-3}$ has been assumed in Figure 6.8 a), which should result in an electron concentration[8] of $n \approx 10^{18}\text{cm}^{-3}$. The simulations shown in Figure 6.8 b) and c) should correspond to the equilibrated and oxidized state, for which oxygen vacancy concentrations of 1.8 and $1.0 \times 10^{20}\,\text{cm}^{-3}$ have been used. The three different oxygen vacancy concentrations result in bulk Fermi energies close to the conduction band in a), close to the $Mn^{2+/3+}$ transition in b), and close to the $Mn^{3+/4+}$ transition in c), respectively.

In the case of the reduced sample in Figure 6.8 a), the overall band bending towards the RuO_2 electrode exceeds 1.1 eV. This is a result of the high Schottky barrier, which in the case of reduced $BaTiO_3$ (with E_F close to E_{CB}) implies a high difference in Fermi energy between the bulk and the interface and thus results in a strong band bending. Due to the strong band bending, the Fermi energy is crossing the $Mn^{2+/3+}$ charge transition level in the space-charge region. This is noticeable by a change of curvature of the energy bands in the space-charge-region, which is induced by the strong increase of the effective charge density from 10^{18} to

---

[8]Reduced specimens show conductivities of 0.01 to 0.1 S/cm correspond to electron concentrations of $10^{17}-10^{18}\,\text{cm}^{-3}$ for an electron mobility of 0.5 cm²/Vs.
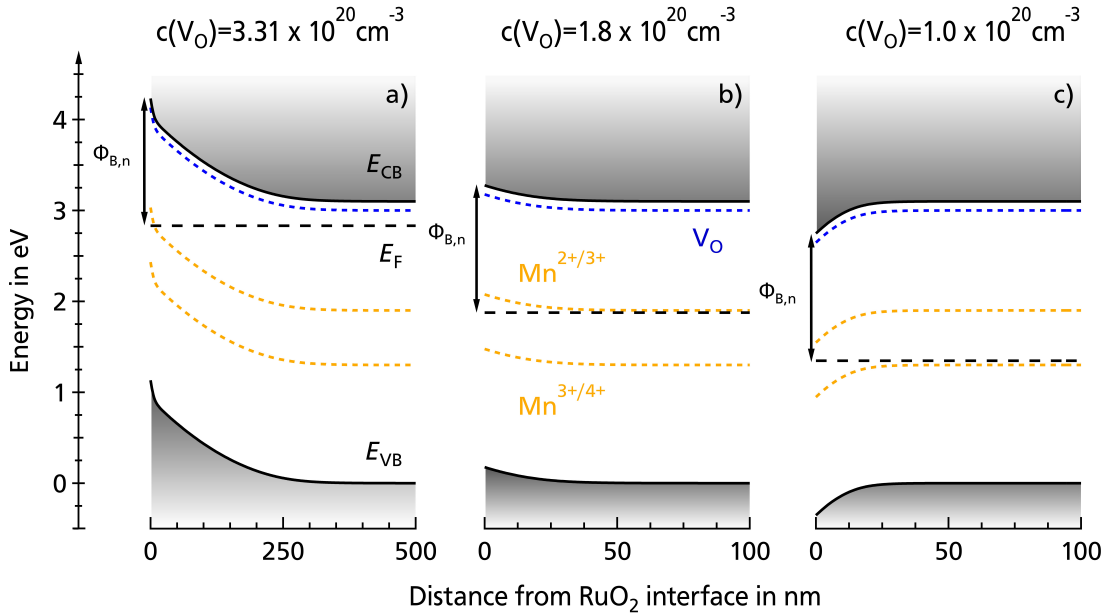
Figure 6.8.: Simulated energy band diagrams of 0.5 wt.% Mn-doped BaTiO$_3$ corresponding to a Mn-concentration of 3.3×10^{20} cm^{-3}. The concentrations of oxygen vacancies is 3.31×10^{20} cm^{-3} a), 1.8×10^{20} cm^{-3} b), and 1.0×10^{20} cm^{-3} c), respectively. Other parameters for the simulation are given in the text and in Section 4.1. The energy scale is referenced to the valence band maximum positions in the bulk.

3.31×10^{20} cm^{-3}. The changed curvature is better visible from the black curve in Figure 6.9 a), which corresponds to the potential profile (band bending) of the reduced specimen from Figure 6.8 a). Nevertheless, the steeper part of the band bending still extends over ~ 10 nm. As this is considerable larger than the inelastic mean free path of the photoelectrons of ~ 2 nm, the binding energy of the measured core levels during the interface formation towards RuO$_2$ still represent mostly the potential close to the interface and not the desired/expected bulk value. For the equilibrated and oxidized case the width of the space charge region is smaller than for the reduced case, due to the lower band bending and the lower resulting change, that needs to be compensated (for more information see the respective defect reactions in Section 4.1). However, in all cases the width of the space-charge-region is considerable larger than the inelastic mean free path of the photoelectrons.

Three simulations have been carried out using the same defect concentrations for reduced 0.5 wt.% Mn-doped BaTiO$_3$ and energy levels (same case as in Figure 6.8 a)) but different relative dielectric permittivities of $\epsilon = 1900$, 500, and 10. The value of $\epsilon = 1900$ corresponds to the measured room temperature permittivity of undoped BaTiO$_3$ without further treatment, while the value of $\epsilon = 500$ corresponds to the lowest measured room temperature permittivity upon Mn-doping (see Figure 5.8). As those experimentally permittivity values corresponds to untreated samples, the effective permittivity after the respective treatment (especially for the
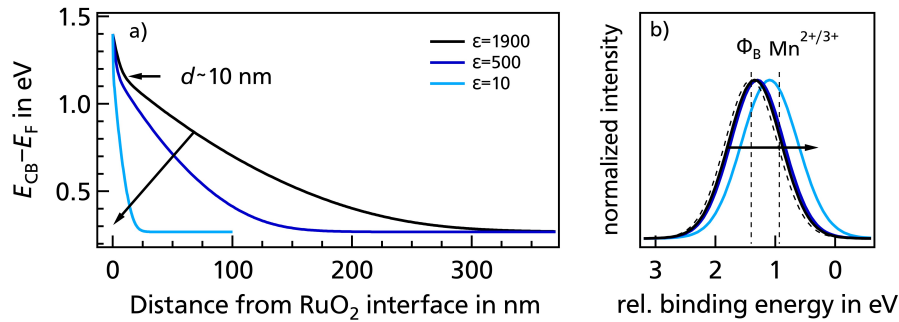
Figure 6.9.: a) Variation of the conduction band energy E_{CB} for the conditions given in Figure 6.8 a) but for different relative permittivities ϵ. Simulated core level spectra are shown in b). Here, the dashed black spectrum corresponds to a Gaussian peak with a full width at half maximum of 1 eV for a flat potential with $E_{CB} = 1.4\,eV$. The black, dark blue, and light blue spectra correspond to the spectra induced by the potential profiles shown in a) for an inelastic mean free path of the photoelectrons of 2 nm. The two dashed black vertical lines in the insert correspond to the position of the Fermi energy at the interface and to that of the $Mn^{2+/3+}$ charge transition level assumed in the simulations.

reduced samples with high oxygen vacancy concentrations) remains unknown. Thus, a rather low permittivity of 10 is added as comparison. The corresponding potential profiles are shown by the black, dark blue, and light blue curves in Figure 6.9 a), respectively. Reducing ϵ from 1900 to 500 to 10 leads, as expected from the Poisson equation, to a decreased space charge region width.

In order to quantify the influence of the Mn oxidation state on the binding energy of the core level emissions, simulations of spectra profiles have been carried out for the three cases[9]. An inelastic mean free path for photoelectrons of 2 nm and a Gaussian peak with a full width at half maximum of 1 eV has been assumed. More information about the application and the nature of such calculations can be found in Refs. [14, 199, 200].

The resulting calculated photoelectron spectra are shown by the black, dark blue, and light blue curves in Figure 6.9 b), respectively. The dashed curve corresponds to an infinite width of the space-charge region and thus to a peak position at Φ_B as indicated in Figure 6.9 b).

The solid black line, which corresponds to the calculated photoelectron spectrum of the potential profile with $\epsilon = 1900$, is barely shifted from the spectrum obtained for an infinite width of the space charge region. The reduction of ϵ from 1900 to 500 does not lead to a pronounced shift of the calculated photoelectron spectra in Figure 6.9 b). However, the maximum of the calculated photoelectron spectra is shifted by almost 0.4 eV for the lowest assumed permittivity of $\epsilon = 10$ and gets close to the position expected for a Fermi energy pinned at the $Mn^{2+/3+}$ transition.

---

[9]The simulations of the spectra profiles have been carried out by A. Klein using the IGOR Pro software (Wavemetrics).

Thus, the strong dependence of the position of the (calculated) photoelectron spectra on the width of the space-charge-region indicate, that the missing dependence of Schottky barrier height at the $BaTiO_3$:Mn/RuO_2 interface on doping is related to the high permittivity of the $BaTiO_3$ samples[10]. Accordingly, the introduction of defects (acceptor-dopants and oxygen vacancies) in low and high permittivity materials does not have the same influence on the space charge region width, which is much larger for high permittivity materials. This is most likely the reason why the results of Gieseke *et al.* indicate a Fermi level pinning at low permittivity Fe-doped $SrTiO_3$/RuO_2 interfaces [14] and no pinning was observed for the present high permittivity Mn-doping $BaTiO_3$/RuO_2 interfaces.

---

[10]The calculated dependence of the position of the photospectra on the permittivity raises the question whether a comparison of the extracted Fermi energies between different Mn-doping concentrations and different oxidation states is still reasonable. For the present samples the permittivity of sintered (Mn-doped) $BaTiO_3$ decreases from initially 1900 for undoped $BaTiO_3$ to 500 for 0.5 wt.% Mn-doped $BaTiO_3$. Additionally, a considerable fraction of the 0.5 wt.% Mn-doped specimens exhibits the hexagonal structure, which is assumed to have a substantial lower permittivity. Furthermore, a change of the oxidation state is reflected by a change in the oxygen vacancy concentration, which additionally affects (decreases) the permittivity. Hence, the different Mn- and $V_O^{\bullet\bullet}$-content of the specimens results in different permittivities, which result in different widths of the space charge region and possibly in different positions of the photoelectron spectra. The simulation in Figure 6.9 b) only revealed minor changes in the position of the (calculated) photoelectron spectra for a permittivity decrease from 1900 to 500. Thus, a considerable influence of the doping induced permittivity change on the peak position is excluded. An influence of the different oxygen vacancy concentration on the permittivity was not studied in this work. However, the extracted Fermi energies in Figure 6.6 revealed an oxidation state independent Fermi level of 1.7 eV. Thus, a significant influence of oxygen vacancy induced permittivity change is also excluded for the present samples. But still, treatment and doping induced permittivity changes should be kept in mind for further similar investigations on space charge region widths and Fermi level pinning experiments.

6.2.3. Voltage alterations at *RT* with RuO$_2$ electrodes

Cations and anions in BaTiO$_3$ are considered to be immobile at room temperature [27, 78]. However, the threshold value for oxygen (vacancy) diffusion in BaTiO$_3$ of about 200 °C is substantially lower than the one for cation diffusion of >1000 K [79]. During the photoemission the specimens are illuminated with X-rays ($E_{\text{Al-K}_\alpha}$ = 1486.6 eV), which may influence the oxygen diffusivity at room temperature. Unfortunately, the influence of light irradiation (of different wavelengths) on the room temperature diffusion of oxygen in polycrystalline BaTiO$_3$ is rarely studied. An increased *RT* oxygen out-diffusion has been observed for UV irradiation of YBa$_2$CuO$_x$ [236]. If the oxygen diffusivity would be affected by the illumination of X-rays as well, the charge density close to the surface of the BaTiO$_3$:Mn/RuO$_2$ will alter. Changes in the effective doping density ($c_{V_O^{\bullet\bullet}}$) will affect the width of the SCR, which is the crucial parameter for successful defect level identification by means of XPS. For a reduced single crystalline SrTiO$_3$/Pt interface it has been demonstrated, that that mobile oxygen vacancies accumulate in the SCR region, which increases the effective doping density and narrows the SCR to the electron tunneling distance (see Section 7.1). In the latter scenario it is expected, that the measured Fermi level would rather correspond to the bulk value than to the interface value. If the lower limit of $E_F - E_{\text{VBM}}$ = 1.7 eV would be a result of the X-ray induced diffusion of oxygen away from the surface/interface, an applied voltage should prevent/enhance the diffusion depending on the polarization direction. Here, an applied negative voltage at the bottom should prevent the oxygen diffusion away from the surface/interface and enhance the diffusion of positively charged oxygen vacancies towards the bottom cathode.

In order to investigate whether the X-ray illumination during the PES measurements affects the barrier height toward RuO$_2$, a 0.1 wt.% Mn-doped BaTiO$_3$ specimen was polished on both sides and equilibrated. In a first step a 100 nm thick RuO$_2$ electrode was deposited on the bottom of the specimen, followed by the deposition of an approximately 3 nm thick RuO$_2$ electrode on the top. In this geometry the bottom electrode serves as contact to the voltage source. The top electrode is thick enough for the electric contact (and thus to serve as grounding) and thin enough to measure the Fermi energy of the 0.1 wt.% Mn-doped BaTiO$_3$ at the interface. XPS measurements of the Ti 2$p_{3/2}$ and Ba 4d emission lines were performed with and without applying +/-200 V at the bottom electrode. The core level spectra were measured repeatedly with time intervals of approximately 20 min with neither turning off the X-ray nor the applied voltage of -200 V. After applying -200 V for more than 1 h also +200 V were applied for one XPS core level measurement in order to exclude any differences between both polarization directions. A polarization dependence of the Schottky barrier height, as has been observed by Chen [213] and Hubmann [213] for single crystalline BaTiO$_3$, has not been observed due to the low applied voltage with respect to the coercive field (see $P(E)$ loops in Figure 5.9). The
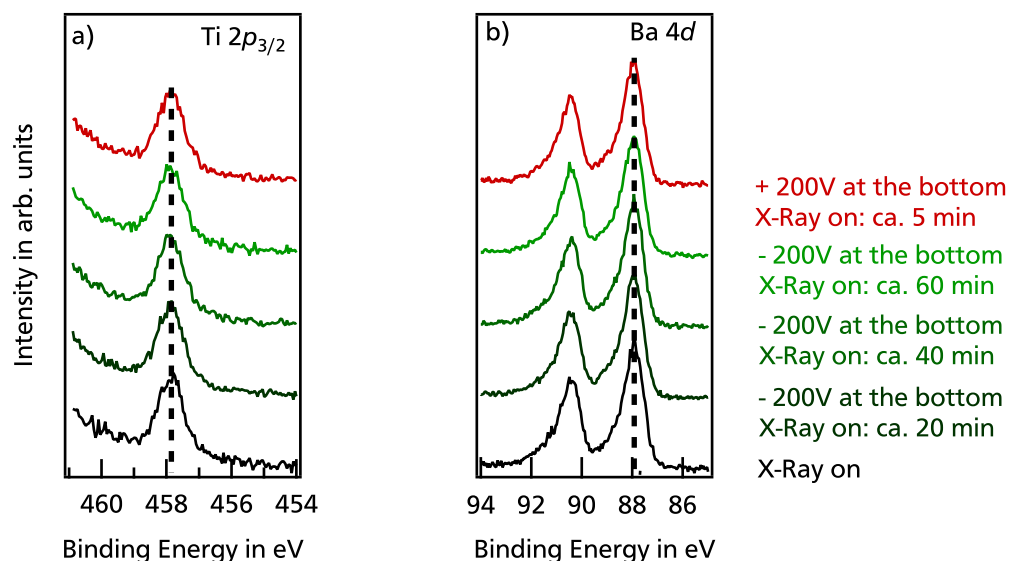
Figure 6.10.: a) Ti $2p_{3/2}$ and b) Ba $4d_{5/2}$ emission lines of an equilibrated 0.1 wt.% Mn-doped BaTiO$_3$ specimen measured during applied voltage through a 3 nm thick RuO$_2$ top electrode. The sample is grounded through the top 3 nm thick RuO$_2$ electrode and the voltage is applied to the 100 nm thick RuO$_2$ back electrode as depicted in c). A constant bias of +/-200 V was applied on the bottom electrode for the time indicated in the legend below c).

corresponding Ti $2p_{3/2}$ and Ba $4d$ emission lines for the different applied voltages are shown in Figure 6.10 a) and b).

The Ti $2p_{3/2}$ as well as Ba $4d$ core level do neither show a shift nor a modification of the emission line shape during the whole experiment. As no difference was observed between the XPS measurement without or with applied bias of +/-200 V, it can be concluded, that the X-ray irradiation during the XPS measurements has no significant influence on the oxygen diffusivity. Hence, the lower limit of the Fermi level at $E_\mathrm{F} - E_\mathrm{VBM} = 1.7$ eV is not an measurement artifact of PES as an result of the X-ray illumination.

6.2.4. Additional experiments

The strong upwards band bending at the reduced BaTiO$_3$:Mn/RuO$_2$ interface leads to a accumulation of positive charge carriers in the SCR region. The simulation of these interfaces (see Fig. 6.8) revealed a SCR width considerably larger than the tunneling distance of electrons, making a defect level identification impossible. However, post-heating of the interfaces may enable oxygen vacancy diffusion, which could lead to a further enhanced oxygen vacancy concentration close to the interface and a narrowing of the space charge region. In order to examine the maximum effect, an interface experiment of a reduced and ground 0.5 wt.% Mn-doped BaTiO$_3$ specimen towards RuO$_2$ was conducted, followed by post-heating in reducing

atmosphere to further enhance the oxygen vacancy concentration. The corresponding data is discussed in Appendix A.3.1. Unfortunately, the highly reduced 0.5 wt.% Mn-doped BaTiO$_3$ specimen in combination with vacuum annealing resulted in a reduction of the RuO$_2$ electrode to metallic Ru and island formation (see Fig. A.16). The examined Schottky barrier height decreased due to the reduction of RuO$_2$ to metallic Ru and the corresponding lower work function of metallic Ru. No utilizable information for defect level identification could be derived from this experiment.

In addition one set of equilibrated undoped, 0.1 wt.%, and 0.5 wt.% Mn-doped BaTiO$_3$ specimens have been investigated during contact formation towards PtO$_x$. The evolution of the binding energies is given in Figure A.17 in the Appendix. Again a Mn-concentration independent Fermi level at $E_F - E_{VBM} \approx 1.6\,\text{eV}$ was found. Both, PtO$_x$ and RuO$_2$ are high work function electrode materials. Hence, further experiments on PtO$_x$ have been omitted as similar results as for the RuO$_2$ interfaces are expected, which would not contribute to a successfully Mn defect energy level identification.

6.3. Interface formation of Mn-doped BaTiO$_3$ to Sn-doped In$_2$O$_3$

6.3.1. The barrier heights

Further interface experiments between BaTiO$_3$ specimens with different Mn- and V$_O^{\bullet\bullet}$-content to low work function Sn-doped In$_2$O$_3$ electrodes have been performed. From the previous Section on the interface properties towards RuO$_2$ the following is expected for the BaTiO$_3$:Mn/ITO interface experiments:

(a) The simulation revealed, that the space charge region width at the interface is considerably larger than the information depth of the XPS. Here, the wide space charge region is related to the high permittivity of BaTiO$_3$ and not to the electrode properties. Thus, also for the BaTiO$_3$:Mn/ITO interface no dependence of the Schottky barrier height on doping is expected.

(b) The Ba-rich surface layer of reduced specimens had strong influence on the resulting Schottky barrier height at BaTiO$_3$:Mn/RuO$_2$ interfaces. A similar influence of the Ba-rich surface after reduction is expected for the BaTiO$_3$:Mn/ITO interfaces as well.

(c) Sn-doped In$_2$O$_3$ has a work function of 4.5 eV, which is considerable lower than the one of RuO$_2$ of 5.6 eV. Hence, a substantial smaller Schottky barrier height for electrons is expected for BaTiO$_3$:Mn/ITO interfaces.

The evolution of the Schottky barrier during contact formation to room-temperature deposited Sn-doped In$_2$O$_3$ has been studied for nominally undoped, 0.1 wt.%, and 0.5 wt.% Mn-doped BaTiO$_3$ specimens in different oxidation states[11]. The corresponding Fermi level position has been derived from the binding energy shifts of the Ba $3d_{5/2}$, Ti $2p_{3/2}$, and Ba $4d_{5/2}$ core level emissions and is shown in Figure 6.11 as a function of ITO thickness. Whereas the Fermi level of the highly conductive reduced specimens is again near or slightly above the conduction band minimum, the conductivity of the equilibrated and oxidized samples is too low to derive reliable Fermi level positions of the bare specimens. The Fermi level positions at the interface are identical after the deposition of 1.66 nm and 3.33 nm thick ITO, indicating that the barrier formation is already completed at an ITO thickness of 1.66 nm. This is in good agreement with previous interface studies on (Ba,Sr)Ti$_3$/ITO interfaces, where the Schottky barrier height was fully developed at an ITO thickness of approximately 1.6 nm [235].

Reduced specimens show, independent on the Mn-content, only a slight decrease in Fermi level position from initially 3.2 eV to 3.0 ± 0.05 eV after contact formation to ITO. The deviations in the Ba and Ti core level shifts are only minor compared to the significant difference being observed for the RuO$_2$ interface to reduced specimens. The comparable shift of the Ba and Ti emissions for the BaTiO$_3$:Mn/ITO interfaces is consistent with the proposed origin of high electric fields at reduced BaTiO$_3$:Mn/RuO$_2$ interfaces. In the case of reduced BaTiO$_3$:Mn/ITO

---

[11]The oxygen plasma source treatment of the BaTiO$_3$ specimen for the ITO interface was conducted at room temperature, while the one for the RuO$_2$ interface was conducted at 200 °C (see Section 3.1).
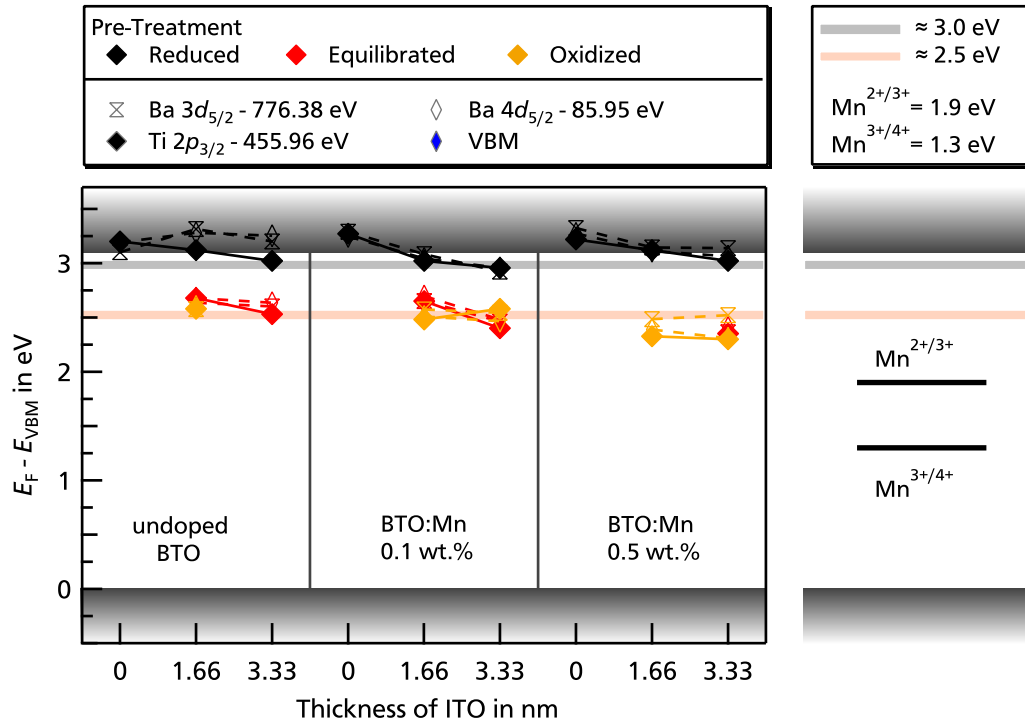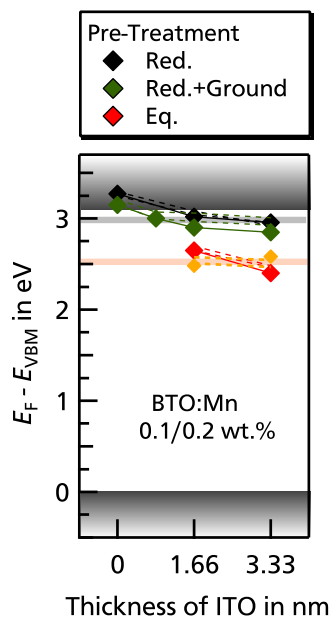
Figure 6.11.: Left: Evolution of the Ba $3d_{5/2}$, Ti $2p_{3/2}$, and Ba $4d_{5/2}$ binding energies with increasing ITO thickness for undoped, 0.1 wt.%, and 0.5 wt.% Mn-doped BaTiO$_3$ ceramics in an oxidized (orange), equilibrated (red), and reduced state (black). The valence band maximum binding energies $E_F - E_{VBM}$ are derived by subtracting the respective core level to VBM distances given in the legend above. The film thickness of ITO was calculated based on the respective accumulated deposition time with an assumed deposition rate of 5 nm/min. Dashed lines connect values derived from the Ba $3d$ and $4d$ emissions and solid lines those from Ti $2p$ emissions. Independent on the Mn-doping concentration, equilibrated and oxidized samples exhibit $E_F - E_{VBM} \approx 2.5$ eV, while reduced samples exhibit $E_F - E_{VBM} \approx 3.0$ eV at the interface, which is indicated by the reddish and greyish horizontal line, respectively. Right: Comparison of the derived interface $E_F - E_{VBM}$ values to the literature values of manganese charge transition levels [21] inside the band gap of BaTiO$_3$.

interfaces only a low band bending is observed, which results in a low electric field in the space charge region and a lower/negligible influence on the core level shift of the Ba emissions.

After ITO deposition, the equilibrated and oxidized samples exhibit comparable Fermi level positions of $E_F - E_{VBM} \approx 2.5$ eV. Neither the resulting Fermi level of the reduced nor the one of the equilibrated/oxidized specimen agree with the known Mn-charge transition levels, which are compared in Figure 6.11 on the right. This was expected from the simulation of the BaTiO$_3$:Mn/RuO$_2$ interfaces, which revealed an absent influence of Mn-doping due to a wide space charge region. In order to reveal whether the Ba-rich surface component of the reduced specimens is responsible for the difference in Fermi level position upon ITO contact formation between reduced and equilibrated/oxidized specimens, the surface of a 0.2 wt.% BaTiO$_3$ sample has been removed after reduction and the interface formation towards ITO was repeated.

The evolution of the Fermi level position during ITO contact formation is depicted in Figure 6.12. The values of the ground 0.2 wt.% Mn-doped BaTiO$_3$ are compared to ones of reduced and non-ground 0.1 wt.% Mn-doped BaTiO$_3$. Surprisingly, the ground 0.2 wt.% Mn-doped specimen exhibits a Fermi energy of 2.85 eV at the ITO interface, which is only slightly lower than the one of the 0.1 wt.% non-ground sample. The value of 2.85 eV is still significantly higher than the one of the equilibrated and oxidized 0.1 wt.% BaTiO$_3$ specimens. This was not expected in the light of the BaTiO$_3$:Mn/RuO$_2$ interface experiments, where the removal of the Ba-rich surface layer resulted in identical Fermi level position for all three oxidation states.

The comparison of the Ba emission lines confirmed the successful removal of the Ba-rich surface, which is indicated by a similar peak shape and position as for the specimens being evaluated in the ground BaTiO$_3$:Mn/RuO$_2$ interface. Thus, different initial substrate properties of the reduced and ground 0.2 wt.% Mn-doped BaTiO$_3$ specimen are excluded as origin. Possibly, an insufficient charge compensation of the ITO thin film for the high space charge density of the reduced samples is responsible for the higher Fermi level of reduced specimens. ITO thin films deposited at room temperature typically have a conductivity of $<1\times10^3$ S/cm [237–240] (as comparison: room temperature deposited RuO$_2$ has a conductivity of 4250 S/cm [241]). The low ITO conductivity is accompanied by a low charge carrier concentration, which is additionally depending on the film thickness. Here, the charge carrier concentration is decreasing for decreasing ITO film thickness [240]. Hence, it could be possible, that the charge carrier concentration of the 1.66 nm and 3.33 nm thick ITO films prepared in this work is insufficient for the necessary charge compensation upon reduced BaTiO$_3$:Mn/ITO contact formation. For future experiments it is recommended to prepare the ITO thin films at 400 °C, which results in a conductivity $> 1 \times 10^4$ S/cm [242, 243] accompanied by a higher charge carrier concentration.

Figure 6.12.: Evolution of the Ba 3$d_{5/2}$, Ti 2$p_{3/2}$, and Ba 4$d_{5/2}$ binding energies with increasing ITO thickness for reduced (black) 0.1 wt.% and reduced and ground (green) 0.2 wt.% Mn-doped BaTiO$_3$ ceramics. $E_F - E_{VBM}$ for the equilibrated 0.1 wt.% Mn-doped specimen is given for an ITO thickness of 3.33 nm as comparison.

In summary, the three expectations (a)-(c) for the BaTiO$_3$:Mn/ITO interface could only be partially confirmed. (a) As expected, no significant dependence of the Schottky barrier height

on the Mn-content could be observed for the performed BaTiO$_3$:Mn/ITO interfaces. (b) The dependence of the barrier on the oxidation state (reduced vs. equilibrated/oxidized), however, could not be eliminated by removing the Ba-rich surface layer of the reduced samples. The remaining difference is attributed to the insufficient compensation of the high space charge of reduced samples due to the low conductivity and, thus, low charge carrier concentration of room temperature deposited ITO thin films. (c) The resulting $E_F - E_{VBM}$ after ITO contact formation to equilibrated/oxidized BaTiO$_3$ specimens is 2.5 eV, while it is 1.7 eV for the BaTiO$_3$/RuO$_2$ interface. Hence, a considerable lower Schottky barrier height for electrons (which means higher $E_F - E_{VBM}$) at the ITO interface compared to RuO$_2$ interfaces could be confirmed, which was expected due to the lower work function of the former.

The observed interface Fermi level variation of 0.8 eV for Mn-doped BaTiO$_3$ in contact to RuO$_2$ and ITO is considerable lower as the Fermi level variations of >1 eV observed for other oxides in similar interface experiments [30]. This could potentially be attributed to the room temperature deposition of the ITO thin films.

## 6.3.2. Heating experiments with *RT*-deposited Sn-doped In$_2$O$_3$ electrodes

The oxygen content inside the Sn-doped In$_2$O$_3$ electrode is directly correlated to its conductivity, Fermi energy, and work function [19, 81, 244]. Sn-doped In$_2$O$_3$ thin films with low oxygen concentration reveal a higher conductivity, a higher Fermi level, and consequently a lower work function than ITO thin films with a high oxygen content[12]. An altered work function of the ITO electrode due to oxygen incorporation or extraction will result in a modified Schottky barrier height at the BaTiO$_3$:Mn/ITO interface. A potentially increased ITO conductivity by post heating is of particular interest, as the low charge carrier concentration of the *RT*-deposited ITO is assumed to be responsible for the observed difference in Schottky barrier height between reduced and equilibrated/oxidized samples (follow discussion of the previous Section). In order to investigate the influence of oxygen content on the interface properties towards Mn-doped BaTiO$_3$, different post-heating experiments have been conducted in oxidizing and reducing atmospheres.

Reduced and ground 0.2 wt. % Mn-doped

In the first heating experiment ITO was stepwisely deposited on a reduced and ground 0.2 wt.% Mn-doped BaTiO$_3$ specimen until a total ITO electrode thickness of 3.33 nm was reached. Afterwards, the interface configuration has been post-heated in a first step for 1 h at 300 °C in vacuum, followed by a second heating step for 1 h at 400 °C in vacuum. The core level spectra of

---

[12]A higher ITO conductivity is also expected for deposition temperatures of 400 °C [81,244]. Two interface experiments between equilibrated 0.5 wt.% Mn-doped BaTiO$_3$ and *HT*-ITO have been investigated. However, in both cases the ceramic 0.5 wt.% Mn-doped BaTiO$_3$ substrate broke during heating, which is why a detailed discussion of this results is omitted in this thesis.
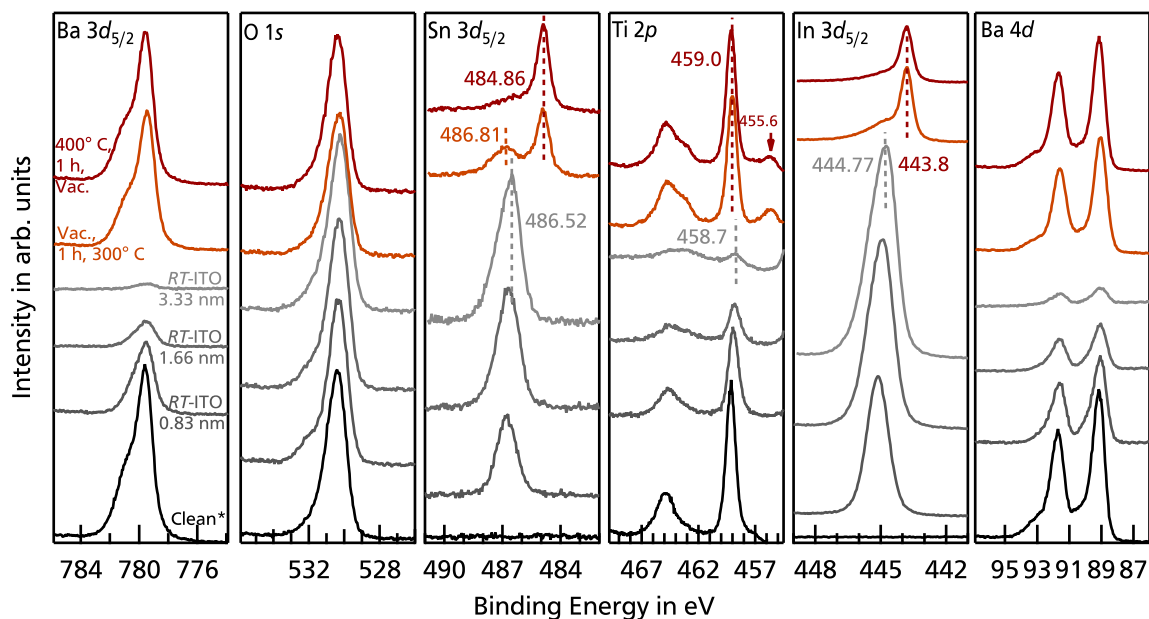
Figure 6.13.: X-ray photoelectron core level spectra of the Ba $3d_{5/2}$, O $1s$, Sn $3d_{5/2}$, In $3d_{5/2}$, Ti $2p$, and Ba $4d$ emissions of a reduced and ground 0.2 wt.% Mn-doped $BaTiO_3$. The spectra were recorded during contact formation to ITO and after post-heating in vacuum. The Sn-doped In_2O_3 electrode thickness as well as the used post-treatment parameters are indicated in the Ba $3d_{5/2}$ spectrum. The film thickness of ITO was calculated based on the respective accumulated deposition time with an assumed deposition rate of 5 nm/min. The binding energy indicated by the vertical dashed lines in the Sn, In, and Ti core levels are given in eV. The spectra were recorded with monochromatic Al K$_\alpha$ radiation.

the Ba $3d_{5/2}$, O $1s$, Sn $3d_{5/2}$, In $3d_{5/2}$, Ti $2p$, and Ba $4d$ emission during stepwise ITO deposition as well as after heating for 1 h at 300 °C and 400 °C in vacuum are shown in Figure 6.13 from bottom to top. During ITO deposition the Ba and Ti emission attenuate, while the In and Sn emissions are growing. After the first heat treatment, however, the Ba and Ti related emissions gained again in intensity, while the intensity of the Sn and In core level decreased.

After heat treatment, significant changes in the Sn $3d_{5/2}$ and In $3d_{5/2}$ emission lines are observed. For the 3.33 nm ITO film, the Sn $3d_{5/2}$ emission shows a single peak structure with its binding energy referring to Sn^{4+}. After the first heating in vacuum the Sn^{4+} related peak is significantly decreased in intensity and a second peak at 484.86 eV rises. The latter binding energy refers to metallic Sn [245, 246]. Similar changes have been observed in the In $3d_{5/2}$ emissions shown in Figure 6.13. While the single emission for the 3.33 nm ITO film belongs to an In^{3+}, the rising second peak at 443.8 eV after the first heat treatment in vacuum belongs to metallic In [246]. The proportion of the metallic contribution to the Sn $3d_{5/2}$ and In $3d_{5/2}$ emissions further increases during the second heating step in vacuum.

After heat treatment, the Ba $3d$ and $4d$ emissions reveal a slightly decreased intensity of the Ba II component compared to the respective core levels of the clean surface. The peak shape of

the Ti $2p$ core level however, is significantly altered. Whereas the Ti $2p$ emission of the bare surface represents the well known $2p_{3/2}$ and $2p_{1/2}$ doublet due to the spin-orbit splitting, heat treatment leads to the appearance of an additional peak doublet at the lower binding energy side of the originally double structure. The main emission line at 459.0 eV corresponds to a Ti^{4+}, while the rising intensity at 455.6 eV in the Ti $2p_{3/2}$ emission could have two potential origins. Kashiwaya et $al.$ reported a relative binding energy shift of 1.7 eV and 3.5 eV for Ti^{3+} and Ti^{2+} to the main emission line of Ti^{4+} in TiO$_2$, respectively [247]. For the present sample the distance between the Ti^{4+} emission and the rising unknown emission is 3.4 eV, which could indicate Ti^{2+} as origin. However, a relation to the plasmon loss feature of metallic In is more likely. In literature a distance of 11.7 eV between the parent In $3d_{5/2}$ core level emission and the corresponding plasmon loss peak is reported for metallic In [248, 249]. Taking 443.8 eV as binding energy for the metallic In, the corresponding plasmon satellite is expected at 455.5 eV. The latter value agrees well with the rising intensity at 455.6 eV in the Ti $2p_{3/2}$ emission. Hence, the altered peak shape of the Ti $2p$ is assumed to be not related to a reduction of the Ti, but originated from the plasmon loss feature of metallic In.

The appearance of metallic In and Sn at vacuum annealing temperatures of 300 °C are in clear contrast to recent experiments on a 20 nm thick ITO film, which has been heated for $>$2 h at 300 °C in vacuum [250]. Within the latter experiment no metallic In or Sn has been observed in the corresponding core level spectra [250]. Hence, for the present interface either the thinner ITO film thickness or the reduced Mn-doped BaTiO$_3$ substrate are responsible for the appearance of metallic Sn and In. The metallic Sn and In in combination with the rising intensity of the Ba and Ti lines most likely indicates an island formation of metallic Sn and In. Similar findings have already been observed for the heating experiment of a reduced 0.5 wt.% Mn-doped BaTiO$_3$/RuO$_2$ interface in vacuum (see Section A.3.1). Here, the Ba and Ti intensity also increased after vacuum heating and metallic Ru was observed.

The valence band of the clean reduced and ground 0.2 wt.% Mn-doped BaTiO$_3$ specimen before ITO deposition and after the second heating in vacuum are shown in Figure 6.14 a). The $E_F - E_{VBM} = 3.19$ eV of the bare 0.2 wt.% Mn-doped BaTiO$_3$ surface proves the high reduced state of the specimen before ITO deposition. After ITO deposition the valence band of the ITO electrode is superimposed with the one of BaTiO$_3$. Therefore, the recorded valence band after the second vacuum heating contains contributions from metallic In and Sn and 0.2 wt.% Mn-doped BaTiO$_3$. Here, the metallic contribution of Sn and In at zero binding energy can be nicely seen in the corresponding valence band spectrum in Figure 6.14 a).

Additionally, the evolution of $E_F - E_{VBM}$ of 0.2 wt.% Mn-doped BaTiO$_3$ during ITO contact formation and heating in vacuum is shown in Figure 6.14 b). Here, the $E_F - E_{VBM}$ was derived from the binding energy shift of the Ti^{4+} in the Ti $2p_{3/2}$ emission. The contact formation to ITO results in a decrease of $E_F - E_{VBM}$ to 2.85 eV, while heating in vacuum leads to an increase
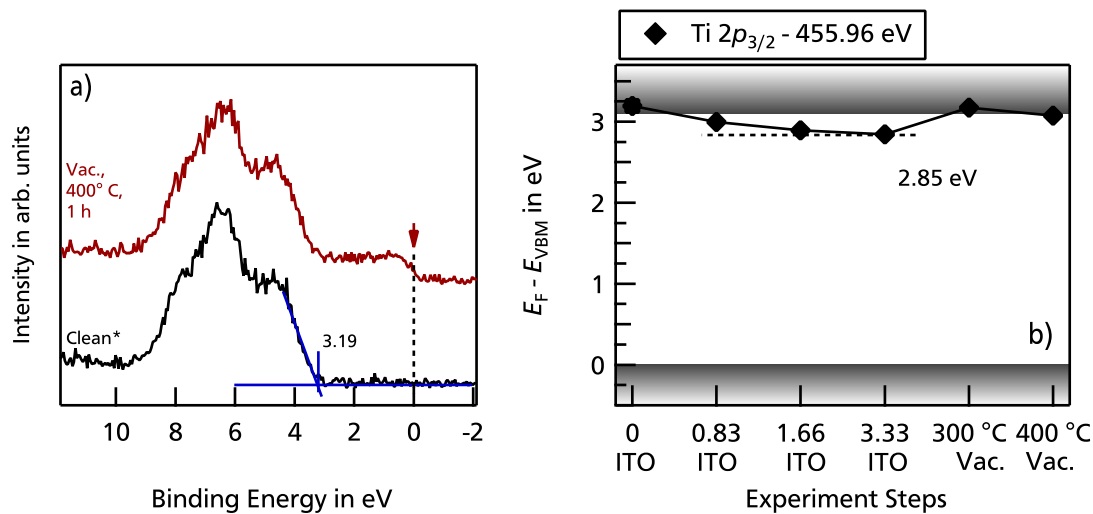
Figure 6.14.: a) Valence band spectra of the bare reduced and ground 0.2 wt.% Mn-doped BaTiO$_3$ surface and after the last heating step of the 0.2 wt.% Mn-doped BaTiO$_3$/ITO interface for 1 h 400 °C in vacuum. b) Evolution of the valence band maximum binding energies $E_F - E_{VBM}$ of a reduced and ground 0.2 wt.% Mn-doped BaTiO$_3$ ceramics during the stepwise deposition of the ITO electrode and the annealing treatments. The valence band maximum binding energies was deduced from the shift of Ti $2p_{3/2}$ core level by substation the core level to valence band maximum distance given in the legend.

of $E_F - E_{VBM}$ to the initial value of 3.18 eV. Most likely the reduced electrode after heating in vacuum is no longer homogeneously covering the 0.2 wt.% Mn-doped BaTiO$_3$ substrate. Furthermore, the ITO electrode is completely reduced to partially metallic In and Sn, which substantially affects the work function of the electrode and, thus the Schottky barrier height. Both, the Sn and In island formation and the altered electrode work function, will affect the resulting barrier formation.

Equilibrated 0.6 wt. % Mn-doped BaTiO$_3$

In order to reveal whether the initial oxidation state of the specimen has a major influence on the heat treatment experiments, also an equilibrated 0.6 wt.% Mn-doped BaTiO$_3$ specimen with 3.33 nm ITO electrode was post-heated. Here, the first heating step was conducted for 1h at 400 °C in 0.5 Pa O$_2$, followed by a second heating step for 1h at 400 °C in vacuum.

The core level spectra of the Ba $3d_{5/2}$, O $1s$, Sn $3d_{5/2}$, In $3d_{5/2}$, Ti $2p$, and Ba $4d$ emission for a ITO thickness of 3.33 nm as well as after heating for 1 h at 400 °C in oxygen and in vacuum are shown in Figure 6.13 from bottom to top. After 3.33 nm ITO deposition, both Ba emissions as well as the Ti $2p$ emission exhibit the regular peak shapes with their binding energies referring to a Fermi energy of 2.45 eV. The O $1s$, Sn $3d_{5/2}$, and In $3d_{5/2}$ show the typical asymmetry towards higher binding energies, which originates from the excitation of plasmons in the free electron gas [205, 251]. The binding energies of the Sn $3d_{5/2}$ and In $3d_{5/2}$ are slightly higher
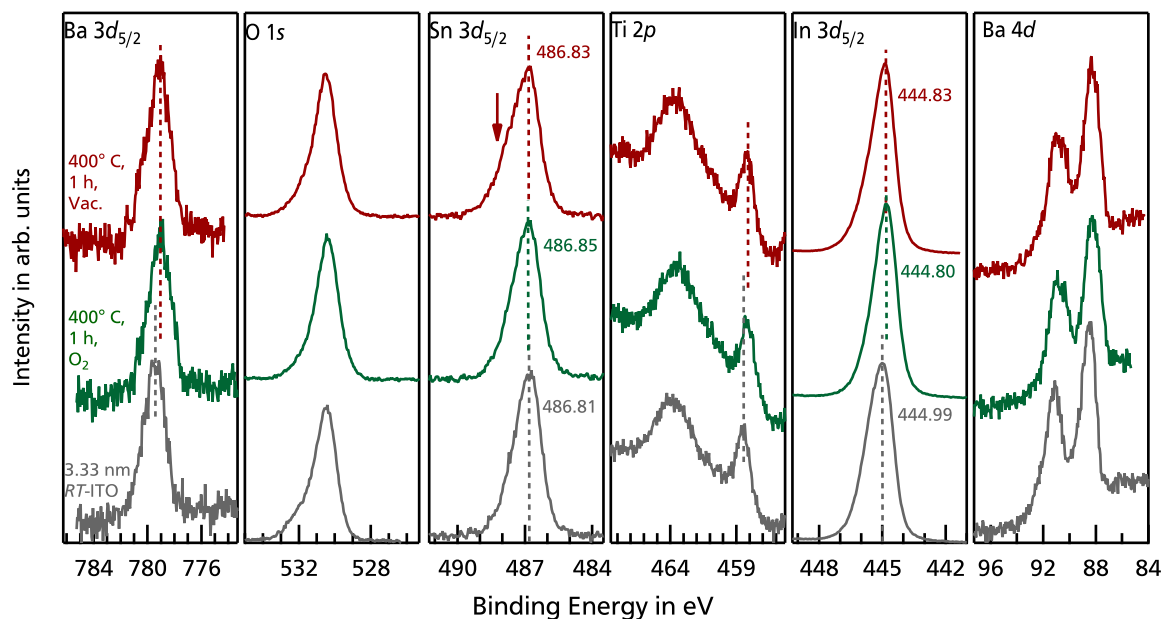
Figure 6.15.: X-ray photoelectron core level spectra of the $Ba\,3d_{5/2}$, $O\,1s$, $Sn\,3d_{5/2}$, $In\,3d_{5/2}$, $Ti\,2p$, and $Ba\,4d$ emissions of an equilibrated 0.6 wt.% Mn-doped $BaTiO_3$. The spectra were recorded during contact formation to ITO and after post-heating in oxygen/vacuum. The Sn-doped In_2O_3 electrode thickness as well as the used post-treatment parameters are indicated in the $Ba\,3d_{5/2}$ spectrum. The film thickness of ITO was calculated based on the respective accumulated deposition time with an assumed deposition rate of 5 nm/min. The binding energy indicated by the vertical dashed lines in the Sn and In core levels are given in eV. The spectra were recorded with monochromatic Al K_α radiation.

than in previous interface experiments for the same thickness[13]. After the heating for 1h at 400 °C in 0.5 Pa O_2 no changes in peak shape of the Ba and Ti emission are detected. Solely a shift of 0.35 eV towards lower binding energy is observed for the latter core levels. Whereas only a slight shift towards higher binding energies is observed for the $Sn\,3d_{5/2}$ emission, the $In\,3d_{5/2}$ is shifted by approximately 0.2 eV towards lower binding energies. The different shift of the Sn and In emission upon oxidation are in good agreement with the work of Gassenbauer, who studied the position of the core level emission lines of thick ITO films in dependence on the oxygen content in the process gas during ITO deposition [244]. Within the latter work, the different shifts have been explained by a different strong screening of the created core hole by the conduction electrons [244]. In order to discuss the small changes in the peak shape of the ITO films prepared in this work, background subtracted and normalized $In\,3d_{5/2}$ and $Sn\,3d_{5/2}$ core level spectra are shown in Figure 6.16 a) and b), respectively. Here, the peaks recorded after heating have been shifted to the binding energy position of the 3.33 nm ITO film for better comparison. Whereas the shape of the $Sn\,3d_{5/2}$ emission is unaffected by heating

---

[13]The target was exchanged only 1.5 month later due to a deep race track and a long live time. Most likely the target was already heavily reduced which may contribute to the higher binding energies.

in oxygen, the $In\,3d_{5/2}$ emission is getting more symmetric, as the plasmon excitation related shoulder towards higher binding energies is decreasing.

After heating in vacuum no significant changes in the peak shape and binding energy position are observed for the Ba and Ti emissions. Only a minor shift towards the original binding energy position is observed in the $In\,3d_{5/2}$ and $Sn\,3d_{5/2}$ core level emissions. Additionally, the shoulder towards higher binding energies increases in the $In\,3d_{5/2}$ as well as in the $Sn\,3d_{5/2}$ emission. This indicates an enhancement of plasmon excitations after heating in reducing atmosphere. The observed trend of decreasing/increasing plasmon excitation upon oxidation/reduction is consistent with the underlying defect model for the creation of free electrons. A more extended discussion on the plasmon excitation in ITO is omitted in this thesis and can be found in detail in Ref. [244].

The evolution of $E_F - E_{VBM}$ of the equilibrated 0.6 wt.% Mn-doped $BaTiO_3$ substrate is shown in Figure 6.16 c). The Fermi level of 2.45 eV after contact formation to ITO is consistent with the ones derived in Figure 6.11. After heating in oxygen a Fermi level of $E_F - E_{VBM} = 2.1\,eV$ is extracted from the $Ti\,2p_{3/2}$ core level emission. A shift towards lower binding energies is generally expected for oxidizing conditions. In the present interface configuration, however, again the property changes of the ITO electrode upon heating in different atmospheres need to be considered as well. Gassenbauer *et al.* showed, that the work function of ITO is increasing from 4.4 eV to 5.2 eV with decreasing Fermi level (which was achieved by increasing the O_2
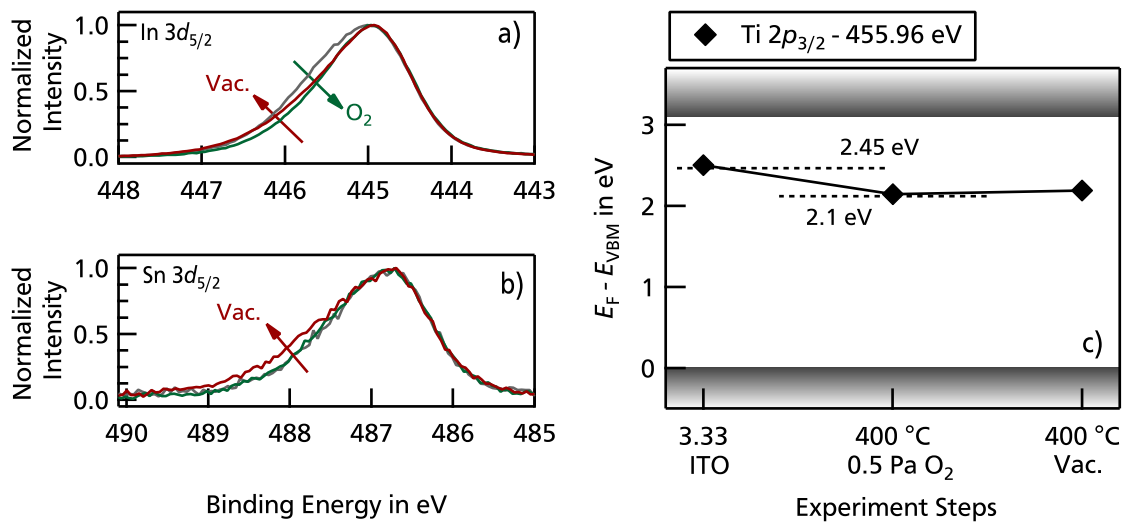
Figure 6.16.: Background subtracted and normalized a) $In\,3d_{5/2}$ and b) $Sn\,3d_{5/2}$ core level emissions of the as-deposited ITO interface (gray) and after heating in oxygen (green) and vacuum (red). The spectra of the heat-treatments have been shifted to the position of the as-deposited spectra for better comparison. c) Evolution of the valence band maximum binding energies $E_F - E_{VBM}$ of a reduced and ground 0.2 wt.% Mn-doped $BaTiO_3$ ceramics during the stepwise deposition of the ITO electrode and the annealing treatments. The valence band maximum binding energies was deduced from the shift of $Ti\,2p_{3/2}$ core level by substation the core level to valence band maximum distance given in the legend.

content during deposition) [252]. In the latter publication the increase in work function was attributed to a passivisation of the electronic surface states by the adsorption of oxygen [252]. For the present interface an increased ITO work function would result in an increased Schottky barrier for electrons and thus in a lowering of the Fermi level of 0.6 wt.% Mn-doped BaTiO$_3$. Thus, the observed decrease in $E_\mathrm{F} - E_\mathrm{VBM}$ could, in principle, be attributed to an altered work function of the ITO electrode upon heating in oxygen. The increase of the ITO work function, however, is related to adsorbed oxygen and thus only to the surface of the deposited ITO thin film. If the interface is affected by a changed surface work function of ITO remains inconclusive. After heating in vacuum no distinct change in Fermi level position of 0.6 wt.% Mn-doped BaTiO$_3$ is observed. Furthermore, no metallic In or Sn has been observed in the spectra, as it was the case for the reduced 0.2 wt.% Mn-doped BaTiO$_3$/ ITO interface, which has been heated in vacuum under the same conditions (see Figure A.15). The Mn-content, the oxidation state of the BaTiO$_3$ substrate, and the additional oxygen heating step are the main differences between both experiments. As no significant influence of the Mn-content has been observed on the interface formation in Figure 6.11, this explanation is excluded. Furthermore, heating at 400 °C for 1 h is assumed to be sufficient for the oxygen diffusion to reach equilibrium in the ITO films. Thus, a major influence of the first heat-treatment in oxygen is also not assumed. Evidently, the oxidation state of the substrate seems to have an influence on the interface during heating in vacuum. Possibly, the equilibrated 0.6 wt.% Mn-doped BaTiO$_3$ substrate serves as an oxygen reservoir for the ITO electrode during heating in vacuum and, thus, prevents the reduction of ITO to metallic In and Sn.

6.3.3. Additional experiments

In-situ resistance degradation experiments have been conducted for equilibrated undoped BaTiO$_3$ with thin ITO as top electrode and Pt as bottom electrode at 145 °C and an electric field of 0.3 kV/mm. The corresponding data is discussed in Appendix A.3.3. The thin ITO top electrode has been connected as anode and cathode for two different undoped BaTiO$_3$ specimens. After degradation of both samples, no considerable changes have been observed in the binding energy and in the peak shape of both, the BaTiO$_3$ substrate and the ITO electrode emission lines. The absent change of the interface Fermi level position corresponds to a constant Schottky barrier height before and after degradation. This missing influence of oxygen vacancy depletion/accumulation of the anode/cathode region on the measured Fermi level was expected due to the high permittivity of BaTiO$_3$ and the high resulting SCR width.

6.4. Summary

The objective of this Chapter was to elaborate if the interface approach can be used to identify the defect energy level in acceptor-doped polycrystalline $BaTiO_3$. For this purpose, a systematic study on the contact formation of RuO_2 and Sn-doped In_2O_3 electrodes to polycrystalline Mn-doped $BaTiO_3$ceramics with different $V_O^{\bullet\bullet}$-content was conducted. From the high introduced defect concentrations a space charge region width comparable to the inelastic mean free path of the photoelectrons was expected, which should allow the identification of the manganese defect levels in the band gap. The main observations can be summarized as follows:

Surface cleaning procedure: As-sintered and equilibrated samples have been heated for 1 h at 400 °C in oxygen in order to successfully removed the carbon species from the surface. Reduced samples have been heated for 1 h at 500 °C to maintain the oxidation states. As expected from literature [205] heating in vacuum was less efficient and resulted in an incomplete carbon removal. Besides the Ca contamination/impurity an additional Si contamination has been observed, which could (partially) be removed by grinding the surface after reduction. As origin the reduction treatment inside a quartz tube is proposed.

Surface Ba-enrichment after reduction: The comparison of reduced and reduced and ground 0.5 wt.% Mn-doped $BaTiO_3$ specimens revealed significant differences. First, the reduced specimens reveal a drastically increased intensity of the surface related high binding energy component Ba II of both Ba emissions and an additional O III component in the O 1s core level spectra. And second, the Ba/Ti ratio is significantly increased to 1.6 for reduced samples compared to 0.9 for reduced and ground samples, indicating a Ba-enrichment at the surface after reduction. The Ba-enrichment seems to be Mn-doping concentration dependent, with a higher enrichment for higher Mn-content. A surface Ba-enrichment has not been reported in literature so far. However, also no XPS studies on extremely reduced acceptor-doped polycrystalline $BaTiO_3$ are available, yet. The chemical nature of the Ba-rich surface phase remains unclear. Potential phases such as BaO, $BaCO_3$, $Ba(OH)_2$, $BaTi_2O_4$, or Ruddlesden-Popper phases with incorporated additional BaO layers have been discussed. However, none of these could be clearly confirmed by XPS or EDX analysis.

$BaTiO_3$:Mn/RuO_2 interface: Contact formation towards RuO_2 electrodes revealed an E_F-E_{VBM} of 2.0 eV for reduced and 1.7 eV for equilibrated/oxidized polycrystalline $BaTiO_3$ independent on the Mn-concentration. The observed Ba-enrichment on the surface of reduced Mn-doped $BaTiO_3$ indicates the presence of a secondary phase, which could affect the Fermi level position during contact formation. Thus, the Ba-rich surface of a 0.5 wt.% Mn-doped $BaTiO_3$ specimen was removed after reduction and the interface formation towards RuO_2 was repeated. The

removal of the Ba-rich surface layer results in a Fermi energy of $E_F - E_{VBM} = 1.7 \pm 0.05$ eV, which is identical with the one derived for equilibrated/oxidized specimens. Hence, the derived value of $E_F - E_{VBM} = 1.7 \pm 0.05$ eV after contact formation to RuO_2 is independent on the Mn-doping and the oxygen vacancy concentration. The absent influence of Mn-doping concentration and oxidation state indicates, that the extracted Fermi level refers to the interface and not to the bulk. This is in clear contrast to the expectations prior the experiments, for which the introduced high doping concentrations was expected to narrow the space charge region to a width comparable to the inelastic mean free path of the photoelectrons, where the measured Fermi level is close to that in the bulk.

Simulation of the $BaTiO_3$:Mn/RuO_2 interface: The space charge region width is the essential parameter for the interpretation of the measured Fermi level. Thus, the resulting energy band diagrams for RuO_2 interface towards 0.5 wt.% Mn-doped $BaTiO_3$ have been simulated based on the experimentally derived values for the Fermi energy of $E_F - E_{VBM} = 1.7$ eV by solving the Poisson equation. The simulated energy band diagrams confirmed that the width of the space charge region is considerable larger than the inelastic mean free path of the photoelectrons. This proves that the measured binding energies correspond to the Fermi level right at the interface and elucidates the absent pinning of the Fermi energy at the charge transition level of Mn for the used interface settings. Furthermore, the results indicate that the space charge region width strongly depends on the permittivity of the material. This explains why Fermi level pinning on defect levels was successfully observed by means of XPS in low permittivity ZnO [28, 29] but not for the present high permittivity Mn-doped $BaTiO_3$.

The measured Fermi level of $E_F - E_{VBM} = 1.7$ eV right at the $BaTiO_3$:Mn/RuO_2 interface corresponds to a Schottky barrier height for electrons of $\Phi_{B,n} = 1.4$ eV. This value is lower than the expected value of $\Phi_{B,n} = 1.7$ eV derived from the Schottky-Mott rule, which could be an indication for a certain degree of interface states. Still, the Schottky barrier height for electrons of $\Phi_{B,n} = 1.4$ eV observed in this work is considerable larger than the ones observed at previous RuO_2 interfaces towards single crystalline $BaTiO_3$, for which $\Phi_{B,n} = 1.0$ eV to 1.1 eV was extracted [215]. Furthermore, the present value of $\Phi_{B,n} = 1.4$ eV is only slightly lower than the highest reported Schottky barrier height for electrons of $\Phi_{B,n} = 1.49$ eV at $BaTiO_3$/NiO interfaces [216].

$BaTiO_3$:Mn/ITO interface: The contact formation towards *RT*-deposited Sn-doped In_2O_3 electrodes revealed a Mn-content independent Fermi energy of $E_F - E_{VBM} = 3.0 \pm 0.05$ eV for reduced and $E_F - E_{VBM} \approx 2.5$ eV for equilibrated/oxidized polycrystalline Mn-doped $BaTiO_3$. The removal of the Ba-rich surface layer of a reduced 0.2 wt.% Mn-doped $BaTiO_3$ specimen results in an interface Fermi energy of 2.85 eV. The discrepancy of the latter value with the ones derived on the equilibrated/oxidized interfaces was unexpected, as the removal of the

Ba-rich surface results in a treatment-independent Fermi level at the RuO_2 interfaces. The remaining difference for the $BaTiO_3$:Mn/ITO interfaces might be attributed to an insufficient compensation of the high space charge of reduced samples due to a low conductivity and, thus, a low charge carrier concentration of *RT*-deposited ITO thin films. The measured Fermi level of $E_F - E_{VBM} \approx 2.5\,\mathrm{eV}$ right at the equilibrated/oxidized $BaTiO_3$:Mn/ITO interface corresponds to a Schottky barrier height for electrons of $\Phi_{B,n} = 0.6\,\mathrm{eV}$. This value is in agreement with the expected value derived from the Schottky-Mott rule, assuming a *RT*-ITO work function of 4.5 eV[14].

Post heating of $BaTiO_3$:Mn/RuO_2 and $BaTiO_3$:Mn/ITO interfaces: Ionic defects, including oxygen vacancies, in $BaTiO_3$ are immobile at room temperature. Therefore, selected RuO_2 and Sn-doped In_2O_3 interfaces have been post-heated in different atmospheres and at different temperatures to reveal the influence of possible oxygen vacancy redistribution on the Schottky barrier heights and width of the space charge region. Vacuum heating of RuO_2 and Sn-doped In_2O_3 interfaces towards reduced Mn-doped $BaTiO_3$ specimens resulted in the reduction of RuO_2 to metallic Ru and the reduction of Sn-doped In_2O_3 to metallic Sn and In. The transition into the metallic electrode components was accompanied by an increase in the $BaTiO_3$:Mn substrate emission lines, which indicates island formation. The interpretation of the modified interface Fermi energy depends strongly on the electrode work function, which is assumed to be considerably altered after the appearance of metallic Ru/Sn/In. Oxygen and vacuum heating of Sn-doped In_2O_3 interfaces towards equilibrated Mn-doped $BaTiO_3$ specimens did not reveal metallic Sn and In. Thus, the appearance of metallic Sn/In is attributed to the reducing heating condition in combination with the reduced Mn-doped $BaTiO_3$ substrate.

Voltage experiments: *RT* voltage experiments have been performed on a $BaTiO_3$:Mn/RuO_2 interface to study the influence of X-rays illumination on the oxygen diffusivity. No considerable changes of the peak shape and position have been observed and, therefore, any influence of the X-rays on the oxygen diffusivity and the resulting Schottky barrier can be excluded.

---

[14]The work function of room-temperature deposited ITO has not been measured within this work and the value of 4.5 eV is only an estimation based on the mean values of measurements conducted in previous works [95, 202, 253–255]. In general, the room temperature work function of ITO scatters in a wide range of approx. 4.2 eV to 5.5 eV, depending on the history (e.g. oxygen content, time of usage) of the target, and hence the derived E_F in the deposited ITO thin films [202, 203].

6.5. Conclusion

The original goal of the work described in this Chapter was the identification of the manganese defect levels by means of XPS analysis. The presented work provides the first systematic study on the contact formation of RuO_2 and Sn-doped In_2O_3 electrodes to polycrystalline $BaTiO_3$ ceramics with different Mn-doping concentrations and $V_O^{\bullet\bullet}$-content. The extracted Fermi energies from this experiments were expected to supply the necessary systematic data for the evolution of the space-charge potential on the bulk Mn- and $V_O^{\bullet\bullet}$-concentrations. The results, however, do not indicate any influence of Mn-doping and $V_O^{\bullet\bullet}$ concentration on the recorded Fermi energies, which implies that the measured binding energies refer to the interface Fermi level. Hence, the original goal of manganese defect level identification could not be achieved. The simulation revealed that the high permittivity of the $BaTiO_3$ ceramic is responsible for the large space charge region, making a defect level identification by means of XPS impossible. From the present results it is clear that the same doping concentration in low and high permittivity materials will have different influences on the space charge region width (see Figure 6.9 a)).

⇒ *Defect level identification of the acceptor energy levels in polycrystalline $BaTiO_3$ is not feasible via the interface approach.*

⇒ *The simulation on the $BaTiO_3$:Mn/RuO_2 qualitatively show the influence of the material's permittivity one the SCR width. These results imply that Fermi level pinning on defect levels can be successfully observed by mean of XPS in low permittivity materials but not in high permittivity materials such as $BaTiO_3$.*

In general, the width of the space charge regions will have consequences on the oxygen diffusion and the electrical properties, which are both essential for resistance degradation. First, the space charge region affects the oxygen exchange kinetics at the surface/electrode interface, where the space charge region can reduce the oxygen incorporation [16]. Second, the width of the space charge region at the grain boundaries has a considerable influence on the electrical transport properties through the ceramic capacitor. Grain boundaries in (acceptor-doped) $BaTiO_3$ are assumed to have a positive grain boundary core charge, which leads to an oxygen vacancy depleted space-charge region [16, 57, 78]. Here, the oxygen diffusion is suppressed in the oxygen vacancy depleted space-charge region compared to the bulk. Additionally, the corresponding downward band bending implies that the electron conduction is enhanced in this region. Due to their larger space charge regions, the influence of grain boundaries on the oxygen diffusion/electronic properties will be more pronounced for materials with higher permittivities. Furthermore, different doping concentrations are necessary for low and high permittivity materials (e.g. $SrTiO_3$ and $BaTiO_3$) to achieve the same influence on the space charge region width.

The influence of post-heating on the interface properties was the secondary goal of the work described in this Chapter. For this purpose, several post-heating experiments with different Mn-doped $BaTiO_3$ substrates have been performed. The presented heating experiments contribute to a new experiment series on the stability of RuO_2 and ITO electrodes on different substrates upon post-heating at different temperatures and atmospheres. The heating experiments with ITO electrodes at 300 °C in vacuum revealed metallic Sn and In for reduced Mn-doped $BaTiO_3$ substrates, whereas no metallic components have been observed for the equilibrated Mn-doped $BaTiO_3$ substrate. The influence of the oxygen vacancy concentration of the Mn-doped $BaTiO_3$ substrate on the reduction of the ITO electrode indicates that the equilibrated substrate serves as an oxygen reservoir, which prevents the reduction to metallic Sn and In. Thus, oxygen exchange is assumed at the BTO:Mn/ITO interfaces during post-heating. A reduced BTO:Mn/RuO_2 interface revealed metallic Ru after vacuum post-heating. Here, an additional vacuum heating experiment of an equilibrated BTO:Mn/RuO_2 interface is necessary to conclude on the oxygen exchange at BTO:Mn/RuO_2 interfaces.

7. Defect level identification in polycrystalline acceptor-doped BaTiO$_3$ using the re-oxidation approach

Within the previous Chapter the influence of acceptor dopants on the space charge region properties, such as Schottky barrier height and the width of the SCR, have been investigated. Another region of interest are the grain boundaries in the ceramic capacitors. In BaTiO$_3$-based ceramic capacitors the oxygen transport across the grain boundaries is rate-limiting for the degradation process of the capacitor. Waser *et al.* introduced the ΔU_{gb}-concept, where a potential drop is assumed at each grain boundary [4]. The potential drop ΔU_{gb} per grain boundary is defined by $\Delta U_{gb} = (d_{gr}/d) \cdot U = d_{gr} \cdot E$, where d_{gr} is the mean grain size, d the dielectric thickness, U the voltage and E the electric field. Thus, the increase in degradation time is directly related to the number of grain boundaries in the capacitor. Besides the total amount of grain boundaries also their blocking characteristics for oxygen transport are of essential importance. Again the Schottky barrier height and the width of the resulting space charge region are determining the oxygen transport across the grain boundaries. Both can be modified by the intentional introduction of acceptor dopants. The Schottky barrier height at the grain boundary is defined by the difference in their Fermi level to the bulk. If the bulk Fermi level is pinned on a charge transition level of an acceptor dopant, the overall Schottky barrier height is altered. Thus, the barrier height and the overall resistance degradation of the capacitor can be controlled by the introduction of dopants with a known defect energy level.

In the previous Chapter it could be shown, that the identification of the defect level via the interface approach is unsuitable due to the high permittivity of BaTiO$_3$. Another approach was recently presented by Suzuki *et al.*, who successfully determined the charge transition levels of Fe during the re-oxidation of a BaTiO$_3$ single crystal [22]. The latter study was based on the idea, that the activation energy of electrical transport depends on the oxygen vacancy concentration, which affects the oxidation state of the introduced multi-valent acceptor. Hence, the pinning of the Fermi level at the defect levels during oxygen incorporation should result in a pinning/a plateau of the activation energy as well.

The main results[1] of Suzuki *et al.* are presented in Figure 7.1. First, a $BaTiO_3$ single crystal with $3.0 \times 10^{17} \, cm^{-3}$ Fe-impurities was reduced by heating in vacuum. This treatment ensures a Fermi level close to the conduction band minimum [216], which was confirmed by the high starting conductivities of $\sim 10^{-2} \, S/cm$. The stepwise re-oxidation of the sample was accomplished by repetitive heating and cooling cycles in air. The conductivity was recorded during each cycle and is shown in Figure 7.1 a). Within each re-oxidation cycle oxygen is incorporated, resulting in a lower conductivity during cooling compared to heating of the same cycle. The hysteresis observed around $128 \, °C$ is related to the phase transition of the tetragonal ferroelectric phase to the cubic paraelectric phase and is enhanced in the inlay (for further
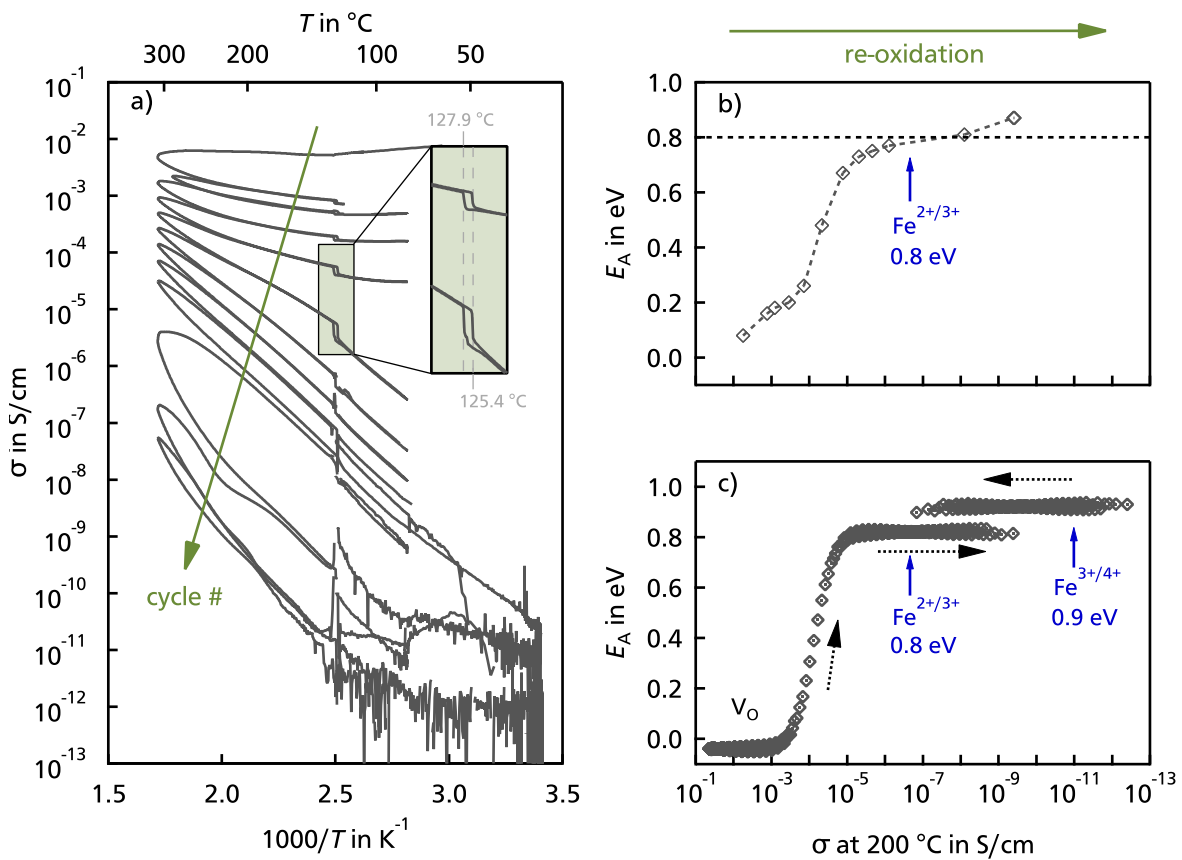

Figure 7.1.: a) Re-oxidation of a reduced nominally undoped $BaTiO_3$ single crystal with $3.0 \times 10^{17} \, cm^{-3}$ Fe-impurities. The phase transition from the tetragonal ferroelectric to the cubic paraelectric phase is magnified in the inlay. b) Experimentally determined activation energy at $200 \, °C$ vs. the corresponding conductivity for the loops presented in a). c) Theoretical activation energy as a function of conductivity derived from the corresponding defect model calculations described in [22]. The experimental data was recorded by I. Suzuki during his stay in the Surface Science group of Materials Science Department at TU Darmstadt. The defect model calculations have be performed by A. Klein of the ESM group from Materials Science Department of TU Darmstadt. The data is published in Ref. [22].

---

[1]The experimental data was provided by A. Klein in a private communication. The data is published in Ref. [22].

discussion see Ref. [22]). The extracted activation energy during re-oxidation is given in Figure 7.1 b). Here, the conductivity at 200 °C serves as a measure for the re-oxidation state and is used as x-axis. During the first re-oxidation cycles the activation energy increases slightly from 0.1 eV to 0.2 eV until a sudden increase in activation energy to 0.8 eV is observed at a conductivity of 10^{-3}-10^{-5} S/cm. The corresponding defect model calculations[2] are shown in Figure 7.1 c). The experimental value of the plateau of 0.8 eV as well as the rise of activation energy at a conductivity of 10^{-3}-10^{-5} S/cm corresponds well with the $E_A(\sigma)$ dependency derived from the defect model. Within the latter the plateau at 0.8 eV is assigned to the $Fe^{2+/3+}$ transition. Here, the experimentally derived value of 0.8 eV is in good agreement with literature values for the $Fe^{2+/3+}$ transition [21]. Thus, the re-oxidation approach of Suzuki *et al.* is assumed to be valid for the determination of the defect level [22].

Within this Chapter re-oxidation experiments have been performed on a series of Mn- and Fe-doped $BaTiO_3$ ceramics. The aim of the experiments was the determination of the Mn and Fe charge transition levels. However, the presence of grain boundaries will add an additional activation energy term in the carrier mobility. Hence, the direct extraction of the defect energy level from the Arrhenius plot of the temperature dependent conductivity during re-oxidation is assumed to be more complex.

Thus, the first experimental step was the study of the different contributions to the overall activation energy. For a single crystal solely the bulk and the electrode interface have a contribution to the overall conductivity. The corresponding equivalent circuit for a single crystal is shown in Figure 7.2 on the left. The measurements of Suzuki *et al.* indicate that the electrode interface has no considerable influence on the the overall activation energy [22]. The authors assumed that the high oxygen vacancy concentration after reduction narrows the SCR at the electrode
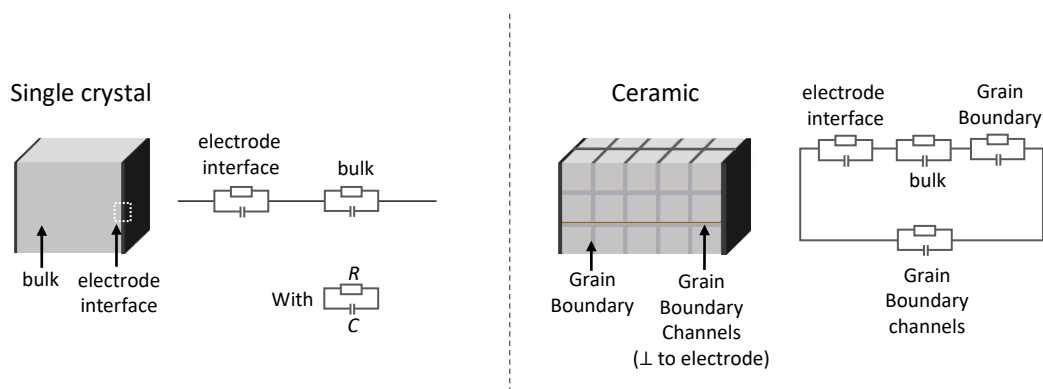
Figure 7.2.: Left: Sketch of a single crystal with the corresponding equivalent circuit. Right: Sketch of a polycrystal simplified by the brick-wall model with the corresponding equivalent circuit. The brick-wall model and the equivalent circuit for the polycrystals have been adapted from Ref. [57].

---

[2]For details on the defect model calculations see Ref. [22].

interface to a width, where electron tunneling is possible [22]. However, the assumption was not experimentally proven in the work of Suzuki *et al.*. Hence, the contribution of the Schottky barrier height at the electrode interface was investigated within a first experimental step in this work. Therefore, *IV*-curves were recorded for STO:Nb and STO:V$_O^{\bullet\bullet}$.

In polycrystalline materials grain boundaries will add an additional conductivity contribution to the equivalent circuit (see Fig. 7.2 on the right). Here, the grain boundary contribution is divided in grain boundaries parallel and perpendicular to the electrodes. The former add an additional activation energy term in the carrier mobility, while the latter may act as an additional path for charge transport. Therefore, the general contribution of grain boundaries on the re-oxidation approach was investigated within a re-oxidation experiment of an nominally undoped polycrystalline BaTiO$_3$. The introduction of acceptor dopants will influence the Fermi level position in the bulk and will affect the Schottky barrier height and width of the SCR at the grain boundaries. Here, the multi-valency (2+/3+/4+) and the corresponding Fermi level pinning on the defect energy levels of Mn and Fe will further complicate the grain boundary characteristics. Thus, the general influence of acceptors was investigated on a fixed-valence Al-doped SrTiO$_3$ polycrystal.

In a third step re-oxidation experiments were performed on Mn- and Fe-doped polycrystalline BaTiO$_3$, where both dopants are so-called multi-valence acceptor dopants. Furthermore, the conductivity across the grain boundaries has been simulated for the Mn- and Fe-doped BaTiO$_3$ ceramics based on the model introduced by De Souza [79]. The extracted experimental activation energy is compared to the simulated values. Based on the grain boundary simulation, predictions on the degradation characteristics of Mn- and Fe-doped BaTiO$_3$ are made.

7.1. Contribution of the electrode interface

The extraction of the defect energy levels from the activation energy of the temperature dependent conductivity is directly related to the different contributions to the latter. Schottky barrier are formed at the interfaces between the dielectric bulk and the electrode, which may affect the charge transport at the interfaces. Thus, the contact characteristics to the platinum electrodes have to be examined in a first step. Based on the interpretation of their results, Suzuki *et al.* ruled out a contribution of the Schottky barrier at the electrode interface on the re-oxidation approach. The authors proposed, that the high oxygen vacancy concentration after reduction narrows the SCR at the electrode interface to a width, where electron tunneling is possible [22]. However, this assumption has not been proven in the scope of the publication. In order to prove this hypothesis for the present work, STO:Nb and STO:V$_O^{\bullet\bullet}$ single crystals were coated

with an ITO back contact and a platinum front contact[3]. Then, the temperature dependent *IV*-characteristics were recorded in order to identify the front contact properties. Due to the ohmic contact properties of the ITO back electrode only the Pt front contact properties are characterized in the experiment. Here, single crystalline samples were used in order to exclude any additional contributions of grain boundaries. STO was used as a host material as no doped BTO single crystals were available. Due to the comparable defect chemistry of both materials, the results of the experiment on STO are assumed to be transferable to BTO.

The following experimental outcome was assumed prior the experiments: Both STO single crystals are doped with donors (Nb or $V_O^{\bullet\bullet}$). However, $V_O^{\bullet\bullet}$ are mobile at moderate temperatures, while Nb-dopants are immobile. During heating the mobile oxygen vacancies in STO:$V_O^{\bullet\bullet}$ will accumulate in the space charge layer at the interface. As a result, the space charge region will become narrow enough for electron tunneling, which will lead to an ohmic contact behavior. The Nb-dopants in STO:Nb are immobile in the whole temperature range of the experiment. Hence, an accumulation of Nb donors in the resulting SCR at the electrode interface is not possible. Therefore, a rectifying current-voltage curve is expected for STO:Nb.
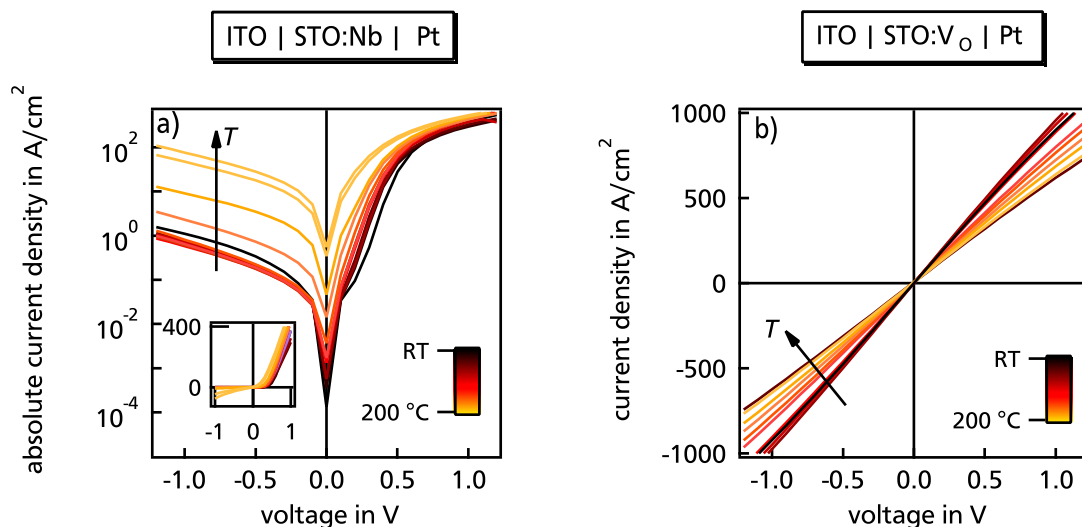
Figure 7.3.: *IV*-curves of a) STO:Nb and b) STO:$V_O^{\bullet\bullet}$ from *RT* to 200 °C in 50 °C steps. The inlay in a) shows the current density. A 50 nm *HT*-ITO was used as back contact and round Pt electrodes with a diameter of 100 μm as front contact.

The corresponding *IV*-curves of STO:Nb and STO:$V_O^{\bullet\bullet}$ are given in Figure 7.3 a) and b), respectively. The *IV*-curves of STO:Nb clearly confirm the rectifying characteristics of the Schottky

---

[3]Here, STO:$V_O^{\bullet\bullet}$ refers to a SrTiO$_3$ single crystal, which was reduced for 12 h at 1100 °C in 5 % H$_2$/95 % Ar gas mixture followed by quenching to room temperature. This experiment was conducted within the scope of the Bachelor Thesis of N. Gutmann. For detailed experimental procedure see Ref. [256].

contact towards the Pt electrode. Here, the left branch corresponds to the reverse bias, while the right branch corresponds to the forward bias. As expected, the rectifying characteristics is maintained for the whole temperature range. Solely the current density j_0 is increasing with increasing sample temperature, which was also expected from the temperature dependence of the current density. The observed rectifying characteristics of the STO:Nb/Pt contact are consistent with other literature reports [257].

The *IV*-curves of STO:$V_O^{\bullet\bullet}$ confirm the ohmic characteristics of the interface towards the Pt electrode. Here, the *IV*-curves are straight lines through the origin. With increasing sample temperature the slope of the *IV*-curve is decreasing, which implies that the resistance is increasing. The ohmic contact behavior is maintained through the whole temperature range. A small Schottky barrier height as an origin for the ohmic behavior is excluded[4]. Thus, the observed ohmic contact confirms the working hypothesis, that the accumulation of oxygen vacancies is the space charge layer results in a narrowing, which enables electron tunneling. In such a case, the Schottky barrier does not inhibit the electron transport.

The experimental results on the *IV*-curves of STO:Nb and STO:$V_O^{\bullet\bullet}$ confirmed the working hypothesis. Hence, no influence of the electrode interface on the conductivity is expected for highly reduced $SrTiO_3$ and $BaTiO_3$ samples. However, the oxygen vacancy concentration is gradually decreasing in the scope of the re-oxidation experiments. Hence, the SCR may become wider with decreasing $V_O^{\bullet\bullet}$ content. The decreasing $V_O^{\bullet\bullet}$ concentration in the $BaTiO_3$ bulk is accompanied by a decreasing bulk Fermi level position, which simultaneously decreases the magnitude of the band banding. Flat band potential (similar Fermi level at the contact and in the bulk) does also not add an additionally contribution to the activation energy of the electrical conductivity. With ongoing re-oxidation, the bulk Fermi level decreases further until the direction of band bending is reversed and oxygen vacancies are depleted in the SCR. However, for such low Fermi level *p*-conductance is expected. In order to experimentally prove the negligible contribution of electrodes for the whole re-oxidation experiment, further *IV*-curve measurements on STO:$V_O^{\bullet\bullet}$ or BTO:$V_O^{\bullet\bullet}$ single crystals with different $V_O^{\bullet\bullet}$ concentrations are recommended. Still, the measurements of Suzuki *et al.* seemed to be unaffected by the electrode interface through the whole re-oxidation experiment [22]. Hence, this is also assumed for the present experiments.

In summary, no influence of the electrode interface on the measured conductivity is assumed for reduced $BaTiO_3$ samples during the whole re-oxidation experiments.

---

[4]From the Mott Schottky rule a Schottky barrier of 1.4 eV is expected, when taking 4.2 eV [232] for the electron affinity of STO and 5.6 eV [232] as work function of Pt.

7.2. Contribution of grain boundaries and fixed-valence acceptors

In order to examine the influence of grain boundaries on the measured conductivity and extracted activation energy, re-oxidation experiments have been conducted on polycrystalline nominally undoped $BaTiO_3$. Furthermore, re-oxidation measurements have been performed on polycrystalline Al-doped $SrTiO_3$ in order to evaluate the influence of fixed-valent acceptors. As Al has no charge transition level inside the band gap of polycrystalline $SrTiO_3$, solely the influence of acceptors is studied without any additional aspects such as valence changes. Due to its availability, an Al-doped $SrTiO_3$ ceramic has been studied instead of an Al-doped $BaTiO_3$ ceramic. Because of their similar crystal and defect structure [84], a transfer of the findings derived on $SrTiO_3$ to $BaTiO_3$ is assumed.

Polycrystalline undoped $BaTiO_3$ and polycrystalline Al-doped $SrTiO_3$
The re-oxidation of polycrystalline nominally undoped $BaTiO_3$ and polycrystalline Al-doped $SrTiO_3$ are shown in Figure 7.4 a) and b). For undoped $BaTiO_3$ a starting conductivity of $>10^{-1}$ S/cm is observed after reduction[5]. The high starting conductivity combined with the color change from light yellow after sintering to black after reduction indicate the highly reduced state of the samples. This was confirmed by XPS measurements on reduced polycrystalline undoped $BaTiO_3$ samples presented in Chapter 6, which revealed a Fermi level close or even inside the conduction band. The slope of the first loop is negative. This either indicates a negative temperature coefficient, which refers to metallic behavior due to the highly reduced state of the sample or it is already related to a beginning re-oxidation during heating. During dwelling, oxygen is incorporated and the conductivity decreases, which confirms that the conduction is n-type (i.e. dominated by electron conductance). The conductivity during cooling is identical with the one of the subsequent heating cycle, indicating that no further oxygen is incorporated during temperature ramping[6]. The hysteresis in the conductivity at $\sim$118 °C during heating and cooling most likely corresponds to the tetragonal to cubic phase transition. A higher magnification of this region is given in Figure A.19. The decrease of the Curie point from initially 130.9 °C after sintering to $\sim$118 °C is in agreement with literature and is attributed to the high concentration of oxygen vacancies after reduction [182]. The conductivity decreases with ongoing re-oxidation until a minimum value is reached. Afterwards the conductivity increases during dwelling, which indicates p-type conduction (i.e. dominated by hole conductance). This is indicated in Figure 7.4 a) by the inversion of the green arrow, which represents the cycle number. The evolution of the activation energy is depicted in Figure 7.5 and will be discussed after the description of polycrystalline Al-doped $SrTiO_3$.

---

[5]The conductivity of the first loop was recorded for temperatures higher than 250 °C. During the cycles the sample was cooled down to either *RT* or 250 °C, which results in the different $1/T$ onsets in the graph.
[6]This only holds for temperatures <400 °C. For higher temperatures the slope during cooling and heating are marked different, indicating oxygen incorporation.

The re-oxidation of polycrystalline Al-doped SrTiO$_3$ is shown in Figure 7.4 b). During the first heating cycle a conductivity of $\sim$5x10^{-3} S/cm is observed. The conductivity decreases with ongoing re-oxidation, which again indicates n-type conductance. SrTiO$_3$ is cubic in the whole temperature range of the re-oxidation experiment, and thus, no hysteresis is observed in the temperature dependent conductivity.

The slope of the loops seems to be slightly temperature dependent, which a higher slope for temperatures >300 °C. The latter indicates a temperature dependent activation energy. This could be related to a temperature induced change in the grain boundary barrier height. During the whole re-oxidation experiment the conductivity remained n-type (decrease of σ during dwelling).
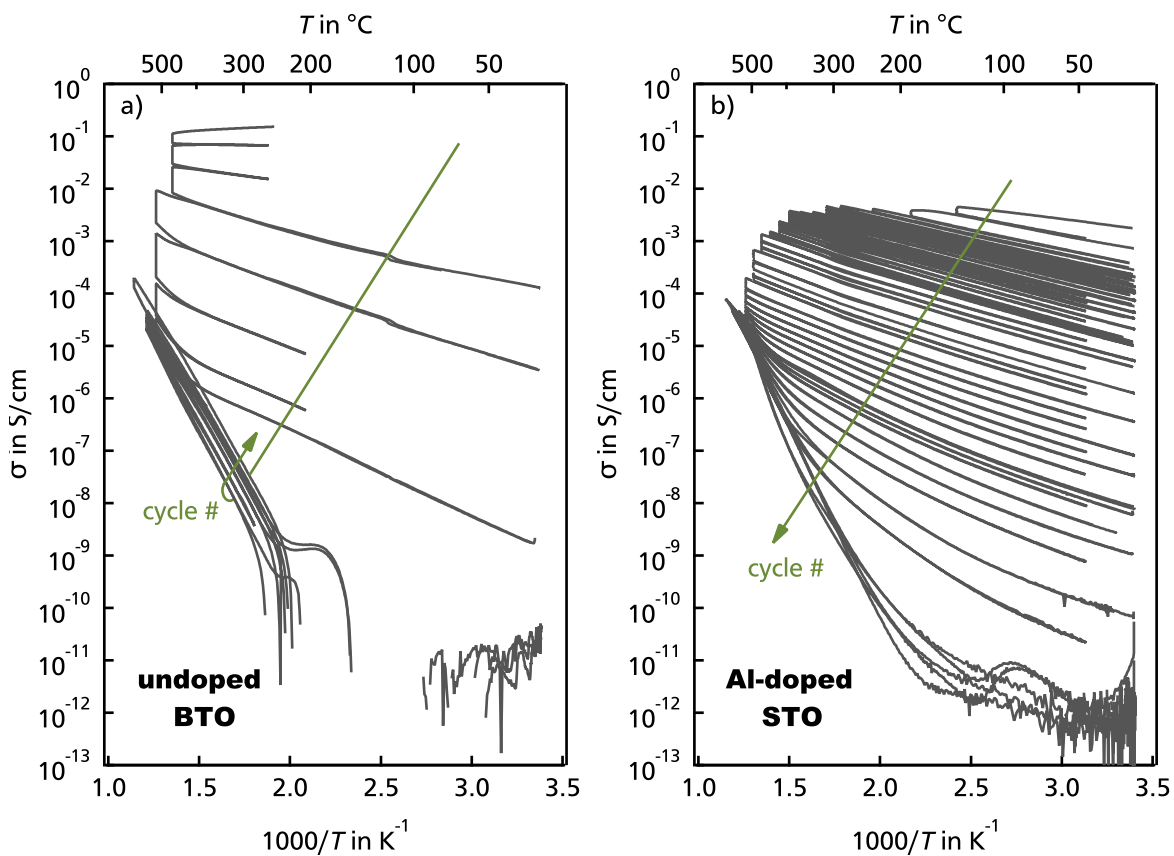
Figure 7.4.: Re-oxidation of a) polycrystalline nominally undoped BaTiO$_3$ and b) polycrystalline Al-doped SrTiO$_3$. The cycle number is indicated by the green arrow: The conductivity of the Al-doped SrTiO$_3$ was n-type during the whole experiment. The conductivity of undoped BaTiO$_3$ was n-type in the beginning of the experiment and p-type in the end, which is indicated by the inversion of the green arrow.

Figure 7.5: Experimental determined activation energy at 400 °C vs. the corresponding conductivity for the loops presented in Figure 7.4 a) and b). The black line refers to polycrystalline nominally undoped BaTiO$_3$, while the green line refers to polycrystalline Al-doped SrTiO$_3$. The transition from n- to p-type conductivity for the undoped BaTiO$_3$ results in an increasing conductivity after the maximum E_A of 1.31 eV was reached.
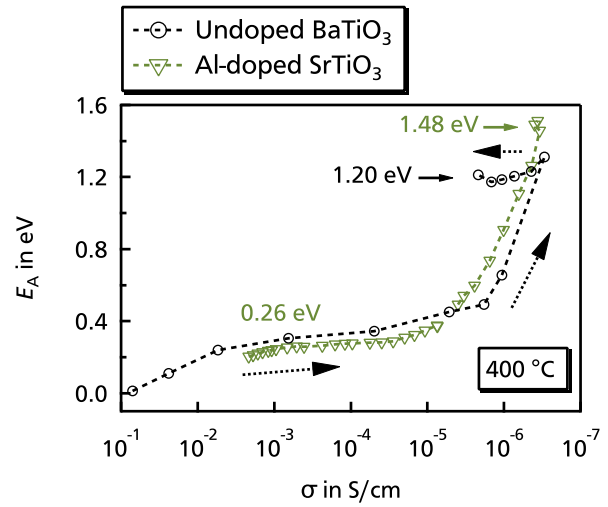
The activation energy as a function of conductivity at 400 °C is shown in Figure 7.5 for polycrystalline nominally undoped BaTiO$_3$ and polycrystalline Al-doped SrTiO$_3$. During the first re-oxidation cycles the activation energy of undoped BaTiO$_3$ increases from 0.0 eV to ~0.35 eV. From the defect level values given by Wechsler and Klein [21], slightly lower activation energies of 0.05 eV and 0.2 eV are expected for the shallow donor levels $V_O^x/V_O^\bullet$ and $V_O^\bullet/V_O^{\bullet\bullet}$, respectively. Hence, the observed plateau in the activation energy in Figure 7.5 is 0.15 eV too high to be clearly assigned to the shallow donor levels of the oxygen vacancies. In addition, oxygen vacancies are rather shallow donors, which are assumed be completely ionized at the present measurement temperature [20, 22]. For this case no temperature-dependence of the charge carrier concentration (and activation energy) is expected. The only contribution to the activation energy of electrical conductivity is expected from the temperature-dependent mobility of free electrons, which is -0.021 eV (see Equation 2.31).

The value of ~0.35 eV might be related to the presence of grain boundaries. However, grain boundaries in acceptor-doped titanates are believed to have a positive core charge, which results in a downward band bending in the SCR. As a result positive charge charge carriers need to overcome a barrier, while negative charge carrier experience no barrier. The conductivity is still n-type in this state of the re-oxidation, hence no additional grain boundary contribution is expected.

At a conductivity of approximately 10^{-6} S/cm the activation energy of undoped BaTiO$_3$ increases to a maximum value of 1.31 eV. Afterwards the conductivity in Figure 7.4 a) is p-type, which is indicated by an increasing conductivity during dwelling. Thus, the conductivity in Figure 7.5 is again increasing after the transition from n- to p-type. The transition from n- to p-type further implies that the Fermi level has crossed the middle of the energy gap[7]. For this scenario it is expected that the activation energy increases to a value of approximately half of

---

[7]Here, the commonly accepted mechanism of band conduction with holes being in the valence band is assumed.

the energy gap. Considering the temperature dependence[8] of the band gap at the evaluation temperature of 400 °C an activation energy of $E_A = E_G(T)/2 = 2.81\,\text{eV}/2 = 1.4\,\text{eV}$ is expected. Hence, the extracted maximum value of 1.31 eV for the activation energy at 400 °C is slightly too low to be clearly assigned to half of the band gap. However, the conductivity switched from n- to p-type after going through this maximum, which indicates that this value of E_A most likely corresponds to mid gap. The activation energy reaches a plateau at 1.2 eV in the p-type region. In this region, the downward band bending at the grain boundaries results in a barrier for the hole conduction, which influences the hole mobility. Both, the carrier concentration as well as their mobility contribute to the measured activation energy. As holes are the majority charge carriers in this region, the measured activation energy of 1.2 eV is assumed to be influenced by the Schottky barrier at the grain boundaries, which contributes via the hole mobility to E_A. Possibly, the 1.2 eV for the activation energy represents the sum of the GB-indued activation energy in the hole mobility and an impurity level, e.g. as Fe in the case of the nominally undoped $BaTiO_3$ single crystal purchased in the paper of Suzuki *et al.* [22] (see Fig. 7.1 c)). During the first re-oxidation cycles the activation energy of the Al-doped $SrTiO_3$ samples is pinned at a plateau of ~0.26 eV. At a conductivity of $\sim 5 \times 10^{-5} - 5 \times 10^{-6}$ S/cm the energy increases to a value of 1.48 eV. This value is again most likely related to the middle of the band gap and refers to band-band excitation. No Al defect level is expected in the band gap and the introduced Al-acceptors are assumed to be charged 3+ during the whole re-oxidation experiment. Hence, no defect related pinning was expected for the Al-doped $SrTiO_3$ samples. This is inline with the evolution of the activation energy in Figure 7.5.

The influence of grain boundaries and acceptor dopants on the re-oxidation time can be extracted by comparing the equivalent re-oxidation time (*ERT*), which is defined by Equation 3.11. The *ERT* is based on the diffusion length of oxygen at the dwell temperature and was established in order to enable a comparison between the different experiments. In Figure 7.6 a) and b) the conductivity and activation energy as a function of *ERT* are compared for polycrystalline undoped $BaTiO_3$, Al-doped $SrTiO_3$, and a $BaTiO_3$ single crystal with Fe-impurities, respectively[9].
For an ideal interpretation of the re-oxidation grade the conductivity and activation energy should be compared at the same temperature. Unfortunately, this was not possible, as the measurement for the $BaTiO_3$ single crystal with Fe-impurities had a maximum dwell temperature of 300 °C, while the measurement of the undoped $BaTiO_3$ ceramic started at 250 °C. Hence, conductivity and E_A values at 200 °C were used for the $BaTiO_3$ single crystal with Fe-impurities, while for nominally undoped $BaTiO_3$ and Al-doped $SrTiO_3$ polycrystals the values at 400 °C

---

[8]The temperature dependent band gap is given by $E_G = E_G^0 - \beta \cdot T$ with $E_G^{0K} = 3.2$ eV and $\beta = 5.7 \times 10^{-4}$ eV/K [6].
[9]The *ERT* for the $BaTiO_3$ single crystal with Fe-impurities was calculated for a dwell time of 5 min from the data of Suzuki *et al.* [22].

were used. Even though the extraction temperature differs, a comparison between those samples is still possible[10].

For the BaTiO$_3$ single crystal with Fe-impurities the re-oxidation is much faster than for polycrystalline BaTiO$_3$. This is indicated by the decrease in conductivity in Figure 7.6 a), which is located at much lower *ERT*s for the BaTiO$_3$ single crystal with Fe-impurities than for polycrystalline undoped BaTiO$_3$[11]. The fast re-oxidation of single crystalline BaTiO$_3$ with Fe-impurities is also reflected by the lower *ERT* value in Figure 7.6 b), for which the activation energy starts to increase. The slower re-oxidation of polycrystalline BaTiO$_3$ can be explained by the presence of grain boundaries. From degradation studies on single and polycrystalline SrTiO$_3$ it is known that the oxygen transport across the grain boundaries is rate limiting[12] [4]. Similar as for the degradation studies, the oxygen blocking behavior of the double Schottky barriers at the grain
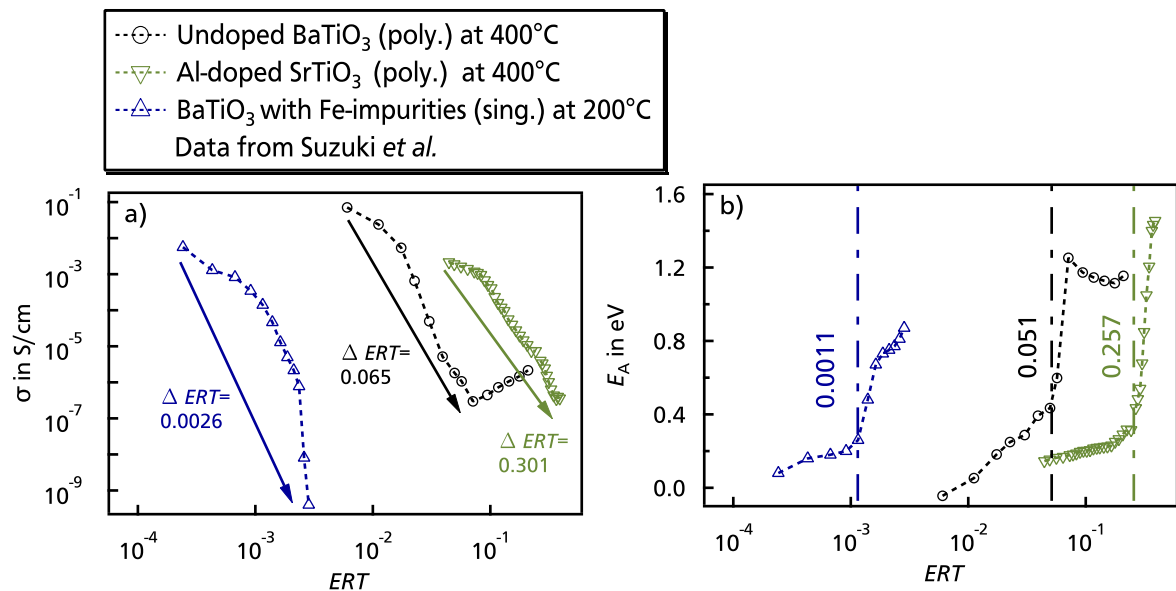
Figure 7.6.: a) Conductivity and b) activation energy as a function of equivalent re-oxidation time (*ERT*) for single crystalline BaTiO$_3$ with Fe-impurities, polycrystalline nominally undoped BaTiO$_3$, and polycrystalline Al-doped SrTiO$_3$. The *ERT* values of single crystalline Fe-doped BaTiO$_3$ were calculated based on the data of Suzuki *et al.* [22] with a dwell time of 5 min.

---

[10]The absolute conductivity value is strongly temperature dependent, which complicates the direct comparison of conductivity vs. *ERT* between the single and polycrystalline samples. However, the evaluation temperature solely affects the absolute conductivity value on the *y*-axis but does not affect the *ERT* on the *x*-axis. Thus, the overall re-oxidation trend, i.e. at which *ERT* the conductivity starts to decrease, is only minor affected by the different extraction temperatures.

[11]The higher starting *ERT* for undoped BaTiO$_3$ is explained by the higher dwell temperature and time during the first loop, which consequently results in a higher *ERT* value (see Eq. 3.11).

[12]Degradation is based on combined temperature and voltage stress, which leads to a redistribution of oxygen vacancies inside the sample. Usually, an oxygen exchange with the surrounding is not assumed. For the present re-oxidation approach, the assumptions are the other way around. The applied voltage during the re-oxidation experiments is assumed to be low enough to exclude degradation and oxygen is incorporated from the surrounding atmosphere. However, both processes are based on the migration of oxygen through the sample.

boundaries is responsible for a slower oxygen diffusion [258] and hence, a slower re-oxidation of the polycrystals.

The re-oxidation rate is further slowed down by the addition of acceptors. This is indicated in Figure 7.6 by the conductivity decrease and activation energy increase at a higher *ERT* value for Al-doped $SrTiO_3$. The slower re-oxidation for fixed valence acceptor-doped samples is most likely related a higher amount of oxygen vacancies and/or defect interactions. The acceptor dopants are compensated by oxygen vacancies ($c(Al^{3+}) = 1/2 \, c(V_O^{\bullet\bullet})$), which possibly increases the total amount of $V_O^{\bullet\bullet}$ after reduction and slows down the re-oxidation.

In summary, no obvious influence of grain boundaries on the experimental activation energy could be observed in the *n*-type region. The origin of the activation energy plateau at 0.35 eV in the beginning of the experiment could not be illuminated. A grain boundary contribution is unlikely due to the expected downward band bending at the grain boundaries and the dominating *n*-type conductivity in this region. In the *p*-type region a plateau at 1.2 eV was observed for the undoped polycrystalline $BaTiO_3$ specimen. The resulting Schottky barrier at the grain boundaries represents a barrier for the hole mobility, which will influence the activation energy of the electrical conductivity. Additionally, grain boundaries evidently slow down the re-oxidation rate. This is related to the blocking effect for oxygen migration, which is also observed during resistance degradation.

The incorporation of fixed-valent acceptors in $SrTiO_3$ has no considerable influence on the experimental derived activation energy in the *n*-type region. Here, no additional activation energy plateau was observed during the re-oxidation of Al-doped $SrTiO_3$. This agrees with the assumption, that Al remains charged Al^{3+} through the whole experiment. The incorporation of Al-acceptors seems to further slow down the re-oxidation rate. This is most likely related to the higher oxygen vacancy concentration in the samples due to the creation of additional oxygen vacancies as compensation mechanism. The maximum activation energy value of 1.48 eV for Al-doped $SrTiO_3$ is considerable higher than the value of 1.31 eV for undoped $BaTiO_3$. If this difference is related to the additionally acceptor doping or due to the different host material ($SrTiO_3$ vs. $BaTiO_3$) could not be further illuminated.

Due to the similar crystal and defect structure of $SrTiO_3$ and $BaTiO_3$ [84], also no considerable influence of fixed-valent acceptors on the activation energy of polycrystalline $BaTiO_3$ is expect.

7.3. Polycrystalline Mn- and Fe-doped BaTiO$_3$

The goal of the re-oxidation experiments on polycrystalline Mn- and Fe-doped BaTiO$_3$ is the identification of the Mn and Fe charge transition levels. The previous experiments have been conducted in order to set a baseline and to distinguish different contributions on the conductivity and activation energy during the re-oxidation approach. From the previous experiments the following assumption are deduced:

(i) The evaluation of the electrode interface by *IV*-characteristics revealed an ohmic contact behavior between reduced STO and Pt electrodes. Due do the similar defect chemistry, similar contact characteristics are assumed for the case of reduced multi-valence acceptor-doped polycrystalline BaTiO$_3$ with Pt electrodes. Thus, no contribution of the electrode on the extracted activation energies is assumed.

(ii) A contribution of grain boundaries on the extracted activation energy is expected. However, the exact contribution of grain boundaries on the activation energy seems to be rather complex and could not be clearly resolved in the preliminary experiments on undoped polycrystalline BaTiO$_3$ and Al-doped polycrystalline SrTiO$_3$. Hence, it remains unclear whether grain boundaries add a constant activation energy in the hole mobility or if the contribution is also dependent on other parameters such as temperature and re-oxidation state of the sample.

From the conducted baseline experiments it is already clear that the main goal of Mn and Fe defect level identification cannot be achieved by simply conducting re-oxidation experiments on the acceptor-doped polycrystals. In order to resolve the grain boundary contribution to the overall activation energy, the charge transport across the grain boundaries has to be simulated. By comparing experiment and simulations conclusions on the grain boundary contribution might be drawn. However, this is only be possible, if the experimental parameters are chosen in such a way, that further contributions on E_A can be excluded:

(iii) The applied voltages during re-oxidation ($<4\,\mathrm{V}$) are assumed to be low enough to avoid degradation and polarization of the sample. Thus, no voltage effects on the measured conductivity are assumed.

(iv) Platinum was chosen as electrode material as it is assumed to be oxygen blocking. Thus, no ionic contribution to the measured conductivity is assumed (follow discussion in Ref. [22]).

Re-oxidation loops have been conducted for polycrystalline 0.1 wt.% and 0.5 wt.% Mn- and Fe-doped BaTiO$_3$. The discussion of the data is structured as follows: First, the conductivity and activation energy after reduction as well as the re-oxidation speed will be discussed on

single-cycle re-oxidation loops. Here, conclusions on the oxidation state of the acceptors after reduction will be drawn. Second, the overall appearance of the re-oxidation loops will be briefly discussed for each sample individually. Third, the temperature dependent conductivity and activation energy will be discussed in a comparison between the samples.

7.3.1. Initial conductivity and activation energy after reduction

Before the re-oxidation loops of Mn- and Fe-doped BaTiO$_3$ will be discussed, their conditions after the reduction treatment will be evaluated. For this purpose, one re-oxidation loop at 450 °C for 1 h has been performed on the reduced Mn- and Fe-doped samples. Single-cycle re-oxidation loops of reduced Mn- and Fe-doped polycrystalline BaTiO$_3$ are shown in Figure 7.7 a) and b), respectively. After reduction, the initial room-temperature conductivity is $> 10^{-3}$ S/cm for
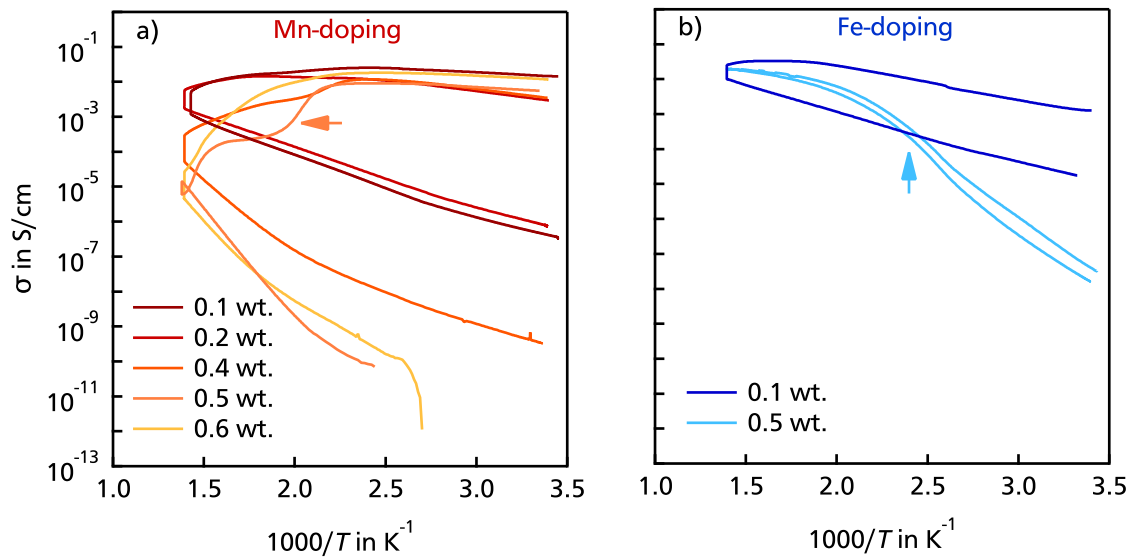
Figure 7.7.: Single-cycle re-oxidation loops of a) Mn-doped and b) Fe-doped polycrystalline BaTiO$_3$. The samples were dwelled for 1 h at 450 °C.
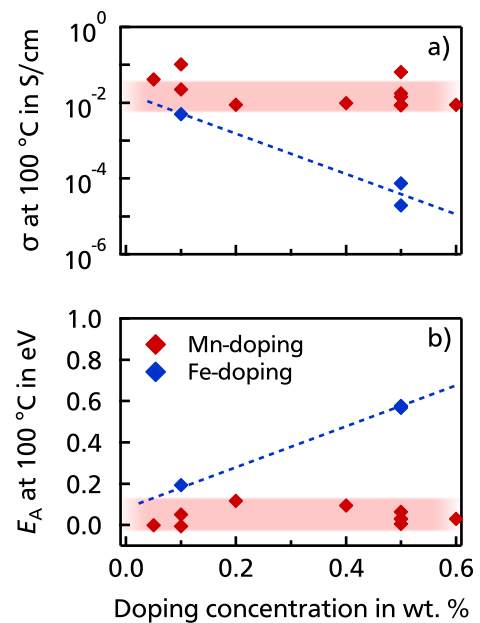
all Mn-doped samples. The re-oxidation speed can be deduced from the difference in room-temperature conductivity before and after one temperature cycle. For 0.1 wt.% and 0.2 wt.% Mn-doped samples the conductivity decreases approximately three orders of magnitude, while for higher Mn-doping concentrations the re-oxidation speed increased with increasing Mn-doping content. Additionally the loop shape alters with increasing Mn-content and exhibits a step-like shape for 0.5 wt.% Mn-doped BaTiO$_3$ (see arrow in Fig. 7.7 a)). Possible origins of this special shape will be discussed in the next section. For 0.1 wt.% Fe-doped samples a comparable initial conductivity after reduction and a comparable single-cycle loop shape as for low Mn-doping concentrations is observed. In contrast, the initial room-temperature conductivity of 0.5 wt.% Fe-doped BaTiO$_3$ is significant lower than for Mn-doped and 0.1 wt.%

Fe-doped $BaTiO_3$. Additionally, the degree of re-oxidation after single-cycle is significant lower and the loop exhibits two activation energy regimes (see arrow in Fig. 7.7 b)). Again, the loop shape will be addressed in the next section.

The differences in room-temperature conductivities and activation energies after reduction of all examined samples within this work have been extracted for a sample temperature[13] of 100 °C and are shown in Figure 7.8 a) and b), respectively. The conductivity at 100 °C is approximately $> 10^{-2}$ S/cm or higher for all Mn-doped samples. No specific trend upon Mn-doping concentration is observed. Upon Fe-doping a clear trend to lower conductivities with increasing Fe-content is observed. While the 0.1 wt.% Fe-doped sample exhibits only a slightly lower conductivity than the Mn-doped samples, the 0.5 wt.% Fe-doped samples exhibit an initial conductivity of only $\sim 5 \times 10^{-5}$ S/cm at 100 °C .

Similar differences between Mn- and Fe-doping can be observed for the activation energy at 100 °C, which is depicted in Figure 7.8 b). The activation energy for reduced Mn-doped samples is found between 0.0 eV to 0.2 eV. The high initial conductivity in combination with the low activation energies indicates the high reduced state of the samples. The oxygen vacancy concentration is assumed to be higher than the Mn-acceptor concentration, the conductivity is dominated by electron conductance, and all Mn-acceptors are charged 2+. The 0.1 wt.% Fe-doped samples exhibit a slightly lower

Figure 7.8.: Initial a) conductivity and b) activation energy at 100 °C after reduction of Mn- and Fe-doped $BaTiO_3$. The data points belong to all examined sample within is work (Fig. 7.7, Fig. 7.11, and additional loops).

conductivity and a slightly higher activation energy than the Mn-doped samples. However, the absolute values still indicate a high reduced state of the 0.1 wt.% samples and the Fe-acceptors are assumed to be mainly charged 2+. For 0.5 wt.% Fe-doped $BaTiO_3$ the initial conductivity at 100 °C is several orders of magnitude lower and the activation energy is 0.6 eV. Both values indicate that the initial state of these samples is considerably different compared to the Mn-doped and low Fe-concentration doped samples. The lower initial conductivity and the higher activation energy are most likely related to an incomplete reduction of the Fe-acceptors.

This assumption can be proven by comparing the experimentally derived conductivities with the theoretical conductivities for the same acceptor concentration. For this purpose, the bulk

---

[13]A sample temperature of 100 °C has been chosen as the data collection for some samples started at temperatures higher than *RT*.

conductivities of 0.5 wt.% Mn- and Fe-doped BaTiO$_3$ have been calculated at 100 °C in dependency of the oxygen vacancy concentration. The results of the calculation are depicted in Figure 7.9. The oxygen vacancy concentration dependent conductivity can be separated in three regions, which are determined by the relative ratio between oxygen vacancy and acceptor concentration. In **REGION I** the oxygen vacancy concentration is higher than the acceptor concentration $[V_O] > [A_{Ti}]$. The Fermi level is close or even inside the conduction band and most of the acceptors are charged 2+. The concentration of ionized oxygen vacancies, which are not required for acceptor compensation, are balanced by free electrons. The latter are dominating the electrical conductivity in this region ($n = [V_O] - [A_{Ti}]$). Hence, the conductivity in region I in Figure 7.9 is independent on the type of multi-valence acceptor. In **REGION II** the oxygen vacancy concentration is defined by $[A_{Ti}] > [V_O] > 1/2[A_{Ti}]$. In this region the Fermi level is pinned at the acceptor 2+/3+ level and the conductivity is still n-type. Hence, the energy position of the acceptors charge transition level will influence the magnitude of conductivity in this region. In the present case, the Fe$^{2+/3+}$ level is located at $E_{CB} - E_F = 0.7$ eV, while the Mn$^{2+/3+}$ level is located at $E_{CB} - E_F = 1.2$ eV. Hence, the Fe level is considerable closer to the conduction band, which results in an considerably higher conductivity in region II. In **REGION III** the oxygen vacancy concentration is lower than half the acceptor concentration $[V_O] < 1/2[A_{Ti}]$. The Fermi level has crossed the mid gap and is pinned at the acceptor 3+/4+ level and the conductivity is p-type. The difference in conductivity of Mn- and Fe-doped samples is again related to the position of the respective charge transition level to the valence band (Fe$^{3+/4+}$ at 0.8 eV and Mn$^{3+/4+}$ at 1.3 eV). The experimentally derived initial conductivities
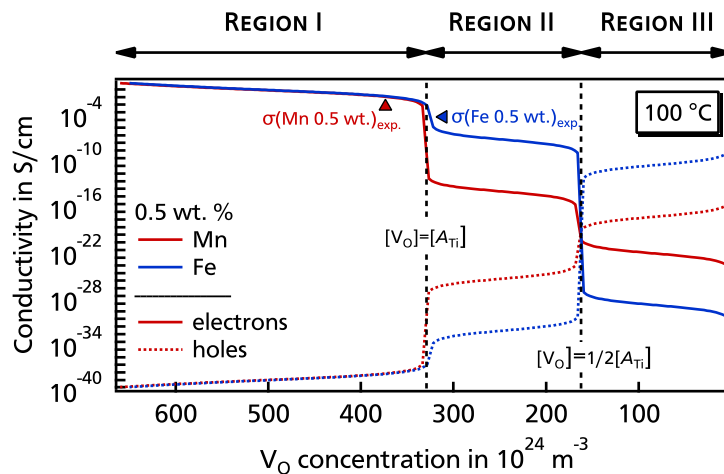

Figure 7.9.: Calculated conductivity of 0.5 wt.% Mn- and Fe-doped bulk BaTiO$_3$ at 100 °C as a function of oxygen vacancy concentration. The calculated conductivity is related to bulk material without any contribution of grain boundaries. The conductivity can be divided in three **REGIONS I-III**, depending on the $[V_O]/[A_{Ti}]$ ratio with A=Mn, Fe. The experimentally derived initial conductivities of reduced 0.5 wt.% Mn- and Fe-doped polycrystalline BaTiO$_3$ are indicated by the red and blue arrow, respectively.

for 0.5 wt.% Mn- and Fe-doped $BaTiO_3$ are indicated by the red and blue arrow in Figure 7.9. The initial conductivity of reduced 0.5 wt.% Mn-doped $BaTiO_3$ is $\sim 1x10^{-2}$ S/cm, which clearly corresponds to an oxygen vacancy concentration in region I and a Mn^{2+} oxidation state. The initial conductivity of 0.5 wt.% Fe-doped $BaTiO_3$ is $\sim 5x10^{-5}$ S/cm after reduction, which corresponds to an oxygen vacancy concentration in region II (close to the transition of region I to region II). The Fermi level is pinned at the $Fe^{2+/3+}$ level. Hence, the comparison between the calculations and the values after reduction successfully confirmed the hypothesis, that the reduction treatment is less effective for 0.5 wt.% Fe-doped $BaTiO_3$ than for Mn-doped $BaTiO_3$. The different oxidation states after reduction are most likely related to the different charge transition levels of Mn and Fe inside the band gap. The Fe-level is closer to the conduction band, which results in a lower reducibility. The lower reducibility of Fe compared to Mn under reducing conditions is consistent with a literature report of Hagemann and Ihrig, who performed extensive studies on the valence change of 3d-acceptor dope $BaTiO_3$ in different annealing atmospheres [46]. In their work, the predominant Fe oxidation state was constantly 3+, while Mn was easily reduced to Mn^{2+} and oxidized to Mn^{4+} between the different treatments [46].

Up to now, the different conductivity of reduced 0.5 wt.% Mn- and Fe-doped $BaTiO_3$ could be successfully explained by the different initial oxidation states after reduction. The previous discussion, however, does not explain why the starting conductivity is approximately constant for all Mn-concentrations, but significantly dependent on the Fe-concentration (see Fig. 7.8 a)). The conductivity at $100\,°C$ is $\sim 1x10^{-2}$ S/cm for 0.1 wt.% Fe-doped $BaTiO_3$ and $\sim 5x10^{-5}$ S/cm for 0.5 wt.% Fe-doped $BaTiO_3$. This difference implies that the reduction treatment is still successful for lower Fe concentrations. In order to evaluate the doping-concentration dependent acceptor oxidation state after reduction, defect calculations have been performed for differed Mn- and Fe-doping concentrations. Within the defect model all samples have been equilibrated at $1100\,°C$ and then quenched to RT. The different oxidation state concentrations of the acceptors (2+, 3+, and 4+) have been extracted as function of $\mu(O)$ and log pO_2 from the equilibrated state. From these values the oxidation state ratios A^{2+}/A^{3+} (solid lines) and A^{3+}/A^{4+} (dashed lines) with A=Mn, Fe have been calculated in the quenched state. In Figure 7.10 a) and b), these ratios are given for different Mn- and Fe-doping concentrations as a function of $\mu(O)$ and log pO_2, respectively. In this representation, a ratio of $(Mn,Fe)^{2+}/(Mn,Fe)^{3+} >> 1$ implies a predominate $(Mn,Fe)^{2+}$-oxidation state, while $(Mn,Fe)^{2+}/(Mn,Fe)^{3+} << 1$ implies a predominate $(Mn,Fe)^{3+}$-oxidation state. The same holds for the interpretation of the $(Mn,Fe)^{3+}/(Mn,Fe)^{4+}$ ratios. For Mn-doping the calculations are shown in Figure 7.10 a) for 0.05 wt.%, 0.1 wt.%, and 0.5 wt.% Mn-doping concentration. For the same oxygen partial pressure the Mn^{2+}/Mn^{3+} ratio decreases with increasing Mn-doping concentration. Or in other words, the crossover point $Mn^{2+}/Mn^{3+}=1$ between both oxidation states decreases to lower oxygen partial pressures with increasing Mn-concentration. As a consequence higher Mn-doping concentrations require a
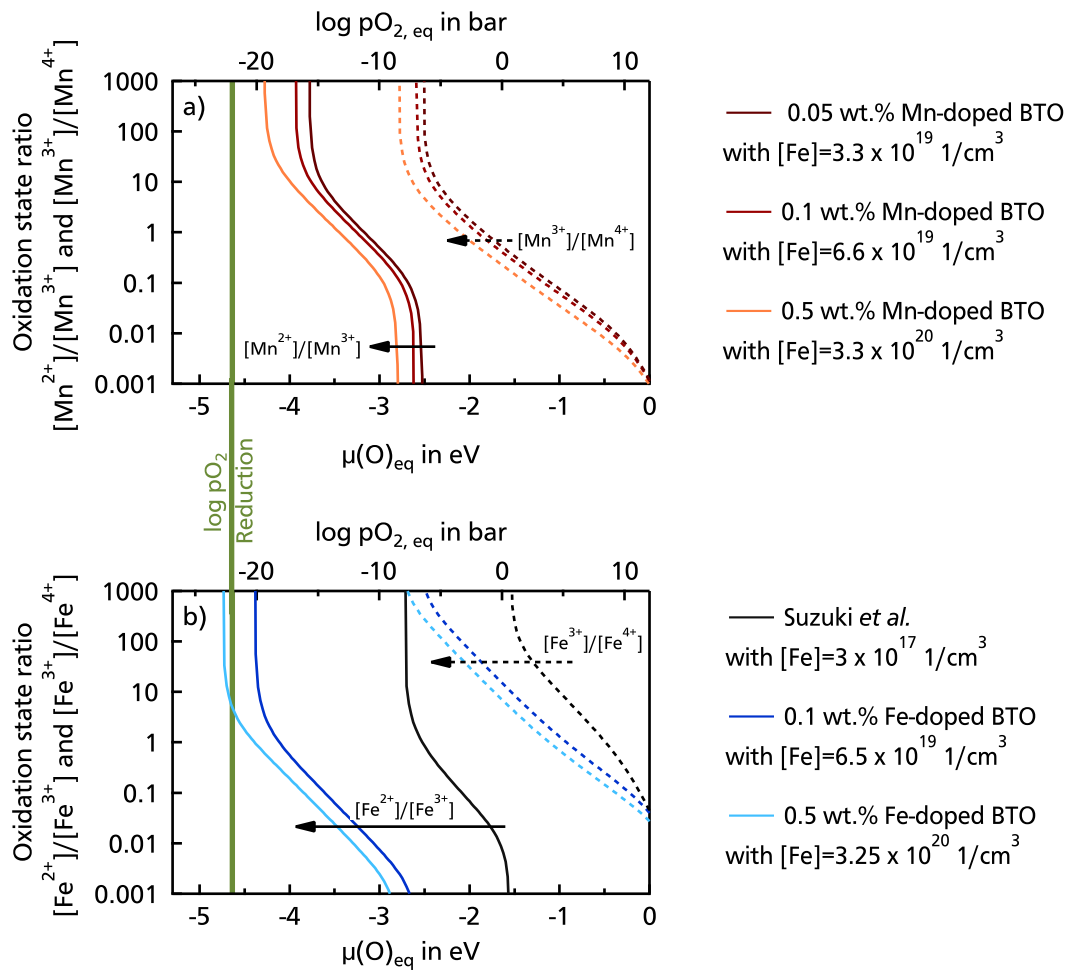
Figure 7.10.: Variation of the oxidation state ratios A^{2+}/A^{3+} (solid lines) and A^{3+}/A^{4+} (dashed lines) with A=Mn, Fe. The calculation has been conducted for an equilibration temperature of 1100 °C and a *RT* quenching temperature. The estimated partial pressure during reduction is indicated by the green vertical line. The IGOR defect calculation macro version 5.3beta of A. Klein has been used. Data representation adapted from [21].

lower oxygen partial pressure in order to reach the same Mn^{2+}/Mn^{3+} ratio. The estimated reduction partial pressure is added as a green vertical line. For all used Mn-concentrations in this work ($\leq$0.6 wt.% Mn) the calculations revealed $Mn^{2+}/Mn^{3+} \gg 1$ and thus a Mn^{2+} oxidation state in all samples after reduction. This is consistent with the experimentally derived high initial conductivities after reduction, which are independent on the Mn-concentration. For the Fe-doped series the calculated ratios are shown in Figure 7.10 b) for the Fe-concentrations of Suzuki *et al.* as well as for the 0.1 wt.%, and 0.5 wt.% Fe-doping concentrations used in this work. A similar shift of the crossover points towards lower oxygen partial pressures is observed for the Fe-series. For the samples of Suzuki *et al.* and 0.1 wt.% Fe-doped BaTiO$_3$ the ratio $Fe^{2+}/Fe^{3+} \gg 1$ and thus a Fe^{2+} oxidation state is expected for these samples. The latter is consistent with the high initial conductivities after reduction. For 0.5 wt.% Fe-doped samples,

the shift of the crossover point towards lower $\log pO_2$ becomes critically close to the oxygen partial pressure used during reduction and Fe^{2+}/Fe^{3+} has a finite value. For the estimated reduction oxygen partial pressure of $\sim 10^{-22}$ bar $Fe^{2+}/Fe^{3+} \sim 5$, which corresponds to 80 % Fe^{2+} and 20 % Fe^{3+}. The absolute ratio is not trustworthy, as the oxygen partial pressure during reduction has not been exactly measured within this work and is only based on an estimation. However, the defect calculation in Figure 7.10 b) clearly indicates at the oxidation state of the 0.5 wt.% Fe-doped samples is a Fe^{2+}/Fe^{3+} mixture, while lower Fe-doped samples and all Mn-doped samples are completely reduced to Fe^{2+} and Mn^{2+}, respectively. The difference is a direct consequence of the different position of the $2+/3+$ charge transition level of Fe and Mn. This level is higher for Fe, which is the reason why a higher Fermi energy is needed to completely reduce all Fe acceptors to Fe^{2+}.

In summary the reduced state of the Mn- and Fe-doped polycrystalline $BaTiO_3$ specimen can be described as follows:

- Mn-doped samples exhibit at 100 °C a conductivity of $\sim 10^{-2}$ S/cm and an activation energy < 0.15 eV. These values have been compared to defect energy calculations, which confirmed the complete reduction of the Mn-acceptors to Mn^{2+}. No dependence of these values on the Mn-concentrations is observed.

- For Fe-doped samples a strong concentration-dependency is observed. 0.1 wt.% Fe-doped samples exhibit at 100 °C a conductivity of $\sim 1 \times 10^{-2}$ S/cm and an activation energy of 0.2 eV, while 0.5 wt.% Fe-doped samples exhibit a conductivity of $\sim 5 \times 10^{-5}$ S/cm and an activation energy of 0.6 eV. In the case of 0.1 wt.% Fe-doped $BaTiO_3$ the magnitude of both values indicate a (nearly) complete reduction of the Fe-acceptors to Fe^{2+}. For 0.5 wt.% Fe-doped $BaTiO_3$ those values correspond to a Fe^{2+}/Fe^{3+} mixture. For such high Fe-concentrations the used parameters are not reductive enough to provide the required low oxygen partial pressure for a complete reduction of all Fe-acceptors.

The different oxidation states of the acceptors after the reducing treatment define the starting regime in Figure 7.9 and are of particular importance for the interpretation of the multiple cycle re-oxidation experiments performed in the next section.

7.3.2. Appearance of the Loops/Loop Shape

The re-oxidation loops of polycrystalline 0.1 wt.% and 0.5 wt.% Mn- and Fe-doped $BaTiO_3$ are depicted in Figure 7.11 a)-d), respectively. First, the overall appearance/shape of the re-oxidation loops will be addresses separately for each composition.
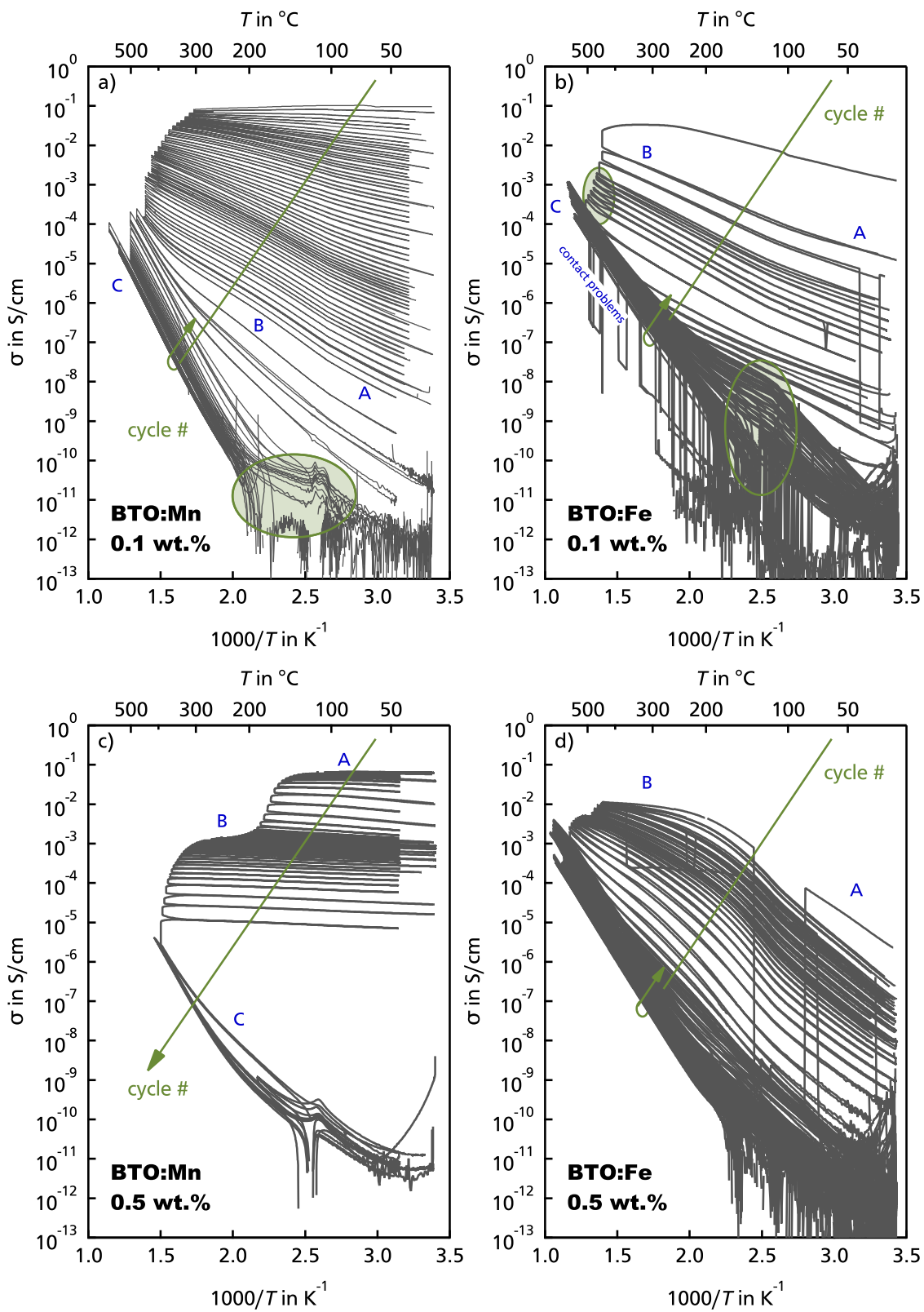
Figure 7.11.: Re-oxidation loops of a) polycrystalline 0.1 wt.% Mn-doped, b) polycrystalline 0.1 wt.% Fe-doped, c) polycrystalline 0.5 wt.% Mn-doped, and d) polycrystalline 0.5 wt.% Fe-doped BaTiO$_3$. Different regions are indicated by the blue label A-C. The cycle number is indicated by the green arrow.

0.1 wt. % Mn-doped polycrystalline BaTiO$_3$

The re-oxidation loops of polycrystalline 0.1 wt.% Mn-doped BaTiO$_3$ are depicted in Figure 7.11 a). The sample starts with an initial conductivity of $\sim 10^{-1}$ S/cm after reduction. The first loops show a negative temperature coefficient, which indicates metallic behavior and confirms the highly reduced state of the sample. With ongoing re-oxidation the loops can be divided in a less steep region A for $T < 100\,^\circ$C and a steeper region B for $T > 100\,^\circ$C. The zoom-in in the transition region is given in Figure A.19 in the Appendix and confirms that the change in slope between both regions is accompanied by a conductivity hysteresis, which originates from the tetragonal to cubic phase transition. The position of the latter phase transition is at $102\,^\circ$C for reduced 0.1 wt.% Mn-doped BaTiO$_3$.

After several re-oxidation cycles a third region develops close to the dwell temperature, which is characterized by an even steeper slope of the loops. With increasing cycle number the transition between region B and region C moves towards lower temperatures until the whole temperature range down to $200\,^\circ$C is dominated by the slope of region C. This indicates that the slope (i.e. the activation energy) in region C could be related to charge carriers originating from a deep defect level. For highly re-oxidized samples an extraction of the activation energy is not reasonable at temperatures below $200\,^\circ$C due to a too low conductivity. This region is highlighted by the shaded green circle in Fig. 7.11 a). Two main aspects restrict the reliability of this values. First, the recorded current for highly re-oxidized samples is close to the lower limit of the used picoampermeter. Thus, the corresponding conductivity data is rather noisy. This problem can be overcome by increasing the applied voltage, which simultaneously will increase the sample current. Second, the polarization related current during temperature ramping across the phase transition will start to influence the total current of the sample. Even though the polarization current is rather low, it will start to affect the measurements at total currents of approximately of $\sim 10^{-11}$ A. This phenomenon is extensively discussed in A.4.1 for 0.5 wt.% Mn-doped BaTiO$_3$. For the present 0.1 wt.% Mn-doped sample the transition from n-type to p-type was observed for the last loops.
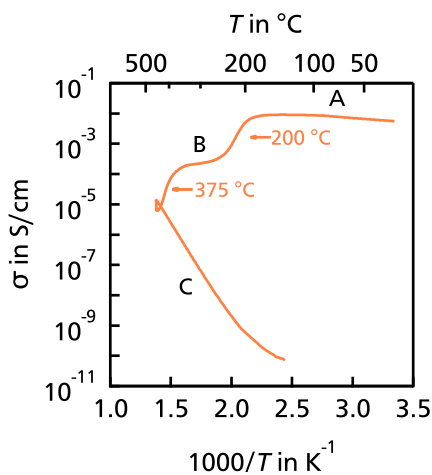
0.1 wt. % Fe-doped polycrystalline BaTiO$_3$

The re-oxidation loops of polycrystalline 0.1 wt.% Fe-doped BaTiO$_3$ are depicted in Figure 7.11 b). The sample starts with an initial RT conductivity of $\sim 10^{-3}$ S/cm after reduction. The first heating cycle shows a positive temperature coefficient at lower temperatures and a coefficient close to zero or slightly negative at temperatures higher than $300\,^\circ$C. After the first dwell time the temperature coefficient is positive throughout the whole experiment. The higher decrease in conductivity during the first cycle of 0.1 wt.% Fe-doped BaTiO$_3$ compared to 0.1 wt.% Mn-doped BaTiO$_3$ is related to the higher dwell temperature of the former and not related to a stronger re-oxidation ability. Similar to the 0.1 wt.% Mn-doped sample also the 0.1 wt.% Fe-doped sample exhibits three different slope regions. The transition between region

A and B is most likely related to the phase transition, while region C is the high temperature region. According to the change in slope the tetragonal to cubic phase transition is located at ~103 °C during the first loop and is increasing to ~120 °C during re-oxidation. In region C the oxygen incorporation already starts during ramping, which results in a decrease in conductivity during heating and a narrowing of the loops close to the dwell temperature (indicated by the green shaded circle at higher T). Additionally, this region exhibits a higher slope during cooling. At a high re-oxidation degree the phase transition related polarization current starts to influence the overall measured DC-current. This is indicated by the bigger green shaded circle at lower T. The abrupt jumps in conductivity to lower values are related to contact problems.

0.5 wt. % Mn-doped polycrystalline BaTiO$_3$

The re-oxidation loops of polycrystalline 0.5 wt.% Mn-doped BaTiO$_3$ are depicted in Figure 7.11 c). After reduction the room temperature conductivity is close to $\sim 10^{-1}$ S/cm. In contrast to the 0.1 wt. % Mn- and Fe-doped samples the activation energy/temperature coefficient remains close to zero throughout a wide number of cycles. No considerable conductivity decrease and, thus, oxygen incorporation is observed during cycling up to ~180 °C. This plateau is assigned to REGION A, in which the activation energy is approximately zero. At ~180 °C the conductivity starts to decrease during dwelling, which indicates oxygen incorporation. During this transition from region A to B the conductivity deceases two orders of magnitude and the activation energy slightly increases from zero to 0.05 eV. In REGION B the conductivity remains approximately constant at a value of $\sim 10^{-4}$ S/cm and only a minor conductivity decrease/oxygen incorporation is observed during dwelling. Again the activation energy is zero in this region. At ~350 °C the oxygen incorporation restarts during dwelling and the conductivity is decreasing. Still, the activation energy is only slightly increasing during the transition from region B to C. An abrupt jump in activation energy is finally observed after dwelling at 405 °C. While the activation energy was close to zero during heating, it suddenly increases to 1.3 eV during cooling. The activation energy loops are labeled as RE-GION C and further cycling does not show significant activation energy changes in this region.

Figure 7.12.: Single-cycle re-oxidation loops of 0.5 wt.% Mn-doped BaTiO$_3$. The was dwelled for 1 h at 450 °C.

In order to prove that the conductivity plateaus of region A and B are not an artifact of the chosen dwell temperatures and times, a single re-oxidation loop experiment with a dwell temperature of 450 °C for 1 h has been conducted. The corresponding loop is shown in Figure 7.12. Even though the absolute transition temperatures between region A-B and B-C are slightly

higher for the single loop experiment, the overall step-like shape remains. Here, the increasing conductivity during dwelling results in a small knot before cooling down. The step-like conductivity profile during re-oxidation of 0.5 wt.% Mn-doped $BaTiO_3$ was unexpected when comparing to the previous experiments. In the following several scenarios are described, which could serve as an explanation for the observed re-oxidation characteristics:

Different grain and grain boundary contributions [256][14]:
This model is based on the corresponding equivalent circuit (see Fig. 7.2 right) and the different contributions to the overall conductivity. In the following, it is assumed that the conductivity is sensible to the re-oxidation dependent changing contribution of grain and grain boundaries to the equivalent circuit. The corresponding band diagrams including two grains and one grain boundary are depicted for region A-C in Figure 7.13 a)-c), respectively. In literature it is commonly accepted that the grain boundaries have a positive core charge due to segregation of oxygen vacancies, which results in the depicted downward band bending in the vicinity of the grain boundaries [79].
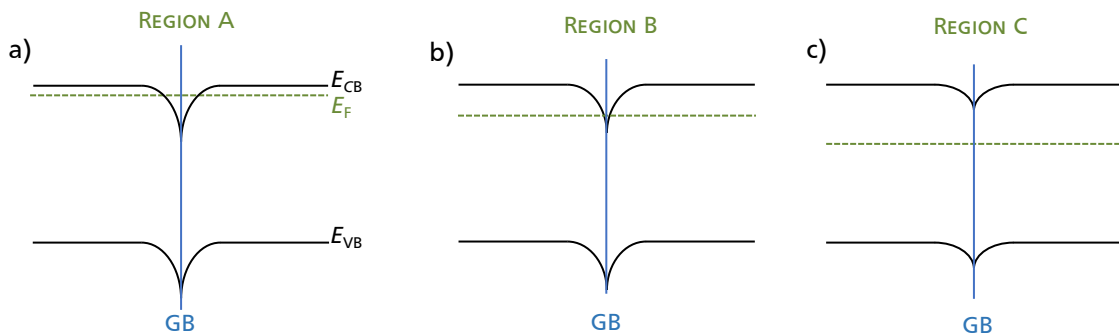
Figure 7.13.: Schematic band diagram depicting the Fermi level position through a double Schottky barrier between two grains. a)-c) refer to the regions A-C in Fig. 7.12 during the re-oxidation of 0.5 wt.% Mn-doped $BaTiO_3$, respectively.

After reduction, 0.5 wt.% Mn-doped $BaTiO_3$ is highly reduced. This state refers to REGION A, where the Fermi level is close to the conduction band in the grains and inside the conduction band at the grain boundary. In this region both, grain and grain boundary are contributing to the overall conductivity. The activation energy in this region is zero, as oxygen vacancies are shallow donors and are assumed to be completely ionized at room temperature. Thus, the charge carrier concentration in this region does not depend on temperature [20]. With ongoing re-oxidation oxygen is incorporated and the Fermi level decreases. In REGION B the oxygen vacancy concentration inside the grains is smaller than the Mn-acceptor concentration.

[14]This model was first suggested in the scope of the Bachelor thesis of N. Gutmann [256].

Accordingly, the grain conductivity decreases and is assumed to be activation energy dependent. However, due to the downward band bending the Fermi level at the grain boundaries is still inside the conduction band. Thus, the grain boundaries can serve as electrical channels with orders of magnitude higher conductivities. Considering the equivalent circuit, the low grain boundary resistance compared to the high grain resistance is dominating the overall conductivity in this region. The oxygen vacancies at the grain boundaries are still assumed to be fully ionized, which results in a temperature independent electron concentration and an activation energy close to zero. With ongoing re-oxidation the Fermi level further decreases and is now located close to midgap. In REGION C the oxygen vacancy concentration of both, grain and grain boundary, is smaller than the Mn-acceptor concentration. The conductivity decreases and the charge carrier concentration in the grain and at the grain boundary becomes activation energy dependent. Thus, the transition from region B to region C is accompanied by a sudden jump in activation energy from zero to the experimentally derived value of 1.2 eV to 1.3 eV.

The above described model for the different dominating contributions of grain and grain boundary to the overall conductivity is qualitatively consistent with the measured re-oxidation loops of 0.5 wt.% Mn-doped $BaTiO_3$ and with the expected equivalent circuit. For other Mn-doping concentrations, however, the re-oxidation loops exhibit different shapes and the applicability of the proposed model to the complete Mn-series is questionable. In Figure 7.7 a) the single-cycle re-oxidation loops have been depicted for a variety of Mn-doping concentrations. For Mn-concentration <0.2 wt.% no step-like shape has been observed. For 0.4 wt.% and 0.5 wt.% Mn-doped samples the step-like shape is clearly visible with a higher step-characteristic for the higher doped samples. Thus, for the doping range 0-0.5 wt.% the presented model would hold, if the step-like shape would be Mn-doping concentration dependent. The amount of Mn-dopants affects the total oxygen vacancy concentration, which may influence the concentration of segregated oxygen vacancies in the grain boundary core. The latter eventually results in Mn-doping concentration dependent band bending. The magnitude of the band bending and the resulting SCR width then defines the conductivity drop during region A and B. Within this model 0.6 wt.% Mn-doped $BaTiO_3$ would exhibit an even stronger step-like shape. The acquired single-cycle re-oxidation loop in Figure 7.7 a), however, does not show a step-like shape. Its appearance rather indicates a direct transition from region A to region C. This observation cannot be explained by the proposed model. Thus, it is necessary to separate the different contributions of grain and grain boundary conductance in region A-C. Here, systematic Hall- and/or impedance measurements on the Mn-series are recommended to evaluate different contributions of grain and grain boundary to the resistance/conductivity and to prove the proposed model.

Non-uniform re-oxidation:

The evaluation of XRD and EBSD measurements on reduced Mn-doped BaTiO$_3$ revealed that a 0.5 wt.% Mn-doped sample consists of about 20 % hexagonal phase with elongated plate-like grain shapes (see Chapter 5.6). Within the limits of the conducted characterization methods it remained questionable, if the introduced Mn-dopants are uniformly distributed in the tetragonal and hexagonal phase. If the solubility in the tetragonal phase is lower than the doping concentration of 0.5 wt.%, the additional Mn-dopants could either be incorporated into the hexagonal phase or could form Mn-rich secondary phases. The XRD pattern reveal small unknown reflections, which could be an indication for an additional secondary phase. However, no reasonable phase could be assigned to the reflections. Thus, in the following Gedankenexperiment the presence of Mn-rich secondary phases is neglected and it is assumed that the solubility limit of Mn-dopants is considerable higher in h-BaTiO$_3$ than in t-BaTiO$_3$. The schematic microstructure of reduced 0.5 wt.% Mn-doped BaTiO$_3$ is depicted in Figure 7.14 on the left. The corresponding equivalent circuit for the charge transport through the sample is given on the right. In contrast to the previous circuit, in this scenario the bulk contribution is separated in a series of tetragonal and hexagonal phase contribution (a hexagonal short cut of one elongated grain is excluded in this scenario). For an equivalent specific resistance of both phases (same conduction mechanism and defect chemistry) no differences to the previous circuits with a single bulk contribution are expected[15]. Thus, for the same conduction mechanism an uniform Mn-doping contribution (i.e. 0.5 wt.% in h- and t-BaTiO$_3$) is not expected to result in considerable changes in the overall conductivity. On the other hand, a non-uniform Mn-doping distribution (due to different solubility limits) could result in a non-uniform oxygen vacancy distribution between both phases. As exemplary case a solubility limit of 0.4 wt.% in reduced t-BaTiO$_3$ is assumed. The latter value was chosen as 0.4 wt.% is the highest Mn-doping concentration, for which phase pure t-BaTiO$_3$ after reduction was achieved (see Fig. 5.14). Thus, 80 % t-BaTiO$_3$ are expected to dissolve a Mn-concentration of 0.4 wt.%, while the remain-
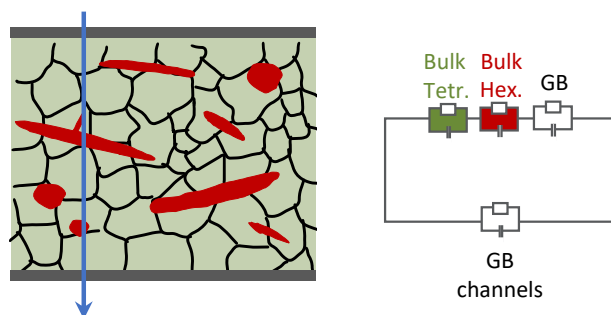
Figure 7.14.: Left: schematic microstructure of reduced 0.5 wt.% Mn-doped BaTiO$_3$. Tetragonal grains are green and hexagonal grains are red. Right: corresponding equivalent circuit.

---

[15]In this Gedankenexperiment GB channels and the different grain shape of h-BaTiO$_3$ are neglected for simplicity.

ing 20 % h-BaTiO$_3$ need to dissolve 0.9 wt. % in order to achieve the overall concentration of 0.5 wt.% Mn-dopants. Accordingly, the necessary oxygen vacancy concentration for maintaining charge neutrality is considerable higher in the hexagonal phase than in the tetragonal phase (assuming that the reduction treatment successfully reduced all Mn-dopants in both h- and t-BaTiO$_3$ to Mn^{2+}). If this assumption is correct, an oxygen vacancy concentration gradient would be present between tetragonal and hexagonal grains.

For the step-like shape of the re-oxidation loop for 0.5 wt.% Mn-doped BaTiO$_3$ the following scenario might take place. In REGION A the oxygen vacancy distribution is still frozen-in from quenching. During the transition from region A to region B oxygen vacancies start to become mobile. Due to the high absolute oxygen vacancy concentration difference between h- and t-BaTiO$_3$ a slight re-distribution between both phases is taking place. Additionally, the incorporated oxygen during re-oxidation might preferably annihilate oxygen vacancies in the hexagonal phase, which eventually would result in a non-uniform re-oxidation of h- and t-BaTiO$_3$. The oxygen vacancy concentration reaches a new equilibrium in REGION B. Here, the redistribution of oxygen vacancies from h- to t-BaTiO$_3$ results in an increased resistivity of the h-BaTiO$_3$ and the observed lower conductivity in region B. During the transition between region B and C the oxygen incorporation proceeds. In REGION C the oxygen vacancy concentration decreases below the Mn-doping concentration and the conductivity becomes temperature dependent. If this is only the case for hexagonal grains or also for the tetragonal grains remains questionable.

In this Gedankenexperiment the step-like re-oxidation loop shape has been associated to the different oxygen vacancy concentrations in hexagonal and tetragonal grains. Non-uniform re-oxidation of both phases could explain the plateau in region B. However, a non-uniform re-oxidation of the hexagonal phase could not explain the small step-like shape of reduced 0.4 wt.% Mn-doped BaTiO$_3$. According to the XRD results, these samples solely show a tetragonal structure. Additionally, the presence of a different Mn-doping concentration is an assumption and could not be proven by the conducted characterization techniques. Finally, it is highly questionable if such a high oxygen vacancy concentration gradient between both phases is reasonable. Hence, this Gedankenexperiment opens some fundamental questions about the behavior of hexagonal and tetragonal phase during re-oxidation. However, no consistent description could be obtained.

Within the scope of the discussion on the 0.5 wt.% Mn-doped BaTiO$_3$ re-oxidation loops two models have been presented. However, none of the models could explain the Mn-doping concentration dependent appearance/disappearance of the step-like loop shape. Yet, it was not possible to identify a consistent and clear mechanism for the loop-shape of 0.5 wt.% Mn-doped BaTiO$_3$. The experimental results of the single-cycle re-oxidation loops indicate that a 0.5 wt.% Mn-doping might refer to a transition between two different re-oxidation behavior. Here, Hall-

0.5 wt. % Fe-doped polycrystalline BaTiO$_3$

The re-oxidation loops of polycrystalline 0.1 wt.% Fe-doped BaTiO$_3$ are depicted in Figure 7.11 d). After reduction the room temperature conductivity is $< 10^{-6}$ S/cm. The temperature-dependent conductivity is increasing until it saturates at 10^{-2} S/cm for temperatures above 200 °C. While the *RT* conductivity of 0.5 wt.% Fe-doped BaTiO$_3$ is significant lower, the saturation conductivity is comparable to the high temperature conductivities of Mn- and Fe-doped BaTiO$_3$. With increasing re-oxidation time the saturation becomes less pronounced, until it fully disappears. At intermediate re-oxidation times the loop shape is dominated by a low temperature (< 120 °C) activation energy region and a thermal hysteresis at intermediate temperatures 250 °C to 350 °C. This hysteresis disappeared for highly re-oxidized samples.

The comparison of defect calculations with the experimental conductivity and activation energy after reduction indicated an incomplete reduction of the Fe-acceptors to Fe^{2+} for higher Fe-concentrations (see Figure 7.8-7.10). While the presence of a Fe$^{2+/3+}$ oxidation state mixture explains the low *RT* conductivity, the presence of a conductivity saturation at temperatures above 200 °C cannot be explained. For the discussion of the conductivity saturation the loop is separated into two region; REGION A refers to the temperature range *RT*-200 °C and REGION B to 200 °C-450 °C. Both regions are labeled in the single-cycle re-oxidation loop of 0.5 wt.% Fe-doped in Figure 7.15. In the following two different models for the conductivity saturation are discussed:

Charge carrier exhaustion:

One possible explanation for a conductivity saturation could be the exhaustion of carriers. This is a well known phenomenon for the temperature-dependent conductivity of doped semiconductors. With increasing temperature the number of ionized defects increases until all available defects are ionized. The conductivity behaves analogously and increases until it reaches a plateau [20]. In the following the temperature dependent conductivity has been calculated for reduced Fe-doped BaTiO$_3$ assuming a highly compensated semiconductor. For this calculation all Fe acceptors are assumed to be present as Fe^{2+} after reduction. Hence, the number of available defects is given by $[V_O]-[Fe_{Ti}]$. The saturation conductivity of 10^{-2} S/cm corresponds to $n = [V_O]-[Fe_{Ti}] \sim 10^{17}$ cm^{-3}. The calculation of the temperature dependent conductivity has been conducted for an effective mass of 5 m_{eff}, an activation energy of 0.4 eV (extracted from the slope), and a constant carrier mobility of 0.1 cm^2/Vs. The calculated temperature dependent conductivity for a highly compensated semiconductor is included in Figure 7.15. The experimentally derived data could not be reproduced for reasonable parameters of the effective
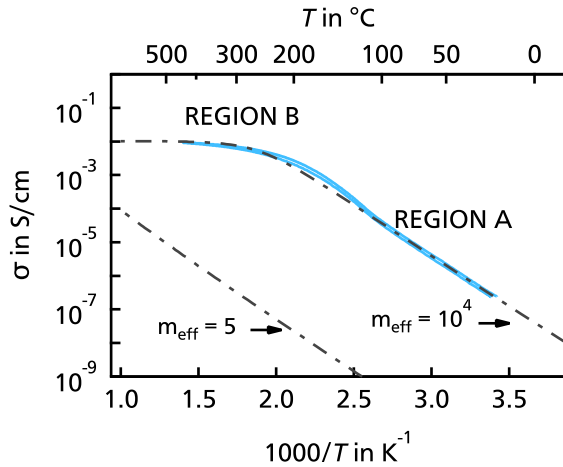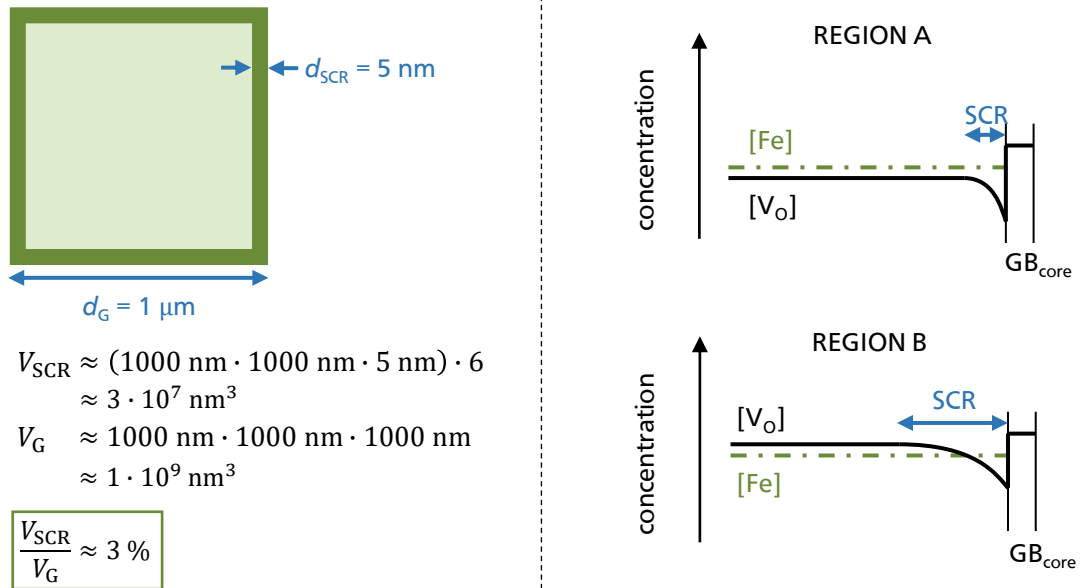
Figure 7.15: Single-cycle re-oxidation loop of 0.5 wt.% Fe-doped BaTiO$_3$ (blue-solid curve) with simulated temperature dependent conductivity assuming a highly compensated semiconductor with $E_A = 0.4$ eV, $\mu = 0.1$ cm^2/Vs, $n = [V_O] - [Fe_{Ti}] \sim 10^{17}$ cm^{-3}, and $m_{eff.} = 5\,m_e$, $10^4 m_e$. Region I and II refer to the different activation energy regimes.

mass. Only for the physically unreasonable value of $10^4\,m_{eff}$ the single-cycle re-oxidation loop of 0.5 wt.% Fe-doped BaTiO$_3$ could be replicated. Hence, the exhaustion of carriers is excluded as origin of the conductivity saturation.

Redistribution of oxygen vacancies:

Another possible explanation could be the temperature-dependent redistribution of oxygen vacancies between the bulk and the space charge region. At low temperatures in **REGION A** the oxygen vacancy concentration inside the grains is slightly lower than the Fe concentration $[V_O] < [Fe_{Ti}]$, while at higher temperatures in **REGION B** the oxygen vacancy concentration inside the grains is slightly higher than the Fe concentration $[V_O] > [Fe_{Ti}]$ (see scheme in Figure 7.16 on the right). Two effects may contribute to the redistribution: i) according to the Poisson equation, the temperature dependence of the permittivity will directly influence the width of the space charge region. This effect will be important next to temperatures around the phase transition, as this region shows the highest changes in permittivity. However, any discrepancy of the permittivity between low and high temperatures will have an influence on the SCR width, which eventually results in an oxygen vacancy redistribution from the former to the grain interior. ii) The spatial oxygen vacancy concentration is given by $\frac{c_{VO}(x)}{c_{VO,bulk}} \sim \exp(\frac{-\Delta\phi}{kT})$, where $\Delta\phi$ is the difference in the electrostatic potential from the grain interior. Hence, any temperature change will result in an oxygen vacancy redistribution. An estimation can be done based on the grain size and SCR width of 0.5 wt.% Fe-doped BaTiO$_3$. The corresponding SEM image is given in Figure A.4 c). For the following estimation a mean grain size of 1 µm and a mean SCR width of 5 nm are assumed. For a cubic grain, as being depicted in Figure 7.16 on the left, the corresponding volume fraction of the SCR versus the total grain volume is 3 %. When assuming a homogenous oxygen vacancy concentration distribution, 3 % of the total oxygen vacancy concentration are located in the SCR, which equals to $[V_O] \sim [Fe_{Ti}] \cdot 0.03 = 3.25 \times 10^{20}$ cm$^{-3} \cdot 0.03 = 9.25 \times 10^{18}$ cm^{-3}. This is considerably higher
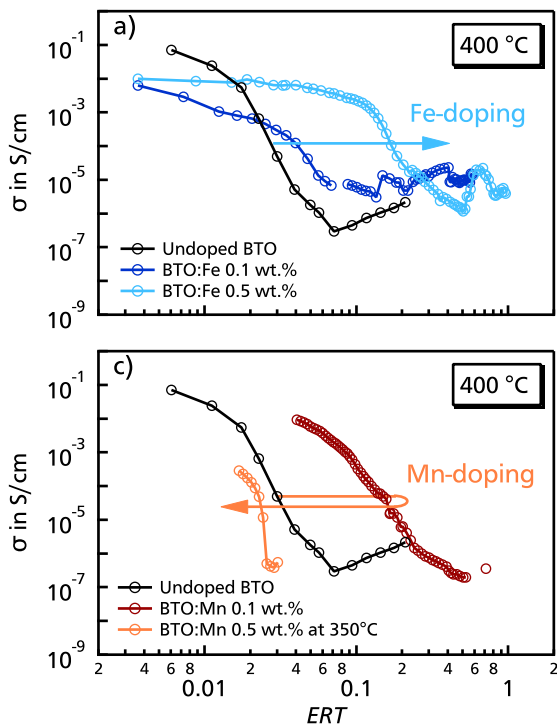
than the carrier concentration of approximately 10^{17} cm^{-3} in REGION B. The necessary time for redistribution can be estimated by $\tau = \frac{L^2}{2D}$ with $D = 6.4 \cdot 10^{-3} \cdot \exp(\frac{-0.7\text{eV}}{K_b T})$ [27]. For the given grain size of 1µm and a temperature of 200 °C the relaxation time is <100 s. Hence, the redistribution of oxygen vacancies is already close to equilibrium during heating. Therefore, the model of oxygen redistribution is consistent considering all the experimental data and the corresponding defect calculations and estimations.

$$V_{\text{SCR}} \approx (1000 \text{ nm} \cdot 1000 \text{ nm} \cdot 5 \text{ nm}) \cdot 6$$
$$\approx 3 \cdot 10^7 \text{ nm}^3$$
$$V_{\text{G}} \approx 1000 \text{ nm} \cdot 1000 \text{ nm} \cdot 1000 \text{ nm}$$
$$\approx 1 \cdot 10^9 \text{ nm}^3$$

$$\boxed{\frac{V_{\text{SCR}}}{V_{\text{G}}} \approx 3 \%}$$

Figure 7.16.: Left: Cubic grain with a diameter of 1 µm and a SCR width of 5 nm. The corresponding volume fraction of the SCR is calculated below. Right: Schematic oxygen vacancy and Fe concentration for region A and B. The integral of the oxygen vacancy concentration is the same in both regions.

7.3.3. Equivalent re-oxidation time

In order to estimate the influence of Mn- and Fe-doping on the re-oxidation speed of polycrystalline $BaTiO_3$, the conductivity at 400 °C has been plotted as a function of equivalent re-oxidation time and is displayed in Figure 7.17 a) and b), respectively. The undoped $BaTiO_3$ has a higher initial conductivity than the Fe-doped samples and exhibits the fastest re-oxidation. The 0.1 wt.% Fe-doped $BaTiO_3$ immediately starts to slightly re-oxidize until a faster re-oxidation is taking place at $ERT = 0.04$. The 0.5 wt.% Fe-doped $BaTiO_3$ shows nearly no re-oxidation until an ERT of 0.04. At higher ERT values of 0.04-0.2 the conductivity slightly decreases until the re-oxidation speed significantly increased at $ERT = 0.2$. The conductivity minimum of the samples was reached at higher ERTs for higher Fe-doping concentration. This indicates that Fe-doping increases the re-oxidation time of the samples.

Low Mn-doping concentrations of 0.1 wt.% also result in an increase of re-oxidation time. The 0.5 wt.% Mn-doped $BaTiO_3$, in contrast, shows an even faster re-oxidation than undoped polycrystalline $BaTiO_3$. This behavior is in clear contrast to the previous observations which indicated that acceptor-doping increases the re-oxidation time in Al-doped polycrystalline $SrTiO_3$, Fe-doped polycrystalline $BaTiO_3$, and low concentration Mn-doped polycrystalline $BaTiO_3$. The fast re-oxidation of 0.5 wt.% Mn-doped $BaTiO_3$ indicates either an incomplete re-oxidation of one contribution of the series connection in the equivalent circuit or faster diffusion path for oxygen (in the grain boundaries), which fastens the overall sample re-oxidation.

Figure 7.17.: Conductivity at 400 °C as a function of equivalent re-oxidation time (ERT) for a) Fe-doped and b) Mn-doped polycrystalline $BaTiO_3$. In both graphs undoped polycrystalline $BaTiO_3$ is added as comparison.

7.3.4. Temperature-dependent activation energy

In order to examine a possible pinning on the defect energy levels, the activation energy has been evaluated at several temperatures[16]. The activation energy at 100 °C, 200 °C, 300 °C, (350 °C) and 400 °C as well as the calculated activation energy for single crystalline materials at 400 °C are given as a function of the corresponding conductivity in Figure 7.18 a)-d).
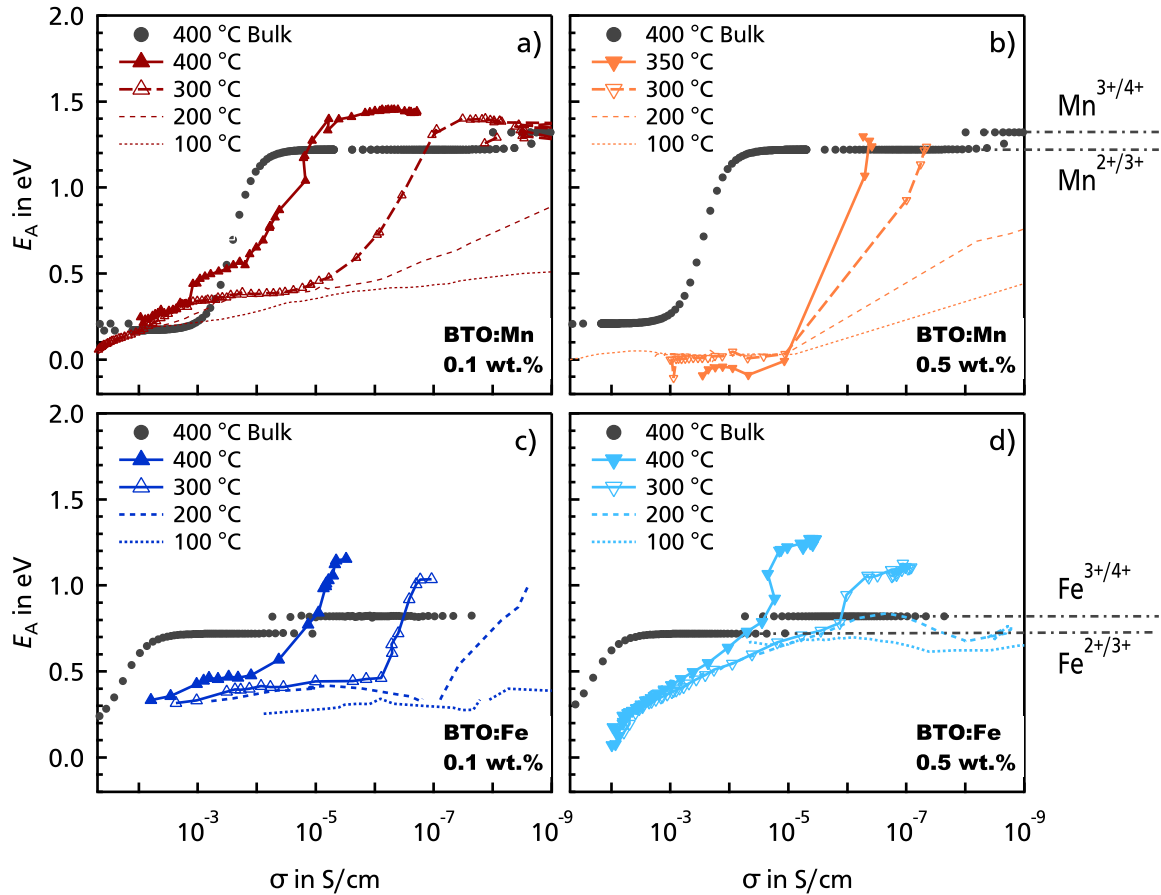
Figure 7.18.: Activation energies at 100 °C, 200 °C, 300 °C, (350 °C) and 400 °C as a function of conductivity for a) 0.1 wt.% Mn-doped, b) 0.5 wt.% Mn-doped, c) 0.1 wt.% Fe-doped, and d) 0.5 wt.% Fe-doped polycrystalline $BaTiO_3$. The gray dots correspond to the bulk activation energy for the corresponding single crystalline material at 400 °C. Only data points for a voltage below 1 V have been taken into account as both, the activation energy as well as the conductivity, are affected by higher voltages [17].

---

[16] The discussion of the loop shape revealed different temperature-dependent activation energy regions (see 7.3.2). For selected loops the temperature-dependent activation energy has been calculated using the differentiate tool of IGOR and is given in Fig. A.21. The plots revealed a different temperature dependence of the activation energy for the different samples. This inconsistency between different dopants and doping concentrations makes it difficult to identify one single $E_A(T)$ for the following discussions in this Chapter. Hence, the activation energy has been determined at 100 °C, 200 °C, 300 °C, and 400 °C. Due to the low maximum dwell temperature, 350 °C has been chosen instead of 400 °C for 0.5 wt.% Mn-doped $BaTiO_3$.

In Figure 7.18 a) the experimentally derived activation energies for the different temperatures are compared with the calculated activation energies of 0.1 wt.% Mn-doped $BaTiO_3$. At high conductivities, which corresponds to a low degree of re-oxidation, all activation energies exhibit a plateau at approximately 0.4 ± 0.1 eV, independent on the extraction temperature. During re-oxidation $E_A(100\,°C)$ only slightly increased to a maximum value of 0.5 eV, while $E_A(200\,°C)$ reached a maximum value of 0.95 eV. For the higher extraction temperatures the activation energies $E_A(300\,°C)$ and $E_A(400\,°C)$ increased to maximum values of 1.40 eV and 1.45 eV, respectively. $E_A(400\,°C)$ stabilized at its maximum value, while the activation energy at $300\,°C$ slight decreased from its maximum to a stable value of 1.30 eV. By comparing the experimentally derived activation energies at $400\,°C$ with the calculated bulk values for a single crystalline material at $400\,°C$, neither the first activation energy plateau at 0.4 ± 0.1 eV nor the second at 1.45 eV could be reproduced. Solely the activation energy of 1.30 eV extracted at $300\,°C$ would theoretically coincide with the $Mn^{3+/4+}$ level. However, as the sample is highly reduced in the beginning of the experiment, all Mn-dopants are reduced to Mn^{2+} and the Fermi level will cross the $Mn^{2+/3+}$ level before the $Mn^{3+/4+}$ level. Either the first plateau at 0.4 ± 0.1 eV corresponds to the $Mn^{2+/3+}$ charge transition level and the second plateau at 1.30 eV to the $Mn^{3+/4+}$ transition or the presence of grain boundaries in the ceramic samples strongly alters the activation energy. An activation energy of 0.4 ± 0.1 eV for to the $Mn^{2+/3+}$ charge transition is significantly lower than those reported in literature [21] and an influence of grain boundaries on this region seems to be more likely. Hence a direct extraction of the Mn charge transition levels from the activation energies during the re-oxidation seems to be not possible without adding a grain boundary contribution to the simulations.

As depicted in Figure 7.18 b), the first activation energy plateau of 0.5 wt.% Mn-doped $BaTiO_3$ is at 0.0 to -0.05 eV. The final activation energy is again dependent on the extraction temperature and reaches a value of 0.55 eV, 0.8 eV, 1.25 eV, and 1.3 eV for $100\,°C$, $200\,°C$, $300\,°C$, and $350\,°C$, respectively. The activation energy values of the two latter temperatures coincide with the $Mn^{2+/3+}$ charge level. As no n- to p-type transition has been observed during the re-oxidation experiments an assignment of the plateau to the first charge transition level would be reasonable. However, this positive result for the charge transition level identification of high Mn-doped $BaTiO_3$ is in contrast to the results on low Mn-doping concentrations, for which a direct assignment without grain boundary contribution failed.

For the lower Fe-doping of 0.1 wt.% again a first activation energy plateau at 0.4 ± 0.1 eV is observed (see Fig. 7.18 c)). The final values for the activation energies are 0.4 eV, 1.0 eV, 1.05 eV, and 1.15 eV for $100\,°C$, $200\,°C$, $300\,°C$, and $400\,°C$, respectively. Neither the first plateau value nor the final plateau value of the activation energy coincide with the known Fe defect levels.

---

[17]The effect of the voltage on the activation energy and conductivity is shown in Figure A.22. This effect was first observed during the Master Thesis of L. Gossel and was examined within the latter in more detail [110].

This result is comparable to the one of 0.1 wt.% Mn-doping, for which a direct identification of the charge transition was also not possible.

The activation energies at 100 °C to 400 °C are given for 0.5 wt.% Fe-doped BaTiO$_3$ in Figure 7.18 d). All extracted activation energies are continuously rising with ongoing re-oxidation. $E_A(100 \, °C)$ stabilizes at a value of 0.7 eV, while $E_A(200 \, °C)$ and $E_A(300 \, °C)$ reach slightly higher plateau values of 0.75 eV to 0.8 eV. Then, the activation energy at 300 °C further increases to a final plateau at 1.1 eV. The activation energy at 300 °C continuously increases up to a value of 0.8 eV, where it suddenly jumped to its final plateau value of 1.25 eV. While the final activation energy values at 100 °C and 200 °C theoretically coincide with the known values of the $Fe^{3+/4+}$ charge transition levels, the ones for the 300 °C and 400 °C are again too high.

The comparison of the extracted activation energies with the corresponding simulated bulk values prove, that a simple extraction of the defect energy levels of doped polycrystalline BaTiO$_3$ is not possible using the re-oxidation approach. Here, grain boundaries are assumed to contribute to the overall activation energy, which complicates the simple extraction of defect levels from the activation energy. Hence, for polycrystalline materials the experimental re-oxidation approach of Suzuki *et al.* [22] might still be usable, but it needs to be supported by a simulation, which includes the contribution of grain boundaries. In order to quantify the grain boundary contribution on the activation energy of the present samples, defect chemical calculations have been performed, which included an oxygen vacancy segregation to the grain boundaries. By this, a Schottky barrier at the grain boundaries and its influence on the total conductivity and, hence, on the activation energy can be simulated.
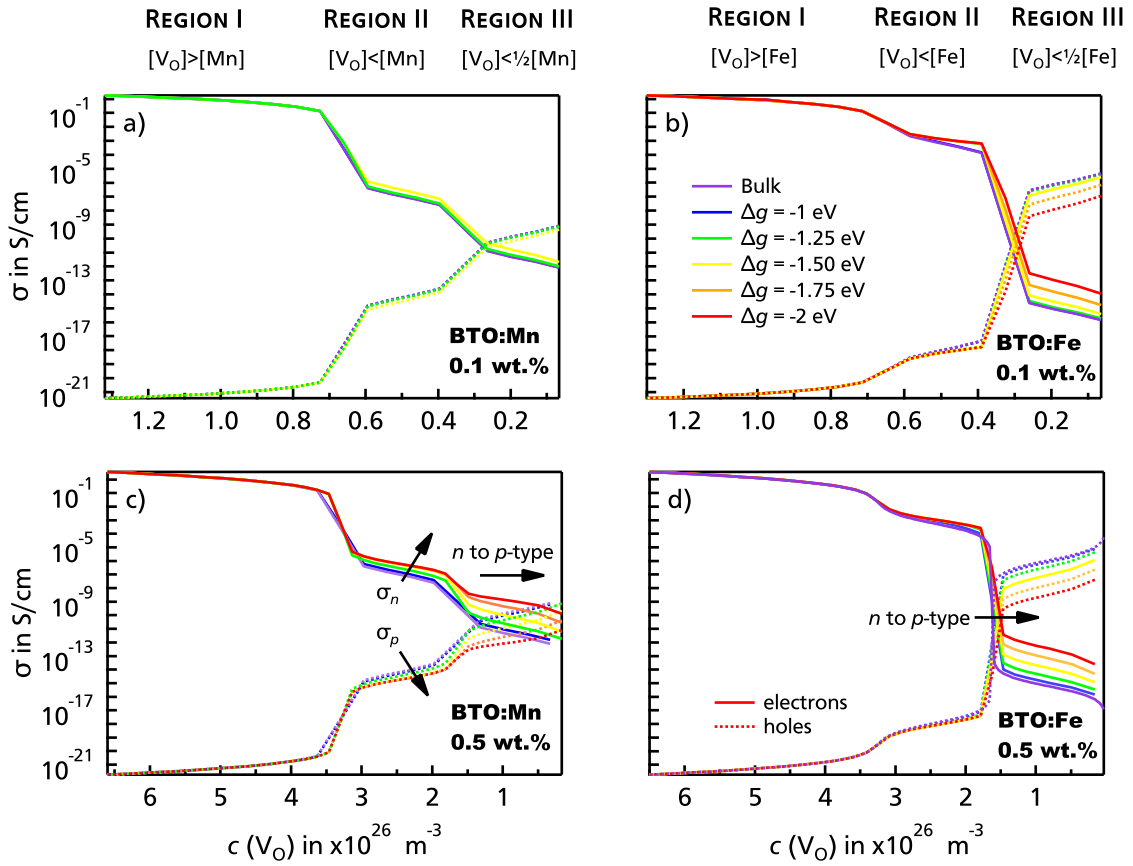
7.4. Simulations

In order to reveal to which degree the re-oxidation approach of Suzuki *et al.* [22] can be used to extract defect energy levels of polycrystalline materials, defect chemical calculations have been performed. These calculations are based on the model and procedure outlined by De Souza [79] and have been implemented by L. Gossel in the scope of her Master thesis [110]. Within this model the one-dimensional Poisson equation is solved including a segregation enthalpy Δg of oxygen vacancies to the grain boundary core. A negative value for Δg eventually results in a positive grain boundary core charge and the development of a space charge region with a downward band bending. The resulting equilibrium distribution of charge carriers in the space-charge zone is obtained by an iterative procedure for a given bulk oxygen vacancy concentration and Δg value. Electrons, holes, and oxygen vacancies are assumed to be mobile, while doped cations (Mn, Fe) are assumed to be immobile. This means that the concentrations of electrons, holes, and V_O depend on the electrical potential, while the concentration of acceptors is fixed. Here, the oxygen vacancy concentration in the grain interior is constant and solely an oxygen vacancy redistribution between the SCR and the grain boundary core is allowed. The electrical conductivity is calculated by considering only electrons and holes. No oxygen vacancy conductivity is expected to contribute to the *DC*-measurement. In order to compare the simulations for polycrystalline materials using Δg with the corresponding single crystalline simulations also the bulk values have been added into this discussion. The known charge transition levels of Wechsler and Klein [21], given in Table 7.1, have been used for the simulation. For detailed information refer to the former reference and/or to Section 4.1.

Table 7.1.: Band gap and defect energy values for Mn- and Fe-doped BaTiO$_3$ from Wechsler and Klein [21]. A grain half width of $d(0.1\,\text{wt.\%})/2 = 12.5\,\mu\text{m}$ and $d(0.5\,\text{wt.\%})/2 = 0.5\,\mu\text{m}$ has been used for 0.1 wt.% acceptor-doped and 0.5 wt.% acceptor-doped BaTiO$_3$, respectively. No discrimination between the Mn and Fe grain size has been done in order to decrease the amount of different parameters.

	E_G	$V_O^{x/\bullet}$	$V_O^{\bullet/\bullet\bullet}$	$Fe^{2+/3+}$	$Fe^{3+/4+}$	$Mn^{2+/3+}$	$Mn^{3+/4+}$
$E - E_{VBM}$	3.1	3.05	2.9	2.4	0.8	1.9	1.3

The conductivity at $400\,°\text{C}$ has been simulated for the different Δg values as a function of bulk oxygen vacancy concentration. The resulting curves are given for 0.1 wt.% Mn-doped, 0.1 wt.% Fe-doped, 0.5 wt.% Mn-doped, and 0.5 wt.% Fe-doped BaTiO$_3$ in Figure 7.19 a)-d), respectively. The oxygen vacancy concentration dependent conductivity can be separated in the well known three regions **REGION I**: $[V_O] > [A_{Ti}]$, **REGION II**: $[A_{Ti}] > [V_O] > 1/2\,[A_{Ti}]$, and **REGION III**: $[V_O] < 1/2\,[A_{Ti}]$ (see Fig. 7.9). The influence of a segregation enthalpy on the different conductivity regions can be best understood with the help of the corresponding

Figure 7.19.: a)-d) conductivity in dependence of the bulk oxygen vacancy concentration for 0.1 wt.% Mn-doped, for 0.1 wt.% Fe-doped, for 0.5 wt.% Mn-doped, and for 0.5 wt.% Fe-doped BaTiO$_3$, respectively. Simulations have been conducted for single crystalline bulk material (i.e. $\Delta g = 0$ eV) and polycrystalline material with $\Delta g = -1$ eV to -2 eV[18].

potential profiles and defect concentrations in the three regions. The potential profile and the defect concentrations for $\Delta g = -1$ eV and $\Delta g = -2$ eV are given for selected oxygen vacancy concentrations of region I-III for 0.5 wt.% Mn-doped BaTiO$_3$ in Figure 7.20.

Conductivity **REGION I** in Figure 7.19 corresponds to a highly reduced state of the samples. In this region the conductivity is dominated by oxygen vacancy induced electrons and is independent on the type of dopant and its doping concentration. The introduction of a segregation enthalpy Δg for oxygen vacancies to the grain boundary core has a negligible influence on the overall conductivity in this region. The oxygen vacancy concentration in the grain interior is extremely high and the introduction of Δg only results in a small downward

---

[18]For 0.1 wt.% Mn-doped BaTiO$_3$ only single crystalline material (i.e. $\Delta g = 0$ eV) and polycrystalline material with $\Delta g = -1$ eV to -1.5 eV have been simulated due to impractical high simulation times of the iterative MATLAB procedure.

band bending[19] (see Figure 7.20 a), d), and g)). The influence of the slightly more favorable conduction path along the grain boundaries of the polycrystal has no considerable influence on the total conductivity in region I.

For intermediate oxygen vacancy concentrations, which corresponds to **REGION II** in Figure 7.19, the influence of the segregation enthalpy is still low. Decreasing the segregation enthalpy from 0 to $-2\,\mathrm{eV}$ slightly increases the conductivity by one order of magnitude for 0.5 wt.% Mn-doped $BaTiO_3$. The introduction of a segregation enthalpy is more pronounced for Mn-doped samples than for Fe-doped samples (compare Fig. 7.19 c) and d) for Mn-doped and Fe-doped $BaTiO_3$, respectively). The different influence is related to the different position of the $Mn^{2+/3+}$ and $Fe^{2+/3+}$ transition levels in the band gap. The higher position of the Fe-level results in a higher bulk conductivity[20] of Fe-doped samples compared to Mn-doped samples in region II. The downward band bending towards the grain boundary core results in an additional electron conduction path in the space charge region (see Fig. 7.20 b), e) and f)). For Fe-doped samples, which have a higher bulk conductivity than Mn-doped samples, the influence of the additional electron conduction in the SCR on the total conductivity is less strong than for Mn-doped samples. Hence, the influence of oxygen vacancy segregation for a given enthalpy on the overall conductivity in region II depends on the position of the charge transition level of the chosen dopant.

In **REGION III** in Figure 7.19 the bulk conductivity is dominated by hole conduction. Decreasing the segregation enthalpy from 0 to $-2\,\mathrm{eV}$ results in a shift of the n- to p-type transition point towards lower oxygen vacancy concentrations. In general, the lower the segregation enthalpy the higher the shift of the conductivity transition. The magnitude of the influence of the segregation enthalpy on the position of the n- to p-type transition depends on the type of dopant. Here, the shift of the conductivity transition point is more pronounced for Mn-doped samples than for Fe-doped samples. This is again related to the position of the charge transition levels of the dopants. The lower position of the $Fe^{3+/4+}$ compared to the $Mn^{3+/4+}$ transition level results in a higher hole conductivity for Fe-doped samples. For a decreasing value of Δg the Schottky barrier height as well as the space charge region width at the grain boundaries is increasing (see Fig. 7.20 c)). For Mn-doped samples the high Schottky barrier height and the corresponding high band bending has strong influences on the conductivity. For low values of Δg the band bending becomes so high, that the Fermi level eventually crosses the $Mn^{2+/3+}$ level, which results in a charge transition to Mn^{2+} in the vicinity of the grain boundary (see Fig. 7.20 c)). The high band bending additionally results in a relatively wide region where n-conductivity dominates over p-conductivity (see Fig. 7.20 i)).

---

[19]This is directly correlated to the maximum allowed core site density of $10^{17}\mathrm{m}^3$ for oxygen vacancies. In region I all possible core sites are occupied by oxygen vacancies (see Figure A.24). The high Fermi level additionally results in a low ionization fraction of $V_O^{\bullet\bullet}$, which leads to a lower core charge and a moderate $\Delta\phi$.

[20]The higher position of the Fe-level compared to the Mn-level results is a Fermi level more close to the conduction band minimum, which results in a higher electron concentration.

Figure 7.20.: Calculated potential profiles a) to c) for 0.5 wt.% Mn-doped BaTiO$_3$ at $c(V_O)=6.6 \times 10^{26}$ cm^{-3} for **REGION I**, $c(V_O)=2.62 \times 10^{26}$ cm^{-3} for **REGION II**, and $c(V_O)=9.9 \times 10^{25}$ cm^{-3} for **REGION III**. The Mn concentration is $c(Mn)=3.3 \times 10^{26}$ cm^{-3}. The corresponding defect concentration profiles are given in d)-i) for $\Delta g = -1$ eV and $\Delta g = -2$ eV.

For Mn-doped BaTiO$_3$, this n-type conductivity path along the grain boundaries dominates for low Δg over the relatively low p-type bulk conductivity value. As a consequence, the n- to p-type transition point in Figure 7.19 shifts stronger to lower oxygen vacancy concentrations for low Δg values. As a result, an identification of the Mn$^{3+/4+}$ charge transition level from the electrical conductivity measurements might not be possible for lower Δg values due to the dominating n-conductance in this region. For Fe-doped samples the shift is less pronounced, which has two main reasons. First, the hole conductivity in the bulk is higher due to the lower position of the Fe charge transition level inside the band gap. Second, the high band bending still results in a more favorable conduction path for electrons along the grain boundaries. However, due to the higher position the Fermi level does not cross the Fe$^{2+/3+}$ level (see Fig. A.23 a) and b)). The space charge region is still dominated by p-type conductivity. Solely, for $\Delta g = -2$ eV a very small region close to the grain boundary (<1 nm) exhibits a transition from p- to n-conductivity (see Fig. A.23 e) and f)). However, the latter has only a minor influence on the overall conductivity. Hence, the influence of Δg on the conductivity transition point is also much smaller for Fe-doped than for Mn-doped BaTiO$_3$. For higher acceptor concentrations the influence of Δg on the conductivity seems to be more pronounced than for lower acceptor concentration. This is most likely related to the used grain size for the simulation, which were based on the SEM images of Fe-doped BaTiO$_3$ (12.5 μm for 0.1 wt.% and 0.5 μm for 0.5 wt.% samples). Even though the width of the SCR is wider for lower doping concentrations (compare Fig. A.23 a) and b)), the relative width of the SCR compared to the total grain size is smaller for lower doping concentrations. Hence, the result is less related to the magnitude of doping concentration but more to the influence of the grain size.

In order to quantify the influence of oxygen vacancy segregation on the resulting activation energies, the conductivity has been simulated at 400 °C and 380 °C for the different values of Δg. The activation energy has been calculated assuming Arrhenius-type temperature behavior. The corresponding activation energies as a function of oxygen vacancy concentration are given for 0.1 wt.% and 0.5 wt.% Mn- and Fe-doped BaTiO$_3$ in Figure 7.21 a)-d), respectively. Again, the plots can be divided in three different regions depending on the oxygen vacancy concentration. REGION I is dominated by oxygen vacancies and the activation is independent on the type of dopant and its concentration[21].

In REGION II the simulation revealed considerable differences between the type of dopants. For 0.5 wt.% Fe-doped BaTiO$_3$, presented in Fig. 7.21 d), the introduction of Δg only slightly reduced the activation energy. The level at 0.7 eV corresponds to the Fe$^{2+/3+}$ charge transition level. The influence of Δg is only minor, as the bulk conduction is dominantly n-type and the width of the additional electron path along the SCR is only small for 0.5 wt.% doping

---

[21]The peak in region I for 0.1 wt.% Fe-doped BaTiO$_3$ is most likely related to an artifact of the calculations.

concentration. For 0.1 wt.% Fe-doped BaTiO$_3$, depicted in 7.21 b), the introduction of $\Delta g \leq$ -1.25 eV decreases the activation energy in region II linearly with decreasing oxygen vacancy concentration until half of the acceptor concentration is reached. The conductance in this region is still dominated by electrons. For lower doping concentrations the width of the space charge region becomes wider. Thus, the influence of additional electron conduction increases. The influence of electron conduction along the space-charge region is even more pronounced for Mn-doped samples. For 0.1 wt.% Mn-doped BaTiO$_3$, depicted in 7.21 a), the bulk activation energy is 1.2 eV and is related to the Mn$^{2+/3+}$ charge transition level. An oxygen segregation enthalpy of $\Delta g = -1.5$ eV decreases the activation energy to 0.8 eV. For 0.5 wt.% Mn-doped BaTiO$_3$, illustrated in 7.21 c), the situation becomes more complex. The activation energy decreases to a minimum value of 1.0 eV for $\Delta g = -1.25$ eV, followed by an increase to an max-
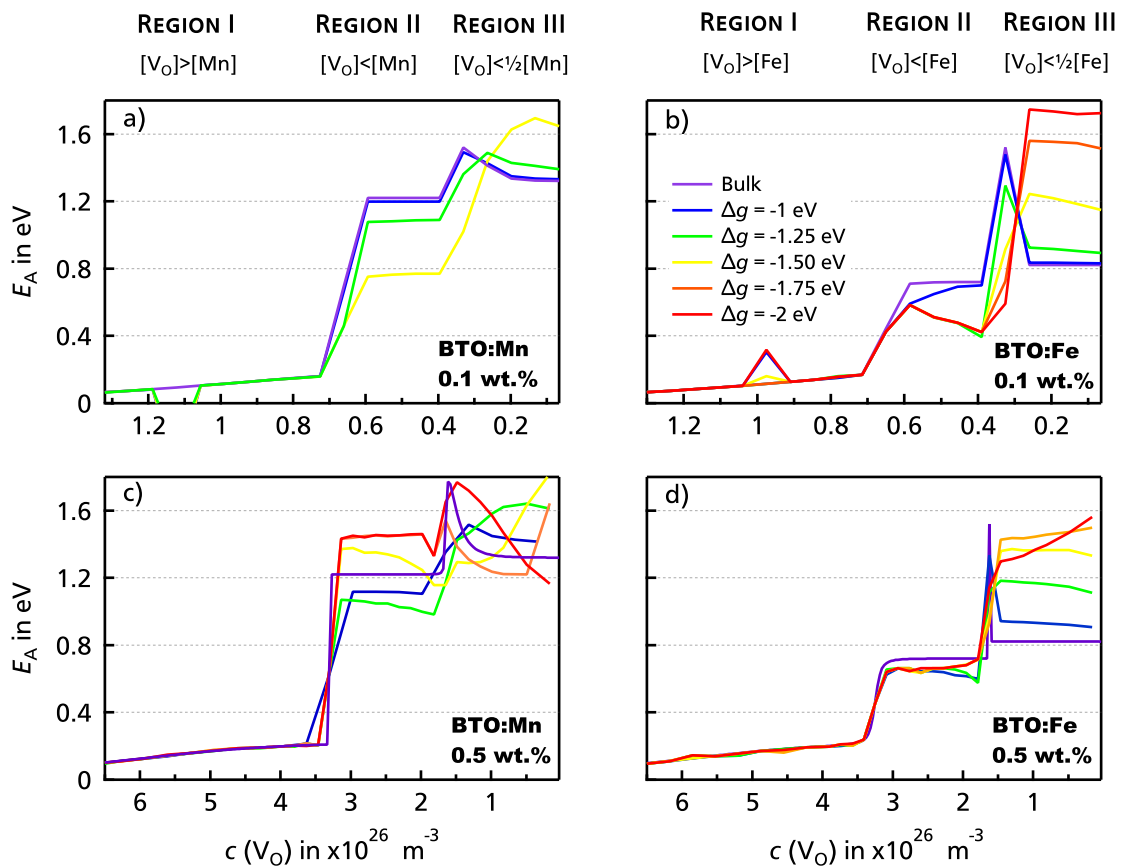
Figure 7.21.: a)-d) activation energy in dependence on the bulk oxygen vacancy concentration for 0.1 wt.% Mn-doped, for 0.1 wt.% Fe-doped, for 0.5 wt.% Mn-doped, and for 0.5 wt.% Fe-doped BaTiO$_3$, respectively. Simulations have been conducted for single crystalline bulk material (i.e. $\Delta g = 0$ eV) and polycrystalline material with $\Delta g = -1$ eV to -2 eV.

imum value of 1.4 eV for lower $\Delta g = -2.0$ eV. To this state of the simulations it is not clear, whether this change in E_A is physically reasonable or if the simulations need to be adapted. At the transition between region II and III almost all simulations reveal a peak in activation energy, which most likely corresponds to band-band excitation. The oxygen vacancy concentration where band-band excitations dominates the activation energy is quite narrow. This can be best seen for the bulk simulation of 0.5 wt.% Fe-doped $BaTiO_3$, for which an lower increment of oxygen vacancy concentrations has been used in the simulations. Hence, the observation of a broader oxygen vacancy concentration range for the band-band excitation for other simulations is misleading and solely refers to the wider step width on the x-axis.

In REGION III the introduction of Δg has considerable influences for all dopants and doping concentrations. In this region the bulk conductivity is dominantly p-type and the additional conduction path along the grain boundaries has considerable influence on the overall conductivity and activation energy. For the bulk simulation of 0.5 wt.% Fe-doped $BaTiO_3$ in Figure 7.21 d) the observed activation energy of 0.8 eV is related to the $Fe^{3+/4+}$ charge transition level. The gradual increase of E_A with increasing absolute value of Δg is related to the gradually increased downward band bending at the grain boundaries, which acts as barrier for hole conductance. Similar dependencies of E_A on Δg are observed in Figure 7.21 a) and b) for 0.1 wt.% Mn- and Fe-doped $BaTiO_3$, respectively. For 0.5 wt.% Mn-doped $BaTiO_3$ the activation energy dependency on Δg becomes unsystematic in a first impression. For the bulk simulation $E_A = 1.3$ eV corresponds to the $Mn^{3+/4+}$ charge transition level. Unlike the other cases, the introduction of Δg did not result in a stable plateau in this region. This is most likely related to the superposition of different factors. One major output of the previous discussion on Figure 7.19 and 7.20 was the shift of the n- to p-type transition to lower oxygen vacancy concentration with decreasing Δg. The shift of the dominating conduction mechanism will have a direct influence on the activation energy calculation. The second outcome was the Fermi level crossing of the $Mn^{2+/3+}$ charge transition level in the vicinity of the grain boundary. Hence, the activation energy is influenced by the Schottky barrier height, the excitation of electrons from the valence band to the $Mn^{3+/4+}$ level, and the excitation of electrons from the $Mn^{2+/3+}$ level to the conduction band. The dependence of E_A can be explained best by comparing the n- to p-type transition and the evolution of E_A for two examples of Δg. For $\Delta g = -1$ eV a stable plateau value is reached for $c(V_O) < 1.32 \times 10^{26}$ cm^{-3}. The latter value refers to the oxygen vacancy concentration, for which the conductance changes from n- to p-type. For $\Delta g = -1.75$ eV the transition point moves to $c(V_O) = 4.95 \times 10^{25}$ cm^{-3}. After the band-band-excitation the activation energy of $\Delta g = -1.75$ eV decreases down to a value of 1.2 eV until E_A suddenly increases, as soon as the $c(V_O)$ value passes the value of the n-to-p-type transition. Hence, after the band-band excitation E_A is decreasing in the n-type regime, while it is increasing in the p-type regime. For $\Delta g \geq -1.25$ eV the $c(V_O)$ range of the simulations was sufficient to display a (beginning) plateau of E_A in the p-type region. For $\Delta g \leq -1.5$ eV the $c(V_O)$ range of the simulations was

insufficient to display the corresponding plateau. Here, $\Delta g = -1.5$ eV and -1.75 eV already show the increase to the plateau value, while $\Delta g = -2$ eV is still in the decreasing region due to dominating n-type conductance in the SCR. By taking the shift of the n- to p-type transition for the 0.5 wt.% Mn-doped sample into account, all four simulations reveal an increase of the activation energy with decreasing Δg in the p-type region.

The experimentally derived activation energies will now be compared to the simulations in order to identify the magnitude of the oxygen vacancy segregation energy Δg. Therefore, the experimentally and simulated activation energies at 400 °C are given as a function of conductivity in Figure 7.22.

For the 0.1 wt.% Mn-doped sample in Figure 7.22 a), a first plateau is observed at approximately 0.4 eV. This value could corresponds to the $Mn^{2+/3+}$ with a Δg of -1.75 eV. However, the experimental conductivity is considerably higher than the simulated conductivity for the $Mn^{2+/3+}$ level. In addition, De Souza derived considerable lower values for the oxygen vacancy segregation in an acceptor-doped $SrTiO_3$ bicrystal [79]. Furthermore, the plateau at 0.4 eV has
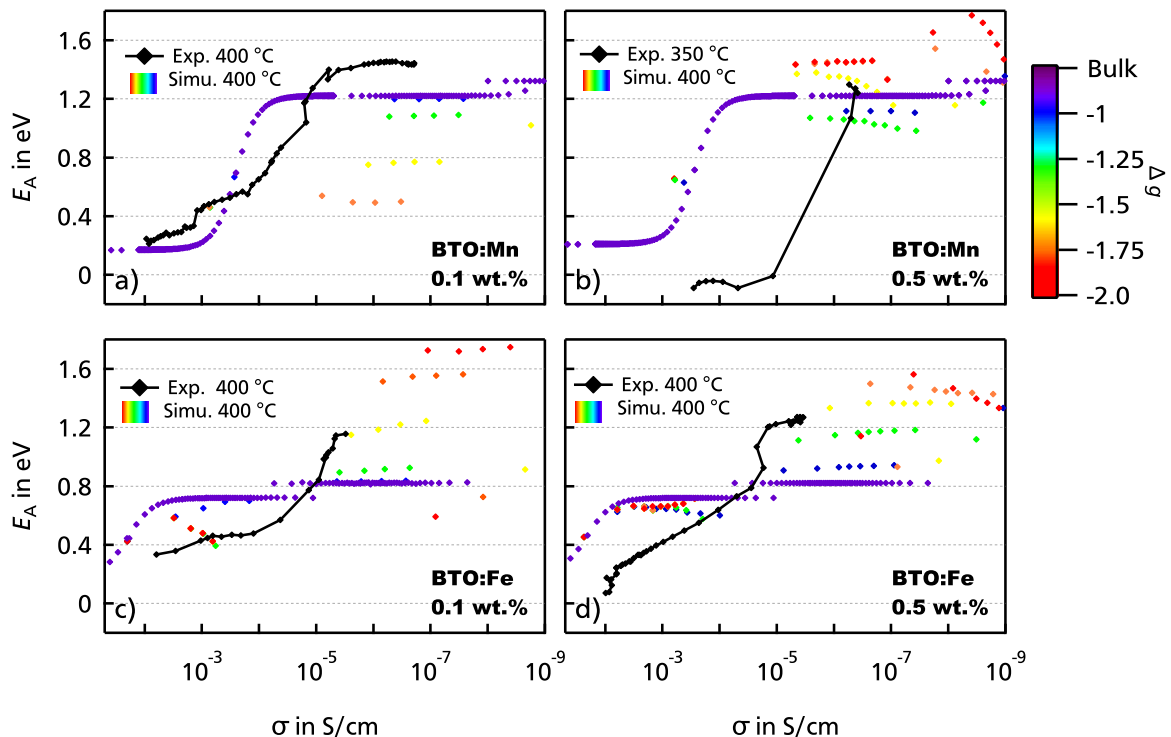
Figure 7.22.: Experimentally and simulated activation energies at (350 °C) 400 °C as a function of conductivity for a) 0.1 wt.% Mn-doped, b) 0.5 wt.% Mn-doped, c) 0.1 wt.% Fe-doped, and d) 0.5 wt.% Fe-doped polycrystalline $BaTiO_3$. Simulations have been conducted for single crystalline bulk material (i.e. $\Delta g = 0$ eV) and polycrystalline material with $\Delta g = -1$ eV to -2 eV.

also been observed for 0.1 wt.% Fe-doped samples. Hence, it is unlikely, that this plateau is related to the $Mn^{2+/3+}/Fe^{2+/3+}$ levels in the corresponding samples. So far, the simulations cannot give an indication on the origin of this first plateau. Possibly, defect association could be related to the activation energy plateau at 0.4 eV. In order to quantify the influence of defect complexes, for future simulation tool development it is recommended to include the contribution of defect interactions to the electrical conductivity.

The final plateau of the 0.1 wt.% Mn-doped sample is located at 1.4 eV and, thus, 0.2 eV and 0.1 eV higher than the $Mn^{2+/3+}$ and $Mn^{3+/4+}$ transition levels for $\Delta g = 0$ eV, respectively. The corresponding experimental conductivities are inconsistent with the simulated evolution of the conductivity during re-oxidation. For 0.1 wt.% Mn-doped $BaTiO_3$ p-type conduc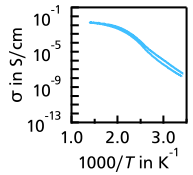tion is observed in the final loops of the re-oxidation experiments (see Fig. 7.11 a)). The comparison of the final experimental conductivity of 0.1 wt.% Mn-doped $BaTiO_3$ with the simulation suggests, that the sample is still in region II, which refers to a pinning on the $Mn^{2+/3+}$ level and n-conductance. This is obviously not the case in the experiments, as the conductivity of 0.1 wt.% Mn-doped $BaTiO_3$ increased during dwelling, which confirms p-type conduction. This discrepancy between experiment and simulation suggests, that the current simulation tool did not yet capture all effects contributing to the electrical conductivity. The comparison of 0.5 wt.% Mn-doped $BaTiO_3$ in Figure 7.22 b) did not reveal any new information. The final values of 1.2 eV for the activation energy as well as the conductivity region coincide with the $Mn^{2+/3+}$ charge transition level for $\Delta g = 0$ eV. If the value of $\Delta g = 0$ eV would be true, this result would indicate that grain boundaries have no direct influence on the activation energy of Mn-doped $BaTiO_3$.

For the 0.1 wt.% Fe-doped sample the comparison is given in Figure 7.22 c). The first plateau at 0.4 eV is in the conductivity region of the $Fe^{2+/3+}$ charge transition. Theoretically, this value could correspond to the final E_A values for $\Delta g \leq -1.25$ eV in this region. However, following the discussion above the appearance of this plateau in Mn- and Fe-doped samples raises the question, whether the plateau is really related to a dopant specific charge transition. The second level is located at approximately 1.2 eV in the conductivity region of the $Fe^{3+/4+}$ charge transition. This value would correspond to an oxygen vacancy segregation enthalpy of $\Delta g = -1.5$ eV. Similar conclusions can be drawn from the comparison of experiment and simulation for the 0.5 wt.% Fe-doped sample in 7.22 d). In the conductivity region of the $Fe^{2+/3+}$ charge transition no stable plateau could be identified. In addition, all experimental activation energy values are considerable lower than the simulated activation energies. Hence, no agreement between experiment and simulation could be observed in this region. The final values of the plateau is slightly higher than 1.2 eV and is located in the conductivity region of the $Fe^{3+/4+}$ charge transition. This activation energy value is in good agreement with an oxygen vacancy segregation enthalpy of $\Delta g = -1.25$ eV to -1.5 eV. In summary, Fe-doped samples have been reduced to a conductivity value corresponding to region III, i.e. the $Fe^{3+/4+}$ charge transition level. In this region the conductance is predominately p-type and the Schottky barrier heights

at the grain boundaries have a significant influence on the activation energy. For both samples an oxygen vacancy segregation enthalpy of $\Delta g = -1.25\,\text{eV}$ to $-1.5\,\text{eV}$ shows the best agreement between experimental and simulated activation energy values. However, the experimental derived conductivities of $0.1\,\text{wt.\%}$ and $0.5\,\text{wt.\%}$ Fe-doped BaTiO$_3$ are again inconsistent with the simulated evolution of the conductivity during re-oxidation.
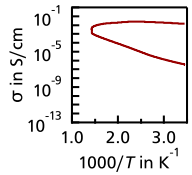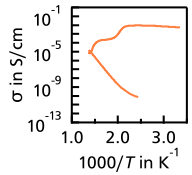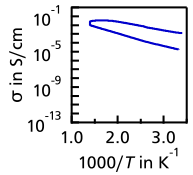
In summary, for Mn-doped samples the best fit between final experimental activation energy and simulation was achieved for $\Delta g = 0\,\text{eV}$, while for Fe-doped samples the best fit was achieved for $\Delta g = -1.25\,\text{eV}$ to $-1.5\,\text{eV}$. Besides all other mentioned discrepancies also the high difference between the best fit values of Δg for both type of dopants adds another question mark. From a physical point of view, comparable values have been expected for both dopants. This discrepancies again emphasizes that the current simulation does not capture all aspects contribution to the electrical conductivity.

7.5. Summary

The original goal of the work described in this Chapter was to evaluate to which extent the re-oxidation approach of Suzuki *et al.* [22] can be used for the identification of defect energy levels in polycrystalline materials. In a first step the contribution of the electrode interface to the activation energy was excluded. In a second step single-loop re-oxidation experiments have been performed on Mn- and Fe-doped samples to understand the properties immediately after reduction. In a third step $0.1\,\text{wt.\%}$ and $0.5\,\text{wt.\%}$ Mn- and Fe-doped polycrystalline BaTiO$_3$ have been slowly re-oxidized. Finally, the experimental derived activation energies have been compared to simulations, which included an oxygen vacancy segregation to the grain boundary core.

The most important experimental findings on the initial state of the $0.1\,\text{wt.\%}$ and $0.5\,\text{wt.\%}$ Mn- and Fe-doped specimens after reduction and the appearance of the single-loop re-oxidation experiments are summarized in Table 7.2. Mn-doped samples with $0.05\,\text{wt.\%}$ to $0.6\,\text{wt.\%}$ doping concentration as well as $0.1\,\text{wt.\%}$ Fe-doped samples are completely reduced to A^{2+} during reduction and start the re-oxidation experiments in region I, i.e. $[\text{V}_\text{O}] > [A_\text{Ti}]$ with $A = $ Mn, Fe. $0.5\,\text{wt.\%}$ Fe-doped BaTiO$_3$ exhibit a considerably lower conductivity and higher activation energy after reduction. The corresponding defect chemistry calculations confirm, that the reduction parameters were insufficient for a complete reduction to Fe^{2+}. Accordingly, $0.5\,\text{wt.\%}$ Fe-doped samples start the re-oxidation experiments in region II, i.e. $[\text{Fe}_\text{Ti}] > [\text{V}_\text{O}] > 1/2\,[\text{Fe}_\text{Ti}]$. The sensitivity of the reducibility on the type of dopant and its concentration could successfully be explained by the conducted defect chemistry calculations. Here, the distance of the defect energy levels to the band edges is the key parameter. Defect energy levels more closely to the band edges (i.e. Fe-levels) require stronger reduction parameters for a complete reduction to

Table 7.2.: Summary of the initial properties after reduction and the appearance of the loops during re-oxidation experiment for 0.1 wt.% and 0.5 wt.% Mn- and Fe-doped polycrystalline $BaTiO_3$.

		0.1 wt. % Mn	0.5 wt.% Mn	0.1 wt. % Fe	0.5 wt.% Fe
Properties after reduction	Experimental Conductivity at 100 °C	$1x10^{-1}$ - $2x10^{-2}$ S/cm	$6x10^{-2}$ - $8x10^{-3}$ S/cm	$5x10^{-3}$ S/cm	$7x10^{-5}$ - $2x10^{-5}$ S/cm
	Experimental E_A at 100 °C	0.0-0.05eV	0.0-0.05eV	0.2 eV	0.57 eV
	Simulated Oxidation state	100 % Mn^{2+}	100 % Mn^{2+}	100 % Fe^{2+}	80 % Fe^{2+}
	Starting Region Classification	Region I $[Mn_{Ti}] < [V_O]$	Region I $[Mn_{Ti}] < [V_O]$	Region I $[Fe_{Ti}] < [V_O]$	Region II $[Fe_{Ti}] > [V_O] > ½ [Fe_{Ti}]$
	Explanation	The sensitivity of the reducibility on the type of dopant and its concentration is related to the defect level position in the band gap (see Fig. 7.10). The Fe levels are located closer to the band edges than the Mn-levels. The $p(O_2)$ used during reduction is insufficient for a complete reduction of Fe to Fe^{2+} in 0.5 wt.% Fe-doped BTO. → The experimental derived starting conditions can be successfully explained by the supporting defect chemistry simulations!			
Loop Shape	Single re-oxidation loop recorded during heating at 450 °C for 1h	• expected loop shape	• step-like loop shape	• expected loop shape • weak saturation	• conductivity saturation
	Proposed Mechanism Colour Legend: ---- consistent ---- questionable ---- excluded	✓ simple oxygen incorporation during dwell time	? Inhomogeneous re-oxidation of tetr. and hex. Phase ? Grain boundary contribution	✓ simple oxygen incorporation during dwell time	✗ Charge carrier exhaustion ✓ Temperature-dependent redistributions of oxygen vacancies between the SCR and the grain interior
ERT	ERT at 400 °C	Low Mn-doping increases ERT, while high Mn-doing decreases ERT compared to undoped BTO (see Fig. 7.17).		Fe-doping increases ERT compared to undoped BTO (see Fig. 7.17).	

A^{2+} than defect energy levels closer to mid-gap (i.e. Mn-levels). The observed saturation phenomena for 0.5 wt.% Fe-doped samples might be attributed to a temperature-dependent redistribution of oxygen vacancies between the SCR and the bulk. An estimation on the given parameters revealed realistic values. The observed step-like loop shape of the 0.5 wt.% Mn-doped samples could not finally be explained. Potentially, different contributions of the grain and the SCR may lead to the observed step.

The simulated influence of oxygen vacancy segregation enthalpy Δg on the conductivity and activation energy in region I to III is summarized in Table 7.3. Grain boundaries represent parallel paths for n-type conductance and barriers for p-type conductance. No influence of

Table 7.3.: Summary of the simulations: influence of grain boundaries, represented by Δg, on the conductivity and activation energy in region I to III.

		Influence of Δg on …	
		… Conductivity (see Fig. 7.19)	… Activation energy (see Fig. 7.21)
Region I $[V_O] > [A_{Ti}]$	No considerable band bending	**n-conductance** defined by oxygen vacancy induced electrons → No influence of Δg	Mn- and Fe-doping: → No influence of Δg
Region II $[A_{Ti}] > [V_O] > \frac{1}{2} [A_{Ti}]$	Low downward band bending → *parallel path along the grain boundaries for electrons*	**n-conductance** conductivity is increasing with higher absolute value of Δg → effect is stronger for Mn-doping due to the lower σ(bulk). Thus, the GB-contribution is higher for Mn.	Mn-doping: → Strong influence of Δg Fe-doping: → Weak effect of Δg
Region III $[V_O] < \frac{1}{2} [A_{Ti}]$	Strong downward band bending → *grain boundaries represent barriers for the hole mobility*	**p-conductance** conductivity is decreasing with higher absolute value of Δg → Stronger for higher doping concentrations Shift of n- to p-transition to lower $[V_O]$ with higher absolute value of Δg → strong downward band bending results in n-type grain boundaries, while the bulk is already p-type → Stronger for Mn doping due to lower defect energy level	Mn- and Fe-doping: → Strong influence of Δg → Stronger influence for higher doping concentrations

Δg is observed in region I. The magnitude of the influence of Δg in region II depends on the conductivity ratio of grain boundary to bulk, where the bulk conductivity is defined by the position of the defect energy level. Fe-doped samples show a higher bulk conductivity and consequently the additional grain boundary conductance by parallel paths on the total conductivity is smaller than for Mn-doped samples. For p-type conductance a strong influence of Δg on both, the conductivity and the activation energy is observed. This was expected, as grain boundaries influence the hole mobility, which is one factor contributing to the activation energy.

The comparison between experiment and simulation is summarized in Table 7.4. Several discrepancies between experimental and simulated conductivity and activation energy are observed:

- The first activation energy plateau at approx. 0.4 eV to 0.5 eV cannot be explained by the simulations. In addition, it is questionable why it is only observed for low Mn- and Fe-doping concentrations as well as for undoped polycrystalline $BaTiO_3$ (0.35 eV).
- For Mn-doped samples a high discrepancy between the experimental and the simulated conductivities is observed. Hence, no consistent assignment to the different regions could be realized. While the experiments on 0.1 wt.% Mn-doped $BaTiO_3$ indicate a final p-type conductivity, the simulations indicate that the sample is still n-type. Moreover, the experimental derived activation energies of 0.1 wt.% Mn could not exactly be reconstructed by the simulation for any value of Δg. For 0.5 wt.% Mn-doped $BaTiO_3$ the best fit for the final activation energy is achieved for the $Mn^{2+/3+}$ level and $\Delta g = 0$ eV.
- The experimental activation energies of Fe-doped samples agree best with simulated activation energies for the $Fe^{3+/4+}$ level and $\Delta g = -1.25$ eV to -1.5 eV. However, the experimental derived conductivities of 0.1 wt.% and 0.5 wt.% Fe-doped $BaTiO_3$ are again inconsistent with the simulated evolution of the conductivity during re-oxidation.
- $\Rightarrow$ High discrepancy between experimental and simulated conductivities and activation energies.
- $\Rightarrow$ No consistent segregation enthalpy could be identified within the comparison of experiment and simulation for Mn- and Fe-doped polycrystalline $BaTiO_3$.

The above mentioned discrepancies indicate, that the implementation of grain boundaries in the simulation is not sufficient to explain the observations of the experiments. Hence, the current simulation tool does not capture all aspects contributing to the electrical conductivity and the the situation is expected to be way more complex than a 'simple' grain boundary contribution.

Table 7.4.: Comparison of experimental and simulated conductivity and activation energy evolution of 0.1 wt.% and 0.5 wt.% Mn- and Fe-doped polycrystalline $BaTiO_3$.

	0.1 wt. % Mn	0.5 wt.% Mn	0.1 wt. % Fe	0.5 wt.% Fe
Experimental 1st plateau at 400 °C	$\sigma = 10^{-3}$-10^{-4} S/cm E_A = 0.4 - 0.5 eV n-type	$\sigma = 5\times10^{-4}$-10^{-5} S/cm E_A = -0.05 eV n-type	$\sigma = 6\times10^{-3}$-1×10^{-4} S/cm E_A = 0.45 eV n-type	No distinct plateau
Simulation	? σ fits to transition of region I → II ? E_A best fit for Δg=-1.75 eV with the $Mn^{2+/3+}$ level	-	✔ σ fits to region II ? E_A best fit for Δg<-1.5 eV with the $Fe^{2+/3+}$ level	-
Comment	The observation of an activation energy plateau at 0.4 eV cannot be explained by the simulations. It is questionably why only the low Mn- and Fe-doping concentrations reveal such a plateau and why it is also present in undoped polycrystalline $BaTiO_3$ and in Al-doped polycrystalline $SrTiO_3$. Possibly, defect complexes or charge carrier trapping on Ti^{3+} could play a role.			
Experimental 2nd plateau at 400 °C values for the last loop	σ=3.6×10^{-7}S/cm E_A=1.4 eV p-type Parameters: 600 °C, 20h, 0.3 V	σ=2.6×10^{-7}S/cm E_A=1.27 eV, n-type (? loop at dwell time) Parameters: 420 °C, 0.33h, 0.1 V	σ=1.4×10^{-5}S/cm E_A=1.21 eV p-type Parameters: 500 °C, 3h, 0.1 V	σ=3.9×10^{-6}S/cm E_A=1.27 eV p-type (? In between n-type) Parameters: 680 °C, 1h, 0.05 V
Simulation	✗ σ fits to region II, i.e. n-type ✗ E_A does not fit to simulations	✗ σ fits to region II, i.e. n-type ✗ E_A best fit to Δg=-0 eV the $Mn^{2+/3+}$ level	✔ σ fits to region III, i.e. p-type ? E_A best fit to Δg=-1.5 eV at the $Fe^{3+/4+}$ level	✔ σ fits to region III, i.e. p-type ? E_A best fit to Δg=-1.25 to -1.5 eV at the $Fe^{3+/4+}$ level
Comment Colour Legend: — consistent — questionable — discrepancy	The experiments reveal a p-type conductivity in the final loops of 0.1 wt.% Mn, which indicates a pinning on the $Mn^{3+/4+}$ level, i.e. region III. In contrast, the corresponding conductivity values are too high to be assigned to region III in the simulations and rather corresponds to region II, i.e. the $Mn^{2+/3+}$ level and n-type conductivity. Additionally, the experimental E_A of 0.1 wt.% does not fit to the simulations while the one of 0.5 wt.% fits to the $Mn^{2+/3+}$ level, without any influence of Δg.		For 0.1 wt.% Fe the experiments reveal a p-type conductivity in the final loops, which indicates a pinning on the $Fe^{3+/4+}$ level, i.e. region III. The corresponding conductivity values fit to the simulated values for region III. The E_A is best fitted by the $Fe^{3+/4+}$ level with Δg=-1.5 eV. For 0.5 wt.% Fe the last loop reveals a n-type conductivity, while previous loop appeared p-type due to higher applied voltages. The corresponding conductivity values fit to region III. The E_A is best fitted by the $Fe^{3+/4+}$ level with Δg of -1.25 to -1.5 eV.	
	If oxygen vacancy segregation to the grain boundary core would be responsible for the observed altered activation energies between single and polycrystal, a similar Δg value is expected for Mn- and Fe-doping.			

The obtained results of this Chapter lead to the following **final conclusion:**

- The re-oxidation experiments on polycrystalline Mn- and Fe-doped BaTiO$_3$ represent the first study on the applicability of the re-oxidation approach for defect level identification in polycrystalline materials. No comparable data is available in literature, yet.
- With help of defect chemistry calculations it was possible to explain the behavior of Mn- and Fe-doped samples immediately after reduction.
- The experimental data revealed considerable differences in the re-oxidation behavior and loop shape between low Mn/Fe and high Mn/Fe concentration. The re-oxidation loops could not be reproduced with the current set of global variables in the simulations. The proposed mechanism of temperature-dependent oxygen vacancy redistribution appears realistic for Fe but could not be proven due to missing possibly of oxygen vacancy exchange between SCR and bulk in simulation. The step-like loop shape and the extremely fast re-oxidation of 0.5 wt.% Mn-doped samples could not consistently be explained.
- No consistent explanation for the plateau at 0.4 eV to 0.5 eV for 0.1 wt.% Mn- and Fe-doped samples could be found. Possibly, this plateau is related to defect complexes or a charge carrier trapping on Ti^{3+}.
- Neither the experimental derived conductivities nor activation energies fit to the simulations. In addition, the evolution of E_A does also not fit. Hence, no consistent segregation enthalpy could be identified within these experiments on Mn- and Fe-doped BaTiO$_3$.
- The current simulation tool does not capture all necessary affects to successfully describe the electric conductivity in polycrystalline acceptor-doped BaTiO$_3$. The high discrepancy of the activation energies could indicate that the band conduction model is insufficient to describe the observed conductivity behavior and charge carrier trapping might play a crucial role.

For future simulation tool development the following **adaptions of the simulations** are recommended:

- Conduct simulations for lower temperatures, i.e. 200 °C as in Suzuki *et al.* [22].
- Adapt thepotential profile (Gouy-Chapman) at the grain boundaries and compare results to current profile.
- Implement oxygen vacancy exchange between SCR and bulk to prove the model of a temperature-dependent redistribution of oxygen vacancies between SCR and bulk for 0.5 wt.% Fe-doped samples.
- Include defect interactions, such as $(A''_{\mathrm{Ti}}-V_O^{\bullet\bullet})$ and $(A'_{\mathrm{Ti}}-V_O^{\bullet\bullet})^{\bullet}$ complexes with $A=$Mn, Fe.
- Enable a possible segregation of Mn/Fe and barium vacancies to grain boundaries.
- Include charge carrier trapping (Ti^{3+}) and/or hole-traps at lower E_F.
- Modify kinetic of re-oxidation by adding discontinuous oxygen incorporation due to the blocking characteristics of grain boundaries for oxygen diffusion.

8. Resistance Degradation of Mn- and Fe-doped polycrystalline BaTiO$_3$

Within this Chapter the resistance degradation of Mn- and Fe-doped polycrystalline BaTiO$_3$ is being discussed. Resistance degradation in BaTiO$_3$ is based on the redistribution of oxygen vacancies. Combined temperature and voltage stress results in the migration of oxygen vacancies towards the cathode. The oxygen vacancy migration process will result in an oxygen vacancy accumulation (depletion) at the cathode (anode), which leads to an increased electron (hole) concentration and an overall decreased resistance of the sample. In case of acceptor-doped BaTiO$_3$ the influence of doping on the degradation behavior depends on the type of dopant. This has been investigated by Yoon *et al.*, who studied the influence of fixed- and multivalent acceptors on the resistance degradation of polycrystalline BaTiO$_3$ [9]. While the introduction of fixed-valence Mg-dopants reduced the degradation time, the introduction of multivalent Mn-dopants considerable increased the life time stability. The higher efficiency of multivalent acceptors has been explained by the ability of changing their oxidation state in the *n*- and *p*-type regions at the electrodes. Hence, electrons and holes are trapped at the dopants and the overall resistance degradation is effectively suppressed [9]. While the influence of Mn-doping on the resistance degradation of polycrystalline BaTiO$_3$ has been studied intensively [7,9,70,259,260], only few publications are available for Fe-doped BaTiO$_3$ (single crystals) [261].

Both dopants used in this work are multivalent dopants and hence, a suppression of resistance degradation is expected in both cases. As no reports on the efficiency of Fe-doping on the life time stability of polycrystalline BaTiO$_3$ are available, the comparison of both dopants is the first aim of this Chapter. The present results reveal, that Mn- and Fe-dopants influence the life time stability to different degrees. As a consequence, the influence of the charge transition level on the degradation behavior will be discussed. Here, the results of defect chemistry calculations and re-oxidation experiments with the corresponding simulations will be used to understand the different degradation behavior of Mn- and Fe-doped polycrystalline BaTiO$_3$.

Degradation experiments have been performed[1] on a homemade setup using a constant electric

---

[1]The setup has been built up within the Master thesis of B. Öcal [19]. The degradation curves of Mn-doped samples have been mainly recorded by B. Öcal, while the curves of Fe-doped BaTiO$_3$ have been recorded by L. Gossel in the

field of 0.3 kV/mm. In order to achieve reasonable long degradation times, the degradation temperature varied between the samples. The degradation curves of undoped, 0.2 wt.% Mn-doped, 0.3 wt.% Mn-doped, and Fe-doped polycrystalline BaTiO$_3$ are displayed in Figure 8.1 a)-d), respectively. The corresponding degradations times[2] are given in Figure 8.2. A nominally undoped BaTiO$_3$ sample of each batch was degraded in order to compare the degradation behavior between both. For the same temperature and voltage stress the undoped sample of the second batch degraded noticeably faster than the one of the first batch. This is assigned to the different grain size (see Fig. 5.6), which is considerably larger in the second batch for undoped BaTiO$_3$. In case of polycrystalline materials, the migration of oxygen vacancies across the grain boundaries is rate-limiting [4]. Hence, ceramics with larger grains exhibit a lower total number of grain boundaries for the same sample thickness and are expected to degrade faster.

The degradation curves of 0.2 wt.% Mn-doped BaTiO$_3$ are displayed in Figure 8.1 b). Mn-doping effectively suppresses the degradation and a sample temperature of 160 °C was too
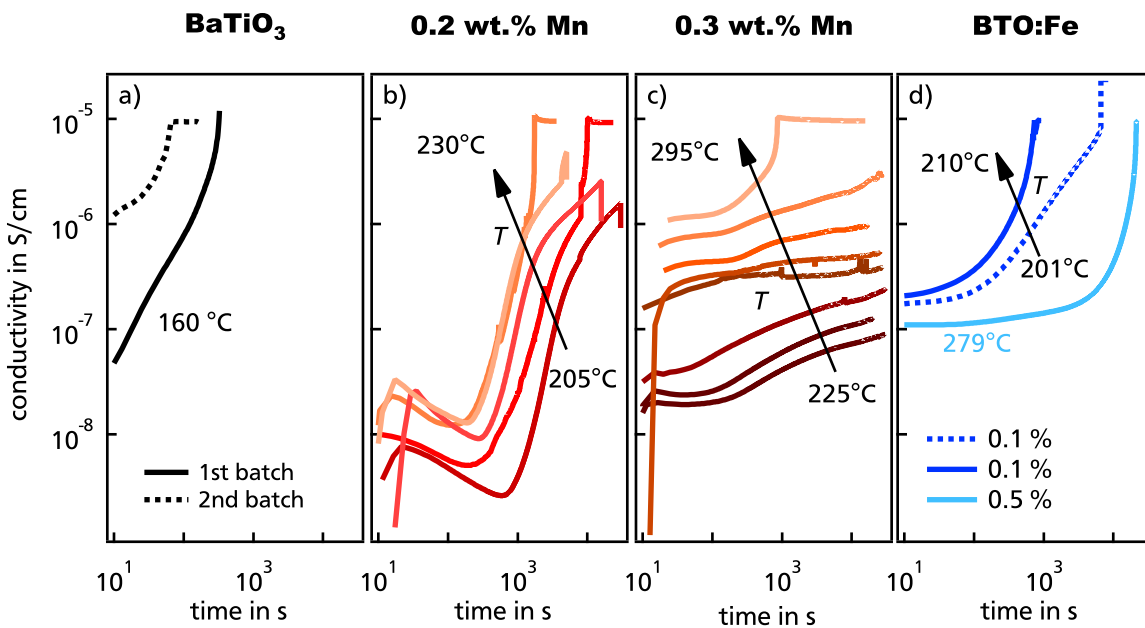
Figure 8.1.: Degradation curves of a) undoped, b) 0.2 wt.% Mn-doped, c) 0.3 wt.% Mn-doped, and d) Fe-doped polycrystalline BaTiO$_3$. For all samples a constant electric field of 0.3 kV/mm has been applied. The sample temperature is indicated by the color in the respective graphs. All samples have been equilibrated for at least 12 h at 900 °C. A conductivity of 10^{-5} S/cm corresponds to the current compliance of the homemade setup.

---

scope of her Master thesis [110]. In the present work, the data of both type of dopants is compared with a main focus on potential origins for the different strong impact of Mn- and Fe-doping on the degradation characteristics.
[2]The degradation time is defined as the time at which the current density (conductivity) has increased by one decade from its minimum value [4].

low to achieve reasonable degradation times. Therefore, the degradation temperature has been increased, which is accompanied by a higher starting conductivity of the samples. With increasing temperature from 205 °C to 230 °C the degradation time t_{deg} is decreasing. Increasing the Mn-doping level from 0.2 wt.% to 0.3 wt.% further suppresses resistance degradation. This is evident from the comparison of the degradation curves at 225 °C for both doping concentrations. While 0.2 wt.% Mn-doped BaTiO$_3$ degraded in 570 s at a sample temperature of 225 °C, no degradation within a working day has been observed for the 0.3 wt.% Mn-doped samples. This indicates a further suppression of degradation with increasing Mn-doping concentration. Hence, the sample temperature of 0.3 wt.% Mn-doped BaTiO$_3$ has been further increased till the sample finally degraded in 860 s at a sample temperature of 295 °C (see Fig. 8.1 c)). For higher Mn-doping concentrations degradation experiments could not be realized with the used setup. Higher degradation temperatures are not feasible as the starting sample current increases with temperature and comes close to the compliance limit of the multimeter used. The present observation of a significant live time extension with Mn-doping concentration is consistent with the literature on resistance degradation of Mn-doped BaTiO$_3$ and (Ba, Sr)TiO$_3$ [7, 9, 70, 259, 260, 262].

The Fe-doped samples in Figure 8.1 d) also exhibit significant higher degradation times than undoped BaTiO$_3$ samples. This observation is consistent with literature reports on the influence of Fe-doping in poly- and single crystalline SrTiO$_3$ [5, 8]. For the same degradation temperature a considerably higher starting leakage conductivity has been observed for Fe-doped
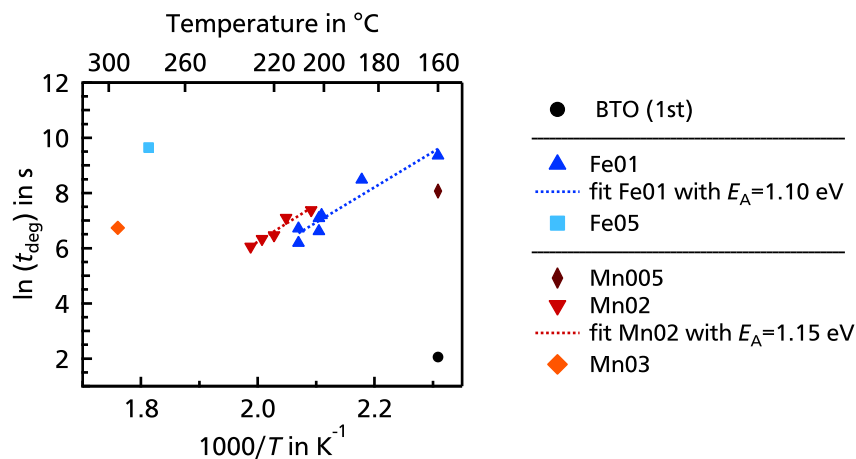
Figure 8.2.: Extracted degradation times as a function of inverse sample temperature for the degradation curves depicted in Figure 8.1. For 0.3 wt.% Mn-doped BaTiO$_3$ only one data point is extracted, as all other samples did not degraded within one working day. For 0.1 wt.% Fe-doped samples degradation times for additional temperatures are included. The corresponding data can be found in Ref. [263]. The activation energy for equilibrated 0.2 wt.% Mn-doped samples is 1.15 eV, while an activation energy of 1.10 eV is extracted for 0.1 wt.% Fe-doped samples.

samples than for Mn-doped samples. This is consistent with the defect chemistry calculations of the previous Chapter, which revealed considerably higher conductivities for Fe-doped samples, due to the closer position of the Fe charge transition levels to the valence/conduction band (see Figure 7.9). The comparison of the degradation data in Figure 8.1 b)-d) on the Mn- and Fe-series reveals, that the improvement of life time stability is significantly better for Mn-doping than for Fe-doping. This can easily be deduced from the sample temperature, for which degradation has been observed. While 0.3 wt.% Mn-doped samples did not degrade at 285 °C, the 0.5 wt.% Fe-doped samples already degrades at 279 °C. Hence, $BaTiO_3$ doped with higher Fe-concentration degraded at considerably lower temperatures than samples being doped with lower Mn-concentration. The different high impact of both dopants on the degradation time is consistent with the experimental findings of Hofman *et al.* on the resistance degradation of Mn- and Fe-doped $SrTiO_3$ thin films [264]. Within the latter, a stronger suppression of the degradation rate has been observed for Mn-doped than for Fe-doped $SrTiO_3$ thin films [264].

In order to explain the different impact of Mn- and Fe-doping on the degradation time, different potential origins are discussed in the following. One major parameter influencing the resistance degradation behavior is the **grain size**. When comparing the effect of Mn- and Fe-doping on the grain size of the present samples, it becomes clear, that Fe-doping is decreasing the grain size, while Mn-doping results in a bi-modal grain size distribution with huge elongated hexagonal and smaller spherical tetragonal grains (see Fig. 5.6). For higher Mn- and Fe-concentrations the average grain size is considerable smaller for Fe-doped samples than for Mn-doped ones. The higher number of grain boundaries in the Fe-samples is expected to suppress resistance degradation more effectively. As the experimental results in Figure 8.1 reveal the opposite, a simple grain size effect as origin for the different strong suppression of degradation for Mn- and Fe-doped samples can be excluded.

Another factor influencing the resistance degradation is the creation of **defect complexes** such as $(A_{Ti}''-V_O^{\bullet\bullet})$ and $(A_{Ti}'-V_O^{\bullet\bullet})^\bullet$ with A=Mn, Fe, which can suppress the migration of oxygen vacancies [259]. Different association enthalpies for complexes with A= Mn and A=Fe could result in different degradation behavior. In case of $SrTiO_3$, Merkle *et al.* reported higher association enthalpies for $(Mn_{Ti}''-V_O^{\bullet\bullet})$ than for $(Fe_{Ti}'-V_O^{\bullet\bullet})^\bullet$ [265]. This would be consistent with the improved life time for Mn-doped samples, which has been observed in this work. However, Maier *et al.* have shown that, unlike for the $SrTiO_3$ system, the activation energy for oxygen vacancy migration is identical in undoped, Mn- and Fe-doped $BaTiO_3$ [27]. This indicates, that defect complexes are minority defects in $BaTiO_3$ with considerable lower impact in the oxygen migration than in the case of $SrTiO_3$ [27]. According to the work of Maier *et al.*, a different defect association enthalpy in Mn- and Fe-doped $BaTiO_3$ as major factor for the different strong suppression of degradation is not likely. Nevertheless it should be stated, that

these defect complexes are not negligible for the discussion of other sample properties, e.g. for ferroelectric properties, as defect complexes can act as pinning centers for domain wall motion, which results in ferroelectric hardening [43, 266].

Besides the effect of acceptor-doping on grain size and defect association also the type of dopant and its defect energy level have a considerable influence on the degradation rate. According to Yoon *et al.* multivalent acceptor-doping leads to an increased life time of $BaTiO_3$ due to the ability of the acceptors to change their oxidation states[3] [9]. Additionally, a potential influence of the acceptor's ionization energy on the resistance degradation behavior was suggested by Baiatu *et al.* in their study on Al-, Ni-, and Fe-doped single crystalline $SrTiO_3$ [5]. In the current thesis, the model of Yoon *et al.* is extended by the assumption of Baiatu *et al.*: It is proposed that for two different kind of multivalent acceptor dopants the effectivity of changing their valence state is based on the **defect energy levels** of the dopants. In the following the impact of the defect energy levels on different degradation related properties is discussed for the present Mn- and Fe-dopants:

1. The charge transition level of the defect acts as a pinning level for the Fermi level. In the last Chapter it has been shown, that the position of the defect energy levels, i.e. the pinning position of E_F, has a direct influence on the resulting conductivity (see Fig. 7.9). Hence, charge transition levels closer to the band edges (Fe) result in a higher **initial leakage current** than charge transition levels near mid gap (Mn). Usually, high leakage currents are undesirable for the application of the $BaTiO_3$-dielectric in multi-layer ceramic capacitors.

2. The **number of oxygen vacancies** being created as charge compensation is obviously related to the oxidation state of the acceptors. The **average oxidation state** of the acceptor for a given temperature and oxygen partial pressure dependents on the position of the defect level. The defect chemistry calculations for the present 0.5 wt.% doped samples indicated that after equilibration 93 % of the Mn-dopants are charged Mn^{4+} and only 24 % of the Fe-dopants are charged Fe^{4+} (see Table 5.3). Hence, the number of oxygen vacancies is assumed to be considerably higher in the Fe-doped than in the Mn-doped samples and a faster degradation is expected for Fe-doped samples. From the argument above a 4+ oxidation state does not result in oxygen vacancy compensation and would therefore be less harmful and in agreement with the experimental findings of a slower degradation of Mn-doped samples compared to Fe-doped samples.

[3]The voltage-induced valency change of Fe-dopants in single crystalline $SrTiO_3$ is well known as electrocoloration and has been intensively described by Waser *et al.* in the scope of their paper series on the dc electrical degradation of perovskite-type titanates [4–6]. The effect of electrocoloration has also been used by Bieger *et al.* to investigate the oxygen kinetics in Fe-doped single crystalline $SrTiO_3$ [267].

The suppression mechanism of multivalent acceptors proposed by Yoon *et al.* is based on electron/hole trapping by the acceptor dopants [9]. Accordingly, electron trapping centers need to be present in the cathode region and hole trapping centers in the anode region. Therefore, the highest efficiency is reached if electron and hole trapping centers are present in the same ratio. Therefore, the Yoon *et al.* [9] proposed a 50 % A^{4+}/50 % A^{3+} with A=Mn, Fe as an optimum to equally control electron and hole trapping[4]. In the following the plausibility of a 50 % A^{4+}/50 % A^{3+} optimum oxidation state ratio, as has been proposed by Yoon *et al.*, is discussed with regard to the present results: According to the defect chemistry calculations presented in this work, none of the dopants reached a 50 % A^{4+}/50 % A^{3+} ratio after equilibration (see Table 5.3). The 0.5 wt.% Fe-doped samples showed a 24 % Fe^{4+}/76 % Fe^{3+} ratio, which is expected to be more efficient than the corresponding 93 % Mn^{4+}/7 % Mn^{3+} ratio. Hence, a higher suppression would be expected for Fe-doping than for Mn-doping. Hence, this argumentation is inconsistent with the experimental observation of a higher efficiency of Mn and an additional factor needs to be involved.

3. Besides the initial oxidation state ratio, the **stability range** of the **oxidation states** is proposed to be the third main factor. Here, the likeliness of the acceptor for changing the oxidation state and by this effectively participating in electron/hole trapping is related to the position of the defect level inside the band gap. The latter assumption is supported by the results of the defect chemistry calculation conducted in this work. The simulations on the oxygen partial pressure dependent valence state of the Fe- and Mn-dopants in Figure 7.10 revealed a considerably wider stable range for the Fe^{3+} oxidation state than for the Mn^{3+} state. The wide stability range of Fe^{3+} is directly related to the position of the $Fe^{2+/3+}$ and $Fe^{3+/4+}$ charge transition levels, which are located 2.4 eV and 0.8 eV above the valence band maximum [21]. For Mn these levels are located at 1.9 eV and 1.3 eV, respectively [21]. Hence, the Mn charge transitions levels are located more close together and the Fermi level range for the presence of Mn^{3+} is much smaller than the one for Fe^{3+}. Accordingly, a reduction (oxidation) of the Mn-dopants is expected to happen for a lower change in oxygen vacancy accumulation (depletion) in the cathode (anode) region. This will result in a more effective suppression of degradation for Mn-doped samples, which is consistent with the experimental observations of this work.

Moreover, the **grain boundary characteristics** are strongly influenced by Fermi level pinning at charge transition levels. The space-charge potential itself is defined by the difference in Fermi level between the grain boundary and the bulk. Hence, the position of the pinning level, i.e. the charge transition level, directly influences the potential and thus, the blocking behavior. The properties of the acceptors, however, are not the only factor influencing the grain boundary

---

[4]A reduction of the dopants in the cathodic region to A^{2+} has been neglected in the publication of Yoon *et al.* [9].

characteristics. As has been intensively discussed in the previous Chapter 7, the oxygen vacancy accumulation in the grain boundary core significantly influences the Fermi level position within and thus the overall space charge properties. Another factor, which has been neglected so far in this thesis, is the influence of cation vacancy segregation. Cation vacancies are expected to be immobile at equilibration, re-oxidation, and degradation temperatures. At sintering and reduction temperatures, in contrast, cation vacancies are mobile and could redistribute. Therefore, the influence of reduction, re-oxidation, and equilibration prior to degradation has been studied on a single set of 0.2 wt.% Mn-doped samples, which is described in Appendix A.5. The results indicate that a reduction with subsequent re-oxidation prior to equilibration slightly increases the degradation time. The latter could be related to an enhanced blocking of the grain boundaries due to a cation vacancy segregation into the negative space charge region during reduction. Those results, however, are based on one sample each and a more detailed discussion is omitted due to the low number of samples. In future works, a more intensive study on the influence of sample history is necessary to verify this observation.

Summary

As expected prior to the experiments, both introduced acceptor-dopants increased the life time of polycrystalline $BaTiO_3$. While the results on Mn-doped $BaTiO_3$ are consistent with literature reports, no publications[5] are available on Fe-doped polycrystalline $BaTiO_3$. Whereas the underlying mechanism for the positive effect of multivalent acceptors on the capacitor's life time is well understood, no comparison between different kind of multivalent dopants in polycrystalline $BaTiO_3$ has been published so far. In this work, the comparison of the degradation behavior of Mn- and Fe-doped $BaTiO_3$ revealed a significant life time extension upon Mn-doping than upon Fe-doping, which raises the question for potential origins.

It is proposed that the position of the defect energy level of the multivalent acceptor dopant is the most important parameter influencing the effectivity of the dopant on the life time extension of $BaTiO_3$-based polycrystalline capacitors. The position of the defect energy levels can impact the performance of the capacitor in three different ways. First, the leakage current is defined by the Fermi level position, which itself is pinned at the lower charge transition level[6] $A^{4+/3+}$ with A=Mn, Fe. Hence, a defect energy level closer to the band edges, as in the case of Fe, increases the leakage current, which is not desired for a capacitor material. Second, the position of the defect energy level defines the average oxidation state of the multivalent dopants before degradation and by this the number of oxygen vacancies. Third, the positive influence

---

[5] To the best of the author's knowledge only reports on Fe-doped single crystalline $BaTiO_3$ and Fe-doped poly- and single crystalline $SrTiO_3$ are available.

[6] A pinning at the lower charge transition level is expected for commonly used temperatures and oxygen partial pressures during annealing and degradation.

of multivalent acceptors on the life time of polycrystalline BaTiO$_3$ is based on the ability to change their valence state in the cathodic and anodic region. Here, the stability range of the oxidation states is directly related to the positions of the $A^{4+/3+}$ and $A^{3+/2+}$ charge transition levels. For Mn-dopants both defect levels exhibit a smaller distance between each other than the defect energy levels of the Fe-dopants. Hence, a Mn valence change is more likely than for Fe-dopants. Therefore, the higher effectivity of Mn-dopants on the life time is expected, which is in agreement with the experimental findings of this work. However, for acceptors with different defect energy levels and similar acceptor doping concentration the observed difference in degradation time is in clear contrast to the theoretical work of Baiatu *et al.* [6], who simulated the influence of the acceptor's defect energy level on the degradation curves of SrTiO$_3$ (see Figure 2.13 in the Fundamental Section). In the simulation of Baiatu *et al.* the value of the defect energy level solely influences the magnitude of the initial and final leakage current, but not the degradation time [6]. However, the simulations therein as well as all other currently available simulations on resistance degradation of acceptor-doped titanates solely include the lower $A^{3+/4+}$ level. This level represents the pinning level in the anode region after degradation. In the cathode region, a Fermi level pinning on the $A^{2+/3+}$ level is expected (as a result of oxygen vacancy accumulation). In order to further understand the influence of multivalent acceptor dopants on the degradation behavior of polycrystalline BaTiO$_3$, it is recommended for future works to extent the simulation by including the $A^{2+/3+}$ defect energy level. By this, it might be possible to reproduce the observed differences in life time extension of Mn- and Fe-dopants.

9. Summary and Conclusion

The goal of this thesis was to elaborate to which extend interface experiments and re-oxidation experiments can be used to identify the defect energy levels of acceptor dopants in polycrystalline $BaTiO_3$. For this purpose, undoped, Mn- and Fe-doped polycrystalline $BaTiO_3$ with different acceptor-doping concentrations has been synthesized via the conventional solid-state-reaction method. This final Chapter of the thesis will give a summary on the obtained results including an outlook on possible future experiments/simulations and unanswered questions.

Basic characterization of Mn- and Fe-doped polycrystalline $BaTiO_3$:
The synthesized Mn- and Fe-doped samples have been probed by a variety of standard characterization methods to validate their quality. In Fe-doped samples the tetragonal crystal structure is almost completely preserved and only 3 % hexagonal phase fraction have been observed for 0.5 wt.% Fe-doped specimens. While the tetragonal crystal structure is completely preserved in Mn-doped samples with low acceptor concentrations, Mn-doping concentrations ≥0.4 wt.% result in a linearly increasing hexagonal phase fraction up to 38 % h-$BaTiO_3$ in 0.5 wt.% Mn-doped samples. Acceptor-doping in polycrystalline $BaTiO_3$ is commonly known to stabilize the hexagonal phase down to room temperature [51–56]. Within this work, five different mechanism for the stabilization of the hexagonal phase have been reviewed with regard to their plausibility. With respect to the present results, the theory of Langhammer and co-workers is supported, who proposed a Jahn-Teller (*JT*) induced stabilization of the hexagonal phase [52, 55, 151, 160]. For the utilized sintering conditions, defect chemistry calculations for the 0.5 wt.% acceptor-concentration revealed that Fe dopants are incorporated predominantly as Fe^{3+}, while Mn dopants are incorporated as 60 % Mn^{3+}/ 40 % Mn^{4+} mixture. The different average valency of both dopants is related to their defect energy level position and has considerable consequences for the resulting crystal structure. Mn^{3+} has a d^4 electron configuration and is *JT*-active, while Mn^{4+} and Fe^{3+} have a d^3 and d^5 electron configuration, respectively, and are *JT*-inactive. Hence, the Mn^{3+} is expected to be responsible for the partial stabilization of the hexagonal phase in highly Mn-doped $BaTiO_3$ [52].

The appearance of the hexagonal phase in Mn-doped samples has further consequences for the microstructure as well as the dielectric properties. Elongated plate-like grains of a size > 200 μm have been observed in 0.5 wt.% Mn-doped samples, which could be assigned to the

hexagonal phase by EBSD. In contrast, Fe-doping resulted in a decreasing grain size and a bimodal grain size distribution, which is attributed to solute drag effects [138]. The room temperature dielectric constant of Mn-doped samples drastically decreased with increasing hexagonal phase fraction, due the low $\epsilon(RT)$ for h-BaTiO$_3$ [180]. The Curie point only slightly decreased upon Mn-doping, while it decreased approximately linearly upon Fe-doping. In accordance with literature, this difference was attributed to the difference in oxidation state of the acceptors towards the host site, as the lower average valency of Fe-ions requires more compensating oxygen vacancies and consequently stronger decreases T_C [182]. In addition, Desu and Subbaro proposed that the Jahn-Teller active ions tend to stabilize the tetragonal phase, which explained the lower decrease of T_C upon Mn-doping [47]. Reduction treatments at $1100\,°$C for $12\,$h in $5\,\%$ H$_2$ altered the average valency of Mn-dopants to Jahn-Teller inactive Mn^{2+}. Consequently, the hexagonal phase fraction as well as the size and amount of elongated grains decreased, which is in accordance with literature reports and the supported theory of Langhammer [52].

Due to the great interest of the community on Mn- and Fe-doped BaTiO$_3$, the results of the basic characterization do not represent new experimental findings. Nevertheless, it could be shown that the examined characteristics of the synthesized undoped, Fe- and Mn-doped samples coincide with the standard literature values, which proved their good quality and usability for further experiments - which was the aim of the extended sample characterization.

Applicability of the interface approach for Mn-doped polycrystalline BaTiO$_3$:

The first original goal of this work was to elaborate, whether it is possible to identify the defect energy levels in acceptor-doped polycrystalline BaTiO$_3$ by means of XPS analysis. For this purpose, the Fermi level position during contact formation of RuO$_2$, PtO$_x$, and Sn-doped In$_2$O$_3$ electrodes to polycrystalline BaTiO$_3$ ceramics with different Mn-doping concentrations and V$_O^{\bullet\bullet}$-content has been examined. The corresponding results represent the first systematic study of such interfaces and have partially been published in Reference [206]. XPS studies on the bare surface of reduced undoped and Mn-doped BaTiO$_3$ revealed a Ba-enrichment with increasing Mn-doping concentration. The following model has been proposed as potential origin:

The highly degenerate surface region of reduced specimens promotes Ti-vacancy formation and a subsequent Ti segregation to the surface, where it forms TiO$_2$ particles, leaving behind a Ba-rich surface phase. The latter scenario is consistent for the combined experimental findings of XPS and SEM analysis conducted in this work.

The contact formation towards RuO$_2$ electrodes revealed an $E_F - E_{VBM}$ of $2.0\,$eV for reduced and $1.7\,$eV for equilibrated/oxidized polycrystalline BaTiO$_3$ independent on the Mn-content. The Ba-enrichment of reduced Mn-doped BaTiO$_3$ surfaces relates to a secondary surface phase, which was proven to affect the Fermi level position during contact formation towards RuO$_2$ electrodes. After the removal of the Ba-rich surface phase, the Fermi energy at the interface

between RuO_2 and reduced samples was found at $E_F - E_{VBM} = 1.7 \pm 0.05$ eV, which agrees with the value determined for equilibrated/oxidized specimens. This implies, that the derived value of $E_F - E_{VBM} = 1.7 \pm 0.05$ eV at $BaTiO_3$:Mn/RuO_2 interfaces is independent on the Mn-doping and the oxygen vacancy concentration.

The contact formation towards RT-deposited Sn-doped In_2O_3 electrodes revealed a Fermi energy of $E_F - E_{VBM} = 3.0 \pm 0.05$ eV for reduced and $E_F - E_{VBM} \approx 2.5$ eV for equilibrated/oxidized poly-crystalline Mn-doped $BaTiO_3$ independent on the Mn-content. After Ba surface phase removal, the Fermi energy of reduced samples was found at 2.85 eV, which represents a 0.35 eV higher Fermi level than derived for the equilibrated/oxidized interfaces. The remaining difference for the $BaTiO_3$:Mn/ITO interfaces might be attributed to an insufficient compensation of the high space charge of reduced samples due to a low conductivity and, thus, a low charge carrier concentration of RT-deposited ITO thin films.

The Fermi energies at the $BaTiO_3$:Mn/ITO and $BaTiO_3$:Mn/RuO_2 interfaces were found to be independent on the Mn-concentration and no Fermi level pinning at the Mn defect energy levels has been observed. MATLAB simulations of the $BaTiO_3$:Mn 0.5 wt.%/RuO_2 interface configuration confirm a space charge region width considerably larger than the inelastic mean free path of photoelectrons. Permittivity dependent simulations revealed that the high permittivity of the $BaTiO_3$-based ceramics is responsible for the large space charge region, making a defect level identification by means of XPS impossible. These results imply that the interface approach is in principal a practicable method to study Fermi level pinning on defect energy levels, but its applicability is restricted to low permittivity materials.

Applicability of the re-oxidation approach for Mn- and Fe-doped polycrystalline $BaTiO_3$:
The second goal of this work was to elaborate to which extend the re-oxidation approach of Suzuki *et al.* [22] can be used to identify the defect energy levels in acceptor-doped polycrystalline $BaTiO_3$. Suzuki *et al.* successfully determined the defect energy level of Fe-impurities in a $BaTiO_3$ single crystal by the evaluation of the activation energy of the electric conductivity during step-wise re-oxidation [22]. The transfer of this approach to polycrystalline materials has not been attempted before. For this purpose, polycrystalline 0.1 wt.% and 0.5 wt.% Mn- and Fe-doped $BaTiO_3$ have been slowly re-oxidized by temperature cycling in dry ambient air mixtures, while the DC-conductivity has been monitored. Additionally, single-loop re-oxidation experiments have been conducted on the doping series' in order to examine the loop shape and initial conditions after reduction.

The evaluation of the reduced samples revealed different initial conductivities and activation energies among the samples. At 100 °C conductivities $> 10^{-2}$ S/cm and activation energies of 0.0-0.05 eV have been examined for 0.1 wt.% and 0.5 wt.% Mn-doped samples. For 0.1 wt.% Fe-doped specimens conductivities of $\sim 5 \times 10^{-3}$ S/cm and $E_A(100\,°C)$ of 0.2 eV have been determined, while for 0.5 wt.% Fe-doped $\sim 5 \times 10^{-5}$ S/cm and 0.57 eV have been derived. For

the temperature and partial pressure utilized during reduction, defect chemistry calculations confirmed that Mn is completely reduced to Mn^{2+} in 0.1 wt.% and 0.5 wt.% Mn-doped samples, while Fe is completely reduced to Fe^{2+} in 0.1 wt.% Fe-doped samples, but only partially reduced to Fe^{2+} in 0.5 wt.% Fe-doped samples. The different reduction behavior of Mn and Fe-doped samples is again related to the position of the defect energy levels. For the validation of the re-oxidation approach the information on the initial state was critical, as it defined the starting region. The present results after reduction imply, that 0.1 wt.% - 0.5 wt.% Mn-doped and 0.1 wt.% Fe-doped specimens start the re-oxidation in region I, $[V_O] > [A_{Ti}]$ where most of the acceptors are in the 2+ oxidation state, while 0.5 wt.% Fe-doped $BaTiO_3$ starts in region II, $[A_{Ti}] > [V_O] > 1/2 [A_{Ti}]$ where most of the acceptors are in the 3+ oxidation state. Considerable differences in the re-oxidation behaviour have been be observed in dependence on dopant species and concentration. While the behaviour of 0.1 wt.% Mn- and Fe-doped samples agree with the expected shape for ordinary oxygen incorporation (i.e. decreasing conductivity during dwell time), 0.5 wt.% Mn-doped samples show a step-like behaviour and 0.5 wt.% Fe-doped samples show a conductivity saturation. Two different models have been proposed and discussed for the step-like behaviour of 0.5 wt.% Mn-doped $BaTiO_3$. Neither the theory of an inhomogeneous re-oxidation of t-$BaTiO_3$ and h-$BaTiO_3$ nor a different contribution of grains and grain boundaries to the total conductivity could consistently explain all experimental observations in the Mn-series. The conductivity saturation in 0.5 wt.% Fe-doped $BaTiO_3$ could be successfully explained by the proposed model of a temperature-dependent oxygen vacancy redistribution between SCR and the grain interior.

The evaluation of the activation energy from the slow re-oxidation experiments revealed substantial differences in dependence on dopant species and concentration. The interpretation and direct extraction of defect energy levels from the activation energy is complicated by the contributions of grain boundaries. In order to quantify their influence on the conduction mechanism, the grain boundary potential has been numerically calculated based on the procedure proposed by De Souza [79], which has been implemented into MATLAB by L. Gossel [110]. The procedure of De Souza is based on the assumption of a reduced formation energy of oxygen vacancies Δg in the grain boundary core, which results in oxygen vacancy segregation and space charge formation. The simulation tool was used to calculate the electrical conductivity of 0.1 wt.% and 0.5 wt.% Mn- and Fe-doped $BaTiO_3$ as a function of oxygen vacancy concentration. The contribution of grain boundaries is represented by Δg, which was varied in a range of -1 eV to -2 eV. The experimental activation energy values at 400 °C have been compared to the simulated activation energies for the different Δg values.

No reasonable origin for the experimental observed first activation energy plateau at 0.4 eV for 0.1 wt.% Mn- and Fe-doped $BaTiO_3$ could be identified. In addition, the corresponding experimental conductivities are inconsistent with the simulated evolution of the conductivity

during re-oxidation. The high discrepancy between the best fit of Δg for Mn- and Fe-doped samples and the substantially differences of activation energy evolution between experiment and simulation suggested that the current simulation tool did not yet capture all effects contributing to the electrical conductivity. For a reliable extraction of defect energy levels and a quantitative description of re-oxidation of polycrystalline materials, additional aspects need to be included into the model. Potential aspects which are suggested for the future development of the simulation tool are i) the segregation of cation vacancies (V_{Ba}) and doping atoms (Mn, Fe) to the grain boundary core, which will alter the core charge and the resulting space charge potential, ii) temperature-dependent oxygen vacancy redistribution between the space charge region and the bulk (as proposed for 0.5 wt.% Fe-doped samples), iii) simulations at lower temperatures taking defect interactions into account, and iv) depth dependent oxygen vacancy concentration (internal grains will oxidize slower than grains at the surface).

Resistance degradation of Mn- and Fe-doped polycrystalline BaTiO$_3$:
Resistance degradation experiments have been performed using a constant electric field of 0.3 kV/mm with variable temperatures for selected doping concentrations of Mn- and Fe-doped polycrystalline BaTiO$_3$. Both introduced acceptor-dopants increased the life time of polycrystalline BaTiO$_3$, which agrees with literature on multi-valent acceptor-doping [7, 9, 70, 259, 260, 262]. The increased life time of multi-valent acceptors is based on their ability to change their oxidation state and to trap charges in the cathodic and anodic region [9]. While the mechanism is well understood, no comparison between different kind of multi-valent dopants in polycrystalline BaTiO$_3$ has been published so far. The results of this work revealed a significant stronger life time improvement upon Mn-doping than upon Fe-doping. This results are in accordance with studies of Hofman *et al.* on the influence of Mn- and Fe-doping on the resistance degradation of SrTiO$_3$ thin films [264], but do not agree with the theoretical work of Baiatu *et al.*, who simulated the influence of the acceptor's defect energy level on the degradation curves of SrTiO$_3$ [6]. To the author's best knowledge, currently no model consistently explains the different strong influence of Mn- and Fe-doping on the life time extension of BaTiO$_3$ ceramic capacitors.

It is proposed that the defect energy level of the multi-valent acceptor dopant is the most important parameter to describe the differently strong life time improvement. Here, the distances of the $A^{2+/3+}$ and $A^{3+/4+}$ energy levels with respect to the band edges are of particular importance. The Fe defect energy levels are closer to the band edges than the Mn defect energy levels. Consequently, Fe-dopants are charged 3+ in a wider Fermi level range than Mn-dopants. As the positive effect of multi-valent acceptors on the degradation behavior is based on the valence change of the dopants, the smaller stability range of Mn^{3+} is more effective for the life time extension. For Mn-dopants smaller changes in oxygen vacancy concentrations in the anodic (cathodic) region are necessary to induce the oxidation (reduction) of Mn^{3+} to Mn^{4+} (Mn^{2+}).

In literature, all currently available simulations on resistance degradation of acceptor-doped titanates solely include the lower $A^{3+/4+}$ level. In order to further understand the influence of multi-valent acceptor dopants, it is recommended for future works to extent the simulation of Baiatu *et al.* [6] by including the $A^{2+/3+}$ defect energy level. By this, it might be possible to reproduce the observed differences in life time extension of Mn- and Fe-dopants.

The result of the differently pronounced effect of Mn- and Fe-doping on the life time improvement and the proposed correlation to the position of the defect energy levels emphasizes again the importance of defect level identification - which was the main objective of this thesis.

In summary, the focus of this thesis was the development and qualification of new methods for defect level identification in polycrystalline $BaTiO_3$. The combination of experiments and simulations revealed that the interface approach is not utilizable for high permittivity materials such as $BaTiO_3$. Even for extremely high Mn and oxygen vacancy concentrations the high value of the dielectric constant results in a space charge region considerably larger than the inelastic mean free path of photoelectrons, making a defect level identification by means of XPS impossible. In order to extract the defect energy levels from re-oxidation experiments of Mn- and Fe-doped polycrystalline $BaTiO_3$, the grain boundary potential and the resulting current flow has been simulated. The comparison between experimental and simulated activation energy evolution revealed considerable differences, which suggests that the current simulation tool did not yet capture all effects contributing to the electrical conductivity. Hence, a reliable extraction of defect energy levels and a quantitative description of re-oxidation of polycrystalline materials is not possible with the current tool. Several aspects for future simulation tool development have been proposed, which should enable a successful reproduction of the experimental values and subsequent defect level identification using the re-oxidation approach. Nevertheless, the combination of experimental results with the corresponding simulations provided a quantitative understanding of the space charge region characteristics at grain boundaries.

This thesis constitutes, to the author's best knowledge, the first systematic study on the applicability of i) the interface and ii) the re-oxidation approach for defect level identification in acceptor-doped polycrystalline $BaTiO_3$. The obtained results represent the first comprehensive investigation, which combines structural and electrical characterization of Mn- and Fe-doped polycrystalline $BaTiO_3$ with the fundamental research on the influence of defect energy levels on space charge region characteristics. The findings of this thesis build a profound basis for the future development of the re-oxidation approach for defect level identification in polycrystals. Simultaneously, the obtained results can guide the dopant selection in future projects[1] on bulk and interface Fermi level engineering in acceptor-doped $BaTiO_3$.

---

[1] The results of this thesis were essential for the definition of the research program in project *B04: Influence of bulk electronic structure on grain boundary properties in perovskite oxides* of the collaborative research center 1548 FLAIR.

Bibliography

[1] K. Hong, T. H. Lee, J. M. Suh, S.-H. Yoon, and H. W. Jang, "Perspectives and challenges in multilayer ceramic capacitors for next generation electronics," *Journal of Materials Chemistry C*, vol. 7, no. 32, pp. 9782–9802, 2019.

[2] H. Kishi, Y. Mizuno, and H. Chazono, "Base-metal electrode-multilayer ceramic capacitors: past, present and future perspectives," *Japanese Journal of Applied Physics*, vol. 42, no. 1R, p. 1, 2003.

[3] J.-J. Wang, H.-B. Huang, T. J. Bayer, A. Moballegh, Y. Cao, A. Klein, E. C. Dickey, D. L. Irving, C. A. Randall, and L.-Q. Chen, "Defect Chemistry and Resistance Degradation in Fe-doped $SrTiO_3$ Single Crystal," *Acta Materialia*, vol. 108, pp. 229–240, 2016.

[4] R. Waser, T. Baiatu, and K.-H. Härdtl, "dc electrical degradation of perovskite-type titanates: I, Ceramics," *Journal of the American Ceramic Society*, vol. 73, no. 6, pp. 1645–1653, 1990.

[5] R. Waser, T. Baiatu, and K.-H. Härdtl, "dc electrical degradation of perovskite-type titanates: II, single crystals," *Journal of the American Ceramic Society*, vol. 73, no. 6, pp. 1654–1662, 1990.

[6] T. Baiatu, R. Waser, and K.-H. Härdtl, "dc Electrical Degradation of Perovskite-Type Titanates: III, A Model of the Mechanism," *Journal of the American Ceramic Society*, vol. 73, no. 6, pp. 1663–1673, 1990.

[7] J. Rödel and G. Tomandl, "Degradation of Mn-doped $BaTiO_3$ ceramic under a high dc electric field," *Journal of materials science*, vol. 19, no. 11, pp. 3515–3523, 1984.

[8] S. Rodewald, J. Fleig, and J. Maier, "Resistance degradation of iron-doped strontium titanate investigated by spatially resolved conductivity measurements," *Journal of the American Ceramic Society*, vol. 83, no. 8, pp. 1969–1976, 2000.

[9] S.-H. Yoon, C. A. Randall, and K.-H. Hur, "Difference between resistance degradation of fixed valence acceptor (Mg) and variable valence acceptor (Mn)-doped $BaTiO_3$ ceramics," *Journal of Applied Physics*, vol. 108, no. 6, p. 064101, 2010.

[10] M. Wojtyniak, K. Szot, R. Wrzalik, C. Rodenbücher, G. Roth, and R. Waser, "Electro-degradation and resistive switching of Fe-doped $SrTiO_3$ single crystal," *Journal of Applied Physics*, vol. 113, no. 8, p. 083713, 2013.

[11] T. J. Bayer, J. Carter, J.-J. Wang, A. Klein, L.-Q. Chen, and C. A. Randall, "Determination of electrical properties of degraded mixed ionic conductors: Impedance studies with applied dc voltage," *Journal of Applied Physics*, vol. 122, no. 24, p. 244101, 2017.

[12] Y. Cao, J. Shen, C. Randall, and L.-Q. Chen, "Effect of ferroelectric polarization on ionic transport and resistance degradation in $BaTiO_3$ by phase-field approach," *Journal of the American Ceramic Society*, vol. 97, no. 11, pp. 3568–3575, 2014.

[13] W. Liu, G.-Y. Yang, and C. A. Randall, "Evidence for increased polaron conduction near the cathodic interface in the final stages of electrical degradation in $SrTiO_3$ crystals," *Japanese Journal of Applied Physics*, vol. 48, no. 5R, p. 051404, 2009.

[14] R. Giesecke, R. Hertwig, T. J. M. Bayer, C. A. Randall, and A. Klein, "Modification of the Schottky barrier height at the RuO_2 cathode during resistance degradation of Fe-doped $SrTiO_3$," *Journal of the American Ceramic Society*, vol. 100, no. 10, pp. 4590–4601, 2017.

[15] S. Rodewald, N. Sakai, K. Yamaji, H. Yokokawa, J. Fleig, and J. Maier, "The Effect of the Oxygen Exchange at Electrodes on the High-Voltage Electrocoloration of Fe-Doped $SrTiO_3$ Single Crystals: A Combined SIMS and Microelectrode Impedance Study," *Journal of Electroceramics*, vol. 7, no. 2, pp. 95–105, 2001.

[16] R. A. De Souza, "Oxygen diffusion in $SrTiO_3$ and related perovskite oxides," *Advanced Functional Materials*, vol. 25, no. 40, pp. 6326–6342, 2015.

[17] R. Giesecke, "Influence of oxygen vacancies on barrier heights at $SrTiO_3$/electrode interfaces," Master's thesis, TU Darmstadt, 2016.

[18] B. Huang, "Resistance degradation of Fe-doped $SrTiO_3$ single crystals with different electrodes," Master's thesis, TU Darmstadt, 2017.

[19] B. Öcal, "Effect of ITO anode on resistance degradation of $BaTiO_3$," Master's thesis, TU Darmstadt, 2019.

[20] S. M. Sze and K. K. Ng, *Physics of Semiconductor Devices*. John Wiley & Sons, 2007.

[21] B. A. Wechsler and M. B. Klein, "Thermodynamic point defect model of barium titanate and application to the photorefractive effect," *J. Opt. Soc. Am. B*, vol. 5, no. 8, pp. 1711–1723, 1988.

[22] I. Suzuki, L. Gura, and A. Klein, "The energy level of the $Fe^{2+/3+}$-transition in $BaTiO_3$ and $SrTiO_3$ single crystals," *Physical Chemistry Chemical Physics*, vol. 21, no. 11, pp. 6238–6246, 2019.

[23] D. K. Schroder, *Semiconductor material and device characterization*. John Wiley & Sons, 2015.

[24] S. S. Hegedus and W. N. Shafarman, "Thin-film solar cells: device measurements and analysis," *Progress in Photovoltaics: Research and Applications*, vol. 12, no. 2-3, pp. 155–176, 2004.

[25] H.-J. Hagemann and D. Hennings, "Reversible Weight Change of Acceptor-Doped $BaTiO_3$," *J. Am. Ceram. Soc.*, vol. 64, no. 10, pp. 590–594, 1981.

[26] R. N. Schwartz and B. A. Wechsler, "Electron-paramagnetic-resonance study of transition-metal-doped $BaTiO_3$: effect of material processing on Fermi-level position," *Phys. Rev. B*, vol. 48, no. 10, p. 7057, 1993.

[27] R. A. Maier and C. A. Randall, "Low temperature ionic conductivity of an acceptor-doped perovskite: II. Impedance of single-crystal $BaTiO_3$," *Journal of the American Ceramic Society*, vol. 99, no. 10, pp. 3360–3366, 2016.

[28] P. Wendel, S. Periyannan, W. Jaegermann, and A. Klein, "Polarization dependence of ZnO Schottky barriers revealed by photoelectron spectroscopy," *Physical Review Materials*, vol. 4, no. 8, p. 084604, 2020.

[29] S. Siol, J. C. Hellmann, S. D. Tilley, M. Graetzel, J. Morasch, J. Deuermeier, W. Jaegermann, and A. Klein, "Band Alignment Engineering at Cu_2O/ZnO Heterointerfaces," *ACS applied materials & interfaces*, vol. 8, no. 33, pp. 21824–21831, 2016.

[30] A. Klein, "Interface properties of dielectric oxides," *Journal of the American Ceramic Society*, vol. 99, no. 2, pp. 369–387, 2016.

[31] M. B. Klein and R. Schwartz, "Photorefractive effect in $BaTiO_3$: microscopic origins," *JOSA B*, vol. 3, no. 2, pp. 293–305, 1986.

[32] E. Possenriede, O. Schirmer, H. Donnerberg, G. Godefroy, and A. Maillard, "ESR identification of Fe containing defects in $BaTiO_3$," *Ferroelectrics*, vol. 92, no. 1, pp. 245–252, 1989.

[33] J.-H. Lee, S.-H. Kim, and S.-H. Cho, "Valence Change of Mn Ions in $BaTiO_3$-Based PTCR Materials," *Journal of the American Ceramic Society*, vol. 78, no. 10, pp. 2845–2848, 1995.

[34] S. Ding, G. Jia, J. Wang, and Z. He, "Electrical properties of Y-and Mn-doped BaTiO$_3$-based PTC ceramics," *Ceramics International*, vol. 34, no. 8, pp. 2007–2010, 2008.

[35] W. Callister, *Materials Science and Engineering: An Introduction 7th Edition with Wiley Plus Set*. Wiley Plus Products Series, John Wiley & Sons, Incorporated, 2006.

[36] D. A. Molodov, *Microstructural design of advanced engineering materials*. John Wiley & Sons, 2013.

[37] S. Hunklinger, *Festkörperphysik*. De Gruyter Oldenbourg, 2017.

[38] R. Waser, U. Böttger, and S. Tiedke, *Polar oxides*. Wiley Online Library, 2005.

[39] A. J. Moulson and J. M. Herbert, *Electroceramics: materials, properties, applications*. John Wiley & Sons, 2003.

[40] R. A. Kishore, "Harvesting thermal energy with ferroelectric materials," in *Ferroelectric Materials for Energy Harvesting and Storage*, pp. 85–106, Elsevier, 2021.

[41] H. Jaffe, "Piezoelectric ceramics," *Journal of the American Ceramic Society*, vol. 41, no. 11, pp. 494–498, 1958.

[42] M. E. Lines and A. M. Glass, *Principles and applications of ferroelectrics and related materials*. Oxford university press, 2001.

[43] M. Acosta, N. Novak, V. Rojas, S. Patel, R. Vaish, J. Koruza, G. Rossetti Jr, and J. Rödel, "BaTiO$_3$-based piezoelectrics: Fundamentals, current status, and perspectives," *Applied Physics Reviews*, vol. 4, no. 4, p. 041305, 2017.

[44] K. Momma and F. Izumi, "Vesta: a three-dimensional visualization system for electronic and structural analysis," *Journal of Applied crystallography*, vol. 41, no. 3, pp. 653–658, 2008.

[45] P. Tolédano, "Extensions and some recent applications of the landau theory of phase transitions," in *EPJ Web of Conferences*, vol. 22, p. 00007, EDP Sciences, 2012.

[46] H.-J. Hagemann and H. Ihrig, "Valence change and phase stability of 3d-doped BaTiO$_3$ annealed in oxygen and hydrogen," *Physical Review B*, vol. 20, no. 9, p. 3871, 1979.

[47] S. Desu and E. Subbarao, "Effect of oxidation states of Mn on the phase stability of Mn-doped BaTiO$_3$," *Ferroelectrics*, vol. 37, no. 1, pp. 665–668, 1981.

[48] S. Lee, C. A. Randall, and Z.-K. Liu, "Modified phase diagram for the barium oxide–titanium dioxide system for the ferroelectric barium titanate," *Journal of the American Ceramic Society*, vol. 90, no. 8, pp. 2589–2594, 2007.

[49] M. Yashima, T. Hoshina, D. Ishimura, S. Kobayashi, W. Nakamura, T. Tsurumi, and S. Wada, "Size effect on the crystal structure of barium titanate nanoparticles," *Journal of applied physics*, vol. 98, no. 1, p. 014313, 2005.

[50] T. A. Colson, M. J. Spencer, and I. Yarovsky, "A DFT study of the perovskite and hexagonal phases of BaTiO$_3$," *Computational materials science*, vol. 34, no. 2, pp. 157–165, 2005.

[51] R. Glaister and H. Kay, "An investigation of the cubic-hexagonal transition in barium titanate," *Proceedings of the Physical Society (1958-1967)*, vol. 76, no. 5, p. 763, 1960.

[52] H. T. Langhammer, T. Müller, K.-H. Felgner, and H.-P. Abicht, "Crystal structure and related properties of manganese-doped barium titanate ceramics," *Journal of the American Ceramic Society*, vol. 83, no. 3, pp. 605–611, 2000.

[53] G. M. Keith, M. J. Rampling, K. Sarma, N. M. Alford, and D. Sinclair, "Synthesis and characterisation of doped 6H-BaTiO$_3$ ceramics," *Journal of the European Ceramic Society*, vol. 24, no. 6, pp. 1721–1724, 2004.

[54] M. Prades, N. Masó, H. Beltrán, E. Cordoncillo, and A. R. West, "Polymorphism of BaTiO$_3$ acceptor doped with Mn^{3+}, Fe^{3+}, and Ti^{3+}," *Journal of the American Ceramic Society*, vol. 91, no. 7, pp. 2364–2366, 2008.

[55] R. Böttcher, H. Langhammer, T. Müller, and H. Abicht, "3C–6H phase transition in BaTiO$_3$ induced by Fe ions: an electron paramagnetic resonance study," *Journal of Physics: Condensed Matter*, vol. 20, no. 50, p. 505209, 2008.

[56] S. Jayanthi and T. Kutty, "Dielectric properties of 3d transition metal substituted BaTiO$_3$ ceramics containing the hexagonal phase formation," *Journal of Materials Science: Materials in Electronics*, vol. 19, no. 7, pp. 615–626, 2008.

[57] R. Waser and R. Hagenbeck, "Grain boundaries in dielectric and mixed-conducting ceramics," *Acta Mater.*, vol. 48, no. 4, pp. 797–825, 2000.

[58] V. M. Goldschmidt, "Die Gesetze der Krystallochemie," *Naturwissenschaften*, vol. 14, no. 21, pp. 477–485, 1926.

[59] C. M. Culbertson, A. T. Flak, M. Yatskin, P. H.-Y. Cheong, D. P. Cann, and M. R. Dolgos, "Neutron total scattering studies of group II titanates (ATiO$_3$, A^{2+} = Mg, Ca, Sr, Ba)," *Scientific reports*, vol. 10, no. 1, pp. 1–10, 2020.

[60] H.-I. Yoo, C.-R. Song, and D.-K. Lee, "BaTiO$_{3-\delta}$: Defect Structure, Electrical Conductivity, Chemical Diffusivity, Thermoelectric Power, and Oxygen Nonstoichiometry," *Journal of electroceramics*, vol. 8, pp. 5–36, 2002.

[61] N.-H. Chan and D. M. Smyth, "Defect Chemistry of Donor-Doped BaTiO$_3$," *Journal of the American Ceramic Society*, vol. 67, no. 4, pp. 285–288, 1984.

[62] F. D. Morrison, A. M. Coats, D. C. Sinclair, and A. R. West, "Charge Compensation Mechanisms in La-Doped BaTiO$_3$," *Journal of Electroceramics*, vol. 6, pp. 219–232, 2001.

[63] D. M. Smyth, "The Defect Chemistry of Donor-Doped BaTiO$_3$: A Rebuttal," *Journal of electroceramics*, vol. 9, pp. 179–186, 2002.

[64] D. M. Smyth, "Comments on the Defect Chemistry of Undoped and Acceptor-Doped BaTiO$_3$," *Journal of electroceramics*, vol. 11, pp. 89–100, 2003.

[65] P. Erhart and K. Albe, "Thermodynamics of mono-and di-vacancies in barium titanate," *J. Appl. Phys.*, vol. 102, no. 8, p. 084111, 2007.

[66] J. N. Baker, P. C. Bowes, J. S. Harris, and D. L. Irving, "Mechanisms governing metal vacancy formation in BaTiO$_3$ and SrTiO$_3$," *Journal of Applied Physics*, vol. 124, no. 11, p. 114101, 2018.

[67] G. Lewis and C. Catlow, "Computer modelling of barium titanate," *Radiation Effects*, vol. 73, no. 1-4, pp. 307–314, 1983.

[68] Osawa, Shin-ichi and Furuzawa, Akira and Fujikawa, Nobuyoshi, "Effect of the manganese valence state on the electrical conductivity of barium titanate," *Journal of the American Ceramic Society*, vol. 76, no. 5, pp. 1191–1194, 1993.

[69] H.-I. Yoo, T.-S. Oh, H.-S. Kwon, D.-K. Shin, and J.-S. Lee, "Electrical conductivity–defect structure correlation of variable-valence and fixed-valence acceptor-doped BaTiO$_3$ in quenched state," *Physical Chemistry Chemical Physics*, vol. 11, no. 17, pp. 3115–3126, 2009.

[70] K. Morita, Y. Mizuno, H. Chazono, and H. Kishi, "Effect of Mn addition on dc-electrical degradation of multilayer ceramic capacitor with Ni internal electrode," *Japanese journal of applied physics*, vol. 41, no. 11S, p. 6957, 2002.

[71] G. Jonker, "Nature of aging in ferroelectric ceramics," *J. Am. Ceram. Soc*, vol. 55, no. 1, pp. 57–58, 1972.

[72] P. Erhart and K. Albe, "Modeling the electrical conductivity in BaTiO$_3$ on the basis of first-principles calculations," *Journal of Applied Physics*, vol. 104, no. 4, p. 044315, 2008.

[73] N.-H. Chan, R. Sharma, and D. M. Smyth, "Nonstoichiometry in undoped BaTiO$_3$," *Journal of the American Ceramic Society*, vol. 64, no. 9, pp. 556–562, 1981.

[74] A. M. J. H. Seuter, "DEFECT CHEMISTRY AND ELECTRICAL TRANSPORT PROPERTIES OF BARIUM TITANATE.," 1974.

[75] H. Ihrig, "On the polaron nature of the charge transport in BaTiO$_3$," *Journal of Physics C: Solid State Physics*, vol. 9, no. 18, p. 3469, 1976.

[76] A. Einstein *et al.*, "Investigations on the Theory of the Brownian Movement," 1915.

[77] M. Von Smoluchowski, "Zur kinetischen Theorie der Brownschen Molekularbewegung und der Suspensionen," *Annalen der physik*, vol. 326, no. 14, pp. 756–780, 1906.

[78] M. Kessel, R. A. De Souza, and M. Martin, "Oxygen diffusion in single crystal barium titanate," *Physical Chemistry Chemical Physics*, vol. 17, no. 19, pp. 12587–12597, 2015.

[79] R. A. De Souza, "The formation of equilibrium space-charge zones at grain boundaries in the perovskite oxide SrTiO$_3$," *Physical Chemistry Chemical Physics*, vol. 11, no. 43, pp. 9939–9969, 2009.

[80] Y. Kajikawa, "Conduction model covering non-degenerate through degenerate polycrystalline semiconductors with non-uniform grain-boundary potential heights based on an energy filtering model," *Journal of Applied Physics*, vol. 112, no. 12, p. 123713, 2012.

[81] M. Frischbier, *Die elektrischen Eigenschaften von Indiumoxid-Dünnschichten: in-situ Hall-Effekt-Messungen zur Aufklärung des Einflusses von Punktdefekten und Korngrenzen*. PhD thesis, Technische Universität, 2015.

[82] J. Y. Seto, "The electrical properties of polycrystalline silicon films," *Journal of Applied Physics*, vol. 46, no. 12, pp. 5247–5254, 1975.

[83] R. L. Petritz, "Theory of photoconductivity in semiconductor films," *Physical Review*, vol. 104, no. 6, p. 1508, 1956.

[84] R. Waser, "Electronic properties of grain boundaries in SrTiO$_3$ and BaTiO$_3$ ceramics," *Solid State Ionics*, vol. 75, pp. 89–99, 1995.

[85] G. Yang, G. Lian, E. Dickey, C. Randall, D. Barber, P. Pinceloup, M. Henderson, R. Hill, J. Beeson, and D. Skamser, "Oxygen nonstoichiometry and dielectric evolution of BaTiO$_3$. Part II–insulation resistance degradation under applied dc bias," *Journal of applied physics*, vol. 96, no. 12, pp. 7500–7508, 2004.

[86] S.-H. Yoon, C. A. Randall, and K.-H. Hur, "Influence of grain size on impedance spectra and resistance degradation behavior in acceptor (Mg)-doped BaTiO$_3$ ceramics," *Journal of the American Ceramic Society*, vol. 92, no. 12, pp. 2944–2952, 2009.

[87] H.-I. Yoo, M.-W. Chang, T.-S. Oh, C.-E. Lee, and K. Becker, "Electrocoloration and oxygen vacancy mobility of BaTiO$_3$," *Journal of Applied Physics*, vol. 102, no. 9, p. 093701, 2007.

[88] L. Simon-Seveyrat, A. Hajjaji, Y. Emziane, B. Guiffard, and D. Guyomar, "Re-investigation of synthesis of BaTiO$_3$ by conventional solid-state reaction and oxalate coprecipitation route for piezoelectric applications," *Ceramics international*, vol. 33, no. 1, pp. 35–40, 2007.

[89] L. K. Templeton and J. A. Pask, "Formation of BaTiO$_3$ from BaCO$_3$ and TiO$_2$ in Air and in CO$_2$," *Journal of the American Ceramic Society*, vol. 42, no. 5, pp. 212–216, 1959.

[90] A. Beauger, J. Mutin, and J. Niepce, "Synthesis reaction of metatitanate BaTiO$_3$," *Journal of materials science*, vol. 18, no. 10, pp. 3041–3046, 1983.

[91] J. Mutin and J. Niepce, "About stoichiometry of polycrystalline BaTiO$_3$ synthesized by solid-solid reaction," *Journal of materials science letters*, vol. 3, no. 7, pp. 591–592, 1984.

[92] B. Malič, D. Kuščer, M. Vrabelj, and J. Koruza, "Review of methods for powder-based processing," *Magnetic, ferroelectric, and multiferroic metal oxides*, pp. 95–120, 2018.

[93] M. Barsoum, *Fundamentals of ceramics*. CRC press, 2019.

[94] A. Klein, "Transparent conducting oxides: Electronic structure–property relationship from photoelectron spectroscopy with in situ sample preparation," *Journal of the American Ceramic Society*, vol. 96, no. 2, pp. 331–345, 2013.

[95] C. Lohaus, "The Fermi Level in Hematite-Doping, Band Alignment, and Charge Transitions," 2019.

[96] R. Anton, T. Wiegner, W. Naumann, M. Liebmann, C. Klein, and C. Bradley, "Design and performance of a versatile, cost-effective microwave electron cyclotron resonance plasma source for surface and thin film processing," *Review of Scientific Instruments*, vol. 71, no. 2, pp. 1177–1180, 2000.

[97] tectra, "TPIS Plasma Source." `https://tectra.de/deposition-progress/plasma-sources/`. Accessed: 2022-04-20.

[98] M. Ohring, *Materials science of thin films*. Elsevier, 2001.

[99] R. Schafranek, J. Schaffner, and A. Klein, "In situ photoelectron study of the (Ba, Sr)TiO$_3$/RuO$_2$ contact formation," *J. Eur. Ceram. Soc.*, vol. 30, no. 2, pp. 187–192, 2010.

[100] D. M. Mattox, *Handbook of physical vapor deposition (PVD) processing*. William Andrew, 2010.

[101] B. Charles and K. J. Fredeen, "Concepts, instrumentation and techniques in inductively coupled plasma optical emission spectrometry," *Perkin Elmer Corp*, vol. 3, no. 2, 1997.

[102] G. Mie, "Beiträge zur Optik trüber Medien, speziell kolloidaler Metallösungen," *Annalen der physik*, vol. 330, no. 3, pp. 377–445, 1908.

[103] G. B. de Boer, C. de Weerd, D. Thoenes, and H. W. Goossens, "Laser diffraction spectrometry: Fraunhofer diffraction versus mie scattering," *Particle & Particle Systems Characterization*, vol. 4, no. 1-4, pp. 14–19, 1987.

[104] R. Xu, "Light scattering: A review of particle characterization applications," *Particuology*, vol. 18, pp. 11–21, 2015.

[105] Micromeritics Instrument Corporation, "Saturn DigiSizer5200 Operators Manual V1.12." `https://www.micromeritics.com/Repository/Files/Saturn_DigiSizer_5200_Operators_Manual.pdf`. Accessed: 2022-04-20.

[106] T. L. Heath *et al.*, *The works of Archimedes*. Courier Corporation, 2002.

[107] C. B. Sawyer and C. Tower, "Rochelle salt as a dielectric," *Physical review*, vol. 35, no. 3, p. 269, 1930.

[108] R. Dittmer, *Multi-Scale Behavior of $Bi_{1/2}Na_{1/2}TiO_3$-Based Lead-Free Piezoceramics*. PhD thesis, Technische Universität Darmstadt, 2008.

[109] J. E. Schultheiß, "Polarization reversal dynamics in polycrystalline ferroelectric/ferroelastic ceramic materials," 2018.

[110] L. B. Gossel, "Influence of Grain Boundaries and Defect Energy Levels on the Electrical Properties of Acceptor-doped Polycrystalline $BaTiO_3$," Master's thesis, TU Darmstadt, 2020.

[111] H. Ding, "Electrical Studies of Acceptor-doped $BaTiO_3$," Master's thesis, TU Darmstadt, 2018.

[112] L. J. van der Pauw, "A method of measuring the resistivity and hall coefficient on lamellae of arbitrary shape," *Philips technical review*, vol. 20, pp. 220–224, 1958.

[113] M. Kakudo and N. Kasai, *X-ray diffraction by macromolecules*. Kodansha Limited and Springer-Verlag Berlin Heidelberg, 2005.

[114] H. Stanjek and W. Häusler, "Basics of X-ray Diffraction," *Hyperfine Interactions*, vol. 154, no. 1-4, pp. 107–119, 2004.

[115] STOE, "Application Report, STOE STADI P: Why powders should always be measured in transmission/ Debye Scherrer geometry." `https://www.stoe.com/wp-content/uploads/2020/11/Transmission.pdf`. Accessed: 2022-04-19.

[116] T. Hartmann, Stoe & Cie GmbH, "LABNOTE STOE STADI P Best Data Quality using Transmission-/Debye-Scherrer-Geometry." `https://devmatech.eu/wp-content/uploads/Labnote-Powder-Transmission-Debye-Scherrer-Geometry.pdf`. Accessed: 2023-04-20.

[117] L. Spieß, H. Behnken, C. Genzel, R. Schwarzer, and G. Teichert, *Moderne Röntgenbeugung,* vol. 2. Springer, 2009.

[118] J. I. Goldstein, D. E. Newbury, J. R. Michael, N. W. Ritchie, J. H. J. Scott, and D. C. Joy, *Scanning electron microscopy and X-ray microanalysis*. Springer, 2017.

[119] L. Reimer, "Scanning electron microscopy: physics of image formation and microanalysis," *Measurement Science and Technology*, vol. 11, no. 12, pp. 1826–1826, 2000.

[120] F. Reinert and S. Hüfner, "Photoemission spectroscopyfrom early days to recent applications," *New Journal of Physics*, vol. 7, no. 1, p. 97, 2005.

[121] C. M. Schneider, "Element-specific probes of magnetism," in *Handbook of Surface Science*, vol. 5, pp. 43–112, Elsevier, 2015.

[122] A. Klein, T. Mayer, A. Thissen, and W. Jaegermann, "Photoelectron spectroscopy in materials science and physical chemistry," *Bunsen-Magazin*, vol. 10, no. 4, pp. 124–139, 2008.

[123] M. P. Seah and W. Dench, "Quantitative electron spectroscopy of surfaces: A standard data base for electron inelastic mean free paths in solids," *Surface and interface analysis*, vol. 1, no. 1, pp. 2–11, 1979.

[124] D. A. Shirley, "High-resolution X-ray photoemission spectrum of the valence bands of gold," *Physical Review B*, vol. 5, no. 12, p. 4709, 1972.

[125] S. Tougaard, "Quantitative analysis of the inelastic background in surface electron spectroscopy," *Surface and Interface Analysis*, vol. 11, no. 9, pp. 453–472, 1988.

[126] J. F. Moulder, W. F. Stickle, P. E. Sobol, and K. D. Bomben, *Handbook of X-ray Photoelectron Spectroscopy*. Eden Prairie: Physical Electronics, Inc., 1995.

[127] W. Schottky, "Zur Halbleitertheorie der Sperrschicht-und Spitzengleichrichter," *Zeitschrift für Physik*, vol. 113, no. 5, pp. 367–414, 1939.

[128] E. A. Kraut, R. W. Grant, J. R. Waldrop, and S. P. Kowalczyk, "Semiconductor core-level to valence-band maximum binding-energy differences: Precise determination by x-ray photoelectron spectroscopy," *Phys. Rev. B*, vol. 28, no. 4, p. 1965, 1983.

[129] S. Li, *Grenzflächenmodifizierung kathodenzerstäubter (Ba,Sr)TiO₃-Dünnschichten*. PhD thesis, 2011.

[130] C. Wittich, *Perowskitsolarzellen-Entwicklung und Charakterisierung*. PhD thesis, 2019.

[131] MATLAB, *version 9.7.0.1190202 (R2019b)*. Natick, Massachusetts: The MathWorks Inc., 2019.

[132] J. Kierzenka and L. F. Shampine, " BVP solver that controls residual and error," *JNAIAM J. Numer. Anal. Ind. Appl. Math*, vol. 3, no. 1-2, pp. 27–41, 2008.

[133] N. Maso, H. Beltran, E. Cordoncillo, P. Escribano, and A. West, "Electrical properties of Fe-doped BaTiO₃," *Journal of Materials Chemistry*, vol. 16, no. 17, pp. 1626–1633, 2006.

[134] I. Burn, "Mn-doped polycrystalline BaTiO₃," *Journal of Materials Science*, vol. 14, no. 10, pp. 2453–2458, 1979.

[135] P. Lambeck and G. Jonker, "The nature of domain stabilization in ferroelectric perovskites," *Journal of Physics and Chemistry of Solids*, vol. 47, no. 5, pp. 453–461, 1986.

[136] H. Ihrig, "The phase stability of BaTiO₃ as a function of doped 3d elements: an experimental study," *Journal of Physics C: Solid State Physics*, vol. 11, no. 4, p. 819, 1978.

[137] K. Albertsen, D. Hennings, and O. Steigelmann, "Donor-acceptor charge complex formation in barium titanate ceramics: Role of firing atmosphere," *Journal of Electroceramics*, vol. 2, no. 3, pp. 193–198, 1998.

[138] W. Rheinheimer and M. J. Hoffmann, "Grain growth in perovskites: What is the impact of boundary transitions?," *Current Opinion in Solid State and Materials Science*, vol. 20, no. 5, pp. 286–298, 2016.

[139] A. Feteira, G. Keith, M. Rampling, C. Kirk, I. Reaney, K. Sarma, N. M. Alford, and D. Sinclair, "Synthesis and characterisation of Ga-doped hexagonal BaTiO₃," *Crystal engineering*, vol. 5, no. 3-4, pp. 439–448, 2002.

[140] S. Das, R. Mishra, and B. Roul, "Magnetic and ferroelectric properties of Ni doped BaTiO₃," *Solid state communications*, vol. 191, pp. 19–24, 2014.

[141] H.-J. Hagemann, "Loss mechanisms and domain stabilisation in doped BaTiO₃," *Journal of Physics C: Solid State Physics*, vol. 11, no. 15, p. 3333, 1978.

[142] Y. Ichikawa, Y. Kitanaka, T. Oguchi, Y. Noguchi, and M. Miyayama, "Polarization degradation and oxygen-vacancy rearrangement in Mn-doped $BaTiO_3$ ferroelectrics ceramics," *Journal of the Ceramic Society of Japan*, vol. 122, no. 1426, pp. 373–380, 2014.

[143] D. Singh, A. Dixit, and P. S. Dobal, "Synthesis and characterization of $BaTi_{1-x}Fe_xO_3$ ceramics," in *AIP Conference Proceedings*, vol. 2352, p. 020005, AIP Publishing LLC, 2021.

[144] F. Ren, S. Ishida, and S. Mineta, "Effect of manganese addition on phase stability of hexagonal $BaTiO_3$," *Journal of the Ceramic Society of Japan*, vol. 102, no. 1181, pp. 105–107, 1994.

[145] A. Kirianov, N. Ozaki, H. Ohsato, N. Kohzu, and H. Kishi, "Studies on the solid solution of Mn in $BaTiO_3$," *Japanese Journal of Applied Physics*, vol. 40, no. 9S, p. 5619, 2001.

[146] F. Gheorghiu, M. Simenas, C. E. Ciomaga, M. Airimioaei, V. Kalendra, J. Banys, M. Dobromir, S. Tascu, and L. Mitoseriu, "Preparation and structural characterization of Fe-doped $BaTiO_3$ diluted magnetic ceramics," *Ceramics International*, vol. 43, no. 13, pp. 9998–10005, 2017.

[147] P. C. Bowes, J. N. Baker, and D. L. Irving, "Site preference of Y and Mn in nonstoichiometric $BaTiO_3$ from first principles," *Physical Review Materials*, vol. 4, no. 8, p. 084601, 2020.

[148] N. Dang, T. Thanh, L. Hong, V. Lam, and T.-L. Phan, "Structural, optical and magnetic properties of polycrystalline $BaTi_{1-x}Fe_xO_3$ ceramics," *Journal of Applied Physics*, vol. 110, no. 4, p. 043914, 2011.

[149] A. Rani, J. Kolte, and P. Gopalan, "Phase formation, microstructure, electrical and magnetic properties of Mn substituted barium titanate," *Ceramics International*, vol. 41, no. 10, pp. 14057–14063, 2015.

[150] S. Rajan, P. M. Gazzali, and G. Chandrasekaran, "Electrical and magnetic phase transition studies of Fe and Mn co-doped $BaTiO_3$," *Journal of Alloys and Compounds*, vol. 656, pp. 98–109, 2016.

[151] H. Langhammer, T. Müller, R. Böttcher, and H. Abicht, "Structural and optical properties of chromium-doped hexagonal barium titanate ceramics," *Journal of Physics: Condensed Matter*, vol. 20, no. 8, p. 085206, 2008.

[152] H. Arend and L. Kihlborg, "Phase composition of reduced and reoxidized barium titanate," *Journal of the American Ceramic Society*, vol. 52, no. 2, pp. 63–65, 1969.

[153] M. Wakamatsu, "Influence of firing atmosphere on the cubic-hexagonal transition and the chemical state of titanium in BaTiO$_3$," *J. CERAM. SOC. JAP. J. Ceram. Soc. Jap.*, vol. 95, no. 12, p. 1181, 1987.

[154] D. Sinclair, J. S. Skakle, F. Morrison, R. Smith, and T. Beales, "Structure and electrical properties of oxygen-deficient hexagonal BaTiO$_3$," *Journal of Materials Chemistry*, vol. 9, no. 6, pp. 1327–1331, 1999.

[155] H. S. Mallik, I. Fujii, Y. Matsui, G. P. Khanal, S. Kim, S. Ueno, T. S. Suzuki, and S. Wada, "Preparation and investigation of hexagonal-tetragonal BaTiO$_3$ powders," *Journal of the Ceramic Society of Japan*, vol. 129, no. 2, pp. 91–96, 2021.

[156] X. Wei, Q. Zhang, F. Li, C. Jin, and R. Yu, "Structural evolution induced by acceptor doping into BaTiO$_3$ ceramics," *Journal of alloys and compounds*, vol. 508, no. 2, pp. 486–493, 2010.

[157] R. Søndenå, S. Stølen, P. Ravindran, T. Grande, and N. L. Allan, "Corner-versus face-sharing octahedra in AMnO$_3$ perovskites (*A*= Ca, Sr, and Ba)," *Physical Review B*, vol. 75, no. 18, p. 184105, 2007.

[158] R. Burbank and H. T. Evans, "The crystal structure of hexagonal barium titanate," *Acta Crystallographica*, vol. 1, no. 6, pp. 330–336, 1948.

[159] J. Dawson, C. Freeman, J. Harding, and D. Sinclair, "Phase stabilisation of hexagonal barium titanate doped with transition metals: A computational study," *Journal of Solid State Chemistry*, vol. 200, pp. 310–316, 2013.

[160] H. T. Langhammer, T. Müller, R. Böttcher, and H.-P. Abicht, "Crystal structure and related properties of copper-doped barium titanate ceramics," *Solid State Sciences*, vol. 5, no. 7, pp. 965–971, 2003.

[161] R. Krishnamurthy and W. B. Schaap, "Computing ligand field potentials and relative energies of *d* orbitals: A simple general approach," *Journal of Chemical Education*, vol. 46, no. 12, p. 799, 1969.

[162] U. Müller, *Inorganic structural chemistry*. John Wiley & Sons, 2007.

[163] R. D. Shannon, "Revised effective ionic radii and systematic studies of interatomic distances in halides and chalcogenides," *Acta crystallographica section A: crystal physics, diffraction, theoretical and general crystallography*, vol. 32, no. 5, pp. 751–767, 1976.

[164] V. Kraševec, M. Drofenik, and D. Kolar, "Genesis of the (111) twin in barium titanate," *Journal of the American Ceramic Society*, vol. 73, no. 4, pp. 856–860, 1990.

[165] R. M. German, P. Suri, and S. J. Park, "Liquid phase sintering," *Journal of materials science*, vol. 44, no. 1, pp. 1–39, 2009.

[166] K. Watanabe, I. Sakaguchi, S. Hishita, H. Haneda, and N. Ohashi, "Oxygen tracer diffusion in BaTiO$_3$ ceramics-Effect of Zr impurity from planetary ball milling," in *Key Engineering Materials*, vol. 566, pp. 262–265, Trans Tech Publ, 2013.

[167] J. Tangsritrakul and R. Yimnirun, "Effects of manganese addition on phase formation and microstructure of barium titanate ceramics," *Chiang Mai Journal of Science*, vol. 37, no. 1, pp. 165–169, 2010.

[168] S. B. Lee, W. Sigle, and M. Rühle, "Investigation of grain boundaries in abnormal grain growth structure of TiO$_2$-excess BaTiO$_3$ by TEM and EELS analysis," *Acta materialia*, vol. 50, no. 8, pp. 2151–2162, 2002.

[169] B.-K. Lee, S.-Y. Chung, and S.-J. L. Kang, "Control of {111} twin formation and abnormal grain growth in BaTiO$_3$," *Metals and Materials*, vol. 6, no. 4, pp. 301–304, 2000.

[170] B.-K. Lee, S.-Y. Chung, and S.-J. L. Kang, "Necessary conditions for the formation of {111} twins in barium titanate," *Journal of the American Ceramic Society*, vol. 83, no. 11, pp. 2858–2860, 2000.

[171] S. Zheng, X. Ma, T. Yamamoto, and Y. Ikuhara, "Atomistic study of abnormal grain growth structure in BaTiO$_3$ by transmission electron microscopy and scanning transmission electron microscopy," *Acta materialia*, vol. 61, no. 7, pp. 2298–2307, 2013.

[172] O. Eibl, P. Pongratz, P. Skalicky, and H. Schmelz, "Extended defects in hexagonal BaTiO$_3$," *Philosophical Magazine A*, vol. 60, no. 5, pp. 601–612, 1989.

[173] A. Rečnik and D. Kolar, "Exaggerated growth of hexagonal barium titanate under reducing sintering conditions," *Journal of the American Ceramic Society*, vol. 79, no. 4, pp. 1015–1018, 1996.

[174] D. Kolar, U. Kunaver, and A. Rečnik, "Exaggerated anisotropic grain growth in hexagonal barium titanate ceramics," *physica status solidi (a)*, vol. 166, no. 1, pp. 219–230, 1998.

[175] K. Kinoshita and A. Yamaji, "Grain-size effects on dielectric properties in barium titanate ceramics," *Journal of applied physics*, vol. 47, no. 1, pp. 371–373, 1976.

[176] J. Jeong and Y. H. Han, "Effects of MgO-doping on electrical properties and microstructure of BaTiO$_3$," *Japanese journal of applied physics*, vol. 43, no. 8R, p. 5373, 2004.

[177] H. Dederichs and G. Arlt, "Aging of Fe-doped PZT ceramics and the domain wall contribution to the dielectric constant," *Ferroelectrics*, vol. 68, no. 1, pp. 281–292, 1986.

[178] P. Hansen, D. Hennings, and H. Schreinemacher, "Dielectric properties of acceptor-doped $(Ba, Ca)(Ti, Zr)O_3$ ceramics," *Journal of electroceramics*, vol. 2, no. 2, pp. 85–94, 1998.

[179] G. Arlt, D. Hennings, and G. De With, "Dielectric properties of fine-grained barium titanate ceramics," *Journal of applied physics*, vol. 58, no. 4, pp. 1619–1625, 1985.

[180] N. H. Yusoff, R. A. M. Osman, M. S. Idris, K. N. D. K. Muhsen, and N. I. M. Nor, "Dielectric and structural analysis of hexagonal and tetragonal phase $BaTiO_3$," in *AIP Conference Proceedings*, vol. 2203, p. 020038, AIP Publishing LLC, 2020.

[181] N. Setter and L. Cross, "The role of B-site cation disorder in diffuse phase transition behavior of perovskite ferroelectrics," *Journal of Applied Physics*, vol. 51, no. 8, pp. 4356–4360, 1980.

[182] K. Härdtl and R. Wernicke, "Lowering the curie temperature in reduced $BaTiO_3$," *Solid State Communications*, vol. 10, no. 1, pp. 153–157, 1972.

[183] S. J. Lee, S. M. Park, and Y. H. Han, "Dielectric relaxation of Al-doped $BaTiO_3$," *Japanese Journal of Applied Physics*, vol. 48, no. 3R, p. 031403, 2009.

[184] J. Jeong and Y. H. Han, "Electrical properties of MgO-doped $BaTiO_3$," *Physical Chemistry Chemical Physics*, vol. 5, no. 11, pp. 2264–2267, 2003.

[185] Y. Huan, X. Wang, J. Fang, and L. Li, "Grain size effect on piezoelectric and ferroelectric properties of $BaTiO_3$ ceramics," *Journal of the European Ceramic Society*, vol. 34, no. 5, pp. 1445–1448, 2014.

[186] Y. Tan, J. Zhang, Y. Wu, C. Wang, V. Koval, B. Shi, H. Ye, R. McKinnon, G. Viola, and H. Yan, "Unfolding grain size effects in barium titanate ferroelectric ceramics," *Scientific reports*, vol. 5, no. 1, pp. 1–9, 2015.

[187] L. Wang, Z. Zhou, X. Zhao, Z. Liu, R. Liang, and X. Dong, "Enhanced strain effect of aged acceptor-doped $BaTiO_3$ ceramics with clamping domain structures," *Applied Physics Letters*, vol. 110, no. 10, p. 102904, 2017.

[188] D. Damjanovic, "Ferroelectric, dielectric and piezoelectric properties of ferroelectric thin films and ceramics," *Reports on Progress in Physics*, vol. 61, no. 9, p. 1267, 1998.

[189] K. Carl and K. Härdtl, "Electrical after-effects in $Pb(Ti, Zr)O_3$ ceramics," *Ferroelectrics*, vol. 17, no. 1, pp. 473–486, 1977.

[190] X. Ren, "Large electric-field-induced strain in ferroelectric crystals by point-defect-mediated reversible domain switching," *Nature materials*, vol. 3, no. 2, pp. 91–94, 2004.

[191] G. P. Khanal, S. Kim, I. Fujii, S. Ueno, C. Moriyoshi, Y. Kuroiwa, and S. Wada, "Effect of thermal annealing on crystal structures and electrical properties in $BaTiO_3$ ceramics," *Journal of Applied Physics*, vol. 124, no. 3, p. 034102, 2018.

[192] E. Subbarao, M. McQuarrie, and W. Buessem, "Domain effects in polycrystalline barium titanate," *Journal of Applied Physics*, vol. 28, no. 10, pp. 1194–1200, 1957.

[193] I. Cutter and R. McPherson, "Surface domain reorientation produced by abrasion and annealing of polycrystalline $BaTiO_3$," *Journal of the American Ceramic Society*, vol. 55, no. 7, pp. 334–336, 1972.

[194] S. Cheng, I. K. Lloyd, and M. Kahn, "Modification of surface texture by grinding and polishing lead zirconate titanate ceramics," *Journal of the American Ceramic Society*, vol. 75, no. 8, pp. 2293–2296, 1992.

[195] W. Chen, X. Zhao, J. Sun, L. Zhang, and L. Zhong, "Effect of the Mn doping concentration on the dielectric and ferroelectric properties of different-routes-fabricated $BaTiO_3$-based ceramics," *Journal of Alloys and Compounds*, vol. 670, pp. 48–54, 2016.

[196] T. Watanabe, M. Shimada, T. Aiba, H. Yabuta, K. Miura, K. Oka, M. Azuma, S. Wada, and N. Kumada, "Structural transformation of hexagonal (0001) $BaTiO_3$ ceramics to tetragonal (111) $BaTiO_3$ ceramics," *Japanese journal of applied physics*, vol. 50, no. 9S2, p. 09ND01, 2011.

[197] S.-G. Cao, Y. Li, H.-H. Wu, J. Wang, B. Huang, and T.-Y. Zhang, "Stress-induced cubic-to-hexagonal phase transformation in perovskite nanothin films," *Nano letters*, vol. 17, no. 8, pp. 5148–5155, 2017.

[198] R. Böttcher, H. Langhammer, T. Müller, and H. Abicht, "Evaluation of lattice site and valence of manganese in hexagonal $BaTiO_3$ by electron paramagnetic resonance," *Journal of Physics: Condensed Matter*, vol. 17, no. 32, p. 4925, 2005.

[199] S. Hirose, H. Okushi, S. Ueda, H. Yoshikawa, Y. Adachi, A. Ando, T. Ohsawa, H. Haneda, and N. Ohashi, "Electric field and temperature dependence of dielectric permittivity in strontium titanate investigated by a photoemission study on $Pt/SrTiO_3$:Nb junctions," *Applied Physics Letters*, vol. 106, no. 19, p. 191602, 2015.

[200] A. F. Zurhelle, X. Tong, A. Klein, D. S. Mebane, and R. A. De Souza, "A space-charge treatment of the increased concentration of reactive species at the surface of a ceria solid solution," *Angewandte Chemie*, vol. 129, no. 46, pp. 14708–14712, 2017.

[201] Y. Hermans, A. Klein, K. Ellmer, R. van de Krol, T. Toupance, and W. Jaegermann, "Energy-band alignment of $BiVO_4$ from photoelectron spectroscopy of solid-state interfaces," *The Journal of Physical Chemistry C*, vol. 122, no. 36, pp. 20861–20870, 2018.

[202] A. H. Hubmann, *Doped Indium Oxide: Surface Potentials, Electronic and Optical Properties*. PhD thesis, Technische Universität, 2021.

[203] A. Klein, C. Körber, A. Wachau, F. Säuberlich, Y. Gassenbauer, R. Schafranek, S. Harvey, and T. Mason, "Surface potentials of magnetron sputtered transparent conducting oxides," *Thin Solid Films*, vol. 518, no. 4, pp. 1197–1203, 2009.

[204] D. Shi, Z. Xiong, J. Li, B. Q. Luo, L. M. Fang, Y. H. Xia, and Z. Gao, "Electron transition and electron-hole recombination processes in epitaxial $BaTiO_3$ films with embedded Co nanocrystals," *Materials Research Express*, vol. 6, no. 10, p. 105021, 2019.

[205] Y. Gassenbauer, R. Schafranek, A. Klein, S. Zafeiratos, M. Hävecker, A. Knop-Gericke, and R. Schlögl, "Surface states, surface potentials, and segregation at surfaces of tin-doped In_2O_3," *Physical Review B*, vol. 73, no. 24, p. 245312, 2006.

[206] K. N. Schuldt, H. Ding, J.-C. Jaud, J. Koruza, and A. Klein, "Influence of Defects on the Schottky Barrier Height at $BaTiO_3/RuO_2$ Interfaces," *physica status solidi (a)*, 2021.

[207] R. Meyer, A. F. Zurhelle, R. A. De Souza, R. Waser, and F. Gunkel, "Dynamics of the metal-insulator transition of donor-doped $SrTiO_3$," *Physical Review B*, vol. 94, no. 11, p. 115408, 2016.

[208] D. M. Long, B. Cai, J. N. Baker, P. C. Bowes, T. J. Bayer, J.-J. Wang, R. Wang, L.-Q. Chen, C. A. Randall, D. L. Irving, *et al.*, "Conductivity of iron-doped strontium titanate in the quenched and degraded states," *Journal of the American Ceramic Society*, vol. 102, no. 6, pp. 3567–3577, 2019.

[209] L. T. Hudson, R. L. Kurtz, S. W. Robey, D. Temple, and R. L. Stockbauer, "Surface core-level shifts of barium observed in photoemission of vacuum-fractured $BaTiO_3$ (100)," *Physical Review B*, vol. 47, no. 16, p. 10832, 1993.

[210] S. M. Mukhopadhyay and T. C. S. Chen, "Surface chemical states of barium titanate: Influence of sample processing," *Journal of materials research*, vol. 10, no. 6, pp. 1502–1507, 1995.

[211] C. Miot, E. Husson, C. Proust, R. Erre, and J. P. Coutures, "Residual carbon evolution in $BaTiO_3$ ceramics studied by XPS after ion etching," *Journal of the European Ceramic Society*, vol. 18, no. 4, pp. 339–343, 1998.

[212] J. D. Baniecki, M. Ishii, T. Shioga, K. Kurihara, and S. Miyahara, "Surface core-level shifts of strontium observed in photoemission of barium strontium titanate thin films," *Applied physics letters*, vol. 89, no. 16, p. 162908, 2006.

[213] F. Chen and A. Klein, "Polarization dependence of Schottky barrier heights at interfaces of ferroelectrics determined by photoelectron spectroscopy," *Physical Review B*, vol. 86, no. 9, p. 094105, 2012.

[214] J. Rault, G. Agnus, T. Maroutian, V. Pillard, P. Lecoeur, G. Niu, B. Vilquin, M. Silly, A. Bendounan, F. Sirotti, *et al.*, "Interface electronic structure in a metal/ferroelectric heterostructure under applied bias," *Physical Review B*, vol. 87, no. 15, p. 155146, 2013.

[215] A. H. Hubmann, S. Li, S. Zhukov, H. Von Seggern, and A. Klein, "Polarisation dependence of Schottky barrier heights at ferroelectric $BaTiO_3$/RuO_2 interfaces: influence of substrate orientation and quality," *Journal of Physics D: Applied Physics*, vol. 49, no. 29, p. 295304, 2016.

[216] D. M. Long, A. Klein, and E. C. Dickey, "Barrier formation at $BaTiO_3$ interfaces with Ni and NiO," *Applied Surface Science*, vol. 466, pp. 472–476, 2019.

[217] T. Suzuki, Y. Nishi, and M. Fujimoto, "Ruddlesden–popper planar faults and nanotwins in heteroepitaxial nonstoichiometric barium titanate thin films," *Journal of the American Ceramic Society*, vol. 83, no. 12, pp. 3185–3195, 2000.

[218] Y. Hu, M. P. Harmer, and D. M. Smyth, "Solubility of BaO in $BaTiO_3$," *Journal of the American Ceramic Society*, vol. 68, no. 7, pp. 372–376, 1985.

[219] M. I. Sosulnikov and Y. A. Teterin, "X-ray photoelectron studies of Ca, Sr and Ba and their oxides and carbonates," *Journal of electron spectroscopy and related phenomena*, vol. 59, no. 2, pp. 111–126, 1992.

[220] R. P. Vasquez, M. C. Foote, and B. D. Hunt, "Reaction of nonaqueous halogen solutions with $YBa_2Cu_3O_{7-x}$," *Journal of applied physics*, vol. 66, no. 10, pp. 4866–4877, 1989.

[221] R. Vasquez, "X-ray photoelectron spectroscopy study of Sr and Ba compounds," *Journal of Electron Spectroscopy and Related Phenomena*, vol. 56, no. 3, pp. 217–240, 1991.

[222] K. Szot, W. Speier, U. Breuer, R. Meyer, J. Szade, and R. Waser, "Formation of microcrystals on the (100) surface of $SrTiO_3$ at elevated temperatures," *Surface science*, vol. 460, no. 1-3, pp. 112–128, 2000.

[223] P. Ren, M. Gehringer, B. Huang, A.-P. Hoang, S. Steiner, A. Klein, and T. Frömling, "High field electroformation of sodium bismuth titanate and its solid solutions with barium titanate," *Journal of Materials Chemistry C*, vol. 9, no. 9, pp. 3334–3342, 2021.

[224] S. Lany, A. Zakutayev, T. O. Mason, J. F. Wager, K. R. Poeppelmeier, J. D. Perkins, J. J. Berry, D. S. Ginley, and A. Zunger, "Surface Origin of High Conductivities in Undoped In$_2$O$_3$ Thin Films," *Physical Review Letters*, vol. 108, no. 1, p. 016802, 2012.

[225] A. Santander-Syro, O. Copie, T. Kondo, F. Fortuna, S. Pailhes, R. Weht, X. Qiu, F. Bertran, A. Nicolaou, A. Taleb-Ibrahimi, *et al.*, "Two-dimensional electron gas with universal subbands at the surface of SrTiO$_3$," *Nature*, vol. 469, no. 7329, pp. 189–193, 2011.

[226] T. C. Rödel, F. Fortuna, S. Sengupta, E. Frantzeskakis, P. L. Fèvre, F. Bertran, B. Mercey, S. Matzen, G. Agnus, T. Maroutian, *et al.*, "Universal fabrication of 2D electron systems in functional oxides," *Advanced Materials*, vol. 28, no. 10, pp. 1976–1980, 2016.

[227] T. Frömling, J. Hou, W. Preis, W. Sitte, H. Hutter, and J. Fleig, "Oxygen tracer diffusion in donor doped barium titanate," *Journal of Applied Physics*, vol. 110, no. 4, p. 043531, 2011.

[228] N. W. Ritchie, D. E. Newbury, and J. M. Davis, "EDS measurements of X-ray intensity at WDS precision and accuracy using a silicon drift detector," *Microscopy and Microanalysis*, vol. 18, no. 4, pp. 892–904, 2012.

[229] H. Qi, X. Chen, E. Benckiser, M. Wu, G. Cristiani, G. Logvenov, B. Keimer, and U. Kaiser, "Formation mechanism of Ruddlesden–Popper faults in compressive-strained ABO$_3$ perovskite superlattices," *Nanoscale*, vol. 13, no. 48, pp. 20663–20669, 2021.

[230] G. Trolliard, N. Teneze, P. Boullay, and D. Mercurio, "TEM study of cation-deficient-perovskite related $A_nB_{n-1}O_{3n}$ compounds: the twin-shift option," *Journal of Solid State Chemistry*, vol. 177, no. 4-5, pp. 1188–1196, 2004.

[231] C. C. Chavarría, S. Payan, J.-P. Salvetat, M. Maglione, and A. Klein, "Fermi Level Engineering for Large Permittivity in BaTiO$_3$-Based Multilayers," *Surfaces*, vol. 3, no. 4, pp. 567–578, 2020.

[232] R. Schafranek, S. Payan, M. Maglione, and A. Klein, "Barrier heights at (Ba,Sr)TiO$_3$/Pt interfaces studied by photoemission," *Physical Review B*, vol. 77, no. 19, p. 195310, 2008.

[233] S. Balaz, Z. Zeng, and L. J. Brillson, "Heterojunction band offsets and dipole formation at BaTiO$_3$/SrTiO$_3$ interfaces," *Journal of Applied Physics*, vol. 114, no. 18, p. 183701, 2013.

[234] S. Li, A. Wachau, R. Schafranek, A. Klein, Y. Zheng, and R. Jakoby, "Energy level alignment and electrical properties of (Ba,Sr)TiO$_3$/Al$_2$O$_3$ interfaces for tunable capacitors," *Journal of Applied Physics*, vol. 108, no. 1, p. 014113, 2010.

[235] S. Li, C. Ghinea, T. J. Bayer, M. Motzko, R. Schafranek, and A. Klein, "Electrical properties of (Ba,Sr)TiO$_3$ thin films with Pt and ITO electrodes: Dielectric and rectifying behaviour," *Journal of Physics: Condensed Matter*, vol. 23, no. 33, p. 334202, 2011.

[236] R. Mogilevsky, R. Levi-Setti, B. Pashmakov, L. Liu, K. Zhang, H. Jaeger, D. Buchholz, R. Chang, and B. Veal, "Direct measurements of room-temperature oxygen diffusion in YBa$_2$Cu$_3$O$_x$," *Physical Review B*, vol. 49, no. 9, p. 6420, 1994.

[237] P. K. Song, Y. Shigesato, M. Kamei, and I. Yasui, "Electrical and structural properties of tin-doped indium oxide films deposited by DC sputtering at room temperature," *Japanese journal of applied physics*, vol. 38, no. 5R, p. 2921, 1999.

[238] C. N. de Carvalho, A. Luis, G. Lavareda, E. Fortunato, and A. Amaral, "Effect of thickness on the properties of ITO thin films deposited by RF-PERTE on unheated, flexible, transparent substrates," *Surface and coatings technology*, vol. 151, pp. 252–256, 2002.

[239] D. Kim, Y. Han, J.-S. Cho, and S.-K. Koh, "Low temperature deposition of ITO thin films by ion beam sputtering," *Thin Solid Films*, vol. 377, pp. 81–86, 2000.

[240] L. Hao, X. Diao, H. Xu, B. Gu, and T. Wang, "Thickness dependence of structural, electrical and optical properties of indium tin oxide (ITO) films deposited on PET substrates," *Applied surface science*, vol. 254, no. 11, pp. 3504–3508, 2008.

[241] R. Hertwig, "Deposition and Characterisation of Reactive Sputtered RuO$_2$ Thin Films," Bachelor's thesis, TU Darmstadt, 2021.

[242] R. Bel Hadj Tahar, T. Ban, Y. Ohya, and Y. Takahashi, "Tin doped indium oxide thin films: Electrical properties," *Journal of Applied Physics*, vol. 83, no. 5, pp. 2631–2645, 1998.

[243] H. Ohta, M. Orita, M. Hirano, H. Tanji, H. Kawazoe, and H. Hosono, "Highly electrically conductive indium–tin–oxide thin films epitaxially grown on yttria-stabilized zirconia (100) by pulsed-laser deposition," *Applied Physics Letters*, vol. 76, no. 19, pp. 2740–2742, 2000.

[244] Y. Gassenbauer, *Untersuchung der elektronischen und chemischen Oberflächeneigenschaften von Zinn-dotiertem Indium-Oxid im Hinblick auf die Funktion in organischen Leuchtdioden*. PhD thesis, Technische Universität Darmstadt, 2007.

[245] J.-M. Themlin, M. Chtaïb, L. Henrard, P. Lambin, J. Darville, and J.-M. Gilles, "Characterization of tin oxides by x-ray-photoemission spectroscopy," *Physical Review B*, vol. 46, no. 4, p. 2460, 1992.

[246] G. K. Deyu, *Defect Modulation Doping for Transparent Conducting Oxide Materials*. PhD thesis, Université Grenoble Alpes (ComUE), 2019.

[247] S. Kashiwaya, T. Toupance, A. Klein, and W. Jaegermann, "Fermi level positions and induced band bending at single crystalline anatase (101) and (001) surfaces: origin of the enhanced photocatalytic activity of facet engineered crystals," *Advanced Energy Materials*, vol. 8, no. 33, p. 1802195, 2018.

[248] A. W. Lin, N. R. Armstrong, and T. Kuwana, "X-ray photoelectron/Auger electron spectroscopic studies of tin and indium metal foils and oxides," *Analytical Chemistry*, vol. 49, no. 8, pp. 1228–1235, 1977.

[249] Z. M. Detweiler, S. M. Wulfsberg, M. G. Frith, A. B. Bocarsly, and S. L. Bernasek, "The oxidation and surface speciation of indium and indium oxides exposed to atmospheric oxidants," *Surface Science*, vol. 648, pp. 188–195, 2016.

[250] A. Frebel, "Testing the Limits of the Electrical Modification of Tin doped Indium Oxide (ITO) by XPS with polarization," Advanced Research Laboratory, TU Darmstadt, 2022.

[251] R. Egdell, T. Walker, and G. Beamson, "The screening response of a dilute electron gas in core level photoemission from Sb-doped SnO_2," *Journal of Electron Spectroscopy and Related Phenomena*, vol. 128, no. 1, pp. 59–66, 2003.

[252] Y. Gassenbauer and A. Klein, "Electronic and chemical properties of tin-doped indium oxide (ITO) surfaces and ITO/ZnPc interfaces studied in-situ by photoelectron spectroscopy," *The Journal of Physical Chemistry B*, vol. 110, no. 10, pp. 4793–4801, 2006.

[253] J. Morasch, *Deposition, Charakterisierung und Bandanpassung oxidischer Dünnschichtmaterialien zur Lichtabsorption*. PhD thesis, 2017.

[254] N. S. Bein, "The Fermi Level in Bismuth Ferrite," Master's thesis, TU Darmstadt, 2018.

[255] K. N. S. Schuldt, "Electronic characterization of thin film Sr-doped $LaFeO_3$," Master's thesis, TU Darmstadt, 2018.

[256] N. Gutmann, "Einfluss der Mn-Dotierung auf die elektrische Leitfähigkeit von polykristallinem $BaTiO_3$," Bachelor's thesis, TU Darmstadt, 2019.

[257] J. Li, N. Ohashi, H. Okushi, and H. Haneda, "Temperature dependence of carrier transport and resistance switching in $Pt/SrTi_{1-x}Nb_xO_3$ Schottky junctions," *Physical Review B*, vol. 83, no. 12, p. 125317, 2011.

[258] K. Watanabe, I. Sakaguchi, S. Hishita, N. Ohashi, and H. Haneda, "Visualization of grain boundary as blocking layer for oxygen tracer diffusion and a proposed defect model in non doped $BaTiO_3$ ceramics," *Applied physics express*, vol. 4, no. 5, p. 055801, 2011.

[259] J. Jeong and Y. H. Han, "Effects of Mn-doping on TSDC and degradation of BaTiO$_3$," *Journal of electroceramics*, vol. 17, no. 2, pp. 1051–1055, 2006.

[260] H.-S. Kwon, S.-H. Yoon, and H.-I. Yoo, "Insulation-resistance degradation kinetics of bulk BaTi$_{1-\xi}$A$_\xi$O$_{3-\Delta}$ and defect-chemical origin of acceptor-type (A) and doping-level (ξ) effect," *Journal of Applied Physics*, vol. 120, no. 4, p. 044101, 2016.

[261] J. Carter, T. Bayer, and C. Randall, "Degradation and recovery of iron doped barium titanate single crystals via modulus spectroscopy and thermally stimulated depolarization current," *Journal of Applied Physics*, vol. 121, no. 14, p. 145106, 2017.

[262] M. Grossmann, S. Hoffmann, S. Gusowski, R. Waser, S. Streiffer, C. Basceri, C. Parker, S. Lash, and A. Kingon, "Resistance degradation behavior of Ba$_{0.7}$Sr$_{0.3}$TiO$_3$ thin films compared to mechanisms found in titanate ceramics and single crystals," *Integrated Ferroelectrics*, vol. 22, no. 1-4, pp. 83–94, 1998.

[263] L. B. Gossel, "Influence of Defect Segregation at Grain Boundaries on Electrical Properties in doped Polycrystalline BaTiO$_3$," Advanced Research Laboratory Report, TU Darmstadt, 2020.

[264] W. Hofman, S. Hoffmann, and R. Waser, "Dopant influence on dielectric losses, leakage behaviour, and resistance degradation of SrTiO$_3$ thin films," *Thin solid films*, vol. 305, no. 1-2, pp. 66–73, 1997.

[265] R. Merkle and J. Maier, "Defect association in acceptor-doped SrTiO$_3$: case study for Mn$'_{\text{Ti}}$–V$^{\bullet\bullet}_{\text{O}}$ and Mn$''_{\text{Ti}}$–V$^{\bullet\bullet}_{\text{O}}$," *Physical Chemistry Chemical Physics*, vol. 5, no. 11, pp. 2297–2303, 2003.

[266] Y. A. Genenko, J. Glaum, M. J. Hoffmann, and K. Albe, "Mechanisms of aging and fatigue in ferroelectrics," *Materials Science and Engineering: B*, vol. 192, pp. 52–82, 2015.

[267] T. Bieger, J. Maier, and R. Waser, "Optical investigation of oxygen incorporation in SrTiO$_3$," *Solid State Ionics*, vol. 53, pp. 578–582, 1992.

[268] Y. Kaga, Y. Abe, H. Yanagisawa, M. Kawamura, and K. Sasaki, "Ru and RuO$_2$ thin films by XPS," *Surface Science Spectra*, vol. 6, no. 1, pp. 68–74, 1999.

[269] Y. J. Kim, Y. Gao, and S. A. Chambers, "Core-level X-ray photoelectron spectra and X-ray photoelectron diffraction of RuO$_2$ (110) grown by molecular beam epitaxy on TiO$_2$ (110)," *Applied surface science*, vol. 120, no. 3-4, pp. 250–260, 1997.

[270] H. Over, Y. D. Kim, A. P. Seitsonen, S. Wendt, E. Lundgren, M. Schmid, P. Varga, A. Morgante, and G. Ertl, "Atomic-scale structure and catalytic reactivity of the RuO$_2$ (110) surface," *Science*, vol. 287, no. 5457, pp. 1474–1476, 2000.

[271] H. J. Jung, J. H. Han, E. A. Jung, B. K. Park, J.-H. Hwang, S. U. Son, C. G. Kim, T.-M. Chung, and K.-S. An, "Atomic layer deposition of ruthenium and ruthenium oxide thin films from a zero-valent (1, 5-hexadiene)(1-isopropyl-4-methylbenzene) ruthenium complex and O_2," *Chemistry of Materials*, vol. 26, no. 24, pp. 7083–7090, 2014.

[272] R. Schafranek, *Kathodenzerstäubte (Ba,Sr)TiO$_3$-Dünnschichten für steuerbare Mikrowellenkomponenten*. PhD thesis, Technische Universität Darmstadt, 2009.

[273] A. J. Hartmann, M. Neilson, R. N. Lamb, K. Watanabe, and J. F. Scott, "Ruthenium oxide and strontium ruthenate electrodes for ferroelectric thin-films capacitors," *Appl. Phys. A*, vol. 70, no. 2, pp. 239–242, 2000.

[274] B. Nieuwenhuys, R. Bouwman, and W. Sachtler, "The changes in work function of group Ib and VIII metals on xenon adsorption, determined by field electron and photoelectron emission," *Thin Solid Films*, vol. 21, no. 1, pp. 51–58, 1974.

A. Appendix

A.1. General Supplementary Information

A.1.1. Phase diagram of the BaO—TiO$_2$ system
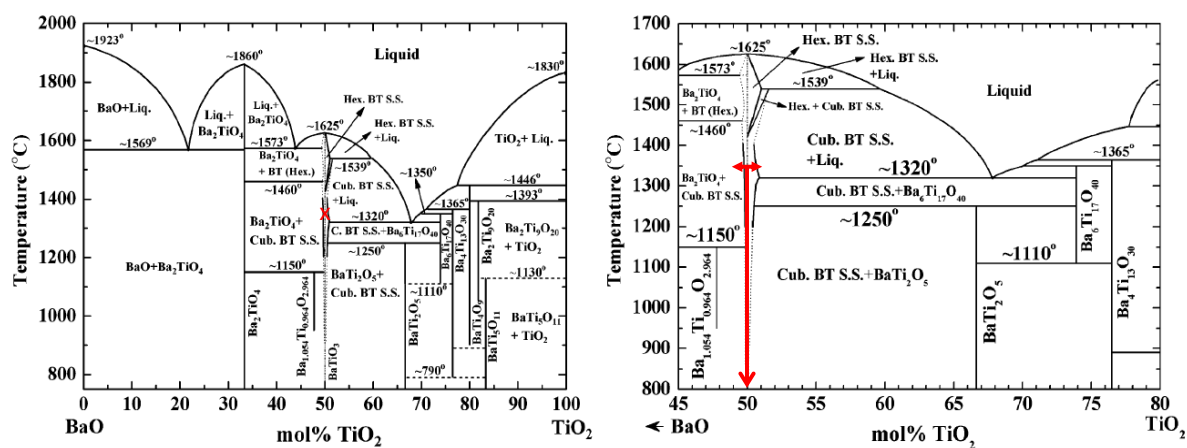
Figure A.1.: Pseudo-binary phase diagram of the BaO—TiO$_2$ system under ambient air conditions taken from [48]. The phase diagram is based on previous studies and is revised from Lee and Randall based on their data for the non-stoichiometric BaTiO$_3$ and compounds around stoichiometric BaTiO$_3$ [48]. The dotted lines were extrapolated. The sintering temperature of 1350 °C for Mn- and Fe-doped BaTiO$_3$ is marked by a red x on the left and a maximum assumed non-stoichiometry range of ± 1 mol% of Ba/Ti-ratio with cooling down (to *RT*) is marked on the right. Reprinted with permission from [48]. Copyright (2007) Journal of the American Ceramic Society.

The phase diagram of the BaO—TiO$_2$ system is depicted in Figure A.1. For a maximum non-stoichiometry range of ± 1 mol% of Ba/Ti ratio the following phases mixtures could be present in the XRD pattern, when assuming that the high temperature phases can be stabilized down to *RT* during cooling: *c*-BaTiO$_3$, Ba$_2$TiO$_4$, *t*-BaTiO$_3$, Ba$_6$Ti$_{17}$O$_{40}$, Ba$_{1.054}$Ti$_{0.967}$O$_{2.964}$ and BaTi$_2$O$_5$.

A.2. Appendix to Chapter 5

A.2.1. Particle Size distribution after second calcination
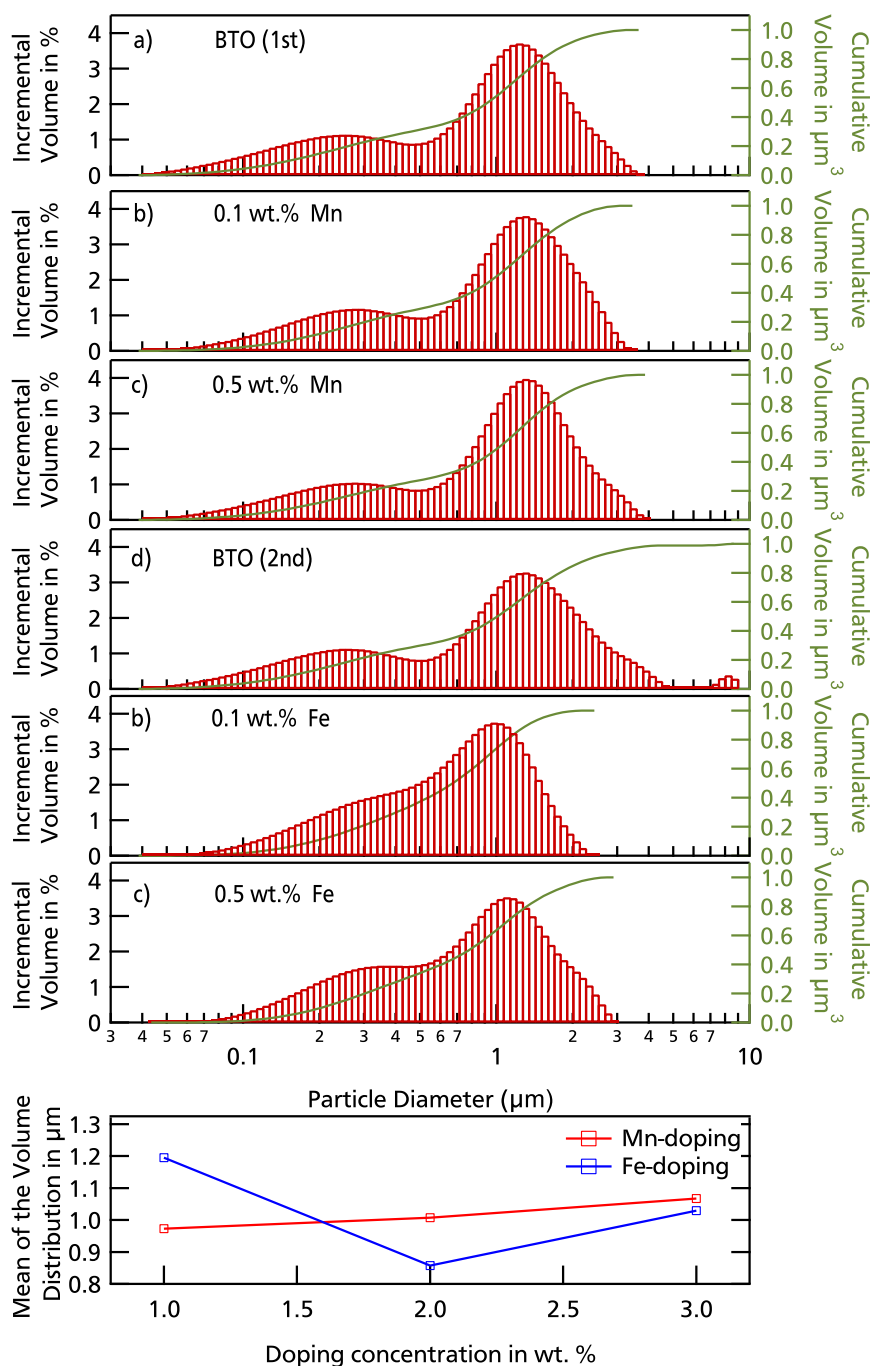
Figure A.2.: The particle size distribution of undoped, 0.1 wt.%, and 0.5 wt.% Mn- and Fe-doped BaTiO$_3$ measured with the particle size analyzer Saturn DigiSizer II from *Micromeritics*. Isopropanol was used as analyzing liquid.

A.2.2. ICP-OES

Table A.1.: Results of the ICP-OES analysis of calcined 0.3 wt.% Mn-doped BaTiO$_3$ powder conducted with a ICP-OES iCAP PRO XP from *ThermoFisher Scientific*. Digestion was done as described in Section 3.2.1. LoD=Limit of detection, RSD = relative standard deviation, Vision: Standard is axial and only radial if marked by *. The blind values of the acid after complexation refer to the digestion acid without BaTiO$_3$.

	Element	Wavelength		Intensity	Conc. Digestion	Conc. Solid	RSD	Intensity	Conc. Digestion	RSD
				BaTiO$_3$ powder complex				Blind value complexation		
		nm		cps	mg/L	mg/Kg	%	cps	mg/L	%
Main Elements	Ba	225.473		824.73	**1729.46**	**10933.69**	0.40	0.13	**0.60**	40.11
	Ba	234.758		5213.92	**1729.57**	**10934.34**	0.27	0.15	**0.07**	113.04
	Ba	413.066		139007.04	**1723.85**	**10898.21**	0.33	7.49	**0.05**	35.77
	Ti	323.452		60168.96	**588.30**	**3719.21**	0.59	12.64	**0.00**	111.20
	Ti	334.941		142272.55	**587.90**	**3716.72**	0.55	1.08	**0.01**	20.01
	Ti	336.121		73932.98	**589.37**	**3726.00**	0.57	1.18	**0.01**	80.35
	Ti	338.376		83433.09	**592.27**	**3744.33**	0.42	-1.05	**0.01**	121.04
	Mn	257.610		4024.19	**8.30**	**52.48**	0.39	-0.20	**0.00**	143.17
	Mn	260.569		1925.75	**8.17**	**51.64**	0.33	-0.10	**0.00**	112.57
	Ca	393.366	*	42333.52	**0.44**	**2.80**	0.10	7139.16	**0.06**	0.29
	Ca	396.847	*	19509.41	**0.44**	**2.79**	0.16	3278.48	**0.06**	0.33
	Si	212.412	*	291.85	**4.62**	**29.20**	2.70	377.68	**5.98**	2.58
	Si	251.611	*	642.05	**4.81**	**30.41**	2.53	839.70	**6.29**	2.70
	Si	288.158	*	947.94	**4.91**	**31.04**	2.59	1223.13	**6.46**	2.63
	Fe	238.204	*	24.07	**0.05**	**0.32**	1.41	8.44	**0.02**	1.33
	Fe	259.940	*	6.02	**0.01**	**0.07**	13.03	7.53	**0.01**	0.81
	Sr	215.284	*	802.02	**4.78**	**30.21**	0.18	3.73	**0.02**	4.56
	Sr	216.596	*	501.81	**4.73**	**29.91**	0.23	-1.21	**< LoD**	12.47
	Sr	421.552	*	151738.99	**5.25**	**33.16**	0.09	24.46	**0.00**	7.93
	K	766.490		92.87	**2.03**	**12.84**	3.59	54.22	**0.73**	7.54
	Li	670.791		-8.18	**0.00**	**0.02**	111.98	-7.56	**0.01**	111.54
	Na	589.592		9.60	**0.11**	**0.69**	22.20	2.66	**0.03**	100.43
Trace Elements	Ag	328.068	*	-1.78	**< LoD**	**< LoD**	1.91	-7.94	**< LoD**	5.27
	Cd	214.438	*	0.09	**0.00**	**0.00**	24.38	0.35	**0.00**	12.57
	Cd	228.802	*	-2.07	**< LoD**	**< LoD**	9.64	-1.13	**< LoD**	1.66
	Co	238.892	*	-1.50	**< LoD**	**< LoD**	17.41	-0.68	**< LoD**	54.17
	Cr	205.560	*	6.02	**0.02**	**0.16**	5.06	1.13	**0.01**	6.26
	Cr	267.716	*	8.75	**0.02**	**0.16**	2.12	2.47	**0.00**	13.52
	Cu	324.754	*	22.67	**< LoD**	**< LoD**	14.80	41.56	**0.01**	4.20
	Mg	279.553	*	1699.26	**0.07**	**0.42**	0.03	145.28	**0.00**	1.05
	Mo	202.030	*	1.73	**0.01**	**0.05**	5.27	1.66	**0.01**	6.09
	Mo	203.844	*	1.75	**0.02**	**0.13**	22.33	0.60	**0.00**	185.35
	Mo	204.598	*	-0.18	**0.01**	**0.03**	21.69	0.00	**0.01**	48.10
	Ni	231.604	*	-1.26	**< LoD**	**< LoD**	222.08	-0.63	**0.00**	10.29
	Pd	363.470	*	200.33	**< LoD**	**< LoD**	6.62	221.42	**< LoD**	618.08
	Pt	214.423	*	0.55	**0.00**	**0.03**	87.69	0.05	**< LoD**	16.29
	Pt	217.467	*	1.65	**0.01**	**0.07**	36.32	1.13	**0.01**	69.88
	Re	197.312	*	-45.10	**< LoD**	**< LoD**	0.77	-2.33	**< LoD**	5.55
	Re	204.908	*	0.24	**0.05**	**0.30**	32.44	0.25	**0.05**	37.18
	Re	221.426	*	-0.66	**< LoD**	**< LoD**	21.44	1.23	**0.00**	28.28
	V	292.402	*	344.86	**0.40**	**2.52**	0.12	-0.57	**< LoD**	80.32
	Zn	202.548	*	167.77	**0.19**	**1.21**	0.20	13.27	**0.01**	6.80

Table A.2.: Certificate of analysis for $BaCO_3$ for the given product and Lot numbers provides by *Alfa Aesar by Thermo Fisher Scientific*. Values given in percent unless otherwise stated.

Product No:	14341
Product:	Barium carbonate, 99.8 %
Lot No.:	P08C024
Assay	99.86
Moisture	0.03
Loss on ignition	0.16
Insoluble in HCl	0
Total sulfur	0.0004
Chlorides	0.0024
Iron	0.0001
Strontium	0.018
Sodium	0.0006
Calcium	0.0006
Aluminum	0.00001
Potassium	0.00001
Magnesium	0.00001
Silicon	0.00002
Medium diameter D50	1.23 µm

Table A.3.: Certificate of analysis for TiO_2 for the given product and Lot numbers provides by *Alfa Aesar by Thermo Fisher Scientific*. Values given in percent unless otherwise stated.

Product No:	36199
Product:	Titanium(IV)oxide, anatase, 99.6% (metal basis)
Lot No.:	T31B027
Al	<0.0004
Ca	<0.002
Cd	<0.0003
Cr	<0.001
Cu	<0.0002
Fe	<0.001
K	0.1288
Li	<0.0002
Mg	<0.0004
Na	0.014
Pb	<0.0003
Si	<0.004
V	<0.001
Fisher size (APS)	0.49 µm
XRD: Major TiO2 (anatase), PDF 21-1272 tetragonal	

A.2.3. Calculated Oxidation States[1]
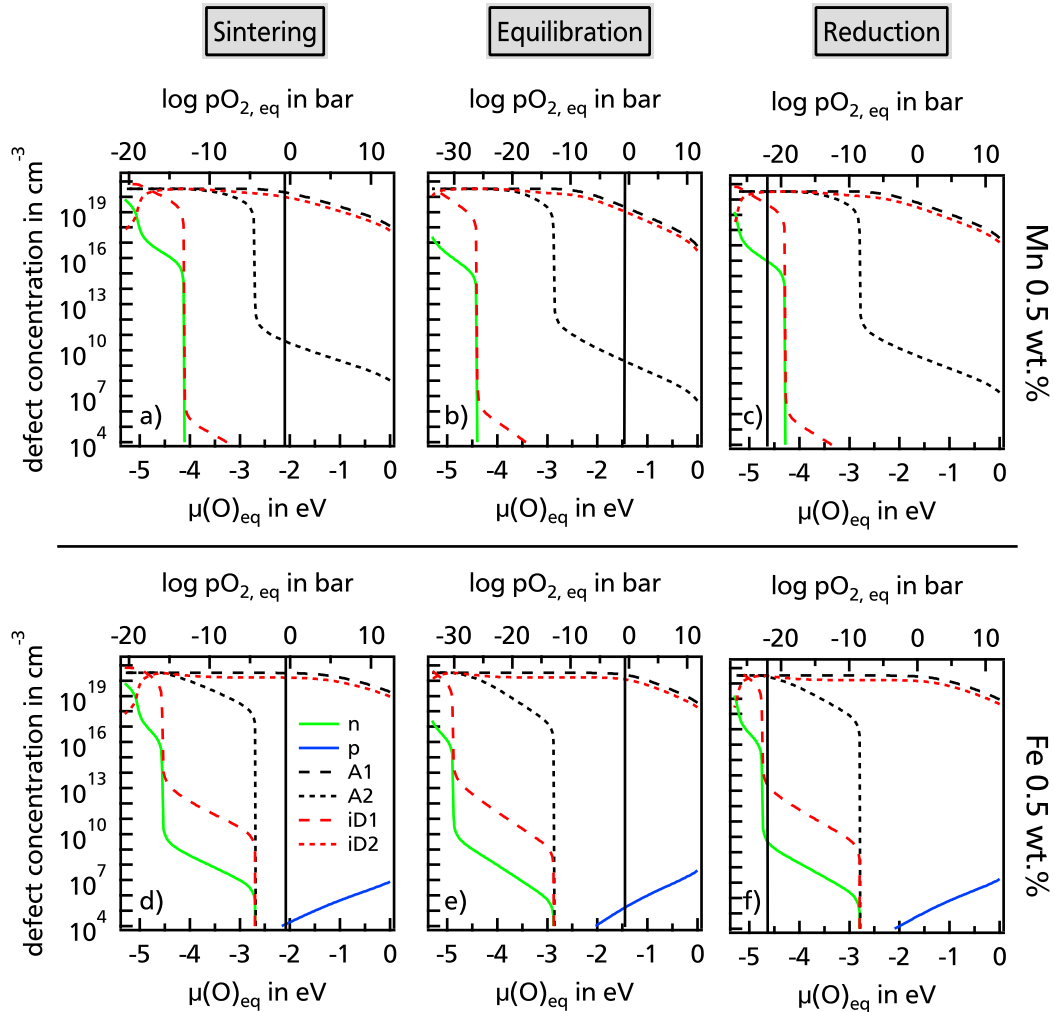
Figure A.3.: Calculated defect concentrations at room temperature according to the corresponding defect chemistry model. The defect equilibrium has been established at therespective sintering/annealing temperature and has been quenched to room temperature. The defect equilibrium has been established at 1350 °C for the calculation of as-sintered samples, while 900 °C have been utilized for equilibration and 1100 °C for reduction. An oxygen partial pressure of 0.2 bar has been assumed for sintering and equilibration, while an oxygen partial pressure of 10^{-22} bar was assumed for reduction. a)-c) refer to 0.5 wt.% Mn-doped $BaTiO_3$ and d)-f) to 0.5 wt.% Fe-doped $BaTiO_3$ with the corresponding defect energy levels given in Table 2.2. The legend for the different curves is given in d) and applies for all calculations: n=electrons, p=holes, A1= at least singly charged acceptor ($A^{3+}+A^{2+}$), A2= doubly charged acceptor (A^{2+}), iD1= at least singly charged intrinsic donor ($V_O^{\bullet\bullet}+V_O^{\bullet}$) and iD2= doubly charged intrinsic donor ($V_O^{\bullet\bullet}$).

The oxidation state concentrations can be calculated from Figure A.3 as follows: A^{4+}=

---

[1]The defect chemistry model, which was used for the calculation of the oxidation states has been implemented in the IGOR Pro software (Wavemetrics) by Andreas Klein.

$A_{total}-A1$, $A^{3+}=$ A1$-$A2 and A^{2+}=A2. After reduction a 81 % Fe^{2+}/19 % Fe^{3+} mixture is expected when assuming an oxygen partial pressure of 10^{-22} bar. This value was not experimentally measured, but is based on the comparison of the used step-up parameters such as gas-mixture and annealing temperature to the oxygen partial pressures being presented in literature for comparable experiments [208]. For Fe-doping, the calculated oxidation state ratio is rather sensitive to the expected oxygen partial pressures upon reduction. This can be seen in Figure A.3 f), as for Fe-doped $BaTiO_3$ the $Fe^{3+/2+}$ transition occurs in the present oxygen partial pressure range and thus, a reliable calculation cannot be done without knowing the exact oxygen partial pressure during the reduction. Furthermore, the derived *DC*-conductivity of 0.5 wt.% Fe-doped $BaTiO_3$ after reduction suggests, that that Fe is rather present as Fe^{3+} than Fe^{2+}.

A.2.4. Further SEM images of 0.5 wt. % Fe- and Mn-doped BaTiO$_3$
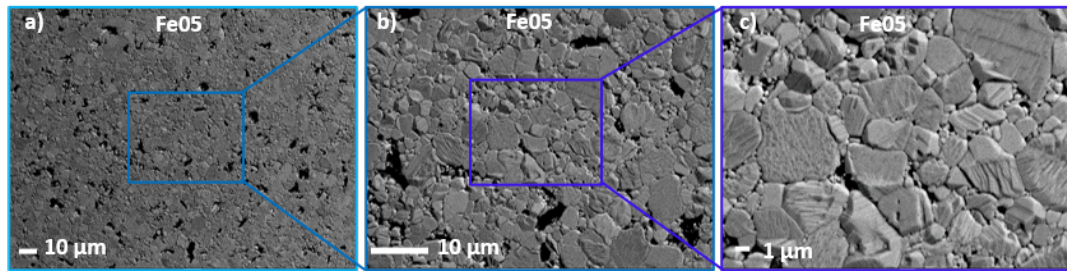
Figure A.4.: SEM on 0.5 wt.% Fe-doped BaTiO$_3$ a) after sintering with enhanced magnifications in b) and c). The images were taken in the BSE mode.
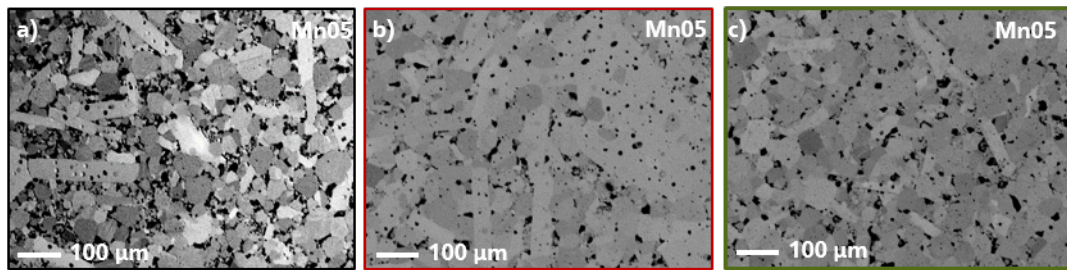
Figure A.5.: SEM on 0.5 wt.% Mn-doped BaTiO$_3$ a) after sintering, b) after equilibration and c) after reduction.

A.2.5. Frequency dependent Permittivity of undoped and 0.5 wt. % acceptor-doped BaTiO$_3$
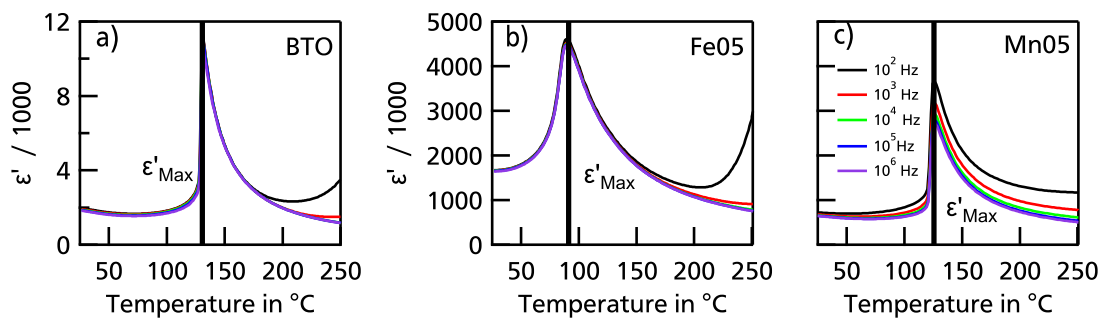
Figure A.6.: Frequency dependent permittivity of a) nominally undoped, b) 0.5 wt.% Fe-doped, and c) 0.5 wt.% Mn-doped BaTiO$_3$ during the first heating cycle. The temperature dependent dielectric constant has been measured for the five frequencies given in the legend in c).

A.2.6. Polarization, strain, and current loops of acceptor-doped BaTiO$_3$
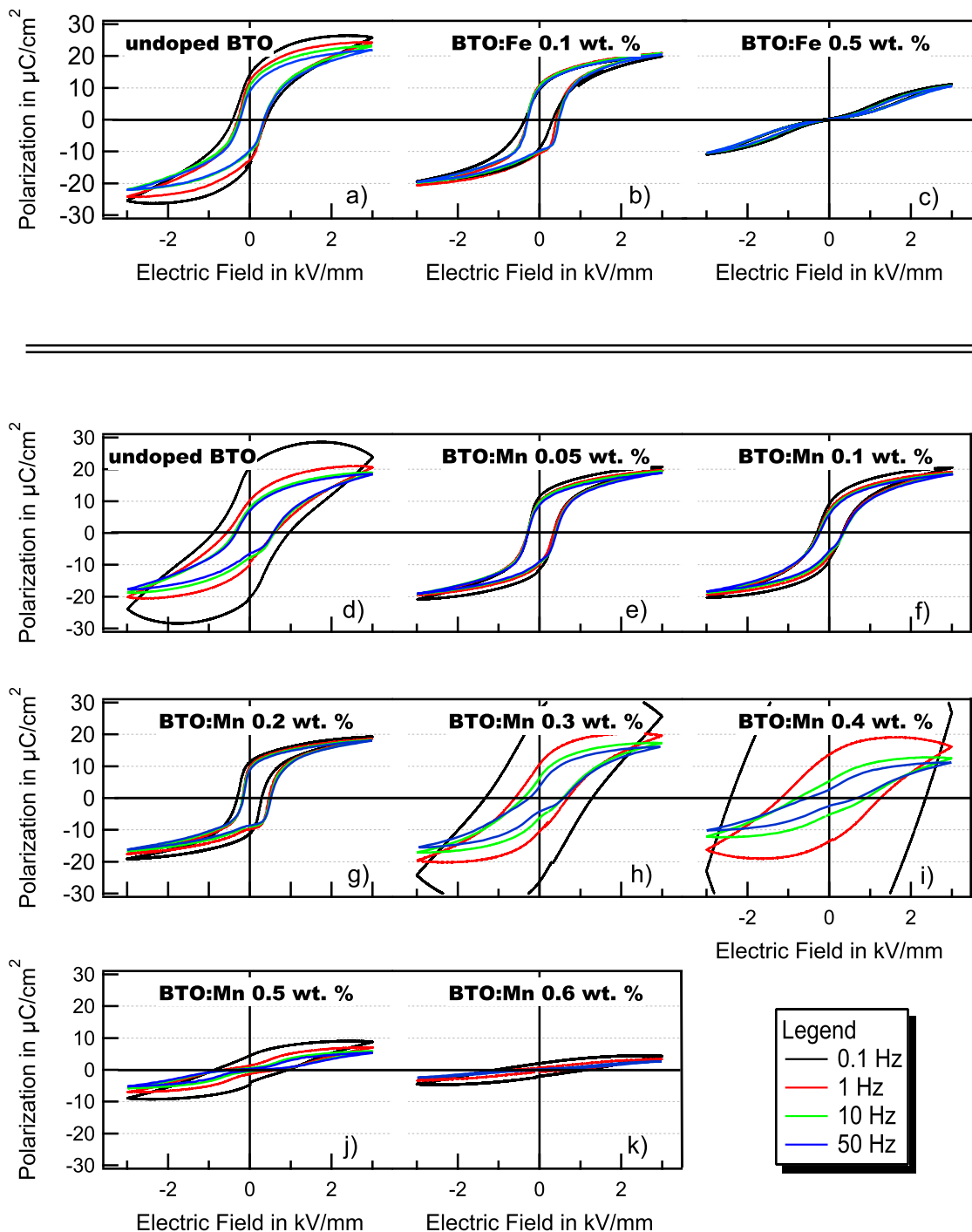
Figure A.7.: Polarization loops as a function of the electric field of polycrystalline BaTiO$_3$ with different Fe- and Mn-content measured at different frequencies. The second loop is depicted.
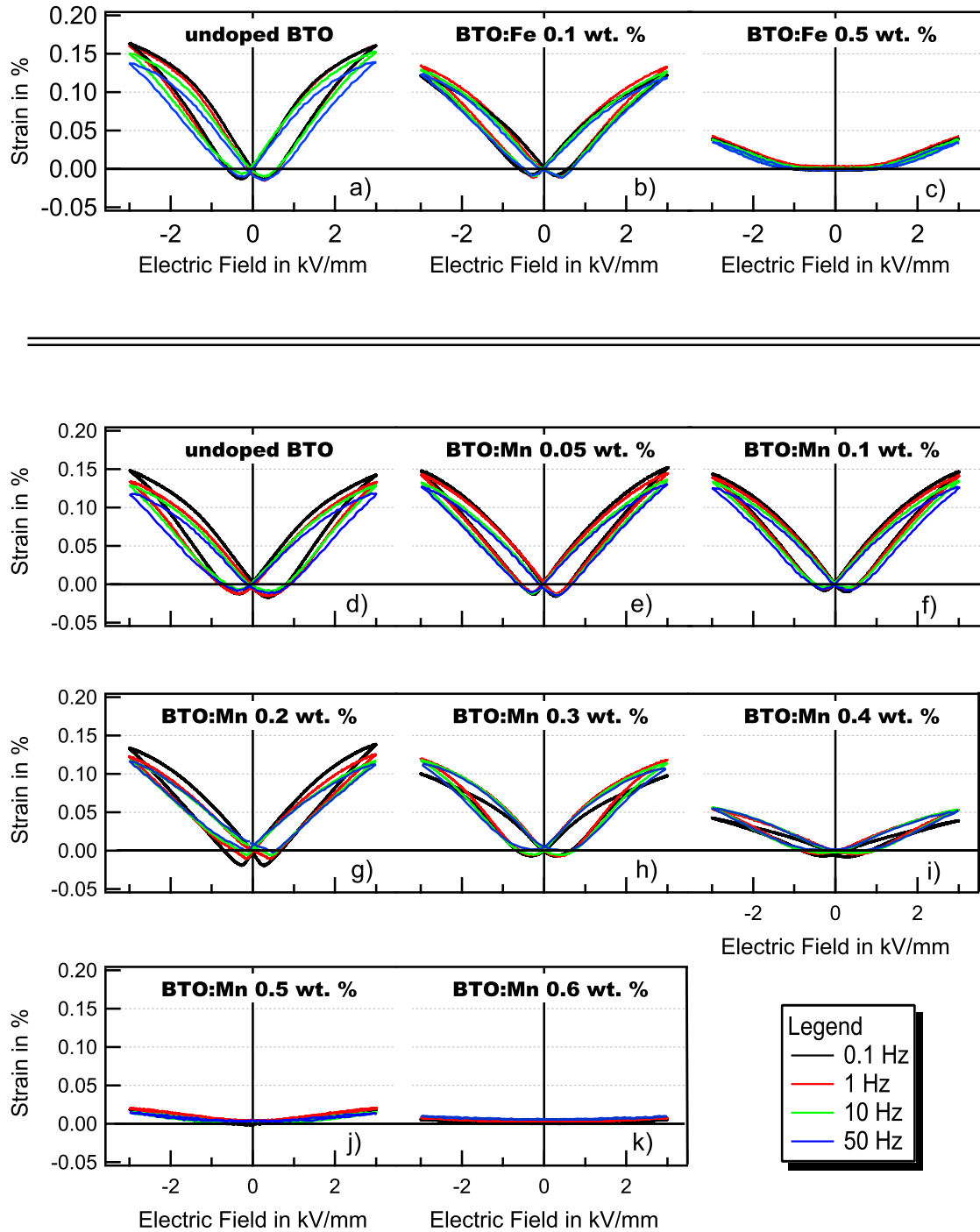
Figure A.8.: Strain loops as a function of the electric field of polycrystalline BaTiO$_3$ with different Fe- and Mn-content measured at different frequencies. The second loop is depicted.
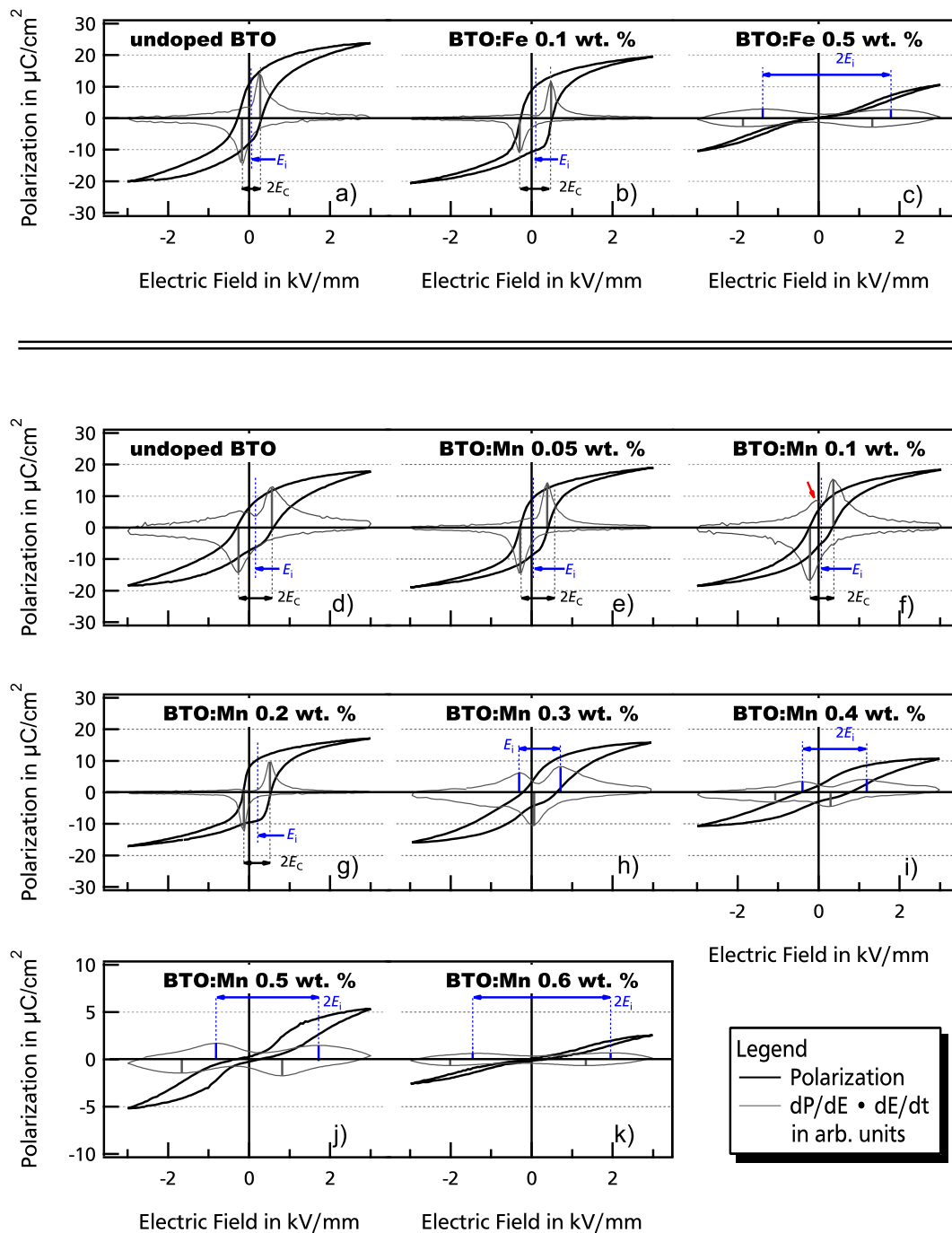
Figure A.9.: Current loops at 50 Hz for polycrystalline BaTiO$_3$ with different Fe- and Mn-content. The current curves, i.e. the differentiated hysteresis loops, are depicted for the respective polarization loop and are smoothed and magnified for clarify. The definition of the internal bias field E_i and the coercive field E_C are given for the respective doping concentration. The second loop is depicted.

A.2.7. Comparison of the unknown reflections with powder diffraction pattern
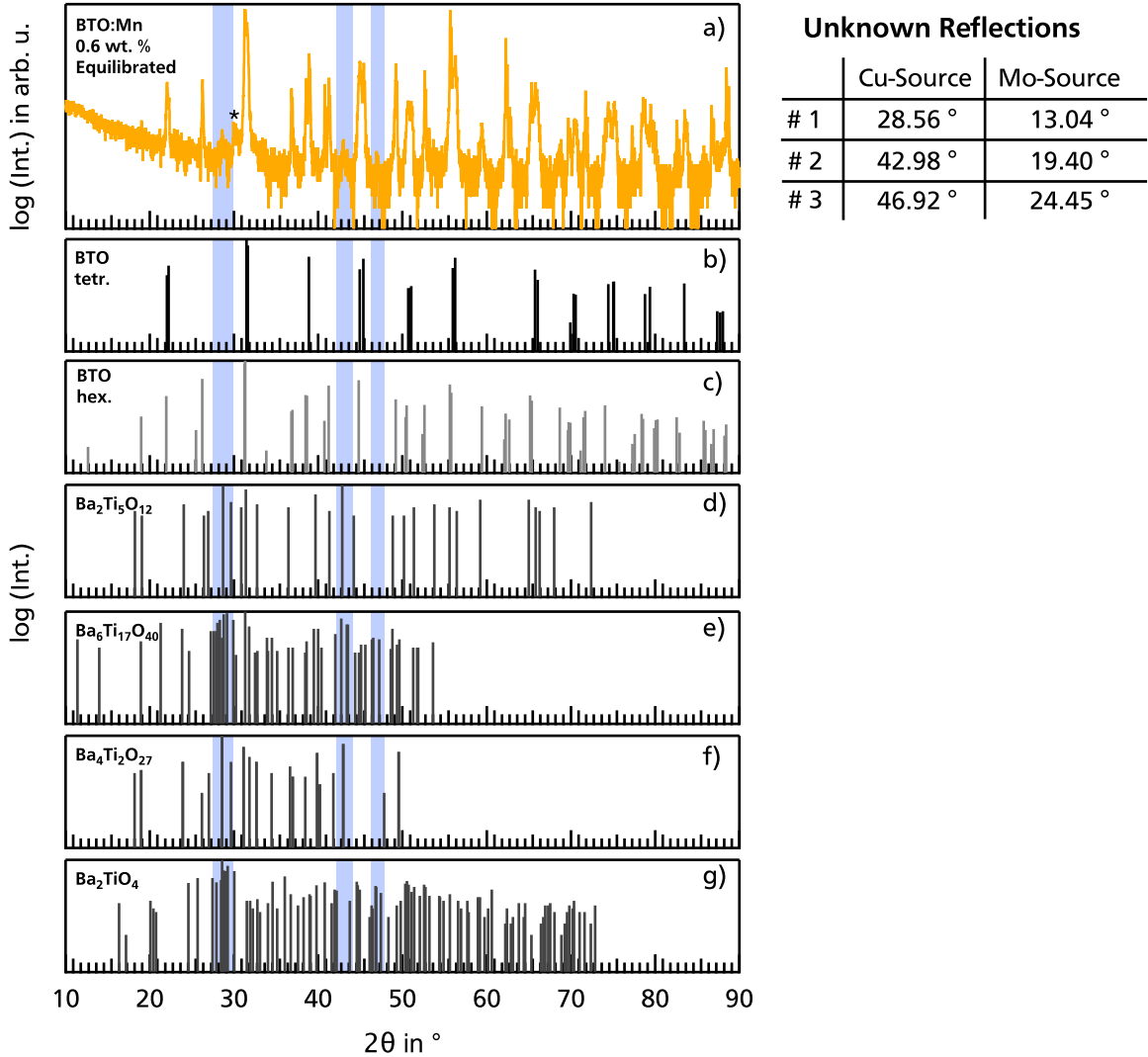
Figure A.10.: Comparison of the unknown reflections highlighted in the XRD pattern of 0.6 wt.% Mn-doped $BaTiO_3$ ceramic pellets to the powder diffraction pattern of t-$BaTiO_3$ [01-075-0583], h-$BaTiO_3$ [01-082-1175], Si [01-089-2749], $Ba_2Ti_5O_{12}$ [00-017-0661], $Ba_6Ti_{17}O_{40}$ [00-026-0321], $Ba_4Ti_2O_{27}$ [00-044-0013], Ba_2TiO_4 [00-035-0813]. The pattern were recorded by Cu $K_{\alpha 1}$ radiation with $\lambda_{CuK_{\alpha 1}} = 1.5406$ Å filtered by a Sol-X detector. The reflection marked with * at 30.22° corresponds to an artificial tungsten reflection, which results from the X-ray tube. The position of the unknown reflections highlighted in a) has been calculated for the Mo-source according to the Bragg Equation and is given in the Table on the right. All other reflections have been successfully assigned to reflections of the tetragonal or hexagonal $BaTiO_3$ powder reflection pattern displayed in b) and c), respectively.
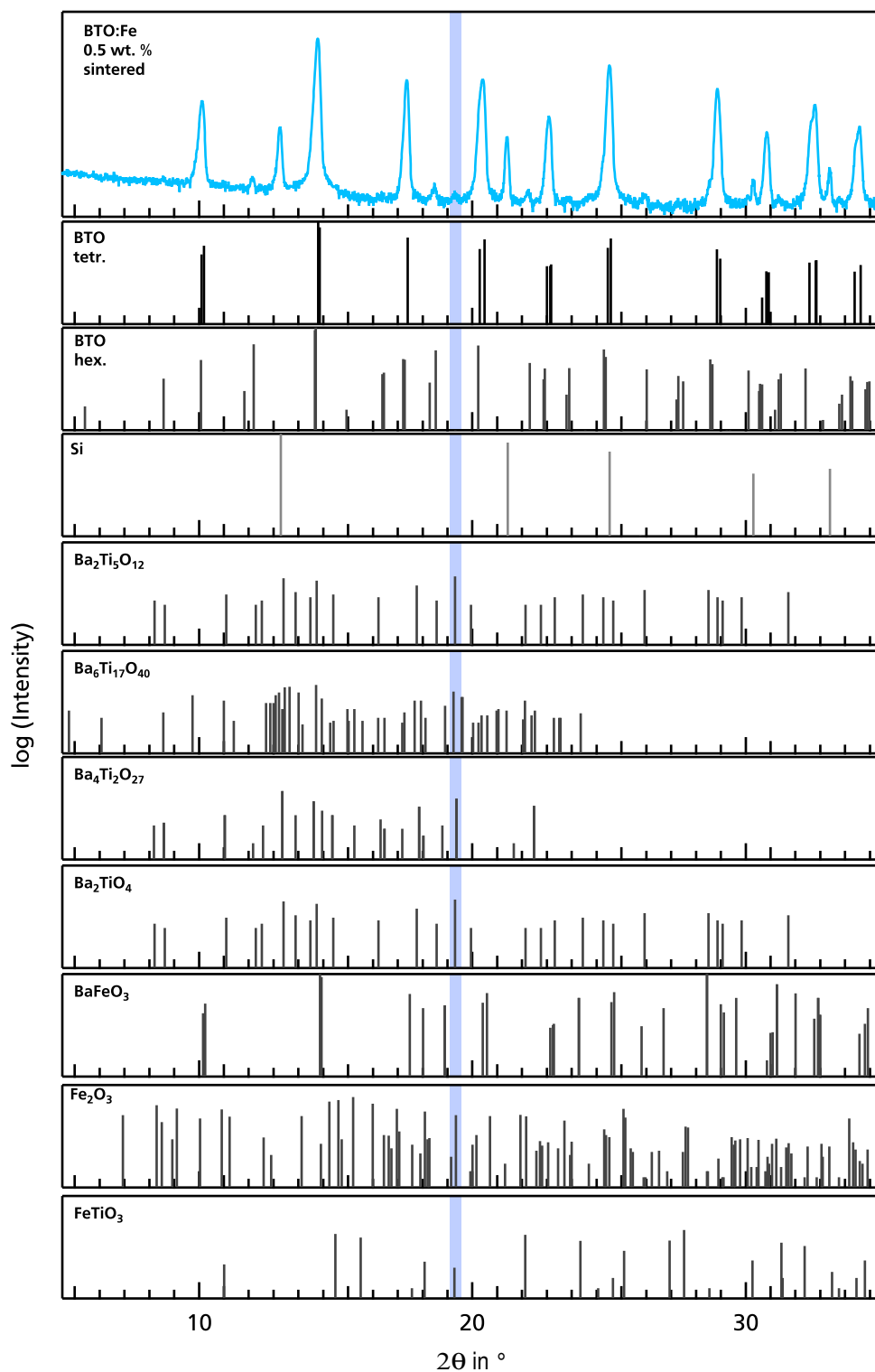
Figure A.11.: Comparison of the unknown reflections highlighted in the XRD pattern of 0.5 wt.% Fe-doped BaTiO$_3$ ceramic pellets to the powder diffraction pattern of t-BaTiO$_3$ [01-075-0583], h-BaTiO$_3$ [01-082-1175], Si [01-089-2749], Ba$_2$Ti$_5$O$_{12}$ [00-017-0661], Ba$_6$Ti$_{17}$O$_{40}$ [00-026-0321], Ba$_4$Ti$_2$O$_{27}$ [00-044-0013], Ba$_2$TiO$_4$ [00-035-0813], BaFeO$_3$ [01-075-0276], Fe$_2$O$_3$ [01-076-1821], and FeTiO$_3$ [00-050-0505] are displayed. The pattern were recorded using Mo K_α radiation with $\lambda = 0.7093$ Å.
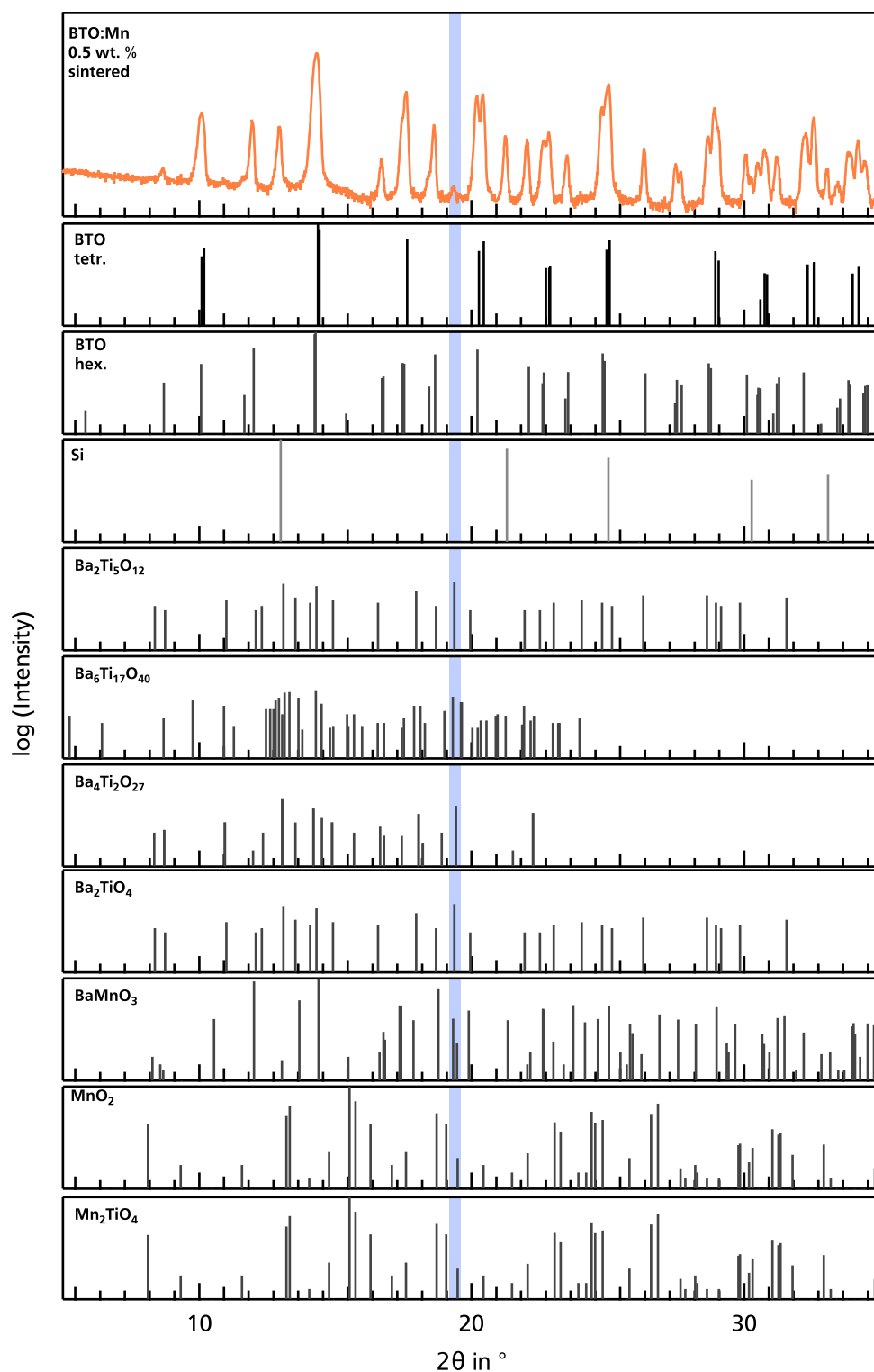
Figure A.12.: Comparison of the unknown reflections highlighted in the XRD pattern of 0.5 wt.% Mn-doped BaTiO$_3$ ceramic pellets to the powder diffraction pattern of t-BaTiO$_3$ [01-075-0583], h-BaTiO$_3$ [01-082-1175], Si [01-089-2749], Ba$_2$Ti$_5$O$_{12}$ [00-017-0661], Ba$_6$Ti$_{17}$O$_{40}$ [00-026-0321], Ba$_4$Ti$_2$O$_{27}$ [00-044-0013], Ba$_2$TiO$_4$ [00-035-0813], BaMnO$_3$ [01-071-1521], MnO$_2$ [03-065-2821], and Mn$_2$TiO$_4$ [01-073-0521] are displayed. The pattern were recorded using Mo K_α radiation with $\lambda = 0.7093$ Å.

A.2.8. XRD of reduced and reduced-ground 0.5 wt. % Mn-doped BaTiO$_3$
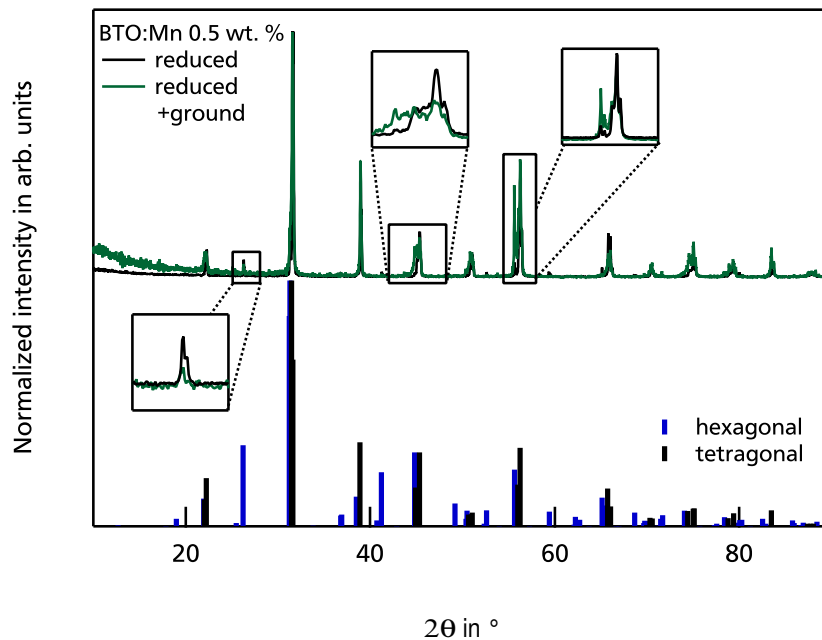
Figure A.13.: XRD-pattern of a reduced 0.5 wt.% Mn-doped sample being ground before and after reduction. Samples have been reduced at 1100 °C for 12 h in 5 % H$_2$ and have been quenched to *RT*. The pattern were recorded by Cu $K_{\alpha1}$ radiation with $\lambda_{CuK_{\alpha1}}$ =1.5406 Å filtered by a Sol-X detector. The reflection at 30.22 ° corresponds to an artificial tungsten reflection, which results from the X-ray tube.

A.3. Appendix to Chapter 6

A.3.1. Heating experiments with RuO$_2$ electrodes

As can be seen from the Poisson equation, the charge density will have a direct influence on the width of the space charge region. Thus, post-treatments of the interfaces may lead to a change (enhancement) of oxygen vacancy concentration in the dielectric bulk and enables oxygen vacancy diffusion, which could result in an modified space charge region width and an altered Fermi energy.

In order to examine the maximum effect, an interface experiment of a reduced and ground[2] 0.5 wt.% Mn-doped BaTiO$_3$ specimen towards RuO$_2$ was conducted, followed by post-heating in reducing atmosphere to further enhance the oxygen vacancy concentration. RuO$_2$ was deposited in two steps (3.5 nm and 5 nm) and afterwards post-heated for 2 h at 200 °C and 1 h at 300 °C in vacuum at a pressure of approximately 1×10^{-8} mbar. The X-ray photoelectron survey spectra of a reduced and ground 0.5 wt.% Mn-doped BaTiO$_3$ specimen are shown in Figure A.14 for the contact formation to RuO$_2$ and after vacuum heating for 2 h at 200 °C and 1 h at 300 °C. The survey of the cleaned specimen reveals considerable amounts of Ca and C. Here, the Ca contamination of the processed samples increased with time, which could be related to an increasing contamination of the polishing equipment and the quartz tube used for the reduction treatment. Other samples prepared at at a similar time reveal comparable Ca contamination and, thus, Ca is excluded as origin for the altered peak shape of this samples (see Figure A.15). This sample, however, was ground with a 4000 silicon carbide grinding paper finish after reduction. All other reduced and ground samples had a surface finish with 1 µm diamond particle finish. Thus, the surface of the present sample is considered to be more rough. This could have consequences for the recorded spectra. Here, a rougher surface may enhance the overall surface area, which might affect the surface related components in the Ba emissions. However, this has not been further investigated within this work, but could be evaluated by measurements of bare reduced and ground surfaces with different grinding/polishing finish.

The resulting core level emissions of the Ba $3d_{5/2}$, O $1s$, Ti $2p$, Ru $3d$, and Ba $4d$ of the clean[*] 0.5 wt.% Mn-doped BaTiO$_3$ surface and during stepwise deposition of RuO$_2$ as well as the post-treatments are depicted in Figure A.15 from bottom to top, respectively.

Both Ba core levels of the bare surface show a significant altered shape compared to the previous reduced and ground specimen shown in Figure 6.3. Possibly the different surface finish in polishing/grinding or the higher amount of impurities affects the emission line shape. However,

---

[2]When speaking of reduced and ground samples in this Chapter normally a grinding followed by a polishing step is meant. For this specific sample only a final grinding step of 4000 silicon carbide grinding paper was conducted and thus the surface is considered to be more rough compared to the other reduced and ground samples.
[2*]Considerable amounts of Ca are found on this samples.

the Fermi energies of 3.13 eV and 1.72 eV extracted from the spectra shown in Figure A.15 of the bare surface and after contact formation towards RuO_2 are identical with the values of the other reduced and ground sample (see Figure 6.7).

After the first post-heating for 2 h at 200 °C in vacuum considerable changes can be observed in the spectra. The Ba and Ti emission lines are shifted to higher binding energies, while the Ru emission is shifted to lower binding energies. The different direction of binding energy shift results in an altered peak shape of the superimposed Ti $2p$ emission, as the Ru $3p$ contribution shifts to lower and the Ti $2p_{1/2}$ emission to higher binding energies, as indicated by the labels in Figure A.15.

Besides the shift in binding energy also the peak shape and intensity of the Ru $3d$ emission line alters. After the deposition of 5 nm RuO_2 the binding energy position of the Ru $3d_{5/2}$ at 281.3 eV as well as the peak shape with the satellite structure[3] between the $3d_{5/2}$ and the $3d_{3/2}$ confirm the expected oxidation state of Ru^{4+} [268]. The post-heating in vacuum reduces the
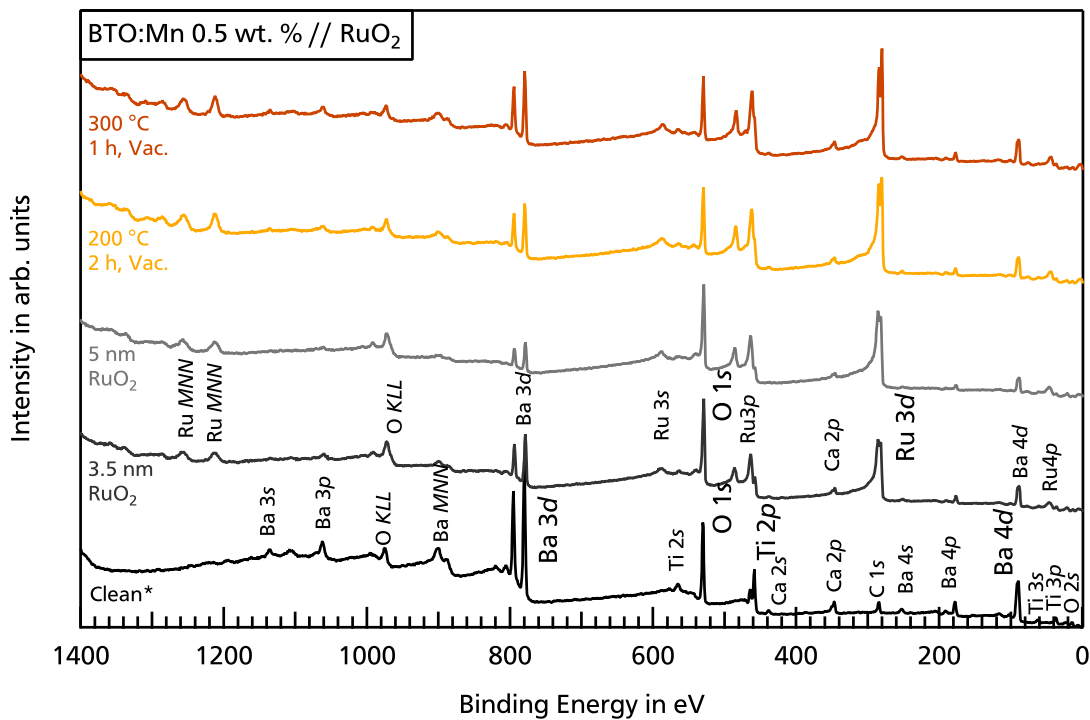
Figure A.14.: X-ray photoelectron survey spectra of a reduced and ground 0.5 wt.% Mn-doped $BaTiO_3$. The spectra were recorded during contact formation to RuO_2 and after vacuum post-heating. The RuO_2 electrode thickness as well as the used post-treatment parameters are indicated in the spectrum.

---

[3]The origin of the satellite peak between the Ru $3d_{5/2}$ and the Ru $3d_{3/2}$ is still under discussion. Possible explanations are Ru being present in a different oxidation state (Ru^{4+}/Ru^{6+}) [268], final state effects [269], and plasmon excitations [270]. Even though it could be excluded that Ru is present in an oxidation mixture [241], a more distinct statement is not possible, yet. However, in all publications the satellite was presence in RuO_2 and absent in the case of metallic Ru.
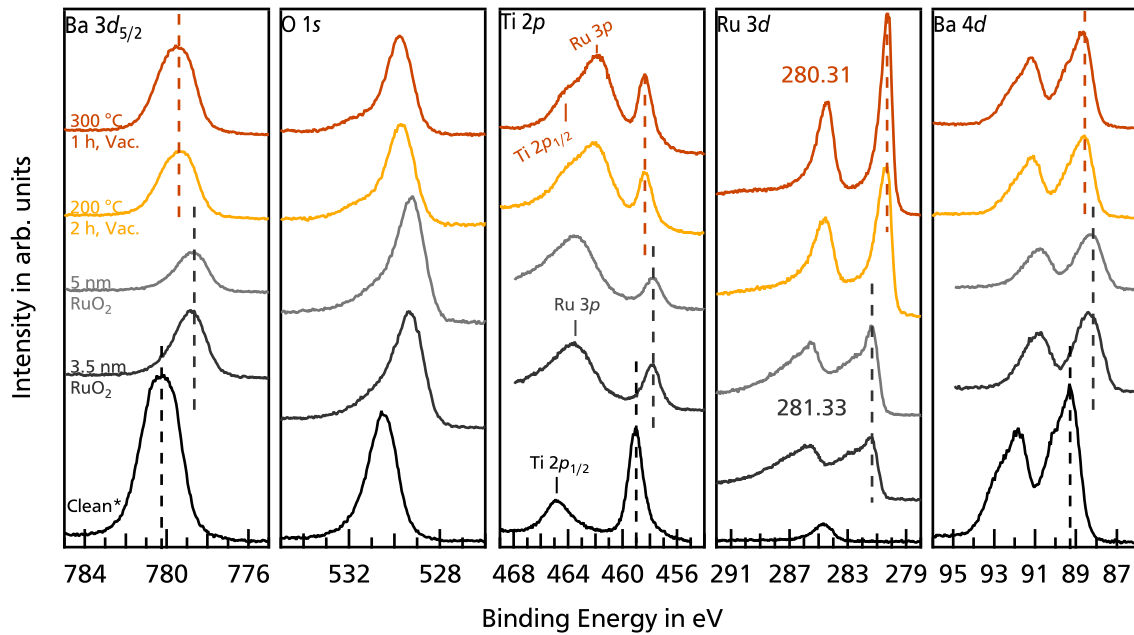
Figure A.15.: X-ray photoelectron core level spectra of the Ba $3d_{5/2}$, O $1s$, Ti $2p$, Ru $3d$, and Ba $4d$ emissions of a reduced and ground 0.5 wt.% Mn-doped BaTiO$_3$. The spectra were recorded during contact formation to RuO$_2$ and after vacuum post-heating. The RuO$_2$ electrode thickness as well as the used post-treatment parameters are indicated in the Ba $3d_{5/2}$ spectrum. The binding energy shifts before and after contact formation as well as after the post-treatments are indicated by the dashed lines in the core level spectra. The binding energy of the Ru $3d_{5/2}$ before and after heat treatment is given in eV. The spectra were recorded with monochromatic Al K$_\alpha$ radiation.

binding energy of the Ru $3d_{5/2}$ emission to 280.3 eV. The latter binding energy position in combination with sharper peak shape and the absence of the satellite refers most likely to Ru^0 and thus metallic ruthenium [99, 268, 271]. Furthermore, the relative intensities of the Ba, Ti, and Ru spectra are enhanced, while the intensity for the O spectra decreased. This change in stoichiometry indicates the loss of oxygen from the RuO$_2$ electrode.

The increased intensity of the substrate (Ba and Ti) emission indicates either a decreased film thickness of the electrode due to recrystallization or the formation of 3-dimensional Ru island. In the case of SrTiO$_3$/Pt interfaces Schafranek *et al.* observed a comparable increase in the substrate emission lines after annealing for 30 min at 400 °C in oxygen and vacuum [232, 272]. The authors performed atomic force microscopy measurements on the as-deposited and on the post-annealed Pt thin film, which could prove the formation of Pt islands on the interface of SrTiO$_3$/Pt [272]. The used post-heating temperature for the present BaTiO$_3$:Mn/RuO$_2$ interface is 100 °C lower than the one of Schafranek. Thus, a direct comparison based on the annealing parameters is not possible. However, the combined observations of increased Ba, Ti, and Ru intensities with the oxygen loss and the appearance of metallic Ru strongly indicate the formation of Ru islands on the present interface.
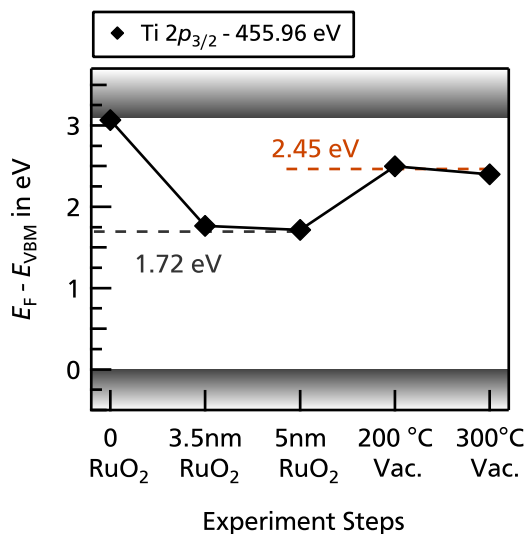
Figure A.16: Evolution of the valence band maximum binding energies $E_F - E_{VBM}$ of a reduced and ground 0.5 wt.% Mn-doped BaTiO$_3$ ceramics during the stepwise deposition of the RuO$_2$ electrode and the annealing treatments. The valence band maximum binding energies was deduced from the shift of Ti $2p_{3/2}$ core level by substation the core level to valence band maximum distance given in the legend. The film thickness of RuO$_2$ was calculated based on the respective accumulated deposition time with an assumed deposition rate of 3 nm/min.

For the present BaTiO$_3$:Mn/RuO$_2$ interface no further changes, neither in the binding energies nor in the peak shape, could be observed by the second heating step for 1 h at 300 °C in vacuum. This indicates, that the reduction of Ru^{4+} to Ru^0 and thus RuO$_2$ towards metallic Ru was already completed after the first heating step. As both, the heating atmosphere as well as the reduced 0.5 wt.% Mn-doped BaTiO$_3$ substrate, are highly reductive, it remains unclear whether the oxygen of the electrode went into the gas phase or diffused into the 0.5 wt.% Mn-doped BaTiO$_3$.

The Fermi level shift of the 0.5 wt.% Mn-doped BaTiO$_3$ specimen during stepwise RuO$_2$ deposition and post-heating was calculated using the Ti $2p_{3/2}$ emission[4] and is shown in Figure A.16. The interface formation to RuO$_2$ results in the well known Fermi level value of $E_F - E_{VBM} = 1.7$ eV. Post-heating in vacuum, independent on the heating time and temperature of both steps, rises the Fermi level towards 2.45 eV.

The interpretation of this Fermi level shift is difficult without further knowledge on the film properties of the observed metallic Ru. In previous works, a series of systematic measurements from RuO$_2$ to RuO$_x$ to metallic Ru revealed a considerable decrease of the work function from 6.1 eV for RuO$_2$ to 5.3 eV for metallic Ru [99]. Even though the reported magnitude of the work function for both, RuO$_2$ and Ru, is under on-going discussion,[5] the decrease of the work function from RuO$_2$ towards Ru is consistent in all reports. For the present BaTiO$_3$:Mn/RuO$_2$ interface, a decrease of the electrode work function would result in a lowered barrier height for electrons and thus in an increasing Fermi level at the interface.

---

[4]As the shape of the Ba emission is significantly altered compared to the other reduced and ground samples the Ti $2p_{3/2}$ was considered to be more reliable for the extraction of the Fermi level position.

[5]The reported magnitude is rather sensitive on the preparation conditions (adsorbed oxygen, stoichiometry, carbon contamination etc.). Following the discussions in [99] and [201], the reported work functions differ between 5.0-6.5 eV [201, 273] for RuO$_2$ and between 4.7-5.3 eV [99, 274] for Ru.

However, following the above discussion on the increased intensity of the substrate emission after the vacuum heating, it remains highly questionable, if the Ru electrode is still homogeneously covering the 0.5 wt.% Mn-doped BaTiO$_3$ substrate. In the case of an 3-dimensional Ru island formation, lateral inhomogeneities of the surface potential are expected due to the inhomogeneous coverage of the surface [272]. An inhomogeneous potential will additional affect and complicate the interpretation of the resulting Fermi level.

A.3.2. Interface formation of Mn-doped BaTiO$_3$ to PtO$_x$
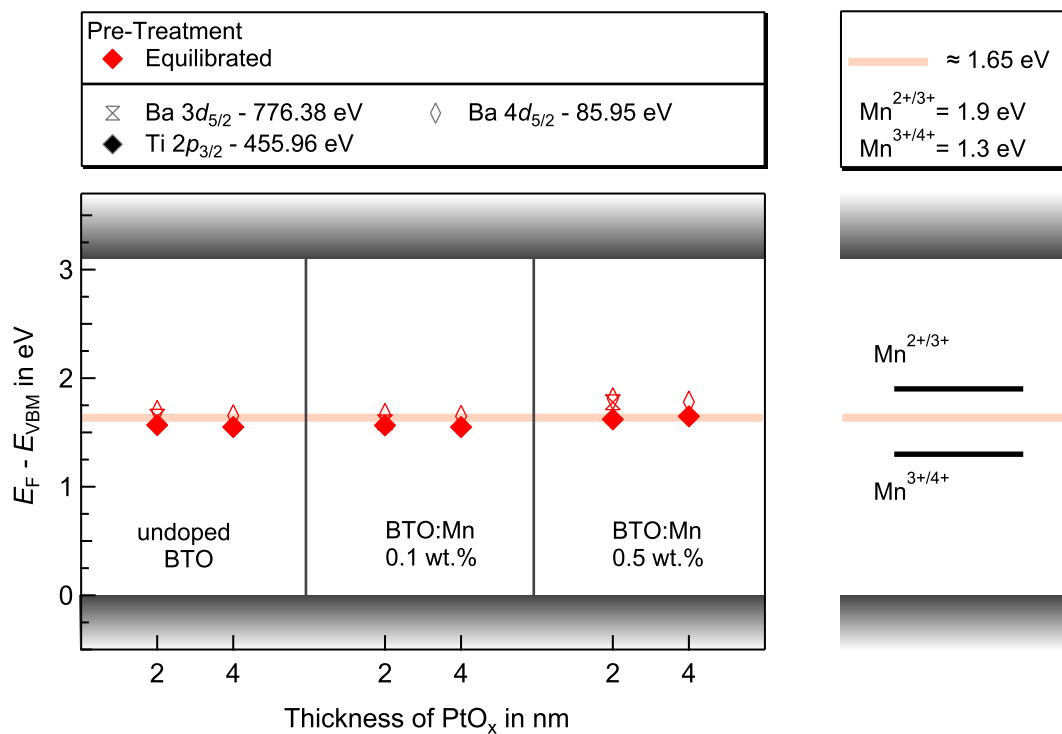
Figure A.17.: Left: Evolution of the Ba $3d_{5/2}$, Ti $2p_{3/2}$, and Ba $4d_{5/2}$ binding energies with increasing PtO$_x$ thickness for undoped, 0.1 wt.%, and 0.5 wt.% Mn-doped BaTiO$_3$ ceramics in an equilibrated state. The binding energy values of the Ba $3d_{5/2}$, Ti $2p_{3/2}$, and Ba $4d_{5/2}$ core level have been determined by the maximum intensity. No fit of the Ba $3d_{5/2}$ and Ba $4d_{5/2}$ core level has been conducted, as the Ba $4d_{5/2}$ core level is partially superimposed by the Pt $4f$ emission. The valence band maximum binding energies $E_F - E_{VBM}$ are derived by subtracting the respective core level to VBM distances given in the legend above. The film thickness of PtO$_x$ was calculated based on the respective accumulated deposition time with an assumed deposition rate of 4 nm/min. Right: Comparison of the derived interface $E_F - E_{VBM}$ values to the literature values of manganese charge transition levels [21] inside the band gap of BaTiO$_3$.

A.3.3. *In situ* degradation with *HT*-deposited Sn-doped In_2O_3 electrodes

Simultaneous temperature and voltage stress will result in resistance degradation of $BaTiO_3$ ceramic capacitors (see fundamental Section 2.3.4). As the resistance degradation of $BaTiO_3$ is based on the oxygen vacancy migration, the applied temperature and voltage stress will result in a depletion and accumulation of oxygen vacancies at the anode and cathode, respectively. The resulting *p*- and *n*-type regions results in a decrease and increase of the Fermi level in the respective region and potentially in a narrowing of the SCR, which is assumed to have a measurable influence on the resulting barrier height. The influence of resistance degradation on the electrode interface properties, especially on the Schottky barrier height, has been studied in previous works of Huang [18] and Gieseke [14, 17] for Fe-doped $SrTiO_3$ single crystals with different electrode materials. In their works, XPS measurements have been carried out before and after *ex situ* degradation. The interpretation of the recorded spectra, however, did not provide clear evidence for systematic Schottky barrier modifications at the cathode/anode. Possibly, the samples recovered between *ex situ* degradation and the second XPS measurement of the interface, which eventually results in a recovery of the modified Schottky barrier. Such sample recovery could be prevented by conducting *in situ* degradation with simultaneous XPS-measurement. A new sample stage for the XPS set-up has been constructed within the ESM working group, which enabled simultaneous heating in vacuum up to 300 °C, while applying a perpendicular voltage through the sample. The modification of the barrier height during resistance degradation can be monitored constantly throughout the whole experiment by conducting XPS measurements.

First experiments with the new XPS heating stage have been carried out using equilibrated undoped $BaTiO_3$ specimens with degradation parameters comparable[6] to *ex situ* degradation in order to facilitate a comparison. The temperature was set to 145 °C, while the electric field was set to 0.3 kV/mm. A roughly 50 nm thick platinum electrode was used as bottom contact. A 3 nm *HT*-ITO electrode was used as top contact. Here, *HT*-ITO denotes ITO being deposited at 400 °C (see experimental Section 3.1.3). A higher ITO deposition temperature should results in an increased charge carrier concentration and conductivity of the ITO electrode [81, 244]. *In situ* degradation experiments have been conducted on two similar samples with *HT*-ITO serving as anode and cathode. The voltage was applied on the bottom platinum electrode, while the top ITO electrode was grounded.

As a consequence of the high permittivity of $BaTiO_3$ no considerable changes of the measured interface Fermi level due to a potential narrowing of the SCR upon voltage and temperature stress induced oxygen diffusion is expected. However, oxygen exchange between the $BaTiO_3$

---

[6]As a side note it should be mentioned that the *in situ* degradation was conducted in vacuum, while the *ex situ* degradation was conducted in air.

substrate and/or the atmosphere with the ITO electrodes could alter the oxygen content in the electrode, which will effect the ITO Fermi level and by this the resulting Schottky barrier height at the BaTiO$_3$:Mn/ITO interface.

The X-ray photoelectron spectra of the Ba $3d_{5/2}$, O $1s$, Sn $3d_{5/2}$, Ti $2p$, In $3d_{5/2}$, and Ba $4d$ core level emissions for equilibrated undoped BaTiO$_3$ with ITO as anode and ITO as cathode are shown Figure A.18 in the upper and lower panel, respectively. Unfortunately, XPS measurements during applied voltage were not feasible, as the peak position was continuously shifting , which will be addressed in the following discussion for the respective electrode configuration. Thus, XP-spectra have been recorded at room temperature after 3 nm *HT*-ITO deposition, before and after degradation without applied voltage at 145 °C. The corresponding spectra are shown from bottom to top within the graph of the respective electrode. The schematic set-up with the magnitude of the voltage being applied at the bottom is illustrated on the right of the spectra. First, the results of ITO being connected as anode will be discussed. The Ba, Ti, Sn, and In emission show the well known peak shape after 3 nm *HT*-ITO deposition. The samples have been shortly exposed to air during mounting them onto a special sample holder for voltage experiments. Thus, the high binding energy shoulder in the O $1s$ spectrum refers to oxygen containing carbon contamination. Whereas the shoulder in the O $1s$ emission decreases during vacuum heating at 145 °C, no distinct changes in the Ba, Ti, Sn, and In core level emissions are observed. The Ba $3d_{5/2}$, Ba $4d$, and Ti $2p$ core level emission are shifted by approximately 50 meV, while the Sn $3d_{5/2}$ and In $3d_{5/2}$ are shifted by 210 meV and 70 meV towards lower binding energies, respectively.

The voltage of −170 V has been applied to the back platinum electrode for 70 min (without recording XP spectra). The initial conductivity of 9×10^{-9} S/cm increased within the first 10 min to 1×10^{-7} S/cm without further increase for the remaining time. Afterwards, another set of XP-spectra have been recorded. No considerable shifts have been observed in the spectra of the Ba and Ti emissions. This indicates that the SCR width is still larger than the tunneling distance for electrons and that the measured Schottky barrier height corresponds to the interface value.

For the present interface configuration XPS measurements with an applied voltage of -170 V at the bottom were not feasible, as the spectra where continuously shifting towards lower binding energies. This was unexpected as the top ITO electrode is grounded via the mask. Most likely, this is explained by a failure of the ITO thin film electrode due to its non-blocking behavior for oxygen. According to the applied electric field, oxygen is diffusing towards the anode region and possibly diffusing from the BaTiO$_3$ substrate into the Sn-doped In$_2$O$_3$ anode, where the oxygen will compensate the Sn donors and, thus, decreases the carrier concentration and the conductivity. This has been proven in the work of Öcal [19], who conducted *ex situ* degradation experiments of Mn-doped polycrystalline BaTiO$_3$ samples with ITO anodes, while
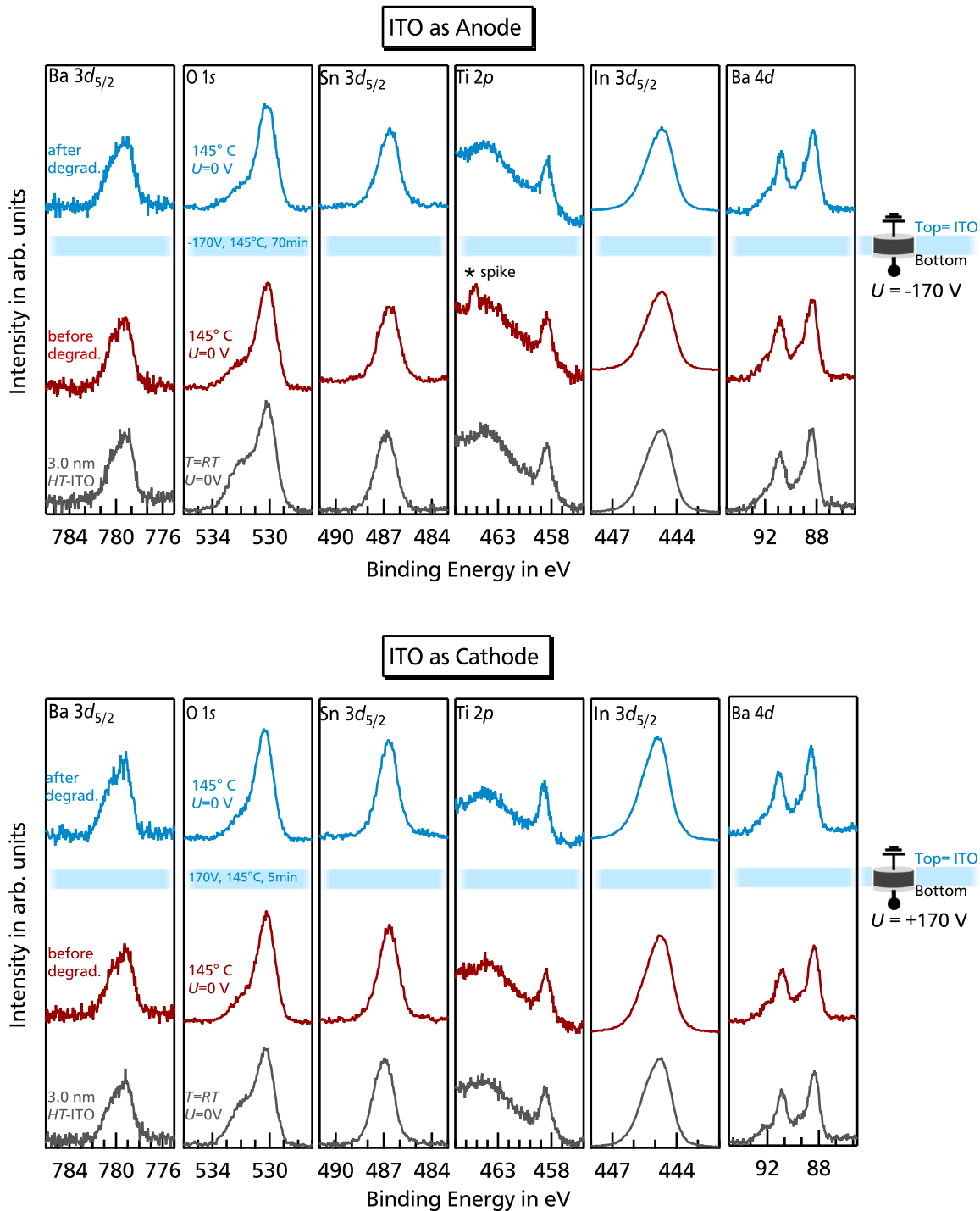
Figure A.18.: X-ray photoelectron core level spectra of the Ba $3d_{5/2}$, O $1s$, Sn $3d_{5/2}$, In $3d_{5/2}$, Ti $2p$, and Ba $4d$ emissions of an equilibrated undoped $BaTiO_3$. The temperature and voltage during XPS acquisition are indicated in the O $1s$ spectrum. The upper panel corresponds to ITO connected as anode, while the lower panel corresponds to ITO connected as cathode. The voltage was applied between the red and the blue spectrum with the parameters and the schematically connection depicted in the respective drawing on the right. The measurements have been performed in the scope of the new manipulator test, during which no binding energy calibration has been carried out. Thus, no binding energy correction is included for the presented spectra.

simultaneously measuring the ITO conductivity. The results show, that the conductivity of the ITO anode was decreasing below 800 S/cm [19]. Too low electrode conductivities may give rise to inhomogeneous electric fields, a suppressed degradation and an insufficient electrical grounding during the XPS measurements, which may result in the observed binding energy shifts of the core level spectra. Recent experiments within the ESM working group on different ITO/substrate combination revealed similar finding for sample currents $> 1\,\mu A$. For the present sample the initial perpendicular current was 1.1×10^{-5} S/cm and increased to 2×10^{-4} S/cm during degradation. Consequently, for such high sample currents the conductivity of ITO is too low (even for *HT*-ITO or reduced ITO).

The results of ITO being connected as cathode will only be discussed briefly, as it was not possible to apply a voltage of $+170\,V$ to the bottom platinum electrode for longer times than $>1\,min$. The resulting current was linearly increasing from initially[7] 1.5×10^{-7} S/cm to the maximum output current of the used picoammeter. For such high currents it is essential, that the sheet resistance $R = \rho/d$ of the ITO electrode is sufficiently high to ensure the charge flow from the middle of the electrode towards the mask contact (with d being the distance between both points). If the sheet resistance is too low, a potential drop develops inside the ITO electrode. The conductivity of the $BaTiO_3$ and the resulting current of up to 1×10^{-3} A is assumed to be too high for the sheet resistance to the ITO electrode, which results in charging.

---

[7]The initial current of this sample was one order of magnitude higher than the one with ITO being connected as anode. This was unexpected because equilibrated samples usually show a good reproducibility in conductivity. A changed initial conductivity might be attributed to a different dwell time and a beginning reduction of the sample during heating in vacuum or the preliminary low voltage test on this sample. Here, a lower voltage has been applied several times due to connection problems of the picoammeter with the LabView program. Properly, this already initialized a beginning degradation and increase in conductivity.

A.4. Appendix to Chapter 7
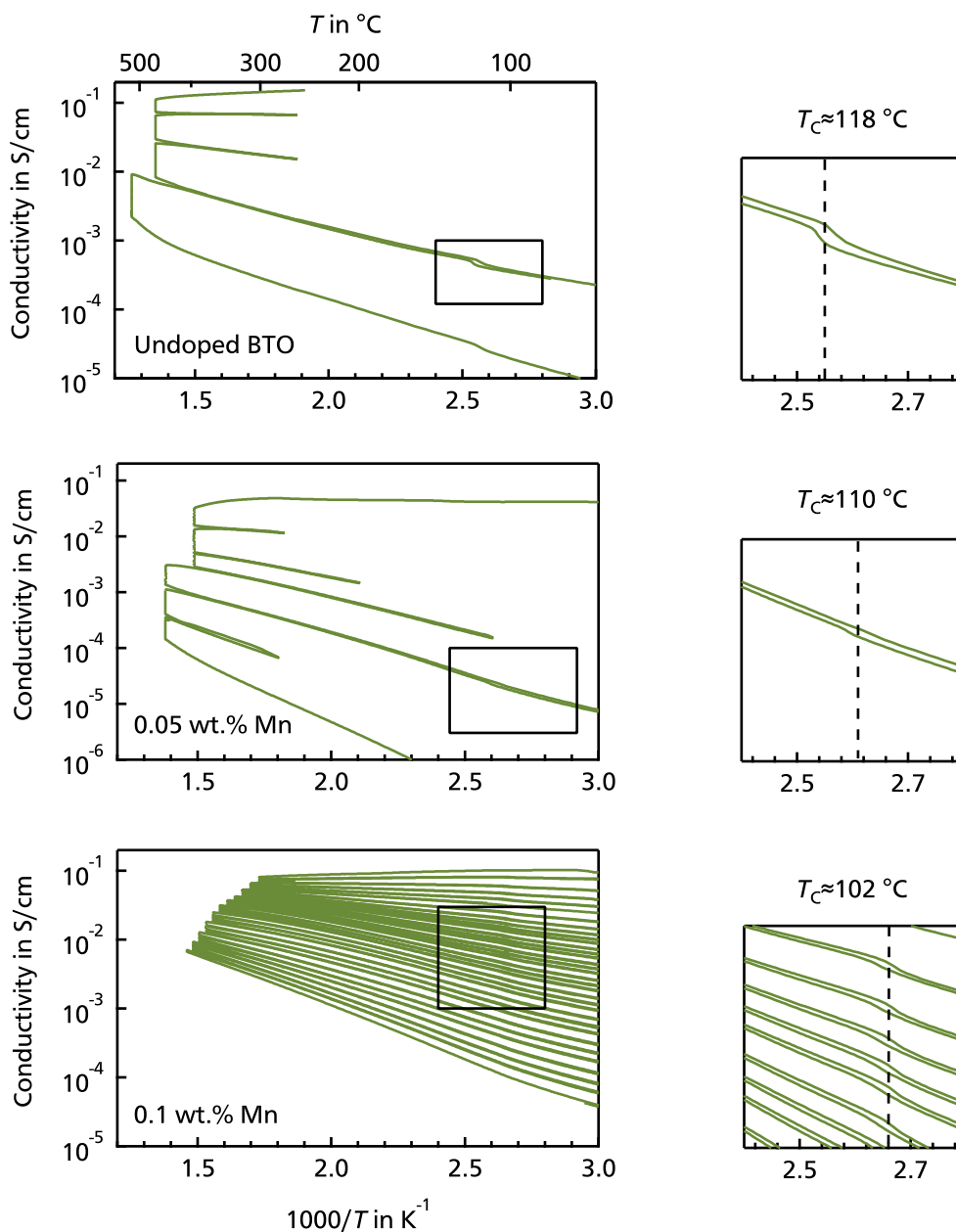
Figure A.19.: Temperature-dependent conductivity of undoped BaTiO$_3$, 0.05 wt.%, and 0.1 wt.% Mn-doped BaTiO$_3$. A hysteresis behavior in the temperature-dependent conductivity is observed, which is most likely attributed to the phase transition. The corresponding region of the re-oxidation loops are magnified on the right. For reduced undoped, 0.05 wt.%, and 0.1 wt.% Mn-doped BaTiO$_3$ a phase transition temperature of approximately 118 °C, 110 °C, and 102 °C has been determined, respectively. A strong decrease of Curie point in highly reduced samples is consistent with literature reports. The decrease in T_C is most likely related to the enhanced charge carrier concentration after reduction [182].

A.4.1. Influence of the polarization current on the total current in vicinity of the phase transition

For low sample currents (i.e. high re-oxidation state) the polarization current across the phase transition temperature starts to influence the overall measured sample conductivity. This influence has been observed for all $BaTiO_3$-base samples. The magnitude of the polarization current is related to the temperature-dependent capacity change of the sample, which can be extracted from the dielectric measurements. If the leakage current and the polarization current are of the same order of magnitude the temperature-dependent conductivity will be influenced by the charging/discharging of the capacitor during heating across the ferroelectric-paraelectric phase transition temperature. The different contribution of the leakage current and the polarization current to the total current can be simulated[8]. First the temperature-dependent polarization current I_{pol} needs to be calculated. This can be done by taking the temperature-dependent capacitance, which was recorded during the LCR-measurements (see Section 3.2.2). The recorded temperature and capacitance as a function of time are depicted for as-sintered 0.5 wt.% Mn-doped $BaTiO_3$ in Figure A.20 a). The polarization current can be calculated by Equation A.1, with $dU/dt = 0$:

$$I_{\text{pol.}} = \frac{dQ}{dt} = \frac{dC_{\text{LCR}}}{dt_{\text{LCR}}} \cdot \frac{dU_{\text{LCR}}}{dt_{\text{LCR}}} = \frac{dC_{\text{LCR}}}{dt_{\text{LCR}}} \cdot U_{\text{LCR}}. \tag{A.1}$$

Figure A.20 b) shows the calculated polarization current as a function of measuring time during heating/cooling. The two peaks coincide with the measuring time at which the phase transition is taking place (compare a) and b)). These peaks refer to the discharging and charging of the capacitor during heating and cooling across the Curie temperature. However, the leakage current derived during the LCR measurements is not directly comparable to the one being expected during re-oxidation. Hence, a measurement specific acceleration factor $x_{\text{Acc.}}$ is implemented in order to change the heating/cooling rate t_{LCR}

$$t_{\text{LCR,mod.}} = t_{\text{LCR}} \cdot x_{\text{Acc.}}. \tag{A.2}$$

Additionally, the Curie temperature of the re-oxidized sample might be slightly shifted due to a higher amount of remaining oxygen vacancies. Such a Curie temperature shift ΔT can be added to the LCR temperature profile T_{LCR} by

$$T_{\text{LCR,mod.}} = T_{\text{LCR}} + \Delta T. \tag{A.3}$$

---

[8]Comparable simulations have first been conducted by B. Huang on PZT. In this work, his IGOR procedure has been adapted for $BaTiO_3$.
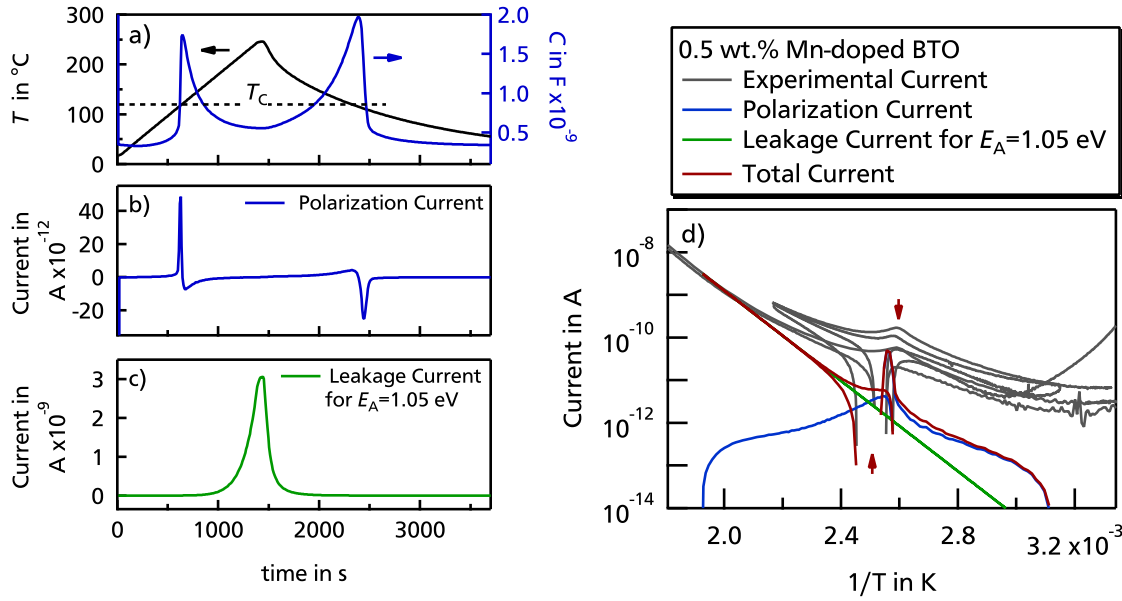
Figure A.20.: a) Temperature and capacitance of an as-sintered 0.5 wt.% Mn-doped sample, b) calculated polarization current and c) calculated leakage current assuming an activation energy of 1.05 eV. d) Comparison of the experimental current loops with the calculations.

While, a change in the heating/cooling rate will directly affect the magnitude of the polarization current, the shift of the Curie temperature will solely result in an offset on the temperature axis.

The temperature-dependent leakage current $I_{\text{leak.}}$ of the sample can be calculated using the Arrhenius law. Here, the activation energy E_A as well as the conductivity and the temperature of any point $(T_1|I_1)$ in the Arrhenius-type region of the re-oxidation loop are extracted. From the Arrhenius law and the mathematics of a straight line Equation A.4 is deduced:

$$I \propto e^{-\frac{E_A}{k_B \cdot T}}$$

$$\ln(I) \propto -\frac{E_A}{k_B \cdot T}$$

$$y = a \cdot x + b$$

where: $y = ln(I)$, $x = 1/T$, $a = -\frac{E_A}{k_B}$ and $b = ln(I_1) - \frac{E_A}{k_B \cdot T_1}$, with $(T_1|I_1)$ being experimentally values to derive the right y-value. The leakage current can then be calculated by Equation A.4:

$$I_{\text{leak.}} = e^{a \cdot x + b} = e^{-\frac{E_A}{k_B \cdot T} + ln(I_1) - \frac{E_A}{k_B \cdot T_1}}. \tag{A.4}$$

The calculated leakage current for the same temperature profile (same rate and dwell parameters) as for the LCR measurement is depicted in Figure A.20 c). The total current is the sum of the leakage current and the polarization current and is given by

$$I_{\text{ges.}} = I_{\text{leak.}} + I_{\text{pol.}}. \tag{A.5}$$

In Figure A.20 d) the experimental current of 0.5 wt.% Mn-doped $BaTiO_3$ during heating and cooling is compared to the calculated total current derived by the sum of the leakage and polarization current. For the polarization current calculation an acceleration factor of $x_{\text{Acc.}} = 0.2$ and a Curie temperature shift of $\Delta T = 5\,°C$ was used. For the leakage current calculation an activation energy of $E_A = 1.05\,eV$ and the point $(T_1|I_1) = (177\,°C\,|\ 4.5 \times 10^{-10}\,S/cm)$ was used. The resulting shape of the calculated total current is comparable to the current of the re-oxidation loop. The calculated total current reveals the small hump as well as the negative currents during ramping, which are indicated by the two small red arrows. However, especially at low temperatures the calculated current is orders of magnitude lower than the experimental. These off-sets indicate non-ideal calculation parameters for the polarization current. The present calculations have been conducted for a broad parameter set of $x_{\text{Acc.}}$ and ΔT. Unfortunately, none of these calculations coincides with the experimental data. It is most likely, that the taken data set from the LCR measurements of an as-sintered 0.5 wt.% Mn-doped $BaTiO_3$ specimens is not reflecting the real temperature-dependent capacitance. Any change in oxygen vacancy concentration and hexagonal phase fraction will affect the values and the shape of the LCR curves. Therefore, it is recommended to collected LCR-measurements for a set of different re-oxidation states of the samples. With this data set a more accurate calculation of the total current shall be possible.
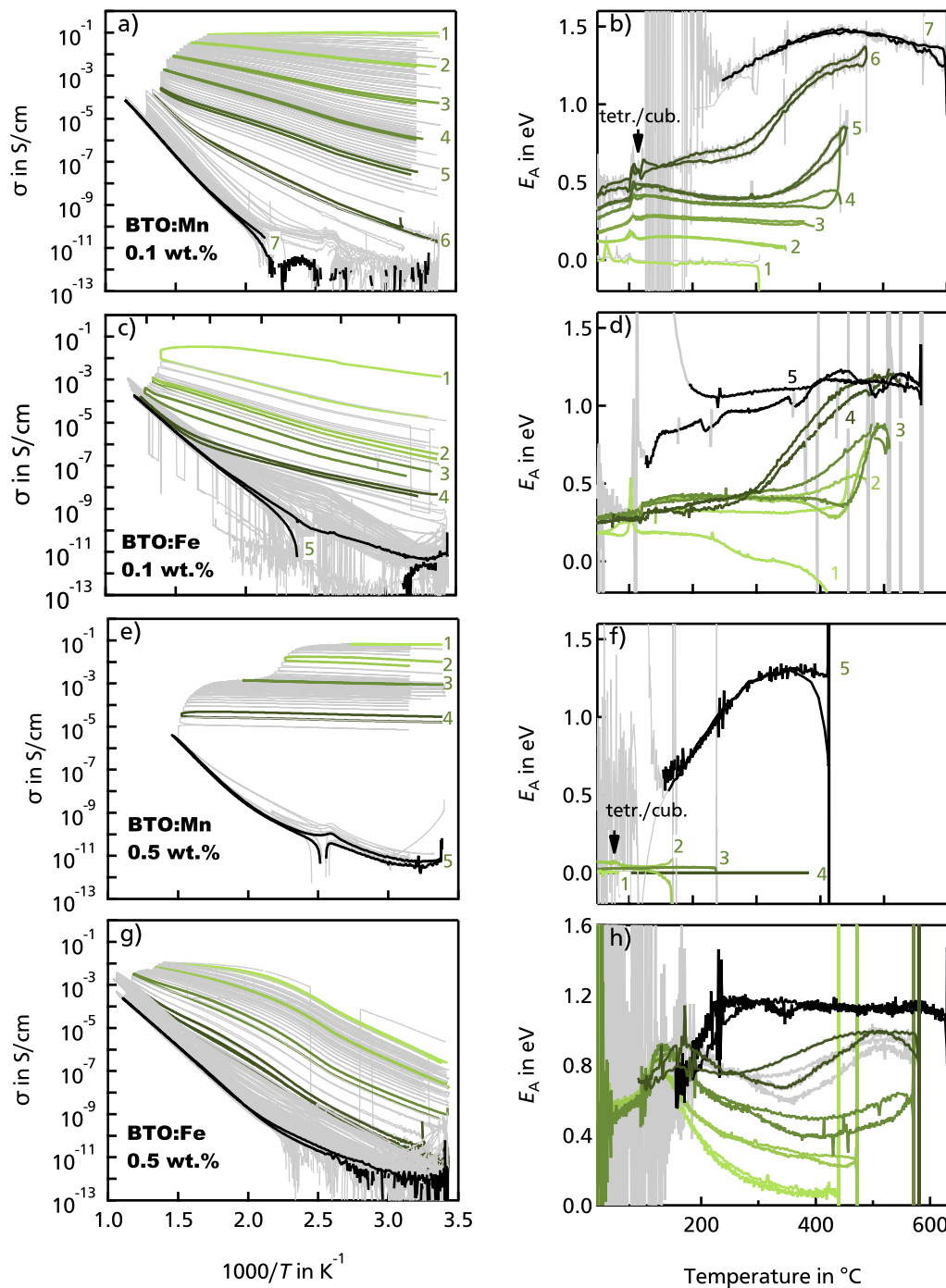
Figure A.21.: a), c), e) and g) Temperature-dependent conductivity loops of 0.1 wt.% and 0.5 wt.% Mn- and Fe-doped BaTiO$_3$. The green highlighted loops have been chosen for a calculation of the temperature dependent activation energy. The gray lines in b), d), f) and h) correspond to the direct calculations of E_A and the green lines to a smoothed calculation to annihilate single peaks.

The calculation of the temperature-dependent activation energy has been done assuming Arrhenius type behavior. The temperature dependent activation energy has been calculated by using the differentiate tool implemented in IGOR Pro software (Wavemetrics) by applying a central differences algorithm and an approximation for the end point.
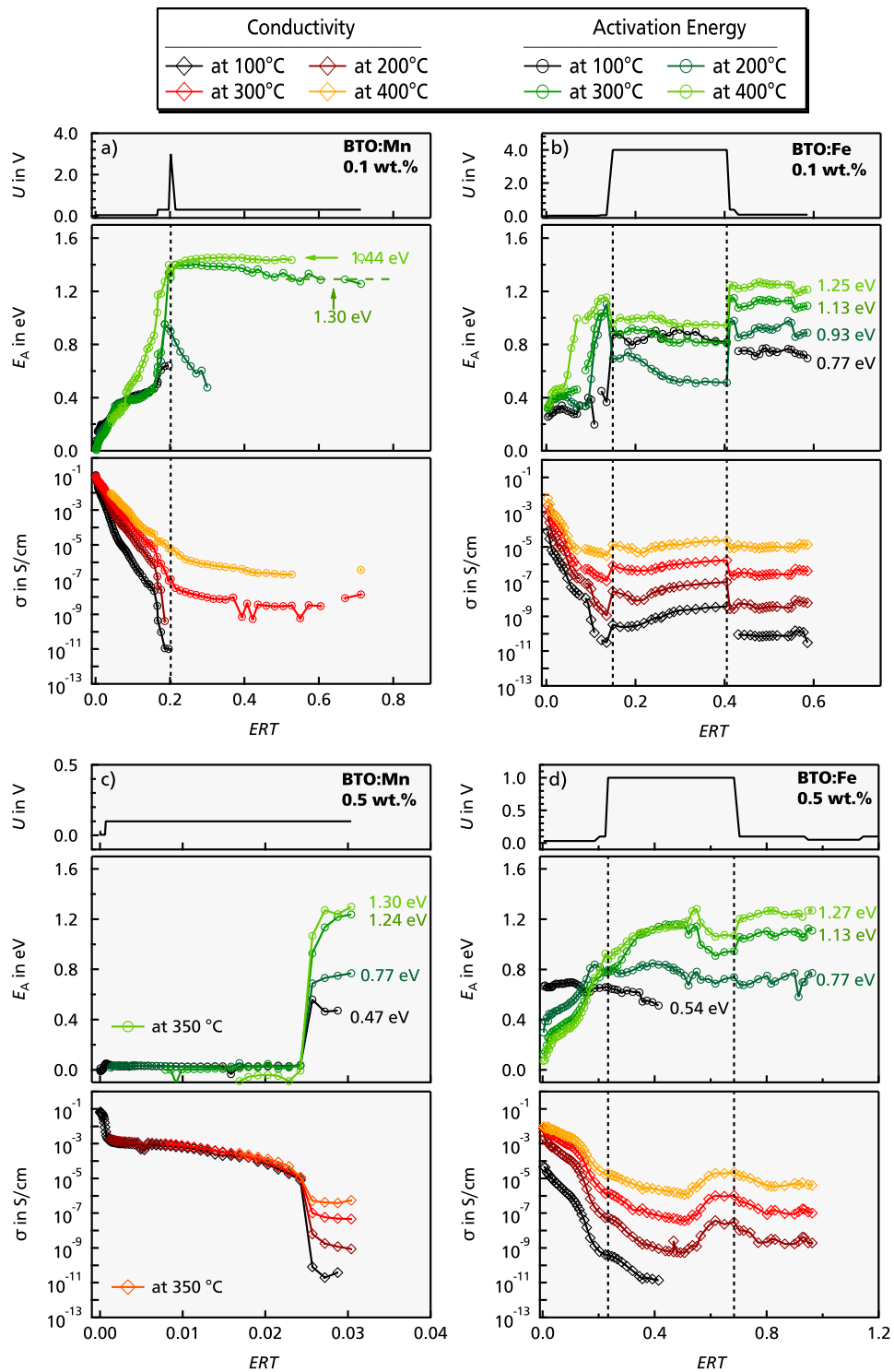
Figure A.22.: Voltage, activation energy, and conductivity in dependence of the equivalent re-oxidation time (*ERT*) for 0.1 wt.% and 0.5 wt.% Mn- and Fe-doped BaTiO₃, respectively.
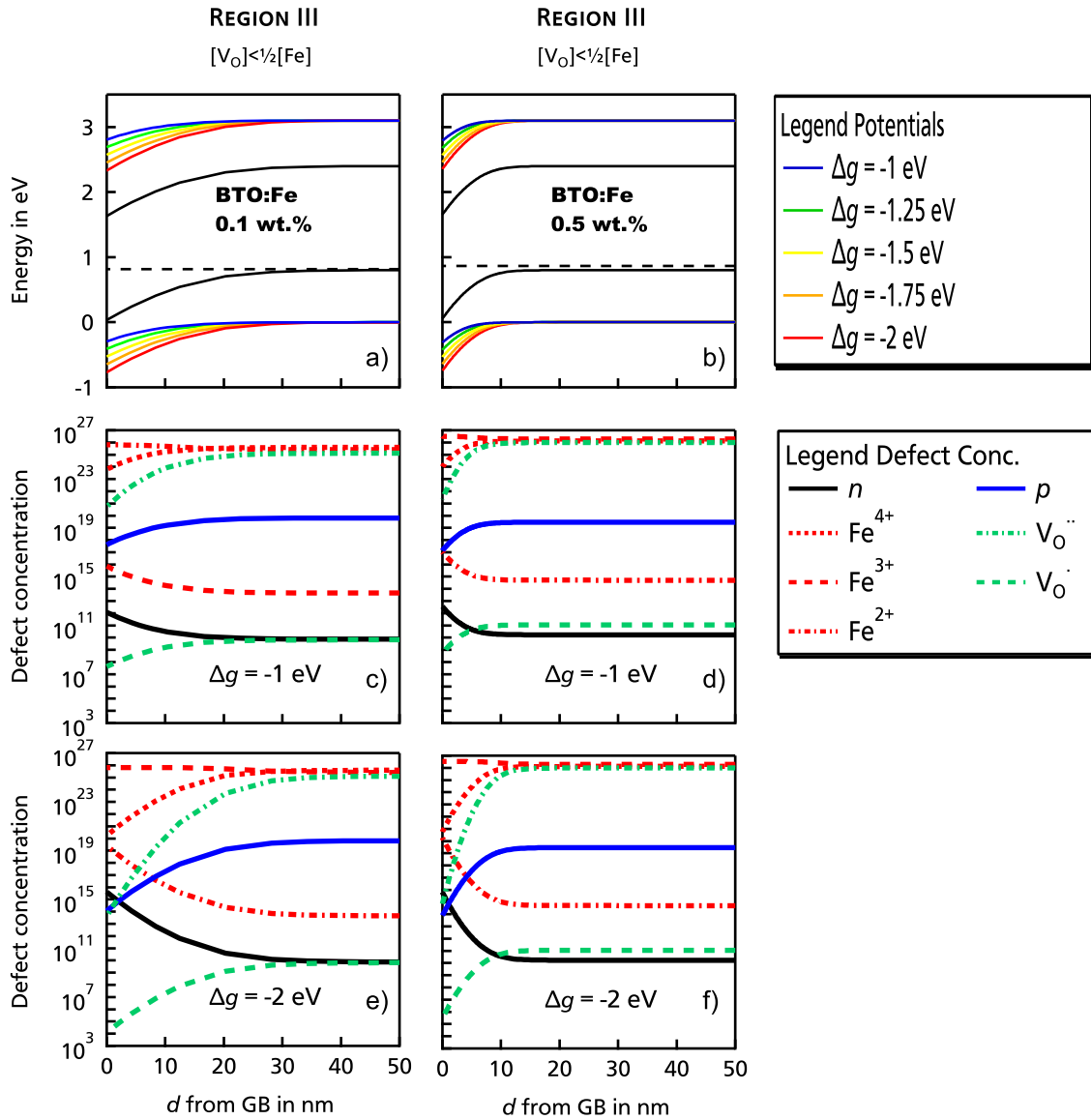
Figure A.23.: Calculated potential profiles a) and b) for 0.1 wt.% and 0.5 wt.% Fe-doped BaTiO$_3$ at 400 °C in **REGION III** at $c(V_O) = 1.3 \times 10^{25}$ cm^{-3} and V$_O$) = 9.75 $\times 10^{25}$ cm^{-3}, respectively. The Fe concentration is $c(\text{Fe}) = 6.5\ 10^{25}$ cm^{-3} and $c(\text{Fe}) = 3.25 \times 10^{26}$ cm^{-3}, respectively. The corresponding defect concentration profiles are given in c)-f) for $\Delta g = -1$ eV and $\Delta g = -2$ eV.
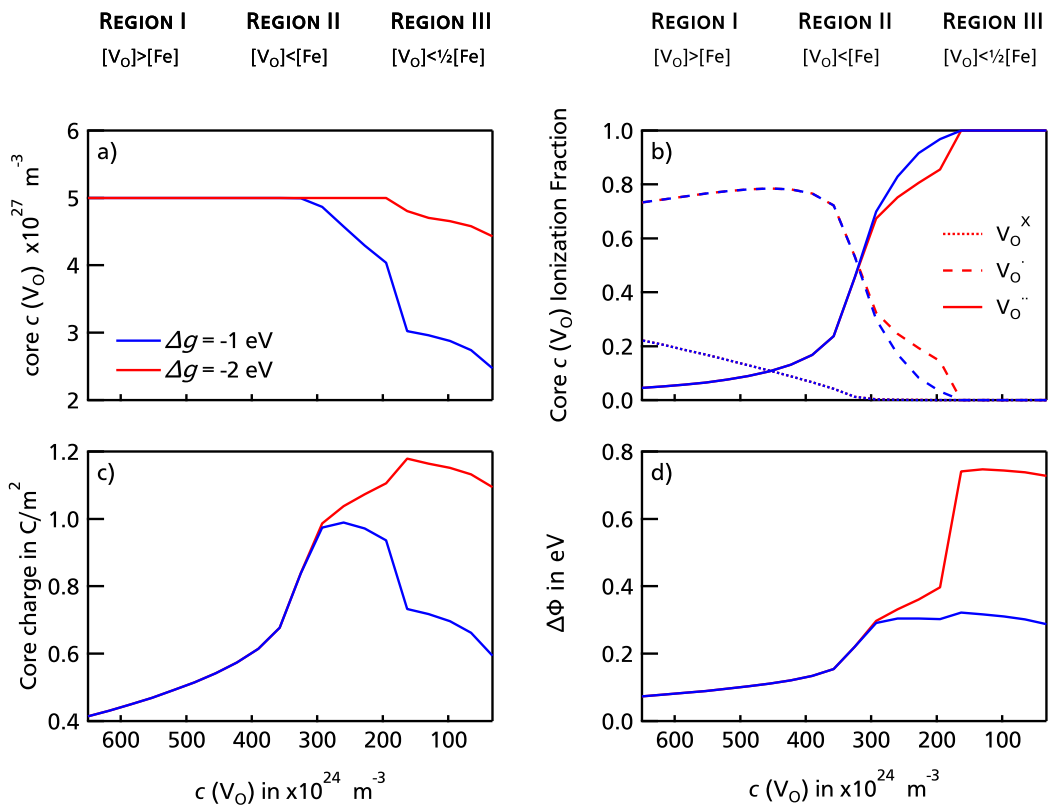
Figure A.24.: a) Core oxygen vacancy concentration, b) core oxygen vacancy ionization fraction, c) core charge, and d) and potential difference between bulk and grain boundary core for 0.5 wt.% Fe-doped BaTiO$_3$ for $\Delta g = -1$ eV and $\Delta g = -2$ eV.

A.5. Appendix to Chapter 8

Another factor, which has been neglected so far in this thesis, is the influence of cation vacancies. Cation vacancies are expected to be immobile at equilibration, re-oxidation, and degradation temperatures. At reduction temperatures, in contrast, cation vacancies are mobile and could re-distribute. During quenching from reduction temperature to RT the cation vacancy distribution is frozen. Hence, only the oxygen vacancy profile is altered during re-oxidation/equilibration. Therefore, the grain boundary characteristics of a directly equilibrated sample could be consid-erably different to one, which has been reduced and re-oxidized before the final equilibration. The influence of reduction, re-oxidation, and equilibration prior degradation has been studied on one set of 0.2 wt.% Mn-doped samples. For this purpose, degradation curves of 0.2 wt.% Mn-doped BaTiO$_3$ samples after three different treatments have been recorded. The first two samples faced the usual equilibration treatment before degradation and are used as reference samples. One equilibrated sample was degraded at 205 °C and the other one at 230 °C. The second two samples have been reduced and re-oxidized before degradation. Again, one reduced equilibrated sample was degraded at 205 °C and the other one at 230 °C. A last sample has first been reduced and re-oxidized, followed by an equilibration before the degradation experiment. This sample has been degraded at 205 °C.

The recorded degradation curves and the corresponding extracted degradation times are given in Figure A.25 a) and b), respectively. For the same degradation temperature reduced and re-oxidized samples degrade significantly faster than the equilibrated samples. This is most likely related to an incomplete re-oxidation of the reduced samples. The comparison of experiment and simulation in Figure 7.22 b) indicated, that the oxygen incorporation during re-oxidation lowers the Fermi level close to the Mn$^{2+/3+}$ charge transition level. The defect chemistry calculations on equilibrated Mn-doped BaTiO$_3$ in contrast, indicated a Fermi level close to the Mn$^{3+/4+}$ charge transition level. Hence, the higher amount of oxygen vacancies in the reduced and re-oxidized 0.2 wt.% Mn-doped sample is most likely responsible for the considerable faster degradation times. In contrast, the reduced, re-oxidized and equilibrated sample exhibits a (slightly) higher degradation time than the reference samples.

As degradation is a thermally activated process the temperature dependence can be described by $t_{\text{deg}} \propto \exp(-E_{\text{A}}/k_{\text{B}}T)$. The extracted degradation times as a function of inverse sample temperature are shown in Figure A.25 b). The activation energy for equilibrated 0.2 wt.% Mn-doped BaTiO$_3$ has been determined as 1.15 eV. This is in good agreement with the value of 1.13 eV for Mn-doped BaTiO$_3$ derived by Rödel and Tomandl [7] and other typical activation energies of 1.1 eV to 1.4 eV for titanates [4, 57]. For reduced and re-oxidized samples the activation energy is increasing to 2.09 eV. As only two data points are available for the activation energy determination of reduced and re-oxidized samples, a high uncertainty is assumed.

Hence, a discussion is omitted and further experiments are recommend to achieve a value with reasonable statistical certainty.

For a degradation temperature of 205 °C the degradation time of the reduced, re-oxidized and equilibrated sample is increased by a factor of 1.5 compared to the reference equilibrated sample. The increased degradation time could indicate a stronger blocking behavior of the grain boundaries of samples in the reduced, re-oxidized and equilibrated state. The reference sample has been equilibrated at 900 °C, for which cation vacancies are assumed to be immobile. Accordingly, these samples show the cation vacancy profile being established during sintering. In contrast, the cation vacancies in the reduced, re-oxidized and equilibrated sample have been mobile during reduction at 1100 °C and have most likely rearranged[9]. The oxygen vacancies are assumed to be accumulated in the grain boundary core, which may lead to an enhanced segregation of the negative charged cation vacancies to the space charge region.
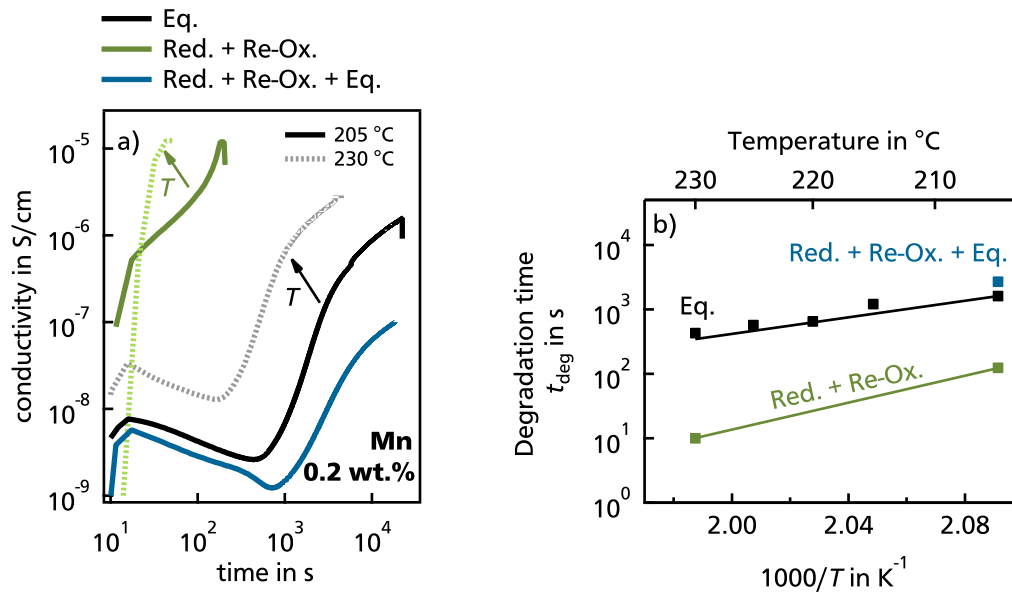
Figure A.25.: a) Degradation curves of 0.2 wt.% Mn-doped BaTiO$_3$ after equilibration, reduction + re-oxidation, and reduction + re-oxidation + equilibration. b) Arrhenius plot of the measured degradation times as a function of inverse sample temperature. For 0.2 wt.% Mn-doped BaTiO$_3$ the degradation time of the other temperatures (see Fig. 8.1 and 8.2) are included as well. The activation energy for equilibrated 0.2 wt.% Mn-doped samples is 1.15 eV, while reduced + re-oxidized samples exhibit an activation energy of 2.09 eV.

---

[9]A change in the defect concentrations is evident from the changed surface stoichiometry observed after reduction (see Subsection 6.1.1). Following mass conservation, the enhanced Ba-concentration at the surface needs to be accompanied by the same concentration of Ba-vacancies. The created Ba-vacancies could then segregated to the position with the lowest formation energy.

Publications and Conference contributions

Publications

2022   Wardenga, H. F., <u>Schuldt, K. N. S.</u>, Waldow, S., De Souza, R. A., & Klein, A. (2022). Surface potentials of acceptor-and donor-doped CeO_2 thin films and their relation to oxygen surface exchange. Physical Chemistry Chemical Physics, 24(2), 1072-1080.

2021   <u>Schuldt, K. N. S.</u>, Ding, H., Jaud, J. C., Koruza, J., & Klein, A. (2021). Influence of Defects on the Schottky Barrier Height at $BaTiO_3/RuO_2$ Interfaces. physica status solidi (a), 218(14), 2100143.

Conference Contributions and Summer Schools

2020   **Materials Science and Engineering Congress (online)**
Defect Level Identification using XPS: Fermi Level pinning, access limitations, and simulations - *oral presentation*

                  Electroceramics Conference XVII (online)
Defect Level Identification using XPS - *oral presentation*

                  Electroceramics Conference XVII (online)
Fermi level variation in Sr-doped $LaFeO_3$ - *poster presentation*

2019   **FLAME Summer School (La Clusaz, France)**
Resistance Degradation - Origin, Electrode Influences and difference between poly- and single crystals - *oral presentation*

                  European Meeting on Ferroelectricity (Lausanne, Switzerland)
Fermi level variation in Sr-doped lanthanum ferrite - *oral presentation*

Supervised Theses

2021   **Sabrina Kahse**

Investigation of the Stability of the BTO|ITO and KNN|ITO Interface, *ARL*

2020   **Lisanne Gossel**

Influence of Grain Boundaries and Defect Energy Levels on the Electrical Properties of Acceptor-doped Polycrystalline BaTiO$_3$, *Masters's Thesis*

Lisanne Gossel

Influence of Defect Segregation at Grain Boundaries on the Electrical Properties of Acceptor-doped Polycrystalline BaTiO$_3$, *Research Internship*

2019   **Dominik Moritz**

Fermi level limitations in copper oxides for solar cell applications, *Master's Thesis*

Nicola Gutmann

Einfluss der Mn-Dotierung auf die elektrische Leitfähigkeit von polykristallinem BaTiO$_3$, *Bachelor's Thesis*

Co-Supervision of **Baris Öcal** and **Achim Alkemper** in the field of solid-state-synthesis of acceptor-doped BaTiO$_3$, electrical measurements, and result interpretation. Supervision of student research assistants **Hui Ding** and **Baris Öcal**.

Danksagung